Detailed Numerical Modelling of the Interaction between Sound and Green Noise Reducing Measures

Gedetailleerde numerieke modellering van de interactie tussen geluidsgolven en groene geluidsreducerende maatregelen

Lei Ding

Promotoren: prof. dr. ir. D. Botteldooren, prof. dr. ir. T. Van Renterghem
Proefschrift ingediend tot het behalen van de graad van
Doctor in de Ingenieurswetenschappen

Vakgroep Informatietechnologie
Voorzitter: prof. dr. ir. D. De Zutter
Faculteit Ingenieurswetenschappen en Architectuur
Academiejaar 2014 - 2015

UNIVERSITEIT
GENT

ISBN 978-90-8578-740-2
NUR 910, 950
Wettelijk depot: D/2014/10.500/86

Universiteit Gent
Faculteit Ingenieurswetenschappen en Architectuur
Vakgroep Informatietechnologie

Promotoren:

Prof. dr. ir. Dick Botteldooren
Prof. dr. ir. Timothy Van Renterghem

Examencommissie:

Prof. dr. ir. Luc Taerwe (voorzitter)	Universiteit Gent
Prof. dr. ir. Dick Botteldooren (promotor)	Universiteit Gent
Prof. dr. ir. Timothy Van Renterghem (promotor)	Universiteit Gent
Prof. Kirill Horoshenkov	University of Sheffield
Prof. dr. ir. Deniel De Zutter (secretaris)	Universiteit Gent
Prof. dr. ir. Bert De Coensel	Universiteit Gent
Prof. dr. ir. Arnold Janssens	Universiteit Gent

Universiteit Gent
Faculteit Ingenieurswetenschappen en Architectuur

Vakgroep Informatietechnologie
Sint-Pietersnieuwstraat 41, B-9000 Gent, België

Tel.: +32-9-264.33.18
Fax.: +32-9-264.35.93

Proefschrift ingediend tot het behalen van de graad van
Doctor in de Ingenieurswetenschappen
Academiejaar 2014 - 2015

Acknowledgements

It would not have been possible to write this doctoral thesis without the help and support of the kind people around me; to only some of whom it is possible to give particular mention here.

I wish to express my gratitude to my principal supervisor Prof. Dick Botteldooren for suggesting me this interesting topic and for providing tireless guidance. This thesis would not have been possible without his advice, help, support and patience. In addition, my great appreciation belongs to another supervisor Prof. Timothy Van Renterghem. His good advice, support, and friendship have been invaluable on both academic and personal level, for which I am extremely grateful.

I would like to acknowledge Prof Kirill Horoshenkov (and others) from the University of Sheffield, who conducted some experimental measurements presented in this thesis.

I am grateful to Peter Guns for his support and assistance in my measurements and Kristien De Meulder for solving all computer-related problems. I also want to thank Dr. Yanlu Li and Dr. Yufeng Niu to let me use their equipment for my measurements.

I would like to thank all current and former colleagues in the acoustics group --- Annelies, Arnaud, Bert, Bram, Damiano, Gemma, Isabelle, Karlo, Laurent, Luc, Michiel, Mirjana, Pieter, Ramanan, Weigang and Xiaodong for their selfless sharing of the knowledge and for their instant help and support. I thank my friends in Belgium, China and elsewhere for their support and encouragement.

Naturally my invaluable gratitude belongs to my family and relatives. Last but not least, my dearest appreaciation goes to my wife Xin Kang and my son Xiangwei Ding.

Lei Ding

Ghent, October 1, 2014

Table of Contents

Samenvatting

Langdurige blootstelling aan omgevingslawaai krijgt stilaan de aandacht die dit milieuprobleem verdient, in hoofdzaak door het feit dat de negatieve impact op de gezondheid en levenskwaliteit steeds duidelijker wordt. Vooral in een stedelijke omgeving is dit een belangrijk probleem; de blootstelling aan wegverkeerslawaai blijft dan ook stijgen door de steeds sterkere verstedelijking en stadsverdichting. Belangrijke gezondheidsgerelateerde effecten door blootstelling aan verkeerslawaai zijn slaapverstoring, hinder en de hieraan gerelateerde stresseffecten, de bijdrage aan cardiovasculaire ziektes alsook bijvoorbeeld de negatieve impact op het cognitief functionering van de mens. Een van de belangrijkste uitdagingen voor onderzoekers in het domein van omgevingslawaai is het zoeken naar oplossingen om de negatieve invloed van verkeer op de maatschappij te beperken in het licht van duurzame stadsontwikkeling.

Het gebruik van natuurlijk en duurzame materialen, zoals bijvoorbeeld vegetatie, groendaken en groene muren wint steeds meer aan populariteit. Dergelijke materialen interageren met de geluidsgolven op het pad tussen bron en ontvanger, en kunnen bij goed ontwerp bijdragen aan geluidsreductie. Dit werk focust op de numerieke modellering bij dergelijke interacties.

De eindige-differenties-in-het-tijdsdomein model (finite-difference time-domain, FDTD) werd reeds succesvol toegepast voor het analyseren van allerhande omgevingslawaaiproblemen en het ontwerp van geluidsreducerende oplossingen. Vooral door zijn hoge flexibiliteit werd geopteerd voor deze numerieke tijdsdomeintechniek, om in het bijzonder de interactie tussen geluidsgolven en bladeren, alsook het effect van lage begroeide geluidsmuren te onderzoeken. Hiervoor werden verschillende uitbreidingen op het basismodel geïmplementeerd.

De interactie tussen geluidsgolven en bladeren werd in detail gemodelleerd in een 3D eindige-differenties-in-het-tijdsdomein model. Het doel is meer inzicht verwerven in de mogelijkheid om vegetatie te gebruiken als geluidsreducerende maatregel en het identificeren wat de relevante parameters zijn. Het buigen en draaien van bladeren onder invloed van een invallend geluidsveld werd geïncludeerd in het rekenmodel, inclusief de interne demping die dergelijke processen veroorzaken. Ook de energie die verloren gaat in de vorticiteits- en entropiegrenslagen van het blad werden meegerekend. Het poreus-elastisch Biot model werd geïmplementeerd om ook de aanwezigheid van poreuze materialen (bijvoorbeeld natuurlijke bodems of groeisubstraten) in detail in te kunnen schatten.

Het model werd gevalideerd door middel van twee soorten metingen. Enerzijds werd de drukval over een enkel blad(oppervlak) in een geluidsveld gemeten, alsook de snelheid waarmee het blad trilt. Een dergelijk experiment werd uitgevoerd voor 7 verschillende types bladeren. In een tweede experiment werd de absorptiecoëfficiënt van een poreus materiaal, bedekt met een blad, bepaald in een impedantiebuis. De numerieke voorspellingen in beide experimenten toonden aanvaardbare tot zeer goede overeenkomsten met de metingen.

In een tweede stap werd de invloed van bladoppervlaktedichtheid numeriek onderzocht. Deze simulaties toonden dat een beperkte bladoppervlaktedichtheid resulteerde in sterkere verbetering van de absorptiecoëfficiënt bij lage frequenties, t.o.v. een substraat dat niet bedekt werd door een blad, dan bij een hogere bladoppervlaktedichtheid. Geluidspropagatie doorheen een reeks bladeren is een meer realistisch setting. Dit werd numeriek gemodelleerd door gebruik te maken van cyclische randvoorwaarden, wat de rekenkost sterk verlaagt in een dergelijke setting. Een dergelijke benadering resolveert expliciet een beperkt aantal bladeren, waarbij de geluidsgolven verschillende malen propageren doorheen doorheen een dergelijke volume.

Het effect van lage absorberende geluidsmuren, geplaatst in een straat, werd onderzocht door middel van numerieke modellering alsook met een schaalmodel. Een dergelijke maatregel kan de geluidsblootstelling voor wandelaars op het voetpad beperken. Een schaalmodel (schaalfactor 30) van een straat werd geconstrueerd, met een zeer sterke graad van geveldetail. De extra attenuatie door de lucht, veroorzaakt door het meten bij hoge (opgeschaalde) geluidsfrequenties, werd gecompenseerd door middel van een wavelet-gebaseerde methode. In een eerste stap werd de accuraatheid van het schaalmodel gevalideerd door vergelijking met metingen in de straat (volle schaal) zelf. In een volgende stap werd het effect van lage absorberende geluidsschermen gemeten in het schaalmodel en numeriek gesimuleerd in een dwarsdoorsnede ter hoogte van de bron. De materiaaleigenschappen van het poreus scherm werden gemodelleerd met behulp van het Zwikker en Kosten model, waarbij een star frame werd verondersteld. Het effect van resonanties van de materiaalmatrix was eerder beperkt, terwijl het gebruik van het Biot model leidde tot een significante stijging in de rekenkost. De simulaties toonden duidelijk het belang aan van een goede benadering van het geveldetail. Diffuse reflectie is bijgevolg een essentieel aspect van geluidspropagatie in een zogenaamde streetcanyon. Met stijgende ontvangerhoogte werd het effect van de schermen zeer beperkt. De aanwezigheid van reflecterende facades zorgde er verder voor dat de efficiëntie van een dergelijk geluidsscherm in de straat sterk daalde bijv. ten opzichte van een toepassing in een niet-stedelijke omgeving.

In aanloop naar de ontwikkeling van een volledig drie-dimensionaal numeriek model werd een andere techniek onderzocht nl. de ultra-weak variational formulation (UWVF). Een dergelijk rekenmodel is nodig om bijvoorbeeld effecten van realistische 3D verstrooiing van geluid op gevels te onderzoeken, het effect van zijstraten te bekijken, of om rekening te houden met de eindige lengte (of onderbrekingen) van een laag geluidsscherm. Een belangrijk voordeel van UWVF is dat slechts 2 rekencellen per golflengte nodig zijn, ten opzicht van 10 rekencellen in FDTD. Een ander voordeel is dat de geluidsbronpositie niet expliciet dient vastgelegd te worden in het rekenrooster, wat nuttig is bij typische verkeersconfiguraties met meerdere rijstroken. Bovendien werd een efficiënte techniek ontwikkeld om te rekenen in octaafbanden, wat nuttig is gezien de meeste omgevingslawaaibronnen breedbandig zijn. Om te verhinderen dat een nieuwe berekening dient gestart te worden voor elke afzonderlijke frequentie, zoals klassiek gebeurt bij een frequentiedomeintechniek, werd het aantal nodige basisfuncties in elke gridcel verkregen door middel van interpolatie. Op deze manier werd de rekenkost die een dergelijke initiële operatie met zich meebrengt sterk gereduceerd (wat leidde tot een finale reductie in totale rekentijd tussen 40 en 70 %). Er werd bovendien aangetoond dat de zogenaamde “perfectly matched layers” (PML) makkelijk kunnen geïmplementeerd worden in de UWVF techniek (om het oneindig propagatiedomein te beperken tot een eindig rekengebied). Een twee-dimensionale versie van de UWVF techniek werd met succes gevalideerd door vergelijking met FDTD als referentie-oplossing, in geval van diffractie over een laag absorberend geluidsscherm met een complexe vorm, alsook voor geluidspropagatie over een vlakke absorberende grond in de aanwezigheid van een verticale geluidssnelheidsgradiënt.

English summary

Noise pollution has drawn people's attention as it negatively impacts human well-being. Especially in an urban environment, traffic noise has inevitably increased with human activities and city expansion. It has been reported that the adverse effects of exposure to traffic noise range from annoyance over sleep disturbance, to negative impacts on cognitive functioning and to cardiovascular diseases. Therefore, one of the main challenges for environmental acousticians is to find ways to reduce the negative influences of traffic noise to ensure sustainable development of our societies.

Recently, natural/sustainable materials or structures, such as vegetation, green roofs or green wall systems are gaining popularity. They interact with sound waves along the path from source to receiver. This work focuses on numerical modeling of such materials.

The finite-difference time-domain (FDTD) method has been used successfully in outdoor acoustics before. Given its high flexibility, the FDTD method is chosen to study the influences of low-height noise barriers and leaves. Several extensions to the FDTD method have been implemented in this thesis.

The bending and twisting of the leaves are implemented in the three-dimensional finite-difference time-domain (3D-FDTD) method in order to provide a more accurate simulation of the effects of the leaves on the sound field. The internal damping in the process of bending is included. The energy damping in the vorticity and entropy boundary layers of the leaves is also taken into account. When a porous material is present (e.g. in case of soil or growing substrates), Biot's model is used.

This model is validated by two types of measurements. The first type measures the pressure difference over the leaf and the velocity of a particular point on the leaf. Seven different leaf species are considered and the measurements agree reasonably well with the simulations. In the second type of measurements, the sound absorption coefficient of a porous material covered by a leaf is measured in an impedance tube. Two porous materials and four types of leaves are used. Biot's model is implemented in the FDTD method to simulate frame resonances in the porous materials. The simulations show a good agreement with the measurements. The integration of the leaf bending successfully models the fluctuations in the measured absorption coefficient.

Afterwards the extended FDTD method is used to study the influences of leaf surface density (LSD) on the materials' absorption coefficient. It shows that the leaves with small LSD result in a stronger enhancement in the low-frequency range. In a next step, this model is applied to study the behaviour of a group of leaves. Cyclic boundary conditions are used in order to improve the efficiency of the calculation. Three types of vegetation are taken into account. The normalized excess attenuation curves show a similar behaviour as in the measurements performed by Aylor. It is also noted that more leaves attenuate more energy because of stronger backscattering and higher energy dissipation.

A two-dimensional FDTD method is also used to study the effect of low-height noise barriers in a street canyon. The absorbing low-height noise barriers are modelled by the rigid-frame Zwikker and Kosten's model, because the effect of frame resonances on the material's absorption coefficient is rather small and the Biot's model involves a higher computational cost. A highly detailed 1:30 scale model is constructed according to a real street canyon and its reliability is confirmed with comparison to the measurements in the real street canyon (full-scale measurements). Furthermore, the scale model measurements in the cross-section of the sound source are compared to simulation. Both flat and uneven facades are considered in the two-dimensional FDTD simulation. The comparison shows the importance of accounting for diffuse reflection at the facades.

The scale model measurements investigate the effect of absorbing low-height noise barriers along the street canyon. Three receiver-height levels above the pavement are considered. In is found that absorbing low-height noise barriers have a significant influence on the sound pressure levels at the lowest observation height. This influence decreases when the height of observation increases. The presence of building facades strongly reduces the shielding provided by such low-height barriers.

This work also plans to develop a full three-dimensional numerical model in order to include effects such as finite length low-height noise barriers or 3D scattering on facades. Because of the high computational cost in full-wave techniques, the method should be sufficiently flexible to allow coupling to other methods. Therefore, the ultra-weak variational formulation (UWVF) method is studied. It is successful in calculating the effects of low-height noise barriers in a two-dimensional problem. Unlike the traditional finite-difference and finite-element methods, needing 10 grid cells per wavelength, the UWVF method can choose fewer grid cells per wavelength. The UWVF method doesn't need the sound source to be included in the computational domain. The overall

conditioning of the UWVF method could be improved by adjusting the number of basis functions within each computational grid cell. An efficient approach to determine the number of basis functions for the frequencies in the same octave band is used in this work. Besides, when the position of sound source is changed, the UWVF method does not need to reassemble all the elements in the linear system and this helps reducing the computational cost in realistic traffic situations. Furthermore, the perfectly matched layer (PML) theory is applied in the UWVF technique to truncate the unlimited propagation domain.

The 2D-UWVF code developed in this work has been successfully validated in two cases by comparison with the finite-difference time-domain (FDTD) method. One practical example about two types of vehicles in a two-lane road is investigated. It is proved that the low-height noise barriers can significantly reduce the noise levels behind them. Moreover, the low-height noise barriers constructed by absorbing materials show a better performance than the rigid barriers.

Nomenclature

A_d	Matrix calculated by the derivatives of complex stretched variables, 2.6
A_{inc}, A_{ref}	Wave amplitude, 5.2
A_{Leaf}	Leaf projected area, 3.4
A_s	Amplitude of the source, 5.1
a_s	Parameter determining the signal bandwidth, 5.1
B	Block diagonal matrix, 4.3
B_1, B_2	Wave amplitude, 5.2
b	Vector related to external boundary and source, 4.3
C	Matrix in UWVF, 4.3
$Cond(.)$	Condition number, 4.4
CN	Courant number, 3.3
C_1, C_2	Wave amplitude, 5.2
c	Speed of sound, 2.2
c'	Modified speed of sound ($c' = c/\sqrt{k_s}$), 2.5
D	Bending stiffness per unit width, 2.3, 3.1
D_i	Bending stiffness per unit width, 2.3
D_0	Bending stiffness per unit width without damping term, 2.3
$\widetilde{D}_i$	Laplace transform of bending stiffness per unit width, 2.3
d	Spatial dimension, 2.6
d_{BL}	Boundary layer thickness, 3.1
d_{PML}	Thickness of the PML, 2.6
d_{Leaf}	Thickness of the leaf, 3.2
d_x, d_y, d_z	Derivatives of complex stretched variables, 2.6, 4.1
d_{PML}	Thickness of the PML, 2.6
D	Bending stiffness per unit width, 2.3, 3.1
E	Young's modulus of the leaf material, 2.3
e	Internal energy per unit mass, 2.1, 2.4
$e_{i,j}$	Shear strain when $i \neq j$ and normal strain when $i = j$
e_{all}	Sum of the normal strain ($e_{i,i} + e_{j,j} + e_{k,k}$), 2.5
f	Porosity, 2.5
f_c	Central frequency, 5.1
f_k	Source term in Ω_k, 4.1
f_s	Source term, 2.6
g_i	Body force per unit mass in i-direction, 2.1
g_k	Boundary source term, 4.1
H_{12}, H_I, H_R	Transfer functions for the incident wave, reflected wave and total sound field, respectively, 5.1

h	Thickness of the leaf/plate, 2.3
I	Unit vector/matrix, 4.4
i	Imaginary unit: $i=\sqrt{-1}$, 2.2
K	Thermal conductivity, 2.4
K_0	Bulk modulus for an open system, 2.5
K_c	Bulk modulus for a closed system, 2.5
K_a	Bulk modulus of the fluid in the porous medium, 2.5
K_f	Bulk modulus of the solid frame in the porous medium, 2.5
k	Permeability matrix, 2.5
k_0	Wave number, 5.1
k_b	Bending wave number in plate/leaf, 3.4
k_s	Structure factor, 2.5
M_D	Leaf dry mass, 3.4
M	Elastic coefficient, 2.5
M_F	Leaf fresh mass, 3.4
M_y, M_z	Bending moments, 2.3
$\widetilde{M}_y, \widetilde{M}_z$	Laplace transforms of the bending moments, 2.3
M_{yz}	Twisting moments, 2.3
$\widetilde{M}_{yz}$	Laplace transform of the twisting moments, 2.3
m	Coefficient determined by the fluid density, the coordinates in the pore and the pore geometry, 2.5
m_a	Mass per unit area, 3.4
n_k, n_j	Outgoing unit normal, 4.1
P	Pressure, 2.2
$\tilde{P}$	Laplace transform of the pressure, 2.3
P_a	Pressure of the fluid averaged in the bulk materials, 2.5
P_{frame}	Pressure of the solid frame, 2.5
P_{normal}	Artificial pressure component normal to the interface between the region of interest and the PML, 2.6
$P_{parallel}$	Artificial pressure component parallel to the interface between the region of interest and the PML, 2.6
P_0	Steady term of pressure P or ambient atmospheric pressure, 2.5
P_f	Fluid pressure, 2.5
P_s	Pressure on the solid materials, 2.5
P_t	Pressure on the total bulk materials, 2.5
p	Time-harmonic acoustic pressure, 2.2
p_k	Time-harmonic acoustic pressure in sub-domain Ω_k, 4.2
Q_k	Complext boundary constant, 4.1
q_i	Heat flux per unit area in i-direction, 2.1

$\vec{q}$	Heat flux, 2.4
R	Flow resistivity, 2.5
R_f	Coefficient for the internal dissipation in the solid frame, 2.5
R_L	Viscous damping coefficient, 2.3
R_n, $R_{i,n}$	Damping coefficients, 2.3
R_s	Ideal gas constant, 2.4
r	Radial coordinate, 2.6
r_c	Reflection coefficient, 5.1
r_{cc}	Correlation Coefficient, 3.4
S	Entropy, 2.4
S_{pulse}	Sound source, 5.1
$\hat{s}$	Signal in frequency domain, 5.2
s	Signal in time domain, 5.2
s_n, $s_{i,n}$	Damping coefficients, 2.3
T_0	Static temperature, 2.4
t_c	Central time, 5.1
U_x, U_y, U_z	Displacement of the fluid in three directions, 2.5
u_x, u_y, u_z	Displacement of the solid frame in three directions, 2.5
u, v, w	Three orthogonal directions, 5.2
$\vec{V}$	Fluid velocity vector, 2.1
$\mathbf{V}_a$	Velocity vectors of the fluid, 2.5
$\mathbf{V}_f$	Velocity vectors of the solid frame, 2.5
V_L	Volume of the leaf, 3.4
V_n	Normal velocity, 2.4
V_t	Tangential velocity, 2.4
v_α	Velocity component normal to the interface between the region of interest and the PML, 2.6
v_{xa}, v_{ya}, v_{za}	Velocities of air in x, y and z directions, 2.5, 3.1
v_β	Velocities components parallel to the interface between the region of interest and the PML, 2.6
v_γ	Velocity parallel to the leaf surface plane, 3.1
v_{xf}, v_{yf}, v_{zf}	Velocities of solid frame in x, y and z directions, 2.5, 3.1
v_i	i-component of the velocity $\vec{V}$ and $i=x, y, z$, 2.1
v_k	Smooth test functions in sub-domain Ω_k, 4.2
v_x	x-component of the velocity $\vec{V}$, 2.1
v_{xp}	Velocity in the x-direction (normal to the plate surface), 2.3
v_y	y-component of the velocity $\vec{V}$, 2.1
v_z	z-component of the velocity $\vec{V}$, 2.1
W	Displacement normal to the leaf surface, 2.3

$\widetilde{W}$	Laplace transform of the displacement, 2.3
w_x, w_y, w_z	Flow of the fluid relative to the solid in three directions but measured in terms of volume per unit area of the bulk medium
α	Elastic coefficient with value between porosity and 1, 2.5
α_j	Incident angles, 2.6
α_{pm}	Absorption coefficient, 5.1
$\sigma_{0,\xi}$	PML decay parameter, 2.6
$\Sigma_{k,j}$	Interface between *k*th and *j*th finite element or subdomain, 4.1
φ	Porosity, 2.5
$\varphi_{k,m}$	Basis function in Ω_k, 4.3
ϕ_0	Bending and twisting moments per unit thickness, 2.3, 3.1
ϕ	Visco-elastic damping during the bending of the leaf or plate, 2.3, 3.1
ε	Foliage bulk elastic modulus, 3.4
ξ	Spatial coordinates (x, y, or z), 2.6
ξ_0	Spatial coordinates of the interface of the PML, 2.6
Γ_k	Exterior boundary, 4.1
κ	Wave number, 2.2, 2.6
κ_k	Wave number in Ω_k, 4.1
κ'	Wave number in the porous medium, 2.5
$\kappa_{1,normal}$, $\kappa_{2,normal}$	Damping coefficients in the direction normal to the interface between the region of interest and the PML, 2.6
$\kappa_{1,max}$	Maximum damping coefficient, 2.6
$\kappa_{2,parallel}$, $\kappa_{2,parallel}$	Damping coefficients in the direction parallel to the interface between the region of interest and the PML, 2.6
η_d	Structural damping coefficient, 2.3
η	$\eta^2=d_x d_y d_z$, 2.6
ρ	Density of medium or bulk materials, 2.1, 2.5
ρ_a	Mass of the fluid per unit volume of bulk materials, 2.5
ρ_A	Average density in the control volume, 3.2
ρ_f	Mass density of the fluid, 2.5
ρ_{frame}	Mass of the solid frame per unit volume of bulk materials, 2.5
ρ_k	Density in Ω_k, 4.1
ρ_{Leaf}	Density of leaf, 3.2
ρ_m	Density of the leaf/plate, 2.3
ρ_0	Mass density of air, 2.2, 3.1
ρ'	Modified density ($\rho_0 k_s/\varphi$), 2.5
Ω_k	*k*-th finite element, 4.1

γ	Ratio of specific heats, 2.4
τ_{ij}	Stress in *i*-direction and acting on a surface normal to the *j*-direction, 2.1
μ	Lame's second parameter or shear modulus, 2.5
μ_f	Fluid dynamic viscosity, 2.4
μ_B	Bulk viscosity, 2.4
ν	Poisson's ratio of the leaf material, 2.3
υ	Specific volume ($1/\rho$), 2.4
ω	Angular frequency of acoustic wave, 2.2
λ	Lame's first parameter for an open system, 2.5
λ_b	Bending wavelength in plate/leaf, 3.4
λ_c	Lame's first parameter for a closed system, 2.5
$\|\cdot\|$	Norm of the matrix, 4.4

CHAPTER 1
Introduction

1.1 Urban traffic noise pollution and its control

Noise pollution in cities is one of the by-products of the technological revolution and urbanisation. Noise is present everywhere, both indoors and outdoors. In general, road traffic is a major contribution to the urban noise climate that has many adverse effects on people's wellbeing.

Nowadays, the influences of urban traffic noise are becoming worse, not only because the number of vehicles in urban transportation networks is gradually increasing, but also because the number of quiet hours during the night tends to be diminishing. The adverse effects of exposure to traffic noise range from annoyance over sleep disturbance, to negative impacts on cognitive functioning and to contribution to cardiovascular diseases (for an overview, see e.g. [1]).

In urban areas, common noise reduction measures are difficult to apply. A standard noise wall as found along the highways is not appropriate in a city centre, because such constructions are visually too intruding for both pedestrians and car drivers. However, there are still a variety of traditional measures that can be used to control and reduce the urban traffic noise, such as limiting vehicle speed, altering road surface materials, prohibiting the entrance of heavy vehicles to cities during some periods of the day, controlling the traffic flow to avoid sudden braking and acceleration, and encouraging the usage and design of low-noise tires. Unfortunately, most of these traditional measures are mainly used to reduce the rolling noise, arising from the contact zone in between the tire and the road surface. Because the typical vehicle speed in urban areas is usually limited, the engine noise is mostly dominant relative to rolling noise.

For the purpose of reducing not only the rolling noise but also engine noise in urban areas, some new approaches have been explored, including low-height noise barriers (the height is usually not more than 1m), the use of vegetation, etc. These new approaches are related to the concept of 'quieter and greener cities' and merit further study because of their potential to tackle some disadvantages in the traditional measures. Recently, a European collaborative project HOSANNA (holistic and sustainable abatement of noise by optimised combinations of natural and artificial means) studied such new approaches. This PhD work is related to and supported by the HOSANNA project; and is focused on studying some of the new approaches to mitigate urban traffic noise.

1.2 Quieter and greener cities

Vegetated areas and surfaces are greatly appreciated in urban environments because most of them have an aesthetical value and are visually pleasing, without involving large costs. Vegetated areas and surfaces are usually mentioned together with recycled materials in the city design, further adding to the benefit of low costs. Only very recently, the potential of urban green to make cities quieter became explored, and this work wants to contribute to such studies.

One important concern in the improvement of the quieter and greener cities is to optimise the use of green spaces, green surfaces and other natural elements in combination with artificial elements for reducing the noise impact of traffic. The corresponding noise mitigation methods act on the noise during its path to the receiver. Because the factors determining the sound levels at the receiver mainly include distance, medium and boundary, therefore, noise barriers, vegetation, ground treatments and combining solutions are the focuses of the noise mitigation methods. The current work concentrates only on the low-height noise barriers and vegetation.

1.2.1 Low-height noise barriers

In urban areas, pedestrians on pavements are located very close to the traffic noise sources, and they are therefore exposed to high sound pressure levels. When people evaluate the noise annoyance in surveys, there is evidence that not only the sound levels inside their houses are considered, but also the soundscape in their neighborhood [2]. This means for example that façade insulation is not the only answer to the urban noise problem.

In the previous section, it has been mentioned that engine noise is mostly dominant to the rolling noise. In order to find a good solution to prevent (mainly) the engine noise from reaching the observers or passengers, a number of studies have been carried out concerning low-height noise barriers along the streets [3,4,5]. Optimising the geometry of such barriers may lead to significant additional reductions of the noise levels in a zone where the pedestrians typically appear [5]. This can be explained by the facts that the typical source generation positions of road traffic noise are located at low heights (ranging from 0.3m to 0.75m for engine noise and 0.01m for rolling noise according to the Harmonoise/Imagine road traffic source model [6]), and that such low-height barriers can be placed very close to the traffic lanes.

The efficiency of low-height noise barriers can also be improved by the choice of its constituting materials. Generally, it is believed that porous materials are advantageous compared to rigid materials. Although the use of rigid materials can avoid wave transmission to the shadow zone behind the noise barriers, sound energy diffracting towards the shadow zone is usually more important. Acoustically semi-transparent low-height noise barriers naturally have a soft top and are beneficial in reducing grazing sound waves. Furthermore, they reduce the reflections towards the other side of the street. At low frequencies, the transparency may even lead to conserving some of the positive ground effect. Such barriers are also easy to integrate in a street and they could be visually more pleasing than the concrete barriers. These may contain different types of materials like densely packed stones, recycled materials or growing substrates.

Another advantage of a porous noise barrier is that it can absorb the scattered and reflected waves from the building façades in a street. Although purely specular reflection on the building façade has been usually assumed in many analyses [7] for simplicity, recently the other hypothesis that the building façades scatter sound completely randomly has drawn attention and has been applied in many research work [8, 9, 10, 11]. These multiple scattered or diffuse reflections occur at the building façades and the ground; and they can be a very substantial contribution to the overall sound levels in urban streets [12]. The porous noise barriers can dampen some scattered sound and then decrease the noise level in the street.

1.2.2 Vegetation

The interaction between sound and vegetation has been the subject of many studies. Already in 1946, Eyring [13] carried out experimental studies on the sound propagation in tropical jungles. Since then, some researchers found rather large reductions of road traffic noise by applying vegetation [14], while others concluded that the influence of vegetation is limited [15].

Vegetation has direct acoustical effects like reflection (mainly on stems or trunks) [16, 17], scattering, diffraction and absorption by canopy and leaves [18, 19, 20]. Moreover, there are also a number of significant indirect effects. When the noise reduction by vegetation belts is considered, the importance of the soil effect is well recognised [21, 22], but there have not been any systematic studies on the effect of plant leaves covering a porous soil. It is known that the presence of vegetation makes the ground more porous and thus acoustically softer. This process is caused by rooting of plants and by a layer of humus originating from the plant litter. This specific type of soil is often referred to as a 'forest floor'. This is a dynamic process in which the presence of the leaves cannot be ignored and the effect of the leaf layer on the ground attenuation is yet to be theoretically explained. Vegetation also influences the micro-meteorology, and this can be used in a positive way, e.g. near noise barriers. It is well known that for downwind sound propagation, barrier efficiency can be largely reduced. The use of a row of trees was experimentally and numerically shown to increase shielding in the presence of wind along a highway noise screen [23]. However, in the absence of wind, the scattering by the tree crown could lead to the increased high frequency scattering into the acoustic shadow zone behind a barrier, compared to a barrier without trees.

Another case of interest is the absorption by a green wall. Such a system consists of a highly porous and light-weight soil substrate layer which is mechanically attached to a building facade. The substrate is used to grow small plants. These plants develop into foliage which densely covers the porous substrate and might affect its acoustic absorption properties. The substrates typically used for growing wall vegetation exhibit high values of the absorption coefficient [24, 25] and can be adopted in noise abatement applications in an urban environment. These applications include the cases when multiple reflections between parallel reflecting building facades lead to a strong amplification of the environmental noise level. It has been demonstrated that increasing wall absorption in a city street generally results in a noticeable noise reduction in an adjacent city canyon as well [26, 27]. Plants in a porous substrate deposited on a green roof reduce the noise diffracting into quiet areas [28, 29, 30]. Wall vegetation and green roof systems might also cover the faces of classical noise barriers to reduce the effects of multiple reflections and diffraction of noise into the shadow zone behind the barriers [24].

Scattering by trees can be wanted. The presence of scattering objects and facades was shown to decrease the sound levels in a street canyon [31], and also for the propagation to nearby canyons or courtyards [26, 32]. It could therefore be beneficial to place trees with a high degree of scattering in such situations.

1.3 Research motivations and methods

The previous section gives brief descriptions of the influences of low-height noise barriers and vegetation on urban noise propagation. Their advantages indicate that they can play an important role in reducing the urban traffic noise and that further studies are necessary.

Noise barriers have been studied extensively by numerical methods. The term "low-height noise barrier" is typically used when the top height does not exceed 1 m. Tyurina et al. [33] and Fard et al. [34] used the 2D finite element method (FEM) to study the effect of noise barriers to abate traffic noise. Especially the boundary element method (BEM) has been used to study noise reductions provided by barriers [5, 35, 36, 37, 38, 39, 40, 41, 42]. Seznec [35] and Hothersall et al. [36] considered noise barriers with different shapes. Baulac et al. [5] found a good agreement by comparing the results by BEM and scale model measurements. Premat and Gabillet's BEM model [39, 40] takes into account, to some extent, refraction phenomena. Baulac et al. [41] optimised the top-profile of noise barriers by BEM and Ishizuka and Fujiwara [42] studied the performance of noise barriers with various edge shapes and acoustical conditions with BEM. Thorssan [4] used the equivalent sources method (ESM) to optimise the low-height noise barriers and the results calculated by ESM showed a good agreement with the results by BEM. Van Renterghem and Botteldooren [43] studied the performance of downwind noise barrier by the finite-difference time-domain (FDTD) method, including the so-called screen-induced refraction of sound by wind.

In addition to the numerical methods mentioned above, there are still many other techniques which can be used to study the performance of noise barriers, such as the domain decomposition method [44], stabilised Galerkin-least square methods [45], partition of unity FEM [46], generalised FEM [47], least-square method [48, 49], wave based method (WBM) [50] and ultra-weak variational formulation (UWVF) [51] method. Some of these methods show a good degree of efficiency allowing to obtain accurate results with a coarser grid than is usual for standard finite element methods. This thesis aims at exploring the UWVF method to estimate the effects of low-height noise barriers.

The UWVF method was first presented by O. Cessenat et al. [51]; and later it was used to model the wave fields in biomedical ultrasonics [52]. For the Helmholtz problem, the UWVF method does not enforce the continuity of normal velocity and pressure on the interfaces of cells; instead, the continuity of their linear combination must be guaranteed and then it is substituted into the corresponding variational formulation. That is why this method has 'ultra' in its name. In general, the UWVF method has several features which make it an attractive candidate to model the acoustic problem of low-height noise barriers. First, this method, like the conventional FEM, needs to split the computational domain into small cells. The priori known information can also be incorporated in the determination of the basis functions. For the Helmholtz problem, plane waves can be used as the basis functions, so the formulation allows using a very large cell, up to two wavelengths [53, 54], without significant loss in accuracy. Second, compared to the conventional FEM, UWVF uses a different variational formulation, which reduces the problem from the whole element to the element surface [51]. That is to say, the dimension of the resulting integral in the system matrix is reduced by one; as a result, computational cost is reduced. Third, the integral operations can be performed in a closed form during the process of assembling the system matrix;

therefore, this improves the efficiency of the computations. Four, because the system matrix contains diagonal matrices, therefore, when the system matrix is assembled, its conditioning can be improved by adjusting the conditioning of each diagonal matrix. Moreover, it is much easier to improve the accuracy by using more basis functions than a finer mesh [52]. Therefore, these advantages allow the UWVF to handle the large domain problems efficiently. Huttunen [52] presented his detailed studies about the accuracy between the UWVF and the standard FEM methods; his conclusion was that in order to obtain a similar accuracy as the standard FEM method, UWVF method could use much larger cells and less storage than the standard FEM.

Like all other frequency domain techniques, such as FEM or BEM, the UWVF method requires a new calculation for each frequency to be considered. However, it will be shown in this thesis that the acoustic response over a broad frequency range can be calculated in a more efficient way. Furthermore, compared to the FDTD method, which needs a new calculation when the source is moved, the UWVF method does not require a full re-calculation. This characteristic makes UWVF potentially competitive when multiple sound sources are considered like in multi-lane road traffic applications. Furthermore, the potential to couple the UWVF and other models, which can be used for simulating the plane wave sound propagation outside the modelling region, could be an asset of UWVF.

Modelling the interaction between sound waves and vegetation needs to include the effects of vegetation elements such as trunks, branches, leaves, etc. Embleton [55] showed the importance of trunk resonances and Martens and Michelsen [18] presented their studies about the absorption of acoustic energy by plant leaves. This thesis aims to investigate the effect of leaves on the sound field by including their properties, such as density and thickness.

Compared to other elements of vegetation, leaves are much softer and lighter, and they can easily bend and twist when they vibrate following the trigger of incident sound waves. Several measurements have been carried out to investigate the influences of leaves on sound transmission through vegetation [20, 56, 57]; and the vibration of plants leaves in a sound field was studied by using a laser Doppler-vibrometer system [18]. Magal et al. [58] studied the influences of leaf structure on vibration propagation in leaves. Tang et al. [59] used the Monte-Carlo technique to study sound propagation through leafy foliage. Although the acoustics of leaves of trees and bushes has been studied for many decades, however, approaches to incorporate leaves in detail in propagation models are lacking. Therefore, developing such an approach is a goal of this thesis. It is expected that such propagation model might help in choosing the type of vegetation to improve noise reduction and combine the influences of vegetation with other propagation related effects.

The vibration process of leaves cannot be easily modelled in frequency domain, so a time domain model is needed. The bending and twisting of leaf can be modelled explicitly according to the vibration theory of a thin plate [60]. Furthermore, the energy dissipation in the boundary layer of the leaf must be considered. Previously, the dissipation in the vorticity and entropy boundary layers have been studied by the finite-difference time-domain method [61], therefore, the FDTD will be used to model the influences of leaves on sound transmission. The finite-difference time-domain (FDTD) technique [62, 63] is one of the most popular finite-difference methods in acoustics, which was firstly presented by K. Yee [64] to numerically solve the Maxwell's equations. As a well-validated reference model, FDTD has been extended for complex acoustic problems, such as room acoustics [65, 66, 67, 68], outdoor noise propagation [69, 70, 71, 72], underwater acoustics [73], and elastic wave propagation [74]. Instead of the Helmholtz equation, pressure-velocity FDTD solves the continuity equation and momentum equation directly.

When low-height noise barriers are designed in an urban environment, building façades should be considered [75]. The reflected waves from the façades can increase the sound pressure levels in a street canyon. Sound propagation in a street or between buildings has been studied for many decades. Wiener et al. [7] studied sound propagation in city streets in 1960s. Lyon [76] studied the multiple reflections of sound in urban street in the early 1970s and he suggested that non-specular reflection from building surfaces might have an important effect. From then on, many models that accounted for the non-specular reflections had been developed. Bullen and Fricke [77] presented a model taking account of the effects of scattering from objects and protrusions in the street by including the evanescent modes in the solutions of the wave equation. Hothersall et al. [78] used a 2D boundary element method to predict the sound field near a tall building. A diffusion-equation model [79] and a radiosity-based model [80] that take into account the multiple diffuse-scattering reflections were presented. Moreover, the finite-difference time-domain method (FDTD) [26, 75] and the equivalent sources method (ESM) [81, 82, 83] have been used to model the sound propagation in a street canyon for 2D problems. Recently, Hornikx and Forssen [84] presented a pseudospectral time-domain method (PSTD) to model sound propagation to 3D urban courtyards.

However, these models have their limitations. For example, the 2D models cannot consider cross streets and variations in cross-section along the street length axis. The current 3D models cannot provide the results at high frequencies because they put a too high demand on the computational resources. Measurement could be an alternative, then. A scale model is a good option to accomplish such measurements in a controlled way, avoiding the limitations in full scale measurements. Horoshenkov et al. [85] used a 1:20 scale model to study the acoustic performance of several noise abatement schemes in a city street canyon. Picaut and Simon [86] made a 1:50 scale model experiment to study sound propagation along a street. Besides the multiple reflections, the façade irregularities were also included in their studies. This was implemented by placing the wooden cubes following the statistical distribution extracted from a real Haussmann building façade, which is a kind of French architectural representation and widespread in Paris and in most of the French cities. Hornikx and Forssen [87] used a 1:40 scale model to study the sound propagation in parallel urban canyons. The influences of surface absorption and diffusion were both considered in their measurements.

Although the façades irregularities have been approximated to some extent, very few studies have considered the full geometrical complexity of façades. It has not been assessed whether this complexity has significant influences on the results. In this thesis, a highly detailed 1:30 scale model is constructed to study the sound propagation in an existing street canyon. The influences of low-height noise barrier on the sound propagation in the street canyon are also studied. The measurement results in the cross section of the sound source are compared with a 2D full-wave model. Previously, it has been mentioned that UWVF is chosen to model the performance of low-height noise barrier. In the scale model, only one point source is present and the frequency of interest in full-scale exceeds 2000 Hz. Therefore, UWVF needs more calculation time for this case. As a result, the 2D FDTD model is chosen, providing a broadband response by using a pulse-like source and applying a Fourier transform afterwards.

1.4 Outline of the dissertation

This thesis consists of seven chapters in total and is organised as follows.

An introduction is given in Chapter 1. In Chapter 2, the basic governing equations for both time-domain and frequency-domain acoustic problems are firstly introduced. Then, the bending equation for thin plates, used to simulate the leaf vibration, is described in section 2.3. Section 2.4 addresses the vorticity and entropy boundary layer which is a source for the energy decay in leaf vibration. Section 2.5 discusses the two models for sound propagation in a porous medium. Finally, section 2.6 gives a short review about the non-reflecting boundary conditions and more attention is paid on the perfectly matched layer theory.

In Chapter 3, the FDTD method, which is used to provide the solution for the problem of acoustic wave propagation through vegetation, is described in detail. The vibration theory of thin plates [60] is employed to simulate the vibration of leaves, including their bending and twisting. The viscous damping inside the leaf boundary layer is simulated by a time-domain approximation for a viscous boundary layer near an infinitely extended flat surface [61]. The visco-elastic damping during the leaf bending is included by employing the generalised Maxwell model. Biot's theory [88, 89] for a poro-elastic frame model is used to model the influence of a porous substrate, on which the vegetation is planted.

The UWVF method, which will be used to estimate the effect of low-height noise barriers, is discussed in Chapter 4. Based on the Helmholtz equation, the UWVF method is derived and discretised. Specific challenges for this numerical technique like the implementation of perfectly matched layers (PML) [90] in UWVF is introduced. Finally, the two-dimensional UWVF method is validated by comparing its results with FDTD calculations.

In Chapter 5, firstly, the vibration of one single leaf, excited by sound, is studied. The FDTD simulation results are validated with measurements in an anechoic room. In total, six types of leaves were considered. Secondly, the behaviour of one leaf placed in front of a porous substrate is investigated by the FDTD method. Measurements in an acoustic impedance tube are used to verify the simulation results. Based on the validated FDTD model, the effects of leaf surface density on the absorption coefficients of two types of hard-backed foams, 25mm Armaforam Sound 240 and 30mm melamine foams, are studied. Finally, this model is applied to simulate acoustic wave propagation through a cluster of leaves by using cyclical boundary conditions. The directional wave separation technique is used to obtain the wave components in three orthogonal directions. Then, the energy scattering and damping along the propagation path can be estimated.

The effect of low-height noise barriers is studied in Chapter 6. In the first section, the effect is estimated by the UWVF method. The porous materials are modelled by Zwikker and Kosten's model [91]. The acoustic shielding of the semi-transparent noise barrier is compared with that of a rigid noise barrier; and the effects of inverse-Γ form noise barriers are compared with those from a rectangular one. In the second section, the application of low-height noise barriers in an urban street is studied by means of a scale model and by two dimensional FDTD simulations. The scale model measurements are performed in a high frequency semi-anechoic room at a scale ratio of 1:30.

Chapter 7 draws conclusions for this dissertation. It summarises the main research achievements and provides some recommendations for future studies.

CHAPTER 2
Governing Equations

This chapter gives a short review of the physical theory of acoustic wave propagation. Theories related to this topic are discussed to an extent that is sufficient for understanding the rest of this thesis. The detailed theories of fluid dynamics and acoustics are discussed in [92, 93]. This chapter begins with an introduction to the conservation laws and their linear approximation. These are needed in the derivation of the governing equations in both time- and frequency-domain. Then, the bending wave equation for a thin uniform homogeneous plate is presented; this equation will be used in this thesis to model the vibration of leaves in vegetation. Next, the theory of the vorticity and entropy boundary layer is briefly reviewed, because this boundary layer theory will be used in this thesis to model the energy decay in the region close to the surface of a leaf. Afterwards, the rigid boundary condition and sound propagation in porous media are summarised. Both the Zwikker and Kosten's model and Biot's model will be used in this thesis to model sound propagation through porous media. Finally, the perfectly absorbing boundary conditions, which are used to truncate the computational domain in case of the unbounded acoustic problems, are discussed.

2.1 Conservation laws

The propagation of sound waves in a fluid (such as air) satisfies the three important conservation laws: conservation of mass, conservation of momentum and conservation of energy, which correspond to the continuity equation, momentum equation and thermal energy equation, respectively. These equations are summarized in this section.

Continuity equation:

$$\frac{\partial \rho}{\partial t} + \nabla \cdot \rho \vec{V} = 0, \tag{2.1}$$

where ρ is the fluid density, $\vec{V} = (v_x, v_y, v_z)$ denotes the fluid velocity, and v_x, v_y and v_z are the x-, y- and z-component of the velocity $\vec{V}$, respectively.

Momentum equation:

$$\rho \frac{dv_i}{dt} = \rho g_i + \frac{\partial \tau_{ij}}{\partial x_j}, \tag{2.2}$$

where v_i is the velocity component with $i = x, y, z$, g_i is the body force per unit mass in direction i, τ_{ij} is the stress, which points in i-direction and acts on a surface normal to the j-direction.

Thermal energy equation (first law of thermodynamics):

$$\rho \frac{d}{dt}\left(e + \frac{1}{2} v_i^{\,2} \right) = \rho g_i v_i + \frac{\partial}{\partial x_j}\left(\tau_{ij} v_i \right) - \frac{\partial q_i}{\partial x_i} \cdot \tag{2.3}$$

where e is the internal energy per unit mass; and q_i is the heat flux per unit area in i direction, where $i=x$, y or z.

2.2 Linear acoustic wave equations

In outdoor acoustics, the body forces can usually be neglected. The thickness of the boundary layer is negligible except when there are many surfaces close together, meaning that the sound propagation medium can be assumed to be inviscid and, as a result, only the normal stress, the pressure, is considered. Equation (2.2) then becomes

$$\rho \frac{\partial \vec{V}}{\partial t} + \rho\left(\vec{V} \cdot \nabla \right)\vec{V} = \rho \frac{\partial \vec{V}}{\partial t} + \rho v_x \frac{\partial \vec{V}}{\partial x} + \rho v_y \frac{\partial \vec{V}}{\partial y} + \rho v_z \frac{\partial \vec{V}}{\partial z} = -\nabla P \, , \tag{2.4}$$

where P is the pressure. Equation (2.4), combined with eqn. (2.1), can be used to derive the linearised acoustic wave equations by neglecting the non-linear terms. Heat conduction is also neglected here. The amplitude of the wave is infinitesimal, therefore, each fluid particle undergoes a nearly isentropic process as the wave passes by. Van Renterghem [69] described this derivation process in his PhD thesis.

The linearised continuity and momentum equations can be summarised as
Continuity equation:

$$\frac{\partial P}{\partial t} + \rho_0 c^2 \nabla \cdot \vec{V} = 0 \, , \tag{2.5}$$

Momentum equation

$$\rho_0 \frac{\partial \vec{V}}{\partial t} + \nabla P = 0 \, , \tag{2.6}$$

where c is the speed of sound, and ρ_0 is the steady term of the fluid density.

Equations (2.5) and (2.6) can result in the wave equation for acoustic pressure. Taking the time derivative of eqn. (2.5), taking the divergence of eqn. (2.6) and eliminating the term $\partial\left(\nabla \cdot \vec{V}\right)/\partial t$ from the two resulting equations gives

$$\frac{\partial}{\partial t}\left(\frac{1}{\rho_0} \frac{\partial P}{\partial t} \right) - c^2 \nabla \cdot \left(\frac{1}{\rho_0} \nabla P \right) = 0 \cdot \tag{2.7}$$

Equation (2.7) is called the wave equation. If it is assumed that the acoustic wave is harmonic, the pressure can be written as

$$P(x,y,z,t) = p(x,y,z) e^{-i\omega t} \, , \tag{2.8}$$

where ω is the angular frequency of the acoustic wave and $i=\sqrt{-1}$ is the imaginary unit. Substituting eqn. (2.8) into eqn. (2.7) gives

$$\nabla\cdot\left(\frac{1}{\rho_0}\nabla p\right)+\frac{\kappa^2}{\rho_0}p=0, \tag{2.9}$$

where $\kappa=\omega/c$ is the wave number. Equation (2.9) is called the Helmholtz equation.

2.3 The bending wave in thin uniform homogeneous plates

When foliage exists, studying its corresponding influence on the acoustic waves is a complicated problem that depends on a number of plant characteristics, such as the biomass distribution, leaf size and shape, the acoustic impedance of the foliage material and so on [94]. There are two possible techniques to characterise the influences of the foliage, which are the multiple scattering approach and the porous medium approach. The multiple scattering approach uses distributed scatters to represent the trunks, branches and the foliage [95, 96]. The latter method, porous medium approach, represents the foliage by a kind of porous material [97, 98], which provides the same influences as the foliage.

Although these two methods can model the influences of the leaf, they don't focus on the details of the leaf, including the bending and twisting moments of the leaf induced by the acoustic wave, energy damping in the process of bending and twisting of the leaf and the energy dissipation in the boundary layer of the leaf. This section presents a model for the leaf vibration induced by sound which includes all the details above.

The leaf is assumed to be a uniform, thin and isotropic plate and it is also assumed to be impermeable for air. Thus, the velocity of the air close to the surface of leaf is exactly the same as the velocity of the leaf. The leaf is supposed to be in the y-z plane and the sound wave is normally incident on the leaf. Then, the vibration of the leaf can be modelled by the bending wave equation [60]

$$\rho_m h\frac{\partial^2 W}{\partial t^2}+D\left[\frac{\partial^4 W}{\partial y^4}+2\frac{\partial^4 W}{\partial y^2\partial z^2}+\frac{\partial^4 W}{\partial z^4}\right]=-\Delta P, \tag{2.10}$$

where ρ_m is the density of the plate (leaf), h is the thickness of the plate (leaf), W is the displacement normal to the leaf surface, $D=E\cdot h^3/12/(1-v^2)$ is the bending stiffness per unit width, E denotes the Young's modulus, v is Poisson's ratio, and ΔP is the pressure drop across the leaf. The time derivative of the displacement W is the velocity in x-direction,

$$\frac{\partial W}{\partial t}=v_x. \tag{2.11}$$

According to the bending equation above, it is noticed that the bending wave inside the leaf has no mechanism to be damped out except energy radiation. This is not consistent with the reality, because internal friction [99] exists in any structure. Hosaka et al. [100] included this internal structural damping for beam bending problem by adding new terms, which are the time derivatives of the fourth-order terms in eqn. (2.10). Rhaouti et al. [101] also used a time derivative term of the displacement to model the internal damping for the vibration of a kettledrum. For the time-harmonic problem, the influence of damping can be included by introducing the structural damping coefficient into the bending stiffness as an imaginary part [102]:

$$D = D_0\left(1 - i\eta_d\right), \tag{2.12}$$

where η_d is the structural damping coefficient; D_0 is real and denotes the bending stiffness per unit width without damping term. Also, based on the generalised Maxwell model, Chaigne and Lambourg [103] and Lambourg et al. [104] presented damped plate equations in which the bending stiffness was modified by perturbation terms corresponding to damping.

Because the inclusion of the time derivative term can cause some stability problem, the perturbation bending stiffness is chosen to include the structural damping. The damped plate equations are expressed in Laplace domain as follows [103]

$$\tilde{M}_y(y,z,s) = -\tilde{D}_1(s)\frac{\partial^2 \tilde{W}(y,z,s)}{\partial y^2} - \left(\tilde{D}_2(s)/2\right)\frac{\partial^2 \tilde{W}(y,z,s)}{\partial z^2}, \tag{2.13}$$

$$\tilde{M}_z(y,z,s) = -\left(\tilde{D}_2(s)/2\right)\frac{\partial^2 \tilde{W}(y,z,s)}{\partial y^2} - \tilde{D}_3(s)\frac{\partial^2 \tilde{W}(y,z,s)}{\partial z^2}, \tag{2.14}$$

$$\tilde{M}_{yz}(y,z,s) = -\left(\tilde{D}_4(s)/2\right)\frac{\partial^2 \tilde{W}(y,z,s)}{\partial y \partial z}, \tag{2.15}$$

$$\rho_m h\left(s^2 + R_L s\right)\tilde{W}(y,z,s) = \frac{\partial^2 \tilde{M}_y}{\partial y^2} + \frac{\partial^2 \tilde{M}_z}{\partial z^2} + 2\frac{\partial^2 \tilde{M}_{yz}}{\partial y \partial z} - \frac{\partial \tilde{P}}{\partial x}h, \tag{2.16}$$

where $\tilde{M}_y(y,z,s)$, $\tilde{M}_z(y,z,s)$ and $\tilde{M}_{yz}(y,z,s)$ are the Laplace transforms of the bending and twisting moments; R_L is the viscous damping coefficient; $\tilde{W}(y,z,s)$ is the Laplace transform of the displacement in the *x*-direction; $\tilde{P}$ is the Laplace transform of the pressure; $\tilde{D}_i(s)$ denotes the bending stiffness with damping term which can be written as:

$$\tilde{D}_i(s) = D_i \cdot \left(1 + \tilde{d}_i(s)\right), \tag{2.17}$$

$$\tilde{d}_i(s) = \sum_{n=1}^{N} \frac{sR_{i,n}}{s + s_{i,n}}, \tag{2.18}$$

where $R_{i,n}$ and $s_{i,n}$ are the damping coefficients.

Next, the inverse Laplace transform is used to transform eqns. (2.13)-(2.16) from the Laplace domain to the time domain. The first term in right hand side of eqn. (2.13) gives

$$L^{-1}\left[\widetilde{D}_1(s)\frac{\partial^2\widetilde{W}}{\partial y^2}\right]=D_1\frac{\partial^2 W}{\partial y^2}+D_1\sum_{n=1}^{N}\left(R_{1,n}L^{-1}\left[\frac{s}{s+s_{1,n}}\frac{\partial^2\widetilde{W}}{\partial y^2}\right]\right). \qquad (2.19)$$

According to the convolution property of Laplace transform, the second term in the right hand side of eqn. (2.19) can be written as

$$\begin{aligned}
D_1\sum_{n=1}^{N}\left(R_{1,n}L^{-1}\left[\frac{1}{s+s_{1,n}}\cdot s\frac{\partial^2\widetilde{W}}{\partial y^2}\right]\right)&=D_1\sum_{n=1}^{N}\left(R_{1,n}\int_0^t\frac{d}{d\tau}\left(\frac{\partial^2 W}{\partial y^2}\right)\cdot e^{-s_{1,n}(t-\tau)}d\tau\right)\\
&=D_1\sum_{n=1}^{N}\left(R_{1,n}\left[\left(\frac{\partial^2 W}{\partial y^2}\cdot e^{-s_{1,n}(t-\tau)}\right)_0^t-\int_0^t\frac{\partial^2 W}{\partial y^2}\cdot e^{-s_{1,n}(t-\tau)}s_{1,n}d\tau\right]\right) \qquad . \qquad (2.20)\\
&=D_1\sum_{n=1}^{N}\left(R_{1,n}\left[\frac{\partial^2 W}{\partial y^2}-\int_0^t\frac{\partial^2 W}{\partial y^2}\cdot e^{-s_{1,n}(t-\tau)}s_{1,n}d\tau\right]\right)
\end{aligned}$$

Therefore, eqn. (2.19) can be written as

$$L^{-1}\left[\widetilde{D}_1(s)\frac{\partial^2\widetilde{W}}{\partial y^2}\right]=D_1\frac{\partial^2 W}{\partial y^2}+D_1\sum_{n=1}^{N}\left(R_{1,n}\left[\frac{\partial^2 W}{\partial y^2}-\int_0^t\frac{\partial^2 W}{\partial y^2}\cdot e^{-s_{1,n}(t-\tau)}s_{1,n}d\tau\right]\right). \qquad (2.21)$$

Similarly, taking the inverse Laplace transform for the second term in the right hand side of eqn. (2.13) gives

$$L^{-1}\left[\frac{\widetilde{D}_2(s)}{2}\frac{\partial^2\widetilde{W}}{\partial z^2}\right]=\frac{D_2}{2}\frac{\partial^2 W}{\partial z^2}+\frac{D_2}{2}\sum_{n=1}^{N}\left(R_{2,n}\left[\frac{\partial^2 W}{\partial z^2}-\int_0^t\frac{\partial^2 W}{\partial z^2}\cdot e^{-s_{2,n}(t-\tau)}s_{2,n}d\tau\right]\right). \qquad (2.22)$$

Then, taking the inverse Laplace transform for eqn. (2.13) and substituting eqns. (2.21) and (2.22) into the resulting equation give

$$\begin{aligned}
M_y=&-D_1\frac{\partial^2 W}{\partial y^2}-D_1\sum_{n=1}^{N}R_{1,n}\left[\frac{\partial^2 W}{\partial y^2}-\int_0^t\frac{\partial^2 W}{\partial y^2}\cdot e^{-s_{1,n}(t-\tau)}s_{1,n}d\tau\right] \qquad . \qquad (2.23)\\
&-\frac{D_2}{2}\frac{\partial^2 W}{\partial z^2}-\frac{D_2}{2}\sum_{n=1}^{N}R_{2,n}\left[\frac{\partial^2 W}{\partial z^2}-\int_0^t\frac{\partial^2 W}{\partial z^2}\cdot e^{-s_{2,n}(t-\tau)}s_{2,n}d\tau\right]
\end{aligned}$$

The same process can be used in the other moments $\widetilde{M}_z(y,z,s)$ and $\widetilde{M}_{yz}(y,z,s)$; then after the inverse Laplace transform, it gives

$$\begin{aligned}
M_z=&-\frac{D_2}{2}\frac{\partial^2 W}{\partial y^2}-\frac{D_2}{2}\sum_{n=1}^{N}R_{2,n}\left[\frac{\partial^2 W}{\partial y^2}-\int_0^t\frac{\partial^2 W}{\partial y^2}\cdot e^{-s_{2,n}(t-\tau)}s_{2,n}d\tau\right], \qquad (2.24)\\
&-D_3\frac{\partial^2 W}{\partial z^2}-D_3\sum_{n=1}^{N}R_{3,n}\left[\frac{\partial^2 W}{\partial z^2}-\int_0^t\frac{\partial^2 W}{\partial z^2}\cdot e^{-s_{3,n}(t-\tau)}s_{3,n}d\tau\right]
\end{aligned}$$

$$M_{yz}=-\frac{D_4}{2}\frac{\partial^2 W}{\partial y\partial z}-\frac{D_4}{2}\sum_{n=1}^{N}R_{4,n}\left[\frac{\partial^2 W}{\partial y\partial z}-\int_0^t\frac{\partial^2 W}{\partial y\partial z}\cdot e^{-s_{4,n}(t-\tau)}s_{4,n}d\tau\right]. \qquad (2.25)$$

Taking the inverse Laplace transform for the first three terms on the right-hand side of eqn. (2.16) and substituting eqns. (2.23)-(2.25) into the resulting equation lead to

$$\begin{aligned}
&\frac{\partial^2 M_y}{\partial y^2}+\frac{\partial^2 M_z}{\partial z^2}+2\frac{\partial^2 M_{yz}}{\partial y\partial z}= \\
&\quad -D_1\frac{\partial^4 W}{\partial y^4}-D_1\sum_{n=1}^{N}R_{1,n}\left[\frac{\partial^4 W}{\partial y^4}-\int_0^t\frac{\partial^4 W}{\partial y^4}\cdot e^{-s_{1,n}(t-\tau)}s_{1,n}d\tau\right] \\
&\quad -\frac{D_2}{2}\frac{\partial^4 W}{\partial z^2\partial y^2}-\frac{D_2}{2}\sum_{n=1}^{N}R_{2,n}\left[\frac{\partial^4 W}{\partial z^2\partial y^2}-\int_0^t\frac{\partial^4 W}{\partial z^2\partial y^2}\cdot e^{-s_{2,n}(t-\tau)}s_{2,n}d\tau\right]\cdot \\
&\quad -\frac{D_2}{2}\frac{\partial^4 W}{\partial y^2\partial z^2}-\frac{D_2}{2}\sum_{n=1}^{N}R_{2,n}\left[\frac{\partial^4 W}{\partial y^2\partial z^2}-\int_0^t\frac{\partial^4 W}{\partial y^2\partial z^2}\cdot e^{-s_{2,n}(t-\tau)}s_{2,n}d\tau\right] \\
&\quad -D_3\frac{\partial^4 W}{\partial z^4}-D_3\sum_{n=1}^{N}R_{3,n}\left[\frac{\partial^4 W}{\partial z^4}-\int_0^t\frac{\partial^4 W}{\partial z^4}\cdot e^{-s_{3,n}(t-\tau)}s_{3,n}d\tau\right] \\
&\quad -D_4\frac{\partial^4 W}{\partial y^2\partial z^2}-D_4\sum_{n=1}^{N}R_{4,n}\left[\frac{\partial^4 W}{\partial y^2\partial z^2}-\int_0^t\frac{\partial^4 W}{\partial y^2\partial z^2}\cdot e^{-s_{4,n}(t-\tau)}s_{4,n}d\tau\right]
\end{aligned} \tag{2.26}$$

It is assumed that the leaf-plate is isotropic. As a result, the four bending stiffnesses (D_i, $i=1,...,4$) can be denoted by D; and the damping coefficients $R_{i,n}$ and $s_{i,n}$ can be denoted by R_n and s_n, respectively. Then, equation (2.26) can be simplified as

$$\begin{aligned}
&\frac{\partial^2 M_y}{\partial y^2}+\frac{\partial^2 M_z}{\partial z^2}+2\frac{\partial^2 M_{yz}}{\partial y\partial z}= \\
&\quad -D\frac{\partial^4 W}{\partial y^4}-D\sum_{n=1}^{N}R_n\left[\frac{\partial^4 W}{\partial y^4}-\int_0^t\frac{\partial^4 W}{\partial y^4}\cdot e^{-s_n(t-\tau)}s_n d\tau\right] \quad . \\
&\quad -2D\frac{\partial^4 W}{\partial z^2\partial y^2}-2D\sum_{n=1}^{N}R_n\left[\frac{\partial^4 W}{\partial z^2\partial y^2}-\int_0^t\frac{\partial^4 W}{\partial z^2\partial y^2}\cdot e^{-s_n(t-\tau)}s_n d\tau\right] \\
&\quad -D\frac{\partial^4 W}{\partial z^4}-D\sum_{n=1}^{N}R_n\left[\frac{\partial^4 W}{\partial z^4}-\int_0^t\frac{\partial^4 W}{\partial z^4}\cdot e^{-s_n(t-\tau)}s_n d\tau\right]
\end{aligned} \tag{2.27}$$

Define

$$\Phi=\phi_0+\phi, \tag{2.28}$$

with

$$\phi_0=D\frac{\partial^2 W}{\partial y^2}+D\frac{\partial^2 W}{\partial z^2} \tag{2.29}$$

denoting the bending of leaf; and

$$\begin{aligned}
\phi=&D\sum_{n=1}^{N}R_n\left[\frac{\partial^2 W}{\partial y^2}-\int_0^t\frac{\partial^2 W}{\partial y^2}\cdot e^{-s_n(t-\tau)}s_n d\tau\right] \\
&+D\sum_{n=1}^{N}R_n\left[\frac{\partial^2 W}{\partial z^2}-\int_0^t\frac{\partial^2 W}{\partial z^2}\cdot e^{-s_n(t-\tau)}s_n d\tau\right]
\end{aligned} \tag{2.30}$$

denoting the damping inside the leaf. Substituting eqns. (2.29) and (2.30) into eqn. (2.27) gives

$$\begin{aligned}\frac{\partial^2 M_y}{\partial y^2}+\frac{\partial^2 M_z}{\partial z^2}+2\frac{\partial^2 M_{yz}}{\partial y\partial z}&=-\frac{\partial^2\phi_0}{\partial y^2}-\frac{\partial^2\phi_0}{\partial z^2}-\frac{\partial^2\phi}{\partial y^2}-\frac{\partial^2\phi}{\partial z^2}\,.\\&=-\frac{\partial^2\Phi}{\partial y^2}-\frac{\partial^2\Phi}{\partial z^2}\end{aligned}\tag{2.31}$$

Taking inverse Laplace transform for eqn. (2.16) and substituting eqn. (2.31) into the resulting equation leads to

$$\rho_m h\left(\frac{\partial v_{xp}}{\partial t}+R_L v_{xp}\right)=-\frac{\partial p}{\partial x}h-\frac{\partial^2\Phi}{\partial y^2}-\frac{\partial^2\Phi}{\partial z^2}\,,\tag{2.32}$$

where v_{xp} is the first order time derivative of W and denotes the velocity in the x-direction. Equation (2.32) is the governing equation for the leaf-plate vibration considering the visco-elastic damping.

2.4 Vorticity and entropy boundary layer

In addition to the decay during the process of the bending of leaf, the acoustic energy can also be dampened in a very thin layer of air close to the leaf surface, which is called the vorticity and entropy boundary layer [105]. Botteldooren [61] reviewed this theory and presented a finite-difference time-domain numerical model for this boundary layer effect.

This theory starts from the three basic conservation laws presented in section 2.1. However, there are important differences. Firstly, it is assumed that the solution of the full set of linear wave equations near a leaf surface can be written as a superposition of an acoustic mode, and entropy mode and a vorticity mode. Secondly, in the thin boundary layer, the acoustic sound field only changes considerably in the direction orthogonal to the leaf surface. This assumption is a good approximation as long as the boundary layer is very thin compared to the wavelength of the acoustic wave and as long as the surface is flat on the same length scale. Therefore, in the thin boundary layer, with the inclusion of the viscous term, the momentum equations can be written as [61]

$$\rho_0\frac{\partial V_t}{\partial t}=\mu_f\frac{\partial^2 V_t}{\partial n^2}\,,\tag{2.33}$$

$$\rho_0\frac{\partial V_n}{\partial t}=\left(\mu_B+\frac{4\mu_f}{3}\right)\frac{\partial^2 V_n}{\partial n^2}-\frac{\partial P}{\partial n}\,,\tag{2.34}$$

where V_t is the tangential velocity, V_n is the normal velocity, μ_B is the bulk viscosity, μ_f is the fluid viscosity, and $\partial/\partial n$ is the spatial derivative in the direction normal to the leaf surface. Thirdly, in the thin boundary layer, the relationship, $c^2=dP/d\rho$, is not valid and as a result, the pressure equation cannot be derived only based on the continuity equation. The entropy change relation (see equation 1.18 in Ref. [92]) combined with the three conservation laws and the state equations are used to derive the pressure equation. The rate of change of entropy

S is related to the rates of changes of internal energy e and specific volume υ ($=1/\rho$) by

$$T_0 \frac{dS}{dt} = \frac{de}{dt} - \frac{P}{\rho_0^{\,2}} \frac{d\rho}{dt}, \tag{2.35}$$

where T_0 is the static temperature. The mechanical energy equation can be obtained by multiplying v_i on both sides of momentum equation (2.2) and summing them over i (see Chapter 4 in Ref. [92]). Removing the mechanical energy from eqn. (2.3) and keeping the linear term lead to the thermal energy equation

$$\rho_0 \frac{de}{dt} = -\frac{\partial q_i}{\partial x_i} - P\nabla \cdot \vec{V} \,. \tag{2.36}$$

Substituting the continuity equation (2.1) and equation (2.36) into eqn. (2.35) gives

$$\rho_0 T_0 \frac{dS}{dt} = -\nabla \cdot \vec{q} \,. \tag{2.37}$$

If the heat flux obeys Fourier's law,

$$\vec{q} = -K\nabla T \,, \tag{2.38}$$

where K is the thermal conductivity, and if K is constant; then eqn. (2.37) can be written as

$$\rho_0 T_0 \frac{dS}{dt} = K\nabla^2 T \,. \tag{2.39}$$

Substituting the entropy and temperature expressed by the state equations into eqn. (2.39), and neglecting the changes of the acoustic sound field in the tangential directions of the leaf surface give the following pressure equation

$$\frac{\partial P}{\partial t} + \gamma p_0 \frac{\partial V_n}{\partial n} - \frac{(\gamma - 1)}{R_s \rho_0} K \frac{\partial^2 P}{\partial n^2} + \frac{(\gamma - 1)c^2}{\gamma R_s \rho_0} \kappa \frac{\partial^2 \rho}{\partial n^2} = 0 \,, \tag{2.40}$$

where V_n is the velocity component which is normal to the leaf surface, R_s is the ideal gas constant, and γ is the ratio of specific heats. Now, the velocity and pressure in the vorticity and entropy boundary layer can be model by eqns. (2.33), (2.34) and (2.40).

2.5 Sound propagation in a porous medium

When sound meets a hard surface that doesn't vibrate with incident wave, no energy can propagate through it. Then, the normal velocity component at this surface is set to zero:

$$V_n = 0 \,. \tag{2.41}$$

In many outdoor acoustic problems, the interaction between sound waves and the ground or porous substrates is important. Most of the ground can be modelled as a porous medium with rigid frames [106]. In Chapter 1, it has been introduced that in many situations, the plant grows on some porous substrates. Therefore, it is necessary to study the sound propagation in the porous medium. Since the middle of last century, the interaction between acoustic wave and porous medium has become a popular research topic. Zwikker and Kosten [91] presented a pororigid model in 1949. In this model, the solid particles in the porous medium are assumed to form rigid frames and only the air between these particles moves. To some extent, the problem of sound wave propagation in the porous medium becomes simple and only three new parameters are needed, which are flow resistivity (R), porosity (φ) and structure factor (k_s). The model is

$$\nabla P + \rho' \frac{\partial \vec{V}}{\partial t} + R\vec{V} = 0, \qquad (2.42)$$

$$\frac{\partial P}{\partial t} + c'^2 \rho' \nabla \cdot \vec{V} = 0, \qquad (2.43)$$

where $\rho' = \rho_0 k_s / \varphi$ and $c' = c / \sqrt{k_s}$, ρ_0 is the density of air and c is the speed of sound in the fluid. Equations (2.42) and (2.43) can be combined to an equation similar to the Helmholtz equation for sound propagation in a porous medium where the rigid-frame approach holds:

$$\nabla \cdot \left(\frac{1}{\rho'} \nabla p \right) + \frac{\kappa'^2}{\rho'} p = 0, \qquad (2.44)$$

$$\kappa' = \frac{\omega}{c} \sqrt{k_s + \frac{i\varphi R}{\omega\rho}}, \qquad (2.45)$$

where ω it is angular frequency of the sound wave and κ' is the wave number in the porous medium. Van Renterghem and Botteldooren [29, 30, 43] used Zwikker and Kosten's model to simulate efficiently the sound propagation in substrate layer and ground.

However, for some porous materials, especially the fibrous materials with low density, the rigid-frame model cannot predict the elastic response/resonance at low frequencies [107] and this elastic response can be triggered by traffic noise. In this situation, these porous materials should be considered as poro-elastic media. The sound not only propagates in air but also in the frame. In 1956, Biot [88, 89] presented a theory for the propagation of stress waves in a porous elastic solid containing a compressible viscous fluid. It considers the wave propagation in both air and frame, and the interaction between them. Allard and Atalla [107] derived the weak integral form of Biot's poro-elasticity equation to realise the finite element modelling of poro-elastic materials. Zeng and Liu [108] used Biot's theory to simulate acoustic wave propagation in a heterogeneous soil in order to detect buried objects. Dong et al. [109] used Biot's theory to model sound propagation in a homogeneous atmosphere over layered poro-elastic ground. Wang et al. [110] studied the effects of compression on the sound absorption of porous materials by using Biot's theory. In this section, the equations used to model the sound propagation in poro-elastic medium are summarised based on Biot's work.

In Biot's theory, the linear stress-strain relations and Darcy's law are used. The dynamic equations (see eqn. (8.24) in Ref. [111]) without considering gravity forces can be written as

$$2\sum^{j}\frac{\partial}{\partial x_j}\left(\mu e_{i,j}\right)+\frac{\partial}{\partial x_i}\left(\lambda_c e_{all}-\alpha M\zeta\right)=\frac{\partial^2}{\partial t^2}\left(\rho u_i+\rho_f w_i\right), \tag{2.46}$$

$$\frac{\partial}{\partial x_i}\left(\alpha M e_{all}-M\zeta\right)=\frac{\partial^2}{\partial t^2}\left(\rho_f u_i+m w_i\right)+\frac{\mu_f}{k_{pm}}\frac{\partial w_i}{\partial t}, \tag{2.47}$$

where μ is Lame's second parameter or shear modulus; α is within the range $\varphi<\alpha<1$; fluid density ρ is defined as the total mass of bulk material per unit volume;

$$e_{i,j}=\frac{1}{2}r_k=\frac{1}{2}\left(\frac{\partial u_i}{\partial x_j}+\frac{\partial u_j}{\partial x_i}\right) \tag{2.48}$$

denotes the shear strain when $i \neq j$ and the normal strain when $i = j$. λ_c and $K_c=\lambda_c+(2/3)\mu$ respectively denote the Lame's first parameter and the bulk modulus for a closed system, in which the pores are sealed. Similarly, λ and $K_0=\lambda+(2/3)\mu$ are the Lame's first parameter and the bulk modulus for an open system, respectively. The term e_{all} can be calculated by $e_{all}=e_{i,i}+e_{j,j}+e_{k,k}$. ζ is determined by

$$\zeta=-\left(\frac{\partial w_x}{\partial x}+\frac{\partial w_y}{\partial y}+\frac{\partial w_z}{\partial z}\right)=-div\left(\vec{w}\right)=div\left[\varphi\left(\vec{u}-\vec{U}\right)\right]; \tag{2.49}$$

u_x, u_y and u_z denotes the displacement of the solid matrix in x, y and z directions, respectively; U_x, U_y and U_z denotes the fluid displacement in x, y and z directions, respectively; $w_i=\varphi(U_i-u_i)$ represents the flow of the fluid relative to the solid in i ($i=x$, y or z) direction but measured in terms of volume per unit area of the bulk medium; ρ_f denotes the mass density of the fluid; m is the coefficient determined by the fluid density, the coordinates in the pore and the pore geometry (more detailed descriptions can be found in section 8 of Ref. [111]); k_{pm} represents the permeability matrix; in this thesis the media is assumed to be isotropic and as a result k_{pm} is a constant; μ_f denotes the flow viscosity; and the coefficient M can be calculated by eqn. (3.26) in Ref. [111].

The left hand side of eqn. (2.46) indicates the force acting on the bulk material (frame and fluid), and the right hand side of eqn. (2.46) indicates the change of momentum of the solid materials and fluid. The left hand side of eqn. (2.47) indicates the force acting on the fluid, and the right hand side of eqn. (2.47) indicates the coupling between solid materials and fluid, the change of momentum of the fluid, and the energy dissipation in the fluid.

The x-components of eqn. (2.46) and eqn. (2.47) can be written as

$$2\left(\frac{\partial}{\partial x}\left(\mu e_{x,x}\right)+\frac{\partial}{\partial y}\left(\mu e_{x,y}\right)+\frac{\partial}{\partial z}\left(\mu e_{x,z}\right)\right)+\frac{\partial}{\partial x}\left(\lambda_c e_{all}-\alpha M\zeta\right)=\frac{\partial^2}{\partial t^2}\left(\rho u_x+\rho_f w_x\right), \tag{2.50}$$

$$\frac{\partial}{\partial x}\left(\alpha M e_{all}-M\zeta\right)=\frac{\partial^2}{\partial t^2}\left(\rho_f u_x+m w_x\right)+\frac{\mu_f}{k_{pm}}\frac{\partial w_x}{\partial t}. \tag{2.51}$$

Substituting eqns. (2.48) and (2.49) into eqn. (2.50) gives

$$\frac{\partial}{\partial x}\left(2\mu e_{x,x}+\lambda_c e_{all}-\alpha M\zeta\right)+\mu\frac{\partial r_z}{\partial y}+\mu\frac{\partial r_y}{\partial z}=\left(\rho-\varphi\rho_f\right)\frac{\partial^2 u_x}{\partial t^2}+\varphi\rho_f\frac{\partial^2 U_x}{\partial t^2}\cdot \tag{2.52}$$

Equation (2.51) can be simplified as

$$-\frac{\partial P_f}{\partial x}=\left(\rho_f-m\varphi\right)\frac{\partial^2 u_x}{\partial t^2}+m\varphi\frac{\partial^2 U_x}{\partial t^2}+\frac{\mu_f\varphi}{k_{pm}}\frac{\partial}{\partial t}\left(U_x-u_x\right), \tag{2.53}$$

where P_f is the fluid pressure and it can be written as (See eqn. (3.8) in Ref. [111])

$$P_f=-\alpha M e_{all}+M\zeta\cdot \tag{2.54}$$

The x-component of the total stress on the bulk materials (solid and fluid) can be written as (See eqn. (3.7) in Ref. [111])

$$\tau_{x,x}=2\mu\, e_{x,x}+\lambda_c e_{all}-\alpha M\zeta,\ \tau_{x,y}=\mu\, r_z,\ \tau_{x,z}=\mu\, r_y\cdot \tag{2.55}$$

The masses of solid and fluid, respectively, per unit volume of bulk material are (See eqn. (8.20) in Ref. [111])

$$\rho_1=\rho-\varphi\rho_f,\ \text{and}\ \rho_2=\varphi\rho_f. \tag{2.56}$$

Multiplying eqn. (2.53) with porosity φ gives

$$-\varphi\frac{\partial P_f}{\partial x}=\left(\varphi\rho_f-m\varphi^2\right)\frac{\partial^2 u_x}{\partial t^2}+m\varphi^2\frac{\partial^2 U_x}{\partial t^2}+\frac{\mu_f\varphi^2}{k_{pm}}\frac{\partial}{\partial t}\left(U_x-u_x\right)\cdot \tag{2.57}$$

Subtracting eqn. (2.57) from equation (2.52) gives

$$\begin{aligned}\frac{\partial}{\partial x}\left(\tau_{x,x}+\varphi P_f\right)+\frac{\partial\tau_{x,y}}{\partial y}+\frac{\partial\tau_{x,z}}{\partial z}&=\left(\rho-2\varphi\rho_f+m\varphi^2\right)\frac{\partial^2 u_x}{\partial t^2}\\&+\left(\varphi\rho_f-m\varphi^2\right)\frac{\partial^2 U_x}{\partial t^2}-\frac{\mu_f\varphi^2}{k_{pm}}\frac{\partial}{\partial t}\left(U_x-u_x\right)\end{aligned}\ . \tag{2.58}$$

We set

$$\rho_{12}=\varphi\rho_f-m\varphi^2,\ \rho_{22}=m\varphi^2,\ \rho_{11}=\rho-2\varphi\rho_f+m\varphi^2\cdot \tag{2.59}$$

Substituting eqns. (2.55) and (2.59) into eqns. (2.57) and (2.58) gives

$$-\frac{\partial\varphi P_f}{\partial x}=\rho_{12}\frac{\partial^2 u_x}{\partial t^2}+\rho_{22}\frac{\partial^2 U_x}{\partial t^2}+\frac{\mu_f\varphi^2}{k}\frac{\partial}{\partial t}\left(U_x-u_x\right), \tag{2.60}$$

$$\frac{\partial}{\partial x}\left(\tau_{x,x}+\varphi P_f\right)+\frac{\partial\tau_{x,y}}{\partial y}+\frac{\partial\tau_{x,z}}{\partial z}=\rho_{11}\frac{\partial^2 u_x}{\partial t^2}+\rho_{12}\frac{\partial^2 U_x}{\partial t^2}-\frac{\mu_f\varphi^2}{k_{pm}}\frac{\partial}{\partial t}\left(U_x-u_x\right)\cdot \tag{2.61}$$

Equation (2.60) is the same as the second one of eqn. (6.5) in Biot's paper [88] published in 1956. Equations (2.60) and (2.61) are the velocity equations for solid materials and fluid; and in equation (2.61) the higher order shear force can be neglected in the linear regime. According to Biot's [111] and Zwikker and Kosten's work [91], defining:

$$\rho_f k_s/v_a^2=m\varphi,\ P_a=\varphi P_f\ \text{and}\ R=\mu_f\varphi^2/k_{pm}, \tag{2.62}$$

the momentum eqns. (2.60) and (2.61) can be written as

$$\rho_a\frac{\partial v_{a,x}}{\partial t}=-\frac{\partial P_a}{\partial x}-R\left(v_{a,x}-v_{f,x}\right)-\rho_a\left(\frac{k_s}{\varphi^2}-1\right)\frac{\partial}{\partial t}\left(v_{a,x}-v_{f,x}\right), \tag{2.63}$$

$$\rho_{frame}\frac{\partial v_{f,x}}{\partial t}=-\frac{\partial P_{frame}}{\partial x}+R\left(v_{a,x}-v_{f,x}\right)+\rho_a\left(\frac{k_s}{\varphi^2}-1\right)\frac{\partial}{\partial t}\left(v_{a,x}-v_{f,x}\right), \tag{2.64}$$

where $\rho_a=\varphi\rho_f$, the velocity of air $v_{a,x}$ and the velocity of solid frame $v_{f,x}$ are

$$v_{a,x}=\dot{U}_x=\frac{\partial U_x}{\partial t},\ v_{f,x}=\dot{u}_x=\frac{\partial u_x}{\partial t}. \tag{2.65}$$

The pressure equations can be derived according to the stress-strain relationships (See equation (3.7) in Ref. [111]), which are

$$\tau_{x,x}=2\mu e_{x,x}+\lambda_c e_{all}-\alpha M\zeta, \tag{2.66}$$

$$\tau_{y,y}=2\mu e_{y,y}+\lambda_c e_{all}-\alpha M\zeta, \tag{2.67}$$

$$\tau_{z,z}=2\mu e_{z,z}+\lambda_c e_{all}-\alpha M\zeta, \tag{2.68}$$

$$P_f=-\alpha M e_{all}+M\zeta. \tag{2.69}$$

The pressure on the total bulk materials can be obtained by

$$-P_t=-P_s-\varphi P_f=\frac{\tau_{x,x}+\tau_{y,y}+\tau_{z,z}}{3}=\left(\lambda_c+\frac{2}{3}\mu\right)e_{all}-\alpha M\zeta, \tag{2.70}$$

where P_s denotes the pressure on the solid materials; φ is the porosity and P_f is the fluid pressure. Taking the time derivative of eqn. (2.69) gives

$$\frac{\partial P_f}{\partial t}=-\alpha M\frac{\partial e_{all}}{\partial t}+M\frac{\partial\zeta}{\partial t}. \tag{2.71}$$

Substituting eqns. (2.48) and (2.49) into eqn. (2.71) and then multiplying it by porosity φ lead to

$$-\frac{\partial\varphi P_f}{\partial t}=M\varphi^2\left(\frac{\partial\dot{U}_x}{\partial x}+\frac{\partial\dot{U}_y}{\partial y}+\frac{\partial\dot{U}_z}{\partial z}\right)+\left(\alpha M\varphi-M\varphi^2\right)\left(\frac{\partial\dot{u}_x}{\partial x}+\frac{\partial\dot{u}_y}{\partial y}+\frac{\partial\dot{u}_z}{\partial z}\right), \tag{2.72}$$

where the dot above the displacement of fluid and solid frame denotes the time derivative. Similarly, taking time derivative of eqn. (2.70) gives

$$-\frac{\partial P_s}{\partial t}-\frac{\partial\varphi P_f}{\partial t}=\left(\lambda_c+\frac{2}{3}\mu\right)\frac{\partial e_{all}}{\partial t}-\alpha M\frac{\partial\zeta}{\partial t}. \tag{2.73}$$

Substituting eqns. (2.48) and (2.49) into eqn. (2.73) leads to

$$-\frac{\partial P_s}{\partial t}-\frac{\partial\varphi P_f}{\partial t}=\left(\lambda_c+\frac{2}{3}\mu-\alpha M\varphi\right)\left(\frac{\partial\dot{u}_x}{\partial x}+\frac{\partial\dot{u}_y}{\partial y}+\frac{\partial\dot{u}_z}{\partial z}\right)+\alpha M\varphi\left(\frac{\partial\dot{U}_x}{\partial x}+\frac{\partial\dot{U}_y}{\partial y}+\frac{\partial\dot{U}_z}{\partial z}\right). \tag{2.74}$$

Combining eqns. (2.72) and (2.74) to eliminate fluid displacement gives

$$-\frac{\partial P_s}{\partial t}+\frac{\alpha-\varphi}{\varphi}\frac{\partial\varphi P_f}{\partial t}=\left(\lambda_c+\frac{2}{3}\mu-M\alpha^2\right)\left(\frac{\partial\dot{u}_x}{\partial x}+\frac{\partial\dot{u}_y}{\partial y}+\frac{\partial\dot{u}_z}{\partial z}\right). \tag{2.75}$$

Define:

$$K_f=\lambda_c+\frac{2}{3}\mu-M\alpha^2,\ K_a=M\varphi\ \text{and}\ P_0=\frac{1-\alpha}{1-\varphi}M\varphi, \tag{2.76}$$

and take the following approximation

$$\frac{\alpha-\varphi}{\varphi}\approx\frac{1-\varphi}{\varphi}; \tag{2.77}$$

eqns. (2.72) and (2.75) can be written as

$$-\frac{\partial P_a}{\partial t} = K_a \varphi \nabla \cdot \mathbf{V}_a + (K_a - P_0)(1-\varphi)\nabla \cdot \mathbf{V}_f , \tag{2.78}$$

$$-\frac{\partial P_{frame}}{\partial t} + \frac{1-\varphi}{\varphi}\frac{\partial p_a}{\partial t} = K_f \nabla \cdot \mathbf{V}_f , \tag{2.79}$$

where P_a and P_{frame} are the pressure of the fluid and solid frame, respectively; K_a and K_f are the bulk moduli of the fluid and solid frame, respectively; P_0 is the ambient atmospheric pressure; $\mathbf{V}_f = (\dot{u}_x, \dot{u}_y, \dot{u}_z)$ and $\mathbf{V}_a = (\dot{U}_x, \dot{U}_y, \dot{U}_z)$ are the velocity vectors for the solid frame and the air, respectively. Equations (2.63) and (2.64) can be written in the vector form as

$$\rho_a \frac{\partial \mathbf{V}_a}{\partial t} = -\nabla P_a - R(\mathbf{V}_a - \mathbf{V}_f) - \rho_a\left(\frac{k_s}{\varphi^2} - 1\right)\frac{\partial}{\partial t}(\mathbf{V}_a - \mathbf{V}_f), \tag{2.80}$$

$$\rho_{frame}\frac{\partial \mathbf{V}_f}{\partial t} + R_f \mathbf{V}_f = -\nabla P_{frame} + R(\mathbf{V}_a - \mathbf{V}_f) + \rho_a\left(\frac{k_s}{\varphi^2} - 1\right)\frac{\partial}{\partial t}(\mathbf{V}_a - \mathbf{V}_f), \tag{2.81}$$

where ρ_a and ρ_{frame} are the masses of the fluid and the solid frame per unit volume of bulk (fluid plus solid frame) materials, respectively; R_f is the coefficient for an extra damping term added to the momentum equation of solid frame in order to approximate dissipation mechanisms other than those caused by the flow resistivity. This term is different from that described in Biot's work [88, 89]. Biot suggested replacing flow velocity, bulk elasticity, etc., by complex functions of frequency to account for different damping mechanisms in the solid fraction. In theory, these complex functions could be approximated by digital filters and transformed to time domain, like will be done for vorticity and entropy boundary layers, but this complicates equations considerably while stability is not guaranteed. The first order approximation obtained by introducing R_f induces the basic frame damping that is needed to reproduce the measured results, at a lower computational cost. Now, the acoustic wave propagation in the poro-elastic medium is governed by eqns. (2.78)-(2.81).

When the solid frame does not vibrate with the sound, Biot's model can be simplified. The pressure and velocity for the frame can be neglected. Eqns. (2.78) and (2.80) can be written as

$$-\frac{\partial P_a}{\partial t} = K_a \varphi \nabla \cdot \mathbf{V}_a , \tag{2.82}$$

$$\rho_a \frac{k_s}{\varphi^2}\frac{\partial \mathbf{V}_a}{\partial t} = -\nabla P_a - R\mathbf{V}_a . \tag{2.83}$$

They correspond to eqns. (2.42) and (2.43) in Zwikker and Kosten's model.

2.6 Non-reflecting boundary conditions

In outdoor acoustics, it is necessary to define a condition that characterises the behaviour of the fields at infinity in order to guarantee a unique solution for wave problems in unbounded domains. Sommerfeld [112] presented a so-called radiation condition to satisfy this requirement. This Sommerfeld radiation condition is written as

$$\lim_{r\to\infty} r^{(d-1)/2}\left(\frac{\partial P}{\partial r} - i\kappa P\right) = 0\,, \tag{2.84}$$

where r is the radial coordinate, P is the pressure, d is the spatial dimension. In the situations that the artificial boundary is close to the sound source, the implementation of Sommerfeld radiation condition can become problematic [113]. As a result, perfectly absorbing boundary conditions or non-reflection boundary conditions (NRBC) are needed.

The NRBC truncates the unbounded propagation domain artificially and this truncation must generate little spurious numerical reflections back into this computational domain. It is desirable that the conditions on such artificial boundaries in the truncated domain approach the solution of the original problem in the infinite domain. Moreover, the NRBC should be efficient (e.g. not needing a huge amount of cells) and be numerically stable.

One standard approach to construct NRBC for time-harmonic problem is the non-local Dirichlet-to-Neumann (DtN) condition [113, 114]. As a non-local condition, the DtN operator needs an integral over the whole boundary and needs to be truncated. The DtN condition requires the artificial boundary to be a circle or sphere. Besides, when the sound frequency is high or the radius of the circle or sphere bordering the computational domain is large, the computation will become more complicated and need more modes.

In order to overcome these drawbacks, some local conditions have been proposed. Engquist and Majda [115] presented a sequence of local approximate boundary conditions of increasing order according to the theory of pseudo-differential operator [116]. These boundary conditions are perfectly absorbing at normal incidence. Based on an asymptotic expansion of the solution at large distances, Bayliss and Turkel [117] presented their boundary conditions in polar coordinates for wave propagation. Feng [118] presented a sequence of local NRBCs for the reduced Helmholtz equation in two dimensions. Kriegsmann and Morawetz [119] presented NRBC for a circular truncated domain.

Higdon [120] presented the NRBCs for two-dimensional wave equation in a rectangular computational domain. When one has a priori information about the directions from which the waves are approaching the boundary, then one should adjust the boundary condition to the appropriate angle of incident to obtain a perfect absorption. Furthermore, the use of a higher-order version of boundary conditions can lead to perfect absorption for the waves, which propagate towards the boundary at angles $\pm\alpha_j$ with $j=1,...n$ and $\alpha_j<\pi/2$. Furthermore, other researchers, such as Trefethen and Halpern [121] and Lindman [122], also presented their NRBCs to truncate the computational domain of the wave problem.

Generally speaking, these NRBCs mentioned above need either the waves with specific incident angles or very large radius R from the source to the boundary in order to avoid significant spurious reflection. In urban acoustics, phenomena, such as the reflection, diffraction and scattering, make the sound waves propagate in all directions. This will limit the uses of these NRBCs or will increase the computational load significantly when placing the boundary far away from the sound source. In 1994, Berenger [90] proposed his Perfectly Matched Layers (PML) for use with Maxwell's equations. After that, the PML method has gained immense popularity in the field of computational electromagnetics and has been introduced to the computational acoustics. The PML is an exterior layer, which surrounds the computational domain and does not reflect the waves hitting it (see Figure 2.1). The damping coefficient is 0 on the interface between the PML and the region of interest. This damping coefficient then gradually increases anisotropically until the exterior boundary of the PML is reached. Optimising the PML's parameters can guarantee that the waves become absorbed before reaching the exterior boundary. The most important advantage of the PML is that they work well for all angles of incidence and for all sound frequencies. In contrast to many other approaches for NRBCs, PML does not depend on the distance relative to the sound sources. Given these nice properties, the PML will be used in this thesis to truncate the computational domain in both the time-domain model (FDTD) and frequency-domain model (UWVF) considered.

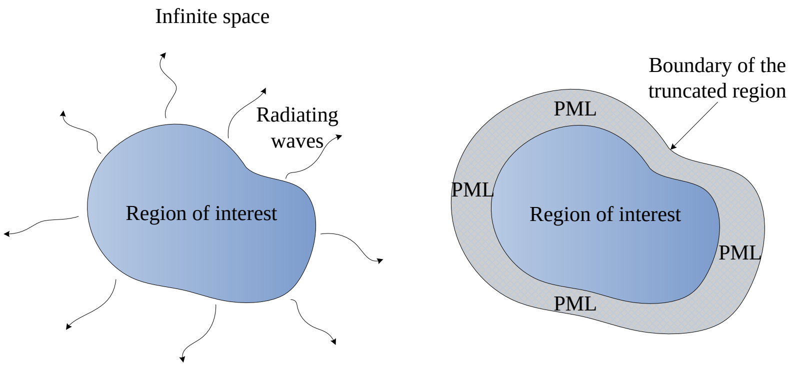

Figure 2.1 Schematic of a typical wave problem. The left denotes the original problem. Some radiating waves escape from the region of interest to infinity. The right one shows the application of PML, which can be directly placed outside the region of interest and absorb outgoing waves with negligible reflections from the edge of the region of interest.

In the FDTD model, the acoustic pressure in the PML is split in two artificial components, which are normal (P_{normal}) and parallel ($P_{parallel}$) to the interface between the region of interest and the PML. When the medium flow is not considered, the PML equations are

$$\frac{\partial P_{normal}}{\partial t}+c^2\rho_0\frac{\partial v_\alpha}{\partial \alpha}+\kappa_{1,normal}P_{normal}=0, \tag{2.85}$$

$$\frac{\partial P_{parallel}}{\partial t}+c^2\rho_0\sum_{\beta\neq\alpha}\frac{\partial v_\beta}{\partial \beta}+\kappa_{1,parallel}P_{parallel}=0, \tag{2.86}$$

$$P=P_{normal}+P_{parallel}, \tag{2.87}$$

$$\rho_0\frac{\partial v_\alpha}{\partial t}+\frac{\partial P}{\partial \alpha}+\kappa_{2,normal}v_\alpha=0, \tag{2.88}$$

$$\rho_0\frac{\partial v_\beta}{\partial t}+\frac{\partial P}{\partial \beta}+\kappa_{2,parallel}v_\beta=0,\ \beta\neq\alpha, \tag{2.89}$$

where v_α is the velocity normal to the interface, v_β denotes the velocity parallel to the interface, $\kappa_{1,normal}$, $\kappa_{1,parallel}$, $\kappa_{2,normal}$, $\kappa_{2,parallel}$ are the damping coefficients, and

$$\kappa_{2,normal}=\rho_0\kappa_{1,normal}. \tag{2.90}$$

Van Renterghem’s PhD thesis [69] provided a proof that the damping terms in the parallel pressure equation and parallel velocity equal zero. Berenger [123] proposed a damping coefficient which gradually increases in the PML, according to

$$\kappa_{1,normal}(x)=\kappa_{1,\max}(x)\left(\frac{x}{d_{PML}}\right)^n, \tag{2.91}$$

where x is the depth inside the layer normal to the interface and d_{PML} is the total thickness of the PML. As to the value of n, Berenger [123] found that the good choice is between 3 and 4; and Hasting et al. [124] found that a value of 4 resulted in the best performance. In this thesis, the value of *m* is fixed at 4.

In the UWVF model, a complex stretching of the spatial coordinates is considered and defined by [52]

$$\xi' = \begin{cases} \xi + \dfrac{i}{\kappa}\displaystyle\int_{\xi_0}^{\xi} \sigma_{0,\xi}\left(|\tau| - \xi_0\right)^n d\tau, & |\xi| \geq \xi_0 \text{ in PML domain}, \\ \xi, & |\xi| < \xi_0 \text{ in non-PML domain}, \end{cases} \tag{2.92}$$

where $\xi = x$, y or z denotes the spatial coordinate, i is the imaginary unit, κ is the wavenumber, and ξ_0 is the spatial coordinate of the interface of the PML. Based on eqn. (2.92), the Helmholtz equation in stretched spatial coordinates is [52]

$$\nabla \cdot \left(\frac{1}{\rho} A_d \nabla p \right) + \frac{\kappa^2 \eta^2}{\rho} p = f_s \eta^2 , \tag{2.93}$$

where f_s is the source term, and the matrix A_d and value η^2 can be calculated by [52]

$$A_d = \begin{bmatrix} \dfrac{d_y d_z}{d_x}, & 0, & 0 \\ 0, & \dfrac{d_z d_x}{d_y}, & 0 \\ 0, & 0, & \dfrac{d_x d_y}{d_z} \end{bmatrix}, \tag{2.94}$$

$$\eta^2 = d_x d_y d_z , \tag{2.95}$$

$$d_\xi = d_\xi(\xi) = \frac{\partial \xi'}{\partial \xi} = \begin{cases} 1 + \dfrac{i}{\kappa} \sigma_{0,\xi} \cdot \left(|\xi| - \xi_0\right)^n, & |\xi| \geq \xi_0, \\ 1, & |\xi| < \xi_0. \end{cases} \tag{2.96}$$

CHAPTER 3

Finite-difference time-domain model for microscopic interaction between an acoustic wave and vegetation[1]

In this chapter, a finite-difference time-domain model, which couples the acoustics and the vibration of leaves, is introduced. The governing equations and boundary conditions have been introduced in Chapter 2. In section 3.1, the governing equations used in this model are summarised. The non-reflecting boundary conditions for the time domain model can be found in eqns. (2.85)-(2.89). In section 3.2, the finite-difference time-domain (FDTD) method, which is used to discretise and solve the current model, is introduced; and its stability analysis is given in section 3.3. Finally, in section 3.4, the choice of appropriate material parameters is discussed.

3.1 Theoretical model

The propagation of acoustic waves in homogeneous and non-moving air is governed by the continuity equation and the momentum equation (see section 2.2)

$$\frac{\partial P}{\partial t} + \rho_0 c^2 \nabla \cdot \vec{V} = 0, \tag{3.1}$$

$$\rho_0 \frac{\partial \vec{V}}{\partial t} + \nabla P = 0, \tag{3.2}$$

where P is the acoustic pressure, c is the speed of sound, ρ_0 is the mass density of air, $\vec{V} = (v_x, v_y, v_z)$ is the velocity vector.

The propagation of acoustic waves in porous elastic media can be formulated based on the dynamic equations and stress-strain relation in Biot's theory [88, 89]. This leads to continuity and momentum equations for both the fluid inside the frame and the frame itself (see section 2.5)

$$-\frac{\partial P_a}{\partial t} = K_a \varphi \nabla \cdot \mathbf{V}_a + (K_a - P_0)(1-\varphi) \nabla \cdot \mathbf{V}_f, \tag{3.3}$$

$$-\frac{\partial P_{frame}}{\partial t} + \frac{1-\varphi}{\varphi}\frac{\partial P_a}{\partial t} = K_f \nabla \cdot \mathbf{V}_f, \tag{3.4}$$

---

[1] Part of this chapter has been published in:
Lei Ding, Timothy Van Renterghem, Dick Botteldooren, Kirill Horoshenkov and Amir Khan: Sound absorption of porous substrates covered by foliage: experimental results and numerical predictions. J. Acoust. Soc. Am. 134 (6), 4599-4609 (2013).

$$\rho_a \frac{\partial \mathbf{V}_a}{\partial t} = -\nabla P_a - R(\mathbf{V}_a - \mathbf{V}_f) - \rho_a\left(\frac{k_s}{\varphi^2} - 1\right)\frac{\partial}{\partial t}(\mathbf{V}_a - \mathbf{V}_f), \tag{3.5}$$

$$\rho_{frame}\frac{\partial \mathbf{V}_f}{\partial t} + R_f \mathbf{V}_f = -\nabla P_{frame} + R(\mathbf{V}_a - \mathbf{V}_f) + \rho_a\left(\frac{k_s}{\varphi^2} - 1\right)\frac{\partial}{\partial t}(\mathbf{V}_a - \mathbf{V}_f), \tag{3.6}$$

where ρ_a is the mass of fluid per unit bulk volume; K_a is the bulk modulus of the fluid; P_a is the pressure of the fluid in the porous medium; φ is the porosity; P_0 is the ambient atmospheric pressure; $\mathbf{V}_a = (v_{a,x}, v_{a,y}, v_{a,z})$, and $v_{a,x}$, $v_{a,y}$ and $v_{a,z}$ are the air-particle velocity components in the x, y and z directions inside the porous medium, respectively; P_{frame} is the pressure on the solid frame; $\mathbf{V}_f = (v_{f,x}, v_{f,y}, v_{f,z})$, and $v_{f,x}$, $v_{f,y}$ and $v_{f,z}$ are the frame velocity components in the x, y and z directions, respectively; k_s is the structure factor; R is the flow resistivity; ρ_{frame} is the density of the frame material; K_f is the bulk modulus of the solid frame; and R_f is the coefficient for an extra damping term added to the momentum equation of the solid frame in order to approximate dissipation mechanisms other than those caused by the flow resistivity.

When the frame's density is large or the frame resonance does not need to be considered (high frequency problems), the Zwikker and Kosten's model can be used. It reads

$$\nabla P + \rho' \frac{\partial \vec{V}}{\partial t} + R\vec{V} = 0, \tag{3.7}$$

$$\frac{\partial P}{\partial t} + c'^2 \rho' \nabla \cdot \vec{V} = 0, \tag{3.8}$$

where $\rho' = \rho_0 k_s / \varphi$ and $c' = c/\sqrt{k_s}$, ρ_0 is the density of fluid and c is the speed of sound. Or, eqns. (2.82) and (2.83) can be used. They are simplified Biot's model and they correspond to Zwikker and Kosten's model.

The leaf is approximated by an acoustically infinitely thin plate forming the shape of the leaf. Bending waves can propagate in the two in-plane directions. Assuming that the plate is orthogonal to x direction, the velocity equation can be written as (see eqn. (2.32) in section 2.3)

$$\rho_m h\left(\frac{\partial v_{xp}}{\partial t} + R_L v_{xp}\right) = -\frac{\partial P}{\partial x}h - \frac{\partial^2 \Phi}{\partial y^2} - \frac{\partial^2 \Phi}{\partial z^2}, \tag{3.9}$$

in which,

$$\Phi = \phi_0 + \phi, \tag{3.10}$$

where $\rho_m h$ is the surface mass density of the plate material (in kg/m^2); h is the thickness of the plate; v_{xp} is the plate velocity vector component in the x direction; R_L denotes the viscous damping in the bending process. ϕ_0 denotes the bending and twisting moments per unit thickness. If the leaf is assumed to be isotropic, they are given by

$$\phi_0 = D\frac{\partial^2 W}{\partial y^2} + D\frac{\partial^2 W}{\partial z^2}, \tag{3.11}$$

where D is the bending stiffness per unit width for plate; W is the displacement component in x direction and its time derivative is the velocity v_{xp}. ϕ denotes the visco-elastic damping during the bending of the leaf which according to generalised Maxwell model can be obtained from:

$$\frac{\partial \phi}{\partial t} = \sum_{n=1}^{N} DR_n \frac{\partial Q_n}{\partial t} = \sum_{n=1}^{N} DR_n \Pi_n, \tag{3.12}$$

$$Q_n = \frac{\partial^2 W}{\partial y^2} + \frac{\partial^2 W}{\partial z^2} - \int_0^t \left(\frac{\partial^2 W}{\partial y^2} + \frac{\partial^2 W}{\partial z^2} \right) \cdot e^{-s_n(t-\tau)} s_n \, d\tau, \tag{3.13}$$

where R_n and s_n are the visco-elastic damping parameters.

Close to the leaves, viscosity (and thermal conductivity) cannot be ignored since viscous energy decay in the boundary layer at the surface of the leaves is one of the mechanisms causing sound attenuation [18]. The basic equations have been summarised in section 2.4. As in Ref. [61], a time-domain approximation for a viscous boundary layer near an infinitely extended flat surface will be used. The viscosity adds an additional term (in frequency domain) to the linearised momentum equations (see Eqn. (3.2)) in the directions which are parallel to the leaf surface plane:

$$\frac{ik_n}{d_{BL}} \langle v_\gamma \rangle, \text{ with } k_n^2 = i\omega \frac{\rho_0}{\mu_f}, \tag{3.14}$$

where the subscript in v_γ denotes that the velocity is parallel to the leaf surface plane, $\langle \; \rangle$ denotes that the velocity v_γ is averaged over a layer of thickness d_{BL}; μ_f is the dynamic viscosity of air; ω is the angular frequency; and $i = \sqrt{-1}$ is the imaginary unit.

The same process can also be applied to the pressure equation in the entropy boundary layer. One additional averaged acoustical pressure term $\langle p \rangle$ is also added to the pressure equation in the frequency domain. When the velocity and pressure equations in the vorticity and entropy boundary layer are transformed back to the time domain, the corresponding equations can be discretised in the finite difference time domain model and the details will be given in section 3.2.

3.2 3D finite-difference time-domain method

The finite-difference time-domain method can be used to solve the set of equations presented in section 3.1. The staggered grid organisation, both in space and time, as suggested in Ref. [62] is considered. A leap-frog scheme is used to update acoustic pressure and velocity components over time. Using this method, second-order accuracy can be obtained in representing the spatial derivatives, with the smallest possible stencil. The spatial organisation of some cells near the interface between the porous substrate and air, including a leaf, are illustrated in Figure 3. 1.

For this specific scheme, the following notations are commonly used to represent the discrete pressures and velocity components in air

$$P^{ldt}_{(idx,jdy,kdz)},\ v_{x((i+0.5)dx,jdy,kdz)}^{(l+0.5)dt},\ v_{y(idx,(j+0.5)dy,kdz)}^{(l+0.5)dt},\ v_{z(idx,jdy,(k+0.5)dz)}^{(l+0.5)dt} \tag{3.15}$$

where *dx*, *dy*, and *dz* are the spatial discretisation steps in three directions; *dt* denotes the time discretisation step; and *i*, *j* and *k* are the spatial indices. The acoustic pressure is always updated at time *ldt* and the velocity components at intermediate times (*l*+0.5)*dt*.

The acoustic pressures P_a and P_{frame} in the porous medium follow the same discretisation as the acoustic pressures in air, and the velocity components ($\mathbf{V}_a$ and $\mathbf{V}_f$) in the porous medium follow the same discretisation as the particle velocities in air. The parameters ϕ_0, ϕ and Π_n related to leaf vibration are all determined at the same grid positions as the particle velocity components v_{xp} (see Figure 3. 1), but they are updated at the integer times steps just like the acoustic pressures *p*,

$$\phi_{0((i+0.5)dx,jdy,kdz)}^{ldt},\ \phi_{((i+0.5)dx,jdy,kdz)}^{ldt} \text{ and } \Pi_{n((i+0.5)dx,jdy,kdz)}^{ldt}. \tag{3.16}$$

The discretised forms of pressure and velocity eqns. (3.1)-(3.2) read

$$P^{l+1}_{i,j,k} = P^{l}_{i,j,k} - dt\rho_0 c^2 \sum_{\beta} \frac{v_{\beta\,\beta+0.5}^{\;l+0.5} - v_{\beta\,\beta-0.5}^{\;l+0.5}}{d\beta}, \tag{3.17}$$

$$v_{\alpha(\alpha+0.5)}^{\;l+0.5} = v_{\alpha(\alpha+0.5)}^{\;l-0.5} - \frac{dt}{\rho_0 d\alpha}\left(P^{l}_{\alpha+1} - P^{l}_{\alpha}\right)\cdot \tag{3.18}$$

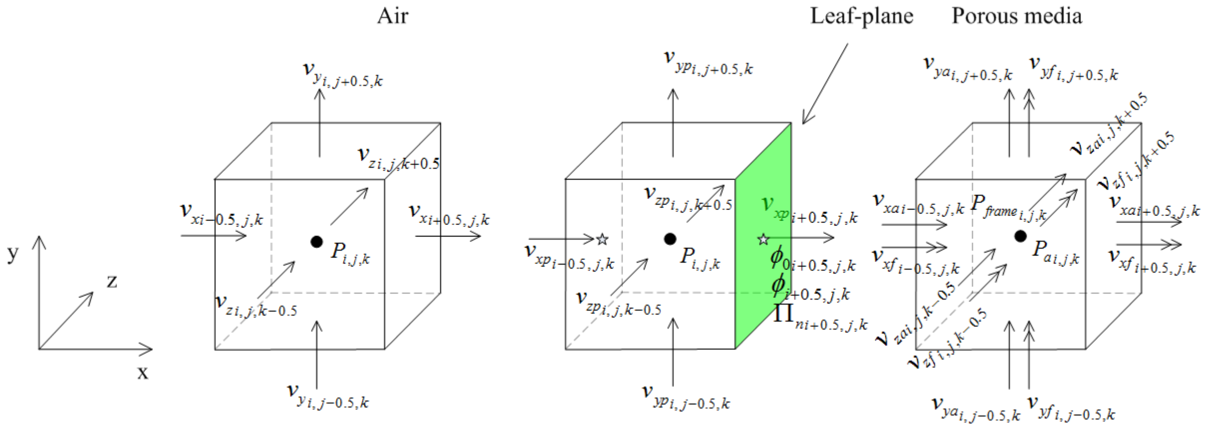

Figure 3. 1 Spatial organisation of the staggered grids for different materials. The left grid denotes the cell in air. The middle grid denotes the cell including the leaf. The star symbol on the leaf-plane which is perpendicular to *x*-axis denotes the site for the parameters ϕ_0, ϕ and Π_n. The right grid denotes the cell in the porous media. There are two pressures and two groups of velocity components shown in this grid, for air and solid frame, respectively. The double arrow denotes the velocity components for the solid frame.

In eqns. (3.17) and (3.18), α represents one of the three Cartesian indices; summation over β runs over all the Cartesian indices; α and β in $\alpha+0.5$, $\alpha+1$ and $\beta\pm0.5$ denote one of the indices i, j and k; v_α and v_β are the velocities in α and β directions, respectively. The pressure at time $(l+1)dt$ is determined by the pressure at previous time ldt and the velocities at time $(l+0.5)dt$. The velocity at time $(l+0.5)dt$ is determined by the velocity at previous time $(l-0.5)dt$ and the pressure at time ldt. Similarly, the discretised forms of the governing equations (3.3)-(3.6) in the elastic porous media are

$$P^{\,l+1}_{a\,i,j,k} = P^{\,l}_{a\,i,j,k} - K_a\varphi dt\sum_{\beta}\frac{v^{\,l+0.5}_{\beta a\,\beta+0.5} - v^{\,l+0.5}_{a\beta\,\beta-0.5}}{d\beta} - \left(K_a - P_0\right)\left(1-\varphi\right)dt\sum_{\beta}\frac{v^{\,l+0.5}_{\beta f\,\beta+0.5} - v^{\,l+0.5}_{\beta f\,\beta-0.5}}{d\beta}\,, \tag{3.19}$$

$$\begin{aligned}\left(\frac{\rho_a k_s}{\varphi^2 dt}+\frac{R}{2}\right)v^{\,l+0.5}_{\alpha a\,i+0.5,j,k} &= \left(\frac{\rho_a k_s}{\varphi^2 dt}-\frac{R}{2}\right)v^{\,l-0.5}_{\alpha a\,i+0.5,j,k} - \frac{P^{\,l}_{a\,i+1,j,k}-P^{\,l}_{a\,i,j,k}}{d\alpha}\quad, \\ &+\left(\frac{\rho_a\left(k_s/\varphi^2-1\right)}{dt}+\frac{R}{2}\right)v^{\,l+0.5}_{\alpha f\,i+0.5,j,k} - \left(\frac{\rho_a\left(k_s/\varphi^2-1\right)}{dt}-\frac{R}{2}\right)v^{\,l-0.5}_{\alpha f\,i+0.5,j,k}\end{aligned} \tag{3.20}$$

$$P^{\,l+1}_{frame\,i,j,k} = P^{\,l}_{frame\,i,j,k} + \frac{1-\varphi}{\varphi}\left(P^{\,l+1}_{a\,i,j,k} - P^{\,l}_{a\,i,j,k}\right) - dtK_f\sum_{\beta}\frac{v^{\,l+0.5}_{\beta f\,\beta+0.5} - v^{\,l+0.5}_{\beta f\,\beta-0.5}}{d\beta}\,, \tag{3.21}$$

$$\begin{aligned}&\left(\frac{\rho_f+\rho_a\left(k_s/\varphi^2-1\right)}{dt}+\frac{R}{2}\right)v^{\,l+0.5}_{\alpha f\,i+0.5,j,k} = \\ &\qquad\left(\frac{\rho_f+\rho_a\left(k_s/\varphi^2-1\right)}{dt}-\frac{R}{2}\right)v^{\,l-0.5}_{\alpha f\,i+0.5,j,k} \quad . \\ &\qquad-\frac{P^{\,l}_{frame\,i+1,j,k}-P^{\,l}_{frame\,i,j,k}}{d\alpha} + \left(\frac{\rho_a\left(k_s/\varphi^2-1\right)}{dt}+\frac{R}{2}\right)v^{\,l+0.5}_{\alpha a\,i+0.5,j,k} \\ &\qquad-\left(\frac{\rho_a\left(k_s/\varphi^2-1\right)}{dt}-\frac{R}{2}\right)v^{\,l-0.5}_{\alpha a\,i+0.5,j,k}\end{aligned} \tag{3.22}$$

It must be noted that eqns. (3.21) and (3.22) need to be added to the usual set of FDTD equations to obtain the velocities of both air and frame.

When the grids include the leaf material, equations (3.9) are used as the momentum equation in the x-direction. The leaf is approximated by one layer of grid cells which together have roughly the form of the leaf. Because of this discretisation, the thickness of the plate, h, equals the grid size in the direction perpendicular to the plate surface. In these cells, the mass of the air cannot be neglected in comparison to the mass of the leaf. Thus, the $\rho_m h$ in the first term of eqn. (3.9) is replaced by $\rho_A dx$ with

$$\rho_A = \rho_0 + \frac{\rho_{Leaf}d_{Leaf}}{dx}\,, \tag{3.23}$$

where ρ_A is the average density in these cells; ρ_0 is the density of air; ρ_{Leaf} is the density of the leaf; d_{Leaf} is the thickness of the leaf; and dx is the grid size. The discretised form of eqn. (3.9) becomes:

$$\begin{aligned}
&\rho_A dx\left(\frac{v_{xp\,i+0.5,j,k}^{\;l+0.5}-v_{xp\,i+0.5,j,k}^{\;l-0.5}}{dt}+R_L\frac{v_{xp\,i+0.5,j,k}^{\;l+0.5}+v_{xp\,i+0.5,j,k}^{\;l-0.5}}{2}\right)=-\left(P_{i+1,j,k}^{l}-P_{i,j,k}^{l}\right)\\
&-\left(\frac{\phi_{0i+0.5,j+1,k}^{\;l}-2\phi_{0i+0.5,j,k}^{\;l}+\phi_{0i+0.5,j-1,k}^{\;l}}{dy^2}+\frac{\phi_{0i+0.5,j,k+1}^{\;l}-2\phi_{0i+0.5,j,k}^{\;l}+\phi_{0i+0.5,j,k-1}^{\;l}}{dz^2}\right).\\
&-\left(\frac{\phi_{i+0.5,j+1,k}^{l}-2\phi_{i+0.5,j,k}^{l}+\phi_{i+0.5,j-1,k}^{l}}{dy^2}+\frac{\phi_{i+0.5,j,k+1}^{l}-2\phi_{i+0.5,j,k}^{l}+\phi_{i+0.5,j,k-1}^{l}}{dz^2}\right)
\end{aligned}\qquad(3.24)$$

Equation (3.24) results in an FDTD equation for the vibration velocity of the leaf

$$\begin{aligned}
v_{xp\,i+0.5,j,k}^{\;l+0.5}&=\frac{\left(1/dt-R_L/2\right)}{\left(1/dt+R_L/2\right)}v_{xp\,i+0.5,j,k}^{\;l-0.5}-\frac{1}{\rho_A dx\left(1/dt+R_L/2\right)}\left(P_{i+1,j,k}^{l}-P_{i,j,k}^{l}\right)\\
&-\frac{1}{\rho_A dx\left(1/dt+R_L/2\right)}\left(\frac{\phi_{0i+0.5,j+1,k}^{\;l}-2\phi_{0i+0.5,j,k}^{\;l}+\phi_{0i+0.5,j-1,k}^{\;l}}{dy^2}+\right.\\
&\qquad\left.\frac{\phi_{0i+0.5,j,k+1}^{\;l}-2\phi_{0i+0.5,j,k}^{\;l}+\phi_{0i+0.5,j,k-1}^{\;l}}{dz^2}\right).\\
&-\frac{1}{\rho_A dx\left(1/dt+R_L/2\right)}\left(\frac{\phi_{i+0.5,j+1,k}^{l}-2\phi_{i+0.5,j,k}^{l}+\phi_{i+0.5,j-1,k}^{l}}{dy^2}+\right.\\
&\qquad\left.\frac{\phi_{i+0.5,j,k+1}^{l}-2\phi_{i+0.5,j,k}^{l}+\phi_{i+0.5,j,k-1}^{l}}{dz^2}\right)
\end{aligned}\qquad(3.25)$$

The bending term ϕ_0 of the leaf can be calculated by taking the time derivative of eqn. (3.11) which gives its discretised form:

$$\begin{aligned}
\frac{\phi_{0i+0.5,j,k}^{\;l}-\phi_{0i+0.5,j,k}^{\;l-1}}{dt}&=D\left(\frac{v_{xp\,i+0.5,j+1,k}^{\;l-0.5}-2v_{xp\,i+0.5,j,k}^{\;l-0.5}+v_{xp\,i+0.5,j-1,k}^{\;l-0.5}}{dy^2}\right.\\
&\qquad\left.+\frac{v_{xp\,i+0.5,j,k+1}^{\;l-0.5}-2v_{xp\,i+0.5,j,k}^{\;l-0.5}+v_{xp\,i+0.5,j,k-1}^{\;l-0.5}}{dz^2}\right).
\end{aligned}\qquad(3.26)$$

Its value is determined by its previous value and the velocity v_{xp} at the intermediate time step

$$\begin{aligned}
\phi_{0i+0.5,j,k}^{\;l}=\phi_{0i+0.5,j,k}^{\;l-1}+dtD&\left(\frac{v_{xp\,i+0.5,j+1,k}^{\;l-0.5}-2v_{xp\,i+0.5,j,k}^{\;l-0.5}+v_{xp\,i+0.5,j-1,k}^{\;l-0.5}}{dy^2}\right.\\
&\qquad\left.+\frac{v_{xp\,i+0.5,j,k+1}^{\;l-0.5}-2v_{xp\,i+0.5,j,k}^{\;l-0.5}+v_{xp\,i+0.5,j,k-1}^{\;l-0.5}}{dz^2}\right).
\end{aligned}\qquad(3.27)$$

For the discretisation of eqn. (3.12), two new variables are defined per damping term

$$Q_n = I_{n,y} + I_{n,z}\,, \tag{3.28}$$

where

$$I_{n,y} = \frac{\partial^2 W}{\partial y^2} - \int_0^t \frac{\partial^2 W}{\partial y^2} \cdot e^{-s_n(t-\tau)} s_n d\tau\,, \tag{3.29}$$

$$I_{n,z} = \frac{\partial^2 W}{\partial z^2} - \int_0^t \frac{\partial^2 W}{\partial z^2} \cdot e^{-s_n(t-\tau)} s_n d\tau\,; \tag{3.30}$$

the subscript 'n' in Q_n corresponds to the n-th damping term in eqn. (2.18); and the letter 'y' or 'z' in the subscript of $I_{n,y}$ and $I_{n,z}$ indicates the partial derivative in y or z direction.

Taking $I_{1,y}$ as an example, its discretisation form can be written as

$$\begin{aligned}
I_{1,y}^{l+1} &= \frac{\partial^2 W}{\partial y^2}^{l+\frac{1}{2}} - \int_0^{(l+1)dt} \frac{\partial^2 W}{\partial y^2} \cdot e^{-s_1[(l+1)dt-\tau]} s_1 d\tau \\
&= \frac{\partial^2 W}{\partial y^2}^{l+\frac{1}{2}} - \int_0^{ldt} \frac{\partial^2 W}{\partial y^2} \cdot e^{-s_1[(l+1)dt-\tau]} s_1 d\tau - \int_{ldt}^{(l+1)dt} \frac{\partial^2 W}{\partial y^2} \cdot e^{-s_1[(l+1)dt-\tau]} s_1 d\tau \\
&= \frac{\partial^2 W}{\partial y^2}^{l+\frac{1}{2}} - \int_0^{ldt} \frac{\partial^2 W}{\partial y^2} \cdot e^{-s_1(ldt-\tau)} s_1 d\tau \cdot e^{-s_1 dt} \\
&\qquad - \frac{1}{2}\left(\frac{\partial^2 W}{\partial y^2}^{l+\frac{1}{2}} + \frac{\partial^2 W}{\partial y^2}^{l-\frac{1}{2}} \right) \int_{ldt}^{(l+1)dt} e^{-s_1[(l+1)dt-\tau]} s_1 d\tau \\
&= \frac{\partial^2 W}{\partial y^2}^{l+\frac{1}{2}} - \int_0^{ldt} \frac{\partial^2 W}{\partial y^2} \cdot e^{-s_1(ldt-\tau)} s_1 d\tau \cdot e^{-s_1 dt} \\
&\qquad - \frac{1}{2}\left(\frac{\partial^2 W}{\partial y^2}^{l+\frac{1}{2}} + \frac{\partial^2 W}{\partial y^2}^{l-\frac{1}{2}} \right) \left(1 - e^{-s_1 dt}\right)
\end{aligned}\,, \tag{3.31}$$

where a linear interpolation was used for the integrand within the time interval dt. The term $I_{1,y}^{l}$ can be written as

$$I_{1,y}^{l} = \frac{\partial^2 W}{\partial y^2}^{l-\frac{1}{2}} - \int_0^{ldt} \frac{\partial^2 W}{\partial y^2} \cdot e^{-s_1(ldt-\tau)} s_1 d\tau\,. \tag{3.32}$$

Substituting eqn. (3.32) into eqn. (3.31) gives

$$
\begin{aligned}
I_{1,y}^{l+1} &= \frac{\partial^2 W}{\partial y^2}^{l+\frac{1}{2}} + \left(I_{1,y}^{l} - \frac{\partial^2 W}{\partial y^2}^{l-\frac{1}{2}} \right) \cdot e^{-s_1 dt} - \left(\frac{\partial^2 W}{\partial y^2}^{l+\frac{1}{2}} + \frac{\partial^2 W}{\partial y^2}^{l-\frac{1}{2}} \right) \frac{\left(1 - e^{-s_1 dt}\right)}{2} . \\
&= I_{1,y}^{l} \cdot e^{-s_1 dt} + \left(\frac{\partial^2 W}{\partial y^2}^{l+\frac{1}{2}} - \frac{\partial^2 W}{\partial y^2}^{l-\frac{1}{2}} \right) \frac{1 + e^{-s_1 dt}}{2}
\end{aligned}
\tag{3.33}
$$

Similarly, the $I_{n,y}$ and $I_{n,z}$ can be discretised as

$$
I_{n,y}^{l+1} = I_{n,y}^{l} \cdot e^{-s_n dt} + \left(\frac{\partial^2 W}{\partial y^2}^{l+\frac{1}{2}} - \frac{\partial^2 W}{\partial y^2}^{l-\frac{1}{2}} \right) \frac{1 + e^{-s_n dt}}{2} ,
\tag{3.34}
$$

$$
I_{n,z}^{l+1} = I_{n,z}^{l} \cdot e^{-s_n dt} + \left(\frac{\partial^2 W}{\partial z^2}^{l+\frac{1}{2}} - \frac{\partial^2 W}{\partial z^2}^{l-\frac{1}{2}} \right) \frac{1 + e^{-s_n dt}}{2} .
\tag{3.35}
$$

Equation (3.28) can be discretised as

$$
Q_n^{l+1} = I_{n,y}^{l+1} + I_{n,z}^{l+1} \cdot
\tag{3.36}
$$

Then, eqn. (3.12) can be discretised as

$$
\phi_{i+0.5,j,k}^{l+1} = \sum_{n=1}^{N} DR_n Q_n^{l+1} \cdot
\tag{3.37}
$$

The time derivative of Q_n^{l+1} is

$$
\begin{aligned}
\prod_n^{l+1} = \frac{\partial Q_n^{l+1}}{\partial t} &= \prod_n^{l} \cdot e^{-s_n dt} \\
&+ \left(\frac{\partial^2 v_{xp}}{\partial y^2}^{l+\frac{1}{2}} + \frac{\partial^2 v_{xp}}{\partial z^2}^{l+\frac{1}{2}} - \frac{\partial^2 v_{xp}}{\partial y^2}^{l-\frac{1}{2}} - \frac{\partial^2 v_{xp}}{\partial z^2}^{l-\frac{1}{2}} \right) \frac{1 + e^{-s_n dt}}{2} ,
\end{aligned}
\tag{3.38}
$$

Taking the time derivative of eqn. (3.37) and substituting eqns. (3.38) into the resulting equation leads to

$$
\phi_{i+0.5,j,k}^{l} = \phi_{i+0.5,j,k}^{l-1} + dt \sum_{n=1}^{N} DR_n \prod_{n\,i+0.5,j,k}^{l} ,
\tag{3.39}
$$

$$
\begin{aligned}
\prod_{n\,i+0.5,j,k}^{l} = \prod_{n\ \ i+0.5,j,k}^{l-1} \cdot e^{-s_n dt} &+ \left(\frac{v_{xp\,i+0.5,j+1,k}^{\ \ l-0.5} - 2 v_{xp\,i+0.5,j,k}^{\ \ l-0.5} + v_{xp\,i+0.5,j-1,k}^{\ \ l-0.5}}{dy^2} \right. \\
&+ \frac{v_{xp\,i+0.5,j,k+1}^{\ \ l-0.5} - 2 v_{xp\,i+0.5,j,k}^{\ \ l-0.5} + v_{xp\,i+0.5,j,k-1}^{\ \ l-0.5}}{dz^2} - \frac{v_{xp\,i+0.5,j+1,k}^{\ \ l-1-0.5} - 2 v_{xp\,i+0.5,j,k}^{\ \ l-1-0.5} + v_{xp\,i+0.5,j-1,k}^{\ \ l-1-0.5}}{dy^2} \\
&\left. - \frac{v_{xp\,i+0.5,j,k+1}^{\ \ l-1-0.5} - 2 v_{xp\,i+0.5,j,k}^{\ \ l-1-0.5} + v_{xp\,i+0.5,j,k-1}^{\ \ l-1-0.5}}{dz^2} \right) \frac{1 + e^{-s_n dt}}{2} .
\end{aligned}
\tag{3.40}
$$

Equations (3.24), (3.26) and (3.39) are the discretised forms for the momentum equation governing leaf vibration. It can be observed that the velocity v_{xp} at time step l+0.5 depends on the velocity v_{xp} at time step l-0.5, pressure p at time step l, ϕ_0 and ϕ at time step l. Furthermore, ϕ_0 at time step l depends on ϕ_0 at time l-1 and velocity v_{xp} at time step l-0.5; ϕ at time step l depends on ϕ at time step l-1, velocity v_{xp} at time steps l-0.5 and l-1-0.5. The calculation process for the pressure and velocities in air and absorbing materials and for the normal velocity on the leaf surface is summarized in Table 3. 1.

Table 3. 1 Calculation process for the pressure and velocities in air and absorbing materials, and for the normal velocity on the leaf surface.

Dependent Values	Independent Values	Corresponding Equation(s)
Pressure in air: $P_{i,j,k}$ at time step l+1	$P_{i,j,k}$ at time step l; $v_{x\ i\pm0.5,j,k}$, $v_{y\ i,j\pm0.5,k}$, $v_{z\ i,j,k\pm0.5}$ at time step l+0.5	Equation (3.17)
Velocity in air: $v_{\alpha\ \alpha+0.5}$ at time step l+0.5 ($\alpha=x/i,y/j,z/k$)	$v_{\alpha\ \alpha+0.5}$ at time step l-0.5; $P_{\alpha+1}$, P_{α} at time step l	Equation (3.18)
Pressure of air in bulk material: $P_{a\ i,j,k}$ at time step l+1	$P_{a\ i,j,k}$ at time step l; $v_{xa\ i\pm0.5,j,k}$, $v_{ya\ i,j\pm0.5,k}$, $v_{za\ i,j,k\pm0.5}$ at time step l+0.5; $v_{xf\ i\pm0.5,j,k}$, $v_{yf\ i,j\pm0.5,k}$, $v_{zf\ i,j,k\pm0.5}$ at time step l+0.5	Equation (3.19)
Pressure of frame in absorbing materials: $P_{frame\ i,j,k}$ at time step l+1	$P_{frame\ i,j,k}$ at time step l; $v_{xa\ i\pm0.5,j,k}$, $v_{ya\ i,j\pm0.5,k}$, $v_{za\ i,j,k\pm0.5}$ at time step l+0.5; $v_{xf\ i\pm0.5,j,k}$, $v_{yf\ i,j\pm0.5,k}$, $v_{zf\ i,j,k\pm0.5}$ at time step l+0.5	Equation (3.21)
Velocities of air and frame in absorbing materials: $v_{\alpha a\ \alpha+0.5}$ and $v_{\alpha f\ \alpha+0.5}$ at time step l+0.5 ($\alpha=x/i,y/j,z/k$)	$v_{\alpha a\ \alpha+0.5}$ at time step l-0.5; $v_{\alpha f\ \alpha+0.5}$ at time step l-0.5; $P_{a\ \alpha}$ and $P_{a\ \alpha+1}$ at time step l; $P_{frame\ \alpha}$ and $P_{frame\ \alpha+1}$ at time step l	Equations (3.20) and (3.22)
Normal velocity at leaf surface: $v_{xp\ i+0.5,j,k}$ at time step l+0.5	$v_{xp\ i+0.5,j,k}$ at time step l-0.5; $P_{i+1,j,k}$, $P_{i,j,k}$, $\phi_{i+0.5,j\pm1,k}$, $\phi_{i+0.5,j,k}$, $\phi_{0i+0.5,j\pm1,k}$ and $\phi_{0i+0.5,j,k}$ at time step l	Equation (3.25)
$\phi_{0i+0.5,j,k}$ at time step l	$\phi_{0i+0.5,j,k}$ at time step l-1; $v_{xp\ i+0.5,j,k}$, $v_{xp\ i+0.5,j\pm1,k}$, $v_{xp\ i+0.5,j,k\pm1}$ at time step l-0.5	Equation (3.27)
$\phi_{i+0.5,j,k}$ at time step l	$\phi_{i+0.5,j,k}$ at time step l-1; $\Pi_{n\ i+0.5,j,k}$ at time step l	Equation (3.39)
$\Pi_{n\ i+0.5,j,k}$ at time step l	$\Pi_{n\ i+0.5,j,k}$ at time step l-1; $v_{xp\ i+0.5,j,k}$, $v_{xp\ i+0.5,j\pm1,k}$, $v_{xp\ i+0.5,j,k\pm1}$ at time steps l-0.5 and l-1-0.5	Equation (3.40)

The updating equation for the velocity parallel to boundaries, v_γ, is adapted to include the effect of the viscous boundary layer. The square root of ω dependence in eqn. (3.14) is hereby approximated by a ratio of polynomials of order M and N in frequency domain. Eventually, this leads to the adapted FDTD update equation [125]:

$$\begin{aligned}\left(\frac{\rho_0}{dt}a_0+\frac{\sqrt{\mu_f\rho_0}}{2\cdot d\delta}b_0\right)v_\gamma^{l+\frac{1}{2}}&=-\sum_{k=0}^{M}a_k\frac{\partial P^{l-k}}{\partial\gamma}-\frac{\rho_0}{dt}\sum_{k=1}^{M+1}\left(a_k-a_{k-1}\right)v_\gamma^{l-k+\frac{1}{2}}\\&\quad-\frac{\sqrt{\mu_f\rho_0}}{2\cdot d\delta}\sum_{i=1}^{N+1}\left(b_i+b_{i-1}\right)v_\gamma^{l-i+\frac{1}{2}}\end{aligned}, \tag{3.41}$$

where $d\delta$ is the grid step in the direction orthogonal to the leaf plane; γ denotes the directions parallel to the leaf surface; and μ_f is the dynamic viscosity. For the simulations in this PhD thesis, M and N are chosen equal to 2. The values for a_k, and b_i are the same as those used by Bockstael et al. [126]: a_0=1, a_1=-1.95, a_2=0.95, a_3=0, b_0=403.73, b_1=-802.77, b_2=399.04, and b_3=0. Similarly, the FDTD update equation for the pressure in the entropy boundary layer is

$$\begin{aligned}\left[\frac{1}{dt}a_0+\sqrt{\frac{(\gamma-1)^2\kappa}{c_p\rho_0}}\frac{1}{2\cdot d\alpha}b_0\right]P^{l+1}&=-\rho_0c^2\sum_{k=0}^{M}a_k\nabla\cdot\vec{V}^{l-k+\frac{1}{2}}\\&\quad-\sum_{k=1}^{M+1}\frac{a_k-a_{k-1}}{dt}P^{l-k+1}\\&\quad-\sum_{i=1}^{N+1}\sqrt{\frac{(\gamma-1)^2\kappa}{c_p\rho_0}}\frac{b_i+b_{i-1}}{2\cdot d\alpha}P^{l-i+1}\end{aligned}, \tag{3.42}$$

where the values for a_k and b_i are the same used in eqns. (3.41). In eqn. (3.42), the influence of heat conduction on sound propagation is neglected because it is assumed that the temperature is constant on the leaf surface.

3.3 Stability analysis

The standard explicit FDTD method is not unconditionally stable, so the spatial and temporal steps in FDTD must be chosen carefully. When the bending wave, the Biot material, and the visco-thermal boundary are not considered, the Fourier stability analysis [127] requires the Courant number CN to satisfy the following relationship [69],

$$CN=cdt\sqrt{\sum_{\beta=x,y,z}\frac{1}{d\beta^2}}\leq 1, \tag{3.43}$$

where c is sound speed. When the bending wave is included, the stability criterion has not been derived.

3.4 Choice of parameters

In the FDTD model, there are many parameters, which must be determined before or during the simulations. Equations (3.9), (3.12) and (3.13) need to know the damping parameters during the bending of leaf. In this thesis, their values are chosen based on the data used in modelling the bending of wood (see Ref. 103), and they are R_1=0.013, R_2=0.038, s_1=2000 rad/s, s_2=33000 rad/s and R_L=2.4 s^{-1}. The parameters for modelling the poro-elastic substrate, such as K_a, K_f, φ, k_s, R, and R_f (see eqns. (3.3)-(3.6)), must be tuned in the corresponding simulation process, which can be found in Chapter 5.

Another important material parameter is bending stiffness of leaf. It is important in simulating the vibration of leaf excited by the sound and appears in the bending wave equation (see eqns. (3.11) and (3.12)).

The bending stiffness of each leaf was estimated according to the following expression [60]

$$D = \frac{E \cdot {d_{Leaf}}^3}{12\left(1-\nu^2\right)}, \tag{3.44}$$

where D is the bending stiffness per unit width for a plate; E is Young's modulus; d_{Leaf} is the leaf thickness; and ν is Poisson's ratio. Equation (3.44) has previously been used to determine the bending stiffness of a thin uniform homogeneous plate [60].

However, this method has limitations when used for the leaves of vegetation. For example, the leaf is not an isotropic plate, which has uniform mass distribution on the plate surface. The veins of the leaf can lead to non-uniform mass distribution and also non-homogeneous stiffness. Because there is no ideal way to get the bending stiffness, eqn. (3.44) will be used to obtain an approximation or order of magnitude for the bending stiffness of a leaf.

In order to estimate the bending stiffness, we need to know the values of Young's modulus E, thickness d_{Leaf} and Poisson's ratio ν of the leaf. The leaf's Young's modulus can be determined by measurement. Saito et al. [128] measured the Young's modulus of Quercus leaves; Satyanarayana et al. [129] measured the Young's modulus of the coconut tree leaf; and Arib et al. [130] provided the data of Young's modulus for pineapple leaf fiber.

When there are no measurement results for the leaf's Young's modulus available, the work done by Saito et al. [128] and Niinemets [131] can be used as a first estimate. Saito et al. [128] presented a linear regression relationship between bulk elastic modulus (ε) and Young's modulus (E) for the leaves of Quercus glauca and Quercus serrata:

$$\varepsilon = A \cdot E + B. \tag{3.45}$$

This relationship is derived based on the single leaf cell which has a spherical shell structure; and it can be used to estimate the Young's modulus from the bulk elastic modulus. For Quercus glauca, A=0.11 and B=1.21 result in a regression with r_{cc}^2=0.78, where r_{cc} is the correlation coefficient; for Quercus serrata, A=0.13 and B=-1.42 give r_{cc}^2=0.84. The leaf's bulk elastic modulus can also be measured. Saito et al.[132], Scholz et al.[133] and Nardini et al.[134] provided the bulk elastic modulus for different leaves by pressure-volume measurement. When the measurement for the leaf's bulk elastic modulus is not available, Niinemets [131] presented a linear regression relationship between leaf volume density and its bulk modulus based on the data from 51 tree and shrub species:

$$\varepsilon = 2.03 + 25.4\rho_{Leaf}, \text{ with } r_{cc}^2=0.35, \tag{3.46}$$

where ε is the foliage bulk elastic modulus and ρ_{Leaf} is the leaf volume density. Therefore, the leaf's Young's modulus can be estimated by eqns. (3.45) and (3.46) when the leaf volume density is known.

The best and fastest way to get the leaf thickness is measurement. The fresh leaf thickness can be measured by digital caliper. However, when the measurement is not available, leaf thickness can be estimated by other methods. White and Montes-R [135] pointed out the importance of variation in water or air content in the tree leaf. They provided the leaf thickness by measurement for the common bean (Phaseolus vulgaris L.) and the relationship between the leaf thickness and the leaf dry weight basis was found. They also proved that the mean leaf thickness had values between 0.11 mm and 0.375 mm depending on the measurement date after planting, planting season and planting site. Marenco et al. [136] studied the relationship between chlorophyll content of leaves and leaf parameters, which includes leaf thickness, for six Amazonian tree species. Vile et al. [137] provided a method to estimate thickness in laminar leaves. The leaf thickness (d_{Leaf}) can be calculated from leaf fresh mass (M_F), average density of the leaf (ρ_{Leaf}) and leaf projected area (A_{Leaf}).

$$d_{Leaf} = \frac{V_L}{A_{Leaf}} = \frac{1}{\rho_{Leaf}} \times \frac{M_F}{A_{Leaf}}, \tag{3.47}$$

where V_L is the volume of the leaf. The leaf dry mass (M_D) was also introduced in the calculation and then eqn. (3.47) becomes

$$d_{Leaf} = \frac{1}{\rho_{Leaf}} \times \frac{M_D}{A_{Leaf}} \times \frac{M_F}{M_D}. \tag{3.48}$$

In the measurements, they chose several hundreds of samples, which came from different parts of the world (including France, Spain, South Africa, central Europe, Great Britain, central Argentina, Canada, and Australia), different species and different growth forms (such as, short-lived forbs, long-lived forbs, short-lived graminoids, long-lived graminoids, ferns, succulents, shrubs and trees). The leaf thickness was determined with a linear variable displacement transducer. The measurement results shown that the average density ρ_{Leaf} could be chosen as 1 g/cm^3 and the leaf thickness could be estimated from

$$d_{Leaf} \approx \frac{M_F}{A_{Leaf}} \approx \frac{M_D}{A_{Leaf}} \times \frac{M_F}{M_D} . \tag{3.49}$$

The Poisson's ratio is another parameter needed to be chosen for the bending stiffness calculation. Saito et al. [128] set 0.25 as the Poisson's ratio in their paper based on the assumption that the specimen was isotropic [138]. It was reported that the Poisson's ratio for parenchyma tissue lay in the range 0.23-0.5 [139]. In this thesis, 0.25 is chosen as the Poisson's ratio.

Grid step is another important model parameter in the calculation. It influences the accuracy and efficiency of the calculation. For sound propagation in fluids a rule of thumb consists in choosing 10 grid cells in one wavelength. Thus for example for an FDTD simulation of sound propagation in air to be accurate up to 10000 Hz a grid cell size smaller than 0.0034 m would be appropriate.

The bending wavelength λ_b on the leaf plate is related to wave number k_b by

$$\lambda_b = \frac{2\pi}{k_b} . \tag{3.50}$$

The bending wave number can be calculated by [60]

$$k_b = \omega^{1/2} (m_a / D)^{1/4} , \tag{3.51}$$

where ω is the angular frequency of the exciting force; m_a is the mass per unit area and D is bending stiffness per unit width. To simulate the bending wave on the leaf accurately, the grid size must not be greater than 1/10 of one bending wavelength. For the leaves studied in this thesis, their mass per unit area (m_a) is between 0.08 and 0.5 kg/m^2; and their estimated bending stiffness (D) is between 0.001 and 0.01 N·m. The wavelength corresponding to 10000 Hz according to eqns. (3.50) and (3.51) is 0.0053 m. Therefore, the grid size must be smaller than 0.00053m. This is more restrictive than the requirement following from the propagation in air. To model sound fields close to the bending leaf accurately, it is recommended that 0.0005m is used as the grid step to model sound propagation over leaf.

CHAPTER 4

The ultra-weak variational formulation (UWVF) method for interaction of sound with porous substrates[2]

In my thesis, the UWVF method is investigated as an alternative to FDTD to study the influences of low-height noise barriers on the sound propagation. The low-height noise barriers are assumed to be constructed by porous materials which have a rigid frame. In this case, Biot's theory [88, 89] is not necessary and instead Zwikker and Kosten's phenomenological model [91] is used. The Zwikker and Kosten's model has been introduced in section 2.5 and is reasonable for the typical materials envisaged in such low-height porous barriers, for instance stones or other granular material. In this rigid frame model, the air between the particles is allowed to vibrate, while the constituting part of the porous medium is assumed to be rigid. Only when there is interest in predicting the attenuation inside the porous medium at high sound frequencies and low flow resistivity, should adaption be made as presented by K. Wilson et al. [140]. Furthermore, this model allows for an easy introduction in the classical Helmholtz equation (see eqn. (2.9)).

In Section 4.1, a generalised Helmholtz equation will be derived based on Zwikker and Kosten's model. In the later sections, the generalised Helmholtz equation will be solved by UWVF method. It must be noted that other porous models can be implemented in UWVF method without additional difficulties.

4.1 Helmholtz problem

4.1.1 Generalised Helmholtz equation

In the Zwikker and Kosten's model, the porous media is described by three parameters, which are the flow resistivity (R), porosity (φ) and the structure factor (k_s). The linear equations for sound propagation in a rigid frame porous medium are

---

[2] Part of this chapter has been published in:
Lei Ding, Timothy Van Renterghem and Dick Botteldooren: Estimating the effect of semi-transparent low-height road traffic noise barriers with ultra weak variational formulation. ACTA ACUSTICA UNITED WITH ACUSTICA, 97(3), 391-402 (2011).

$$\nabla P + \rho' \frac{\partial \vec{V}}{\partial t} + R\vec{V} = 0 , \tag{4.1}$$

$$\frac{\partial P}{\partial t} + c'^2 \rho' \nabla \cdot \vec{V} = 0 , \tag{4.2}$$

$$\rho' = \frac{\rho_0 k_s}{\varphi} , \tag{4.3}$$

$$c' = \frac{c}{\sqrt{k_s}} . \tag{4.4}$$

Similar to the procedure to get eqn. (2.9), taking the divergence of eqn. (4.1), taking the time derivative of eqn. (4.2), and eliminating $\partial\left(\nabla \cdot \vec{V}\right)/\partial t$ from the resulting equations give

$$\frac{1}{c'^2 \rho'} \frac{\partial^2 P}{\partial t^2} - \nabla \cdot \left(\frac{1}{\rho'} \nabla P \right) - \nabla \cdot \left(\frac{R}{\rho'} \vec{V} \right) = 0 . \tag{4.5}$$

The ratio R/ρ' is assumed to be constant, and the third term in eqn. (4.5) can be replaced with eqn. (4.2). Therefore, eqn. (4.5) can be written as

$$\frac{1}{c'^2 \rho'} \frac{\partial^2 P}{\partial t^2} - \nabla \cdot \left(\frac{1}{\rho'} \nabla P \right) + \frac{R}{c'^2 \rho'^2} \frac{\partial P}{\partial t} = 0 . \tag{4.6}$$

As the wave in this research work is assumed to be time harmonic (see eqn. (2.8)), eqn. (4.6) can be expressed as

$$\nabla \cdot \left(\frac{1}{\rho'} \nabla p \right) + \frac{\dfrac{\omega^2}{c'^2} + \dfrac{i\omega R}{c'^2 \rho'}}{\rho'} p = 0 . \tag{4.7}$$

The wave number in porous media can be defined as

$$\kappa' = \frac{\omega}{c} \sqrt{k_s + \frac{i\varphi R}{\omega \rho_0}} . \tag{4.8}$$

Consequently, eqn. (4.7) can be simplified as

$$\nabla \cdot \left(\frac{1}{\rho'} \nabla p \right) + \frac{\kappa'^2}{\rho'} p = 0 . \tag{4.9}$$

In later work, a point source will be considered in the simulation, so the Helmholtz equation with point source is

$$\nabla \cdot \left(\frac{1}{\rho'} \nabla p \right) + \frac{\kappa'^2}{\rho'} p = f_s , \tag{4.10}$$

where f_s denotes the source term. Now the Helmholtz equation in rigid frame porous media has been obtained. It can found that when k_s=1, φ=1 and R=0 are satisfied, eqn. (4.9) becomes eqn. (2.9), which is the Helmholtz equation for sound propagation in air. Therefore, eqn. (4.9) is the generalised Helmholtz equation.

Since UWVF is a volume-discretisation technique, the speed of sound can be location-dependent, and this provides a way to model the refracting atmosphere by using the effective sound speed approach.

4.1.2 Perfectly matched layer for Helmholtz problem

Using efficient and accurate absorbing boundary conditions is of primary importance in numerical models for outdoor sound propagation application. The unbounded sound propagation region has to be truncated to a limited calculation domain. The non-reflection boundary condition (NRBC) has been reviewed in section 2.6; and the perfectly matched layer (PML) approach is chosen in this thesis. The implementation of a PML in the UWVF method is based on extending the domain into a complex spatial coordinate space. In this section, this approach will be introduced and further details can be found in the ref. [52, 141].

In the previous section, the Helmholtz equation in inhomogeneous medium is given. Now, the complex stretching of the spatial coordinates is considered and defined by

$$x' = \begin{cases} x + \dfrac{i}{\kappa}\displaystyle\int_{x_0}^{x} \sigma_{0,x}\left(|\tau| - x_0\right)^n d\tau, & |x| \ge x_0 \text{ in PML domain}, \\ x, & |x| < x_0 \text{ in non-PML domain}, \end{cases} \tag{4.11}$$

$$y' = \begin{cases} y + \dfrac{i}{\kappa}\displaystyle\int_{y_0}^{y} \sigma_{0,y}\left(|\tau| - y_0\right)^n d\tau, & |y| \ge y_0 \text{ in PML domain}, \\ y, & |y| < y_0 \text{ in non-PML domain}, \end{cases} \tag{4.12}$$

$$z' = \begin{cases} z + \dfrac{i}{\kappa}\displaystyle\int_{z_0}^{z} \sigma_{0,z}\left(|\tau| - z_0\right)^n d\tau, & |z| \ge \mathrm{z}_0 \text{ in PML domain}, \\ \mathrm{z}, & |z| < \mathrm{z}_0 \text{ in non-PML domain}. \end{cases} \tag{4.13}$$

The following definitions are given in order to simplify the notation

$$\sigma_\xi(\xi) = \sigma_{0,\xi} \cdot \left(|\xi| - \xi_0\right)^n, \qquad \xi = x, y, z, \tag{4.14}$$

where $\sigma_{0,\xi}$ is constant and n is an integer. The derivative of stretched spatial variables is

$$d_x = d_x(x) = \frac{\partial x'}{\partial x} = \begin{cases} 1 + \dfrac{i}{\kappa}\sigma_x(x), & |x| \ge x_0, \\ 1, & |x| < x_0, \end{cases} \tag{4.15}$$

$$d_y = d_y(y) = \frac{\partial y'}{\partial y} = \begin{cases} 1 + \dfrac{i}{\kappa}\sigma_y(y), & |y| \ge y_0, \\ 1, & |y| < y_0, \end{cases} \tag{4.16}$$

$$d_z = d_z(z) = \frac{\partial z'}{\partial z} = \begin{cases} 1 + \dfrac{i}{\kappa}\sigma_z(z), & |z| \geq z_0, \\ 1, & |z| < z_0. \end{cases} \tag{4.17}$$

This gives a substitution

$$\frac{\partial}{\partial \xi'} = \frac{1}{d_\xi}\frac{\partial}{\partial \xi}, \text{ and } \xi = x, y, z\,. \tag{4.18}$$

The Helmholtz equation with stretched variables is

$$\nabla' \cdot \left(\frac{1}{\rho'}\nabla' p\right) + \frac{\kappa'^2}{\rho'} p = f_s, \tag{4.19}$$

where $\nabla' = (\partial/\partial x', \partial/\partial y', \partial/\partial z')^T$ is defined. Substituting eqn. (4.18) into eqn. (4.19) leads to

$$\frac{1}{d_x}\frac{\partial}{\partial x}\left(\frac{1}{\rho'}\frac{1}{d_x}\frac{\partial p}{\partial x}\right) + \frac{1}{d_y}\frac{\partial}{\partial y}\left(\frac{1}{\rho'}\frac{1}{d_y}\frac{\partial p}{\partial y}\right) + \frac{1}{d_z}\frac{\partial}{\partial z}\left(\frac{1}{\rho'}\frac{1}{d_z}\frac{\partial p}{\partial z}\right) + \frac{\kappa'^2}{\rho'} p = f_s. \tag{4.20}$$

Defining

$$\eta^2 = d_x d_y d_z, \tag{4.21}$$

and multiplying eqn. (4.21) to both sides of eqn. (4.20) gives

$$\frac{\partial}{\partial x}\left(\frac{1}{\rho'}\frac{d_y d_z}{d_x}\frac{\partial p}{\partial x}\right) + \frac{\partial}{\partial y}\left(\frac{1}{\rho'}\frac{d_x d_z}{d_y}\frac{\partial p}{\partial y}\right) + \frac{\partial}{\partial z}\left(\frac{1}{\rho'}\frac{d_x d_y}{d_z}\frac{\partial p}{\partial z}\right) + \frac{\kappa'^2\eta^2}{\rho'} p = f_s\eta^2. \tag{4.22}$$

Equation (4.22) can be written in a more compact form, that is

$$\nabla \cdot \left(\frac{1}{\rho'} A_d \nabla p\right) + \frac{\kappa'^2\eta^2}{\rho'} p = f_s\eta^2, \tag{4.23}$$

where the matrix A_d is defined by

$$A_d = \begin{bmatrix} \dfrac{d_y d_z}{d_x}, & 0, & 0 \\ 0, & \dfrac{d_z d_x}{d_y}, & 0 \\ 0, & 0, & \dfrac{d_x d_y}{d_z} \end{bmatrix}. \tag{4.24}$$

Equation (4.23) is the Helmholtz equation with complex stretched spatial variables. It is noticed that in the non-PML region, the matrix $A_d = I$ is identity matrix and η^2 equals 1. In this case, Helmholtz equation (4.23) with stretched spatial variable becomes the Helmholtz equation (4.10). In other words, eqn. (4.10) is one special case of eqn. (4.23), when one chooses $\xi' = \xi, (\xi = x, y, z)$.

4.1.3 Discretised problem

After determining the governing equation and the non-reflecting boundary condition, the Helmholtz problem in the computational domain will be decomposed into many sub-problems in small elements or cells. A 2D problem about the effect of porous low-height noise barriers is studied in this thesis, so in this section a 2D discretisation of the Helmholtz problem is taken as an example. The triangular cell is chosen for the 2D discretised problem, because it is compatible with a lot of software and can be easily created by mesh-generation tools.

For the 2D problem, the computational domain Ω is partitioned into a collection of disjoint triangular finite cells $\{\Omega_k\}_{k=1}^{N}$. In Figure 4. 1, two elements, Ω_k and Ω_j are shown to explain the notations. The outward unit normal vector on the boundary of Ω_k is denoted by n_k. The boundary which connects the element Ω_k to Ω_j is $\Sigma_{k,j}$ and similarly $\Sigma_{j,k}$ connects Ω_j to Ω_k. The interface $\Sigma_{k,j}$ has outgoing unit normal vector n_k, while the interface $\Sigma_{j,k}$ has outgoing unit normal vector n_j. If the boundary of the element Ω_k is also an exterior boundary of the total domain Ω, then this boundary is denoted as Γ_k.

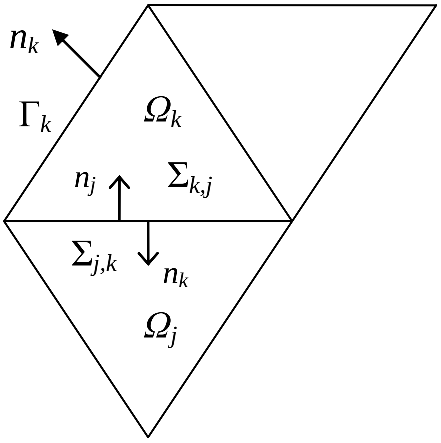

Figure 4. 1 Three adjacent computational cells with notations.

The density and the wave number are assumed to be piecewise constants, so let $\rho_k = \rho|_{\Omega_k}$ and $\kappa_k = \kappa|_{\Omega_k}$. Therefore, the Helmholtz problem (4.23) in the domain Ω can be decomposed into a collection of sub-problems in the elements Ω_k, k=1,2...N,

$$\nabla \cdot \left(A_{d,k} \nabla p_k\right) + \kappa_k'^2 \eta_k^2 p_k = f_k \eta_k^2, \quad \text{in } \Omega_k, \tag{4.25}$$

where the subscript *k* indicates the parameters or variables are in the sub-domain Ω_k; and $f_k = f_s \cdot \rho'_k$ is introduced.

On the interface between two neighboring cells, the continuity of pressure and the continuity of velocity must be satisfied [52, 141]. For time harmonic waves, the continuity of pressure gives

$$p_k = p_j, \qquad \text{on } \Sigma_{k,j}. \tag{4.26}$$

where the subscripts *k* and *j* denote the adjacent cells. Considering the time harmonic wave,

$$\vec{V} = \vec{v} e^{-i\omega t} \text{ and } P = p e^{-i\omega t}, \tag{4.27}$$

eqn. (4.1) can be written as

$$\frac{1}{\rho'} \nabla p e^{-i\omega t} - i\omega \vec{v} e^{-i\omega t} + \frac{1}{\rho'} R \vec{v} e^{-i\omega t} = 0 \cdot \tag{4.28}$$

The velocity can be derived from eqn. (4.28), and it is

$$\vec{v} = \frac{1}{\rho'} \frac{1}{i\omega - \frac{1}{\rho'} R} \nabla p \cdot \tag{4.29}$$

Considering the general form of the Helmholtz problem (4.23), the continuity of the velocity normal to the interface between two neighboring cells *k* and *j* can be written as

$$\frac{1}{\rho_k} \frac{1}{i\omega - \frac{1}{\rho_k} R_k} \vec{n}_k \cdot \left(A_{d,k} \nabla p_k\right) = -\frac{1}{\rho_j} \frac{1}{i\omega - \frac{1}{\rho_j} R_j} \vec{n}_j \cdot \left(A_{d,j} \nabla p_j\right), \text{ on } \Sigma_{k,j}, \tag{4.30}$$

where $\vec{n}_k$ and $\vec{n}_j$ are the outgoing normal direction on the boundaries of the cells. If the medium is not porous, the continuity of velocity gives [52]

$$\frac{1}{\rho_k} \vec{n}_k \cdot \left(A_{d,k} \nabla p_k\right) = -\frac{1}{\rho_j} \vec{n}_j \cdot \left(A_{d,j} \nabla p_j\right), \quad \text{on } \Sigma_{k,j}. \tag{4.31}$$

Therefore, in order to get a more general form for the continuity of velocity, a term '$i\omega$' is multiplied to both sides of eqn. (4.30) and then it becomes

$$\frac{1}{\rho_k} \frac{i\omega}{i\omega - \frac{1}{\rho_k} R_k} \vec{n}_k \cdot \left(A_{d,k} \nabla p_k\right) = -\frac{1}{\rho_j} \frac{i\omega}{i\omega - \frac{1}{\rho_j} R_j} \vec{n}_j \cdot \left(A_{d,j} \nabla p_j\right), \text{ on } \Sigma_{k,j}. \tag{4.32}$$

When, the medium is air, the flow resistivity R_k and R_j are 0, and then eqn. (4.32) becomes eqn. (4.31).

Combining eqns. (4.26) and (4.32) gives

$$\begin{aligned}&\frac{1}{\rho_k}\vec{n}_k\cdot\left(A_{d,k}\nabla p_k\right)\frac{i\omega}{i\omega-\frac{1}{\rho_k}R_k}-i\varsigma\ p_k=\\&\qquad-\frac{1}{\rho_j}\vec{n}_j\cdot\left(A_{d,j}\nabla p_j\right)\frac{i\omega}{i\omega-\frac{1}{\rho_j}R_j}-i\varsigma\ p_j\end{aligned}\quad,\ \text{on}\ \Sigma_{k,j},\qquad(4.33)$$

$$\begin{aligned}&\frac{1}{\rho_k}\vec{n}_k\cdot\left(A_{d,k}\nabla p_k\right)\frac{i\omega}{i\omega-\frac{1}{\rho_k}R_k}+i\varsigma\ p_k=\\&\qquad-\frac{1}{\rho_j}\vec{n}_j\cdot\left(A_{d,j}\nabla p_j\right)\frac{i\omega}{i\omega-\frac{1}{\rho_j}R_j}+i\varsigma\ p_j\end{aligned}\quad,\ \text{on}\ \Sigma_{k,j},\qquad(4.34)$$

where $\varsigma=\varsigma_{k,j}=\frac{1}{2}\left(\frac{\Re(\kappa_k)}{\rho_k}+\frac{\Re(\kappa_j)}{\rho_j}\right)$ is defined on the interface $\Sigma_{k,j}$. Equations (4.33) and (4.34) are called the matching conditions.

On the exterior boundary this is generalised to

$$\begin{aligned}&\left(\frac{1}{\rho_k}\vec{n}_k\cdot\left(A_{d,k}\nabla p_k\right)\frac{i\omega}{i\omega-\frac{1}{\rho_k}R_k}-i\varsigma\ p_k\right)=\\&\qquad Q_k\left(-\frac{1}{\rho_k}\vec{n}_k\cdot\left(A_{d,k}\nabla p_k\right)\frac{i\omega}{i\omega-\frac{1}{\rho_k}R_k}-i\varsigma\ p_k\right)+g_k\end{aligned}\quad,\ \text{on}\ \Gamma_k,\qquad(4.35)$$

where $\varsigma=\varsigma_k=\frac{\Re(\kappa_k)}{\rho_k}$ is defined on the exterior boundary; and Q_k is a complex constant and g_k is a boundary source term. If $Q_k=1$ and $g_k=0$, the exterior boundary condition (4.35) becomes the rigid boundary condition. Equations (4.25), (4.33), (4.34) and (4.35) give the governing equation, transmission conditions, and boundary conditions for the sub-problems.

4.2 The Ultra Weak Variational Formulation of Helmholtz problem

In the previous section, the problem has been decomposed into many sub-problems in element $\{\Omega_k\}_{k=1}^{N}$. The ultra weak variational formulation (UWVF) of the Helmholtz problem in the non-porous medium will be introduced in this section. For the Helmholtz problem in the porous medium, the corresponding UWVF can be obtained by considering the modified density (eqn. (4.3)) and wavenumber (eqn. (4.8)) and including the term $i\omega/(i\omega\text{-}R_k/\rho_k)$ in the transmission conditions (eqns. (4.33) and (4.34)) and boundary condition (eqn. (4.35)).

The following equality holds [51]

$$\begin{aligned}
&\sum_{k=1}^{N}\int_{\partial\Omega_k}\frac{1}{\varsigma}\left(-\frac{1}{\rho_k}\vec{n}_k\cdot\left(A_{d,k}\nabla p_k\right)-i\varsigma\, p_k\right)\times\overline{\left(-\frac{1}{\rho_k}\vec{n}_k\cdot\left(\bar{A}_{d,k}\nabla v_k\right)-i\varsigma\, v_k\right)}\\
&=\sum_{k=1}^{N}\int_{\partial\Omega_k}\frac{1}{\varsigma}\left(\frac{1}{\rho_k}\vec{n}_k\cdot\left(A_{d,k}\nabla p_k\right)-i\varsigma\, p_k\right)\times\overline{\left(\frac{1}{\rho_k}\vec{n}_k\cdot\left(\bar{A}_{d,k}\nabla v_k\right)-i\varsigma\, v_k\right)}- \quad ,\\
&\sum_{k=1}^{N}\int_{\partial\Omega_k}2i\bar{v}_k\left(\frac{1}{\rho_k}\vec{n}_k\cdot\left(A_{d,k}\nabla p_k\right)\right)+\sum_{k=1}^{N}\int_{\partial\Omega_k}2ip_k\overline{\left(\frac{1}{\rho_k}\vec{n}_k\cdot\left(\bar{A}_{d,k}\nabla v_k\right)\right)}
\end{aligned}\tag{4.36}$$

for all smooth p_k and smooth test functions v_k. The upper bars indicate the complex conjugate. Substituting eqn. (4.33) and eqn. (4.35) into eqn. (4.36) gives

$$\begin{aligned}
&\sum_{k=1}^{N}\int_{\partial\Omega_k}\frac{1}{\varsigma}\left(-\frac{1}{\rho_k}\vec{n}_k\cdot\left(A_{d,k}\nabla p_k\right)-i\varsigma\, p_k\right)\times\overline{\left(-\frac{1}{\rho_k}\vec{n}_k\cdot\left(\bar{A}_{d,k}\nabla v_k\right)-i\varsigma\, v_k\right)}\\
&=\sum_{k=1}^{N}\sum_{j=1}^{N}\int_{\Sigma_{k,j}}\frac{1}{\varsigma}\left(-\frac{1}{\rho_j}\vec{n}_j\cdot\left(A_{d,j}\nabla p_j\right)-i\varsigma\, p_j\right)\times\overline{\left(\frac{1}{\rho_k}\vec{n}_k\cdot\left(\bar{A}_{d,k}\nabla v_k\right)-i\varsigma\, v_k\right)}+ \quad .\\
&\sum_{k=1}^{N}\int_{\Gamma_k}\frac{1}{\varsigma}\left[Q\left(-\frac{1}{\rho_k}\vec{n}_k\cdot\left(A_{d,k}\nabla p_k\right)-i\varsigma\, p_k\right)+g_k\right]\times\overline{\left(\frac{1}{\rho_k}\vec{n}_k\cdot\left(\bar{A}_{d,k}\nabla v_k\right)-i\varsigma\, v_k\right)}-\\
&\sum_{k=1}^{N}\int_{\partial\Omega_k}2i\bar{v}_k\left(\frac{1}{\rho_k}\vec{n}_k\cdot\left(A_{d,k}\nabla p_k\right)\right)+\sum_{k=1}^{N}\int_{\partial\Omega_k}2ip_k\overline{\left(\frac{1}{\rho_k}\vec{n}_k\cdot\left(\bar{A}_{d,k}\nabla v_k\right)\right)}
\end{aligned}\tag{4.37}$$

Green’s theorem can simplify the last two terms in right hand side of eqn. (4.37). They become

$$\begin{aligned}
&-\sum_{k=1}^{N}\int_{\partial\Omega_k}2i\bar{v}_k\left(\frac{1}{\rho_k}\vec{n}_k\cdot\left(A_{d,k}\nabla p_k\right)\right)+\sum_{k=1}^{N}\int_{\partial\Omega_k}2ip_k\overline{\left(\frac{1}{\rho_k}\vec{n}_k\cdot\left(\bar{A}_{d,k}\nabla v_k\right)\right)}.\\
&=-\sum_{k=1}^{N}\int_{\Omega_k}2i\bar{v}_k\,\frac{1}{\rho_k}\nabla\cdot\left(A_{d,k}\nabla p_k\right)+\sum_{k=1}^{N}\int_{\Omega_k}2ip_k\,\frac{1}{\rho_k}\nabla\cdot\left(A_{d,k}\nabla\bar{v}_k\right)
\end{aligned}\tag{4.38}$$

In order to simplify the above equality, we introduce the following definitions

$$\chi_k=-\frac{1}{\rho_k}\vec{n}_k\cdot\left(A_{d,k}\nabla p_k\right)-i\varsigma\, p_k\,,\qquad 1\le k\le N\,,\tag{4.39}$$

$$y_k=-\frac{1}{\rho_k}\vec{n}_k\cdot\left(\bar{A}_{d,k}\nabla v_k\right)-i\varsigma\, v_k\,,\qquad 1\le k\le N\,,\tag{4.40}$$

$$F_k(y_k) = \frac{1}{\rho_k}\vec{n}_k \cdot \left(\overline{A}_{d,k}\nabla v_k\right) - i\varsigma\, v_k, \qquad 1 \le k \le N. \tag{4.41}$$

The basis function p_k satisfies eqn. (4.25), and the piecewise smooth test function v_k satisfies the following equation

$$\nabla \cdot \left(A_{d,k}\nabla \overline{v}_k\right) + \kappa_k^2 \eta_k^2 \overline{v}_k = 0, \qquad \text{in } \Omega_k. \tag{4.42}$$

Therefore, substituting eqn. (4.25) and eqn. (4.42) into eqn. (4.38) leads to

$$\begin{aligned} & -\sum_{k=1}^{N}\int_{\partial\Omega_k} 2i\overline{v}_k\left(\frac{1}{\rho_k}\vec{n}_k \cdot \left(A_{d,k}\nabla p_k\right)\right) + \sum_{k=1}^{N}\int_{\partial\Omega_k} 2ip_k\overline{\left(\frac{1}{\rho_k}\vec{n}_k \cdot \left(\overline{A}_{d,k}\nabla\right)v_k\right)} \\ & = -\sum_{k=1}^{N}\int_{\Omega_k} 2i\overline{v}_k \frac{1}{\rho_k}\left(-\kappa_k^2\eta_k^2 p_k + f_k\eta_k^2\right) + \sum_{k=1}^{N}\int_{\Omega_k} 2ip_k \frac{1}{\rho_k}\left(-\kappa_k^2\eta_k^2\overline{v}_k\right) \\ & = -\sum_{k=1}^{N}\int_{\Omega_k} 2i\overline{v}_k \frac{1}{\rho_k} f_k\eta_k^2 \end{aligned} . \tag{4.43}$$

Substituting eqns. (4.39)-(4.41) and eqn. (4.43) into eqn. (4.37) gives

$$\begin{aligned} & \sum_{k=1}^{N}\int_{\partial\Omega_k} \frac{1}{\varsigma}\chi_k\overline{y_k} - \sum_{k=1}^{N}\sum_{j=1}^{N}\int_{\Sigma_{k,j}} \frac{1}{\varsigma}\chi_j\overline{F_k(y_k)} - \sum_{k=1}^{N}\int_{\Gamma_k} \frac{Q}{\varsigma}\chi_k\overline{F_k(y_k)} \\ & \qquad = \sum_{k=1}^{N}\int_{\Gamma_k} \frac{g}{\varsigma}\overline{F_k(y_k)} - \sum_{k=1}^{N}\int_{\Omega_k} \frac{2i}{\rho_\mathrm{k}} f_k\eta_k^2\overline{\mathrm{v}}_\mathrm{k} \end{aligned} . \tag{4.44}$$

The double summation in the second term of left hand side of eqn. (4.44) is limited to cells that share a common face $\Sigma_{k,j}$. Equation (4.44) is called the ultra-weak variational formulation of the Helmholtz problem.

4.3 Linear system for 2D problem

In this thesis, a local basis of plane waves is used for the expansion of the field within each triangular cell [51]

$$\varphi_{k,m} = \begin{cases} \exp\left(i\overline{\kappa}_k\, \vec{a}_{k,m} \cdot \overline{\vec{r}}'\right) & \text{in } \Omega_\mathrm{k}, \\ 0 & \text{elsewhere,} \end{cases} \tag{4.45}$$

where the index k refers to the k^{th} triangular cell, the index m counts the basis functions within the cell, κ_k is the complex wave number in the cell, $\vec{a}_{k,m}$ is the propagation direction of the m^{th} basis function, and $\vec{r}'$ is the spatial coordinate becoming complex within the PML, and the over bars stand for complex conjugate. The angularly equally distributed directions $\vec{a}_{k,m}$ in two-dimension problem are

$$\vec{a}_{k,m} = \left(\cos\left(2\pi\frac{m-1}{N_k}\right), \sin\left(2\pi\frac{m\text{-}1}{N_k}\right)\right), \tag{4.46}$$

where N_k denotes the number of distributed directions and m is chosen from 1 to N_k.

The function χ_k defined in eqn. (4.39) can be approximated as

$$\chi_k^a = \sum_{m=1}^{N_k} \left(\chi_{k,m} \left(-\frac{1}{\rho_k} \vec{n}_k \cdot (A_k \nabla) - i\varsigma \right) \varphi_{k,m} \right) \Bigg|_{\partial\Omega_k} , \tag{4.47}$$

where $\chi_{k,m}$ is the unknown to be determined. Following the Galerkin method used in Ref. [51, 52, 53, 141], $v_k = \varphi_{k,\ell}$ is chosen as the test function. Substituting eqn. (4.47) and the test function v_k into eqn. (4.44) gives the following discrete UWVF problem

$$\begin{aligned}
&\sum_{k=1}^{N} \int_{\partial\Omega_k} \frac{1}{\varsigma} \sum_{m=1}^{N_k} \left(\chi_{k,m} \left(-\frac{1}{\rho_k} \vec{n}_k \cdot (A_{d,k} \nabla) - i\varsigma \right) \varphi_{k,m} \right) \overline{\left(-\frac{1}{\rho_k} \vec{n}_k \cdot (\overline{A}_{d,k} \nabla) - i\varsigma \right) \varphi_{k,\ell}} \\
&- \sum_{k=1}^{N} \sum_{j=1}^{N} \int_{\Sigma_{k,j}} \frac{1}{\varsigma} \sum_{m=1}^{N_j} \left(\chi_{j,m} \left(-\frac{1}{\rho_j} \vec{n}_j \cdot (A_{d,j} \nabla) - i\varsigma \right) \varphi_{j,m} \right) \overline{\left(\frac{1}{\rho_k} \vec{n}_k \cdot (\overline{A}_{d,k} \nabla) - i\varsigma \right) \varphi_{k,\ell}} \\
&- \sum_{k=1}^{N} \int_{\Gamma_k} \frac{Q}{\varsigma} \sum_{m=1}^{N_k} \left(\chi_{k,m} \left(-\frac{1}{\rho_k} \vec{n}_k \cdot (A_{d,k} \nabla) - i\varsigma \right) \varphi_{k,m} \right) \overline{\left(\frac{1}{\rho_k} \vec{n}_k \cdot (\overline{A}_{d,k} \nabla) - i\varsigma \right) \varphi_{k,\ell}} \\
&= \sum_{k=1}^{N} \int_{\Gamma_k} \frac{g}{\varsigma} \overline{\left(\frac{1}{\rho_k} \vec{n}_k \cdot (\overline{A}_{d,k} \nabla) - i\varsigma \right) \varphi_{k,\ell}} + \sum_{k=1}^{N} \int_{\Omega_k} \frac{2i}{\rho_k} f_k \eta_k^2 \overline{\varphi_{k,\ell}} .
\end{aligned} \tag{4.48}$$

It must be stressed that the notation *j* in second term of the left hand side denotes the elements which have interfaces with element *k*. The matrix form of eqn. (4.48) can be given below

$$(B - C) X = b , \tag{4.49}$$

where $X = (\chi_{1,1}, \chi_{1,2}, \ldots, \chi_{1,N_1}, \ldots, \chi_{k,1}, \chi_{k,2}, \ldots, \chi_{k,m}, \ldots, \chi_{k,N_k}, \ldots, \chi_{N,1}, \chi_{N,2}, \ldots \chi_{N,N_N})^T$ contains the unknowns, and the number of unknowns is $\sum_{k=1}^{N} N_k$; *B* is a block diagonal matrix that comes from the first term of left hand side in eqn. (4.48) and contains blocks B_k related to the k^{th} cell, Ω_k; *C* comes from the other two terms of left hand side in eqn. (4.48) and is a sparse block matrix coupling the solution in a single cell to adjacent cells and boundary conditions; *b* is the vector that contains the information from the external boundary and sources; and it comes from the right hand side of eqn. (4.48).

The entries of matrices *B*, C and vector b for two-dimensional problem are given below. The matrix *B* is the positive definite Hermitian block diagonal matrix

$$B=\begin{pmatrix} B_1 & 0 & \cdots & \cdots & 0 \\ 0 & B_2 & \cdots & \cdots & 0 \\ 0 & & \ddots & & \\ \vdots & 0 & B_\mathrm{k} & 0 & 0 \\ \vdots & \vdots & 0 & \ddots & 0 \\ 0 & 0 & 0 & 0 & B_\mathrm{N} \end{pmatrix}. \tag{4.50}$$

The block B_k is created by choosing the test function $\varphi_{k,\ell}$. The entries in B_k are

$$B_k^{\ell,m}=\int_{\partial\Omega_k}\frac{1}{\varsigma}\left(-\frac{1}{\rho_k}\vec{n}_k\cdot\left(A_{d,k}\nabla\varphi_{k,m}\right)-i\varsigma\varphi_{k,m}\right)\overline{\left(-\frac{1}{\rho_k}\vec{n}_k\cdot\left(\overline{A}_{d,k}\nabla\right)-i\varsigma\right)\varphi_{k,\ell}}\,dl\,, \tag{4.51}$$

where ℓ in superscript indicates the row and m indicates the column. Substituting eqns. (4.24), (4.45) and (4.46) into eqn. (4.51) gives

$$B_k[\ell,m]=$$

$$\int_{\partial\Omega_k}\frac{1}{\varsigma}\left(-\frac{1}{\rho_k}\left[n_{kx},n_{ky}\right]\cdot\left(\begin{bmatrix}\dfrac{d_y}{d_x}, & 0\\ 0, & \dfrac{d_x}{d_y}\end{bmatrix}\begin{bmatrix}\cos\left(2\pi\dfrac{m-1}{N(k)}\right)\overline{d_x}\\ \sin\left(2\pi\dfrac{m-1}{N(k)}\right)\overline{d_y}\end{bmatrix}\right)i\overline{\kappa_k}-i\varsigma\right)\exp\left(i\overline{\kappa_k}\vec{a}_{k,m}\cdot\vec{\overline{r}}'\right)\cdot$$

$$\overline{\left(-\frac{1}{\rho_k}\left[n_{kx},n_{ky}\right]\cdot\left(\begin{bmatrix}\dfrac{\overline{d_y}}{\overline{\overline{d_x}}}, & 0\\ 0, & \dfrac{\overline{d_x}}{\overline{\overline{d_y}}}\end{bmatrix}\begin{bmatrix}\cos\left(2\pi\dfrac{\ell-1}{N(k)}\right)\overline{d_x}\\ \sin\left(2\pi\dfrac{\ell-1}{N(k)}\right)\overline{d_y}\end{bmatrix}\right)i\overline{\kappa_k}-i\varsigma\right)\exp\left(i\overline{\kappa_k}\vec{a}_{k,\ell}\cdot\vec{\overline{r}}'\right)}dl. \tag{4.52}$$

Based on the entries of B_k, the entries in matrix B can be written as

$$B[row+\ell,col+m]=B_k[\ell,m], \tag{4.53}$$

where *row* and *col* equal $N_1+N_2+\ldots+N_{k\text{-}1}$, while, if k equals 1, *row* and *col* equal 0.

The matrix C is sparse and also has a block structure. In the k^th block row of the matrix C, the number of blocks corresponds to how many interfaces the element k has with other adjoint elements. The entries in C are given by

$$\begin{aligned}C_{k,j}^{\ell,m}=&\int_{\Sigma_{k,j}}\frac{1}{\varsigma}\left(-\frac{1}{\rho_j}\vec{n}_j\cdot\left(A_{d,j}\nabla\varphi_{j,m}\right)-i\varsigma\varphi_{j,m}\right)\overline{\left(\frac{1}{\rho_k}\vec{n}_k\cdot\left(\overline{A}_{d,k}\nabla\varphi_{k,\ell}\right)-i\varsigma\varphi_{k,\ell}\right)}+\\ &\int_{\Gamma_k}\frac{Q}{\varsigma}\left(-\frac{1}{\rho_k}\vec{n}_k\cdot\left(A_{d,k}\nabla\varphi_{k,m}\right)-i\varsigma\varphi_{k,m}\right)\overline{\left(\frac{1}{\rho_k}\vec{n}_k\cdot\left(\overline{A}_{d,k}\nabla\varphi_{k,\ell}\right)-i\varsigma\varphi_{k,\ell}\right)}\,,\end{aligned} \tag{4.54}$$

where k in subscript indicates the k^{th} block row; j in subscript indicates the j^{th} block column; ℓ in superscript indicates the row in the k^{th} block row; and m in superscript indicates the column in the j^{th} block column. In eqn. (4.54), the first term derives from the interface between two adjacent elements Ω_k and Ω_j; and the second term derives from the external boundary. It is clear that when the element k is located on the exterior boundary, the k^{th} diagonal block have non-zero entries; or else, the entries for the k^{th} diagonal block are 0. The first term in eqn. (4.54) can be rewritten with eqns. (4.24), (4.45) and (4.46) as

$$C_1[\ell,m]=$$

$$\frac{\int_{\Sigma_{k,j}} \frac{1}{\varsigma}\left(-\frac{1}{\rho_j}\left[n_{jx},n_{jy}\right]\cdot\left(\begin{bmatrix}\frac{dy}{dx}, & 0\\ 0, & \frac{dx}{dy}\end{bmatrix}\begin{bmatrix}\cos\left(2\pi\frac{m-1}{N(j)}\right)\overline{d}_x\\ \sin\left(2\pi\frac{m-1}{N(j)}\right)\overline{d}_y\end{bmatrix}\right)\overline{i\kappa_j}-i\varsigma\right)\exp\left(i\overline{\kappa_j}\vec{a}_{j,m}\cdot\vec{\overline{r}}'\right)\cdot}{\left(\frac{1}{\rho_k}\left[n_{kx},n_{ky}\right]\cdot\left(\begin{bmatrix}\frac{\overline{d}_y}{\overline{d}_x}, & 0\\ 0, & \frac{\overline{d}_x}{\overline{d}_y}\end{bmatrix}\begin{bmatrix}\cos\left(2\pi\frac{\ell-1}{N(k)}\right)\overline{d}_x\\ \sin\left(2\pi\frac{\ell-1}{N(k)}\right)\overline{d}_y\end{bmatrix}\right)\overline{i\kappa_k}-i\varsigma\right)\exp\left(i\overline{\kappa_k}\vec{a}_{k,\ell}\cdot\vec{\overline{r}}'\right)}.$$

(4.55)

The row and column of matrix C_1 can be transferred to the row and column in matrix C by

$$C[row+\ell,col+m]=C_1[\ell,m], \tag{4.56}$$

where *row* equals $N_1+N_2+...+N_{k-1}$ and *col* equals $N_1+N_2+...+N_{j-1}$; if k or j equals 1, *row* or *col* equals 0. Similarly, the second term in eqn. (4.54) can be rewritten with eqns. (4.24), (4.45) and (4.46) as

$$C_2[\ell,m]=$$

$$\frac{\int_{\Gamma_k} \frac{Q}{\varsigma}\left(-\frac{1}{\rho_k}\left[n_{kx},n_{ky}\right]\cdot\left(\begin{bmatrix}\frac{dy}{dx}, & 0\\ 0, & \frac{dx}{dy}\end{bmatrix}\begin{bmatrix}\cos\left(2\pi\frac{m-1}{N(k)}\right)\overline{d}_x\\ \sin\left(2\pi\frac{m-1}{N(k)}\right)\overline{d}_y\end{bmatrix}\right)\overline{i\kappa_k}-i\varsigma\right)\exp\left(i\overline{\kappa_k}\vec{a}_{k,m}\cdot\vec{\overline{r}}'\right)\cdot}{\left(\frac{1}{\rho_k}\left[n_{kx},n_{ky}\right]\cdot\left(\begin{bmatrix}\frac{\overline{d}_y}{\overline{d}_x}, & 0\\ 0, & \frac{\overline{d}_x}{\overline{d}_y}\end{bmatrix}\begin{bmatrix}\cos\left(2\pi\frac{\ell-1}{N(k)}\right)\overline{d}_x\\ \sin\left(2\pi\frac{\ell-1}{N(k)}\right)\overline{d}_y\end{bmatrix}\right)\overline{i\kappa_k}-i\varsigma\right)\exp\left(i\overline{\kappa_k}\vec{a}_{k,\ell}\cdot\vec{\overline{r}}'\right)}.$$

(4.57)

The row and the column of matrix C_2 can be transferred to the row and column in C by

$$C[row+\ell,col+m]=C_2[\ell,m], \tag{4.58}$$

where *row* and *col* equal $N_1+N_2+...+N_{k-1}$; *row* and *col* equal 0 if k equals 1.

The entries for vector *b* can be obtained from the right hand side of eqn. (4.48):

$$b_k^{\ell} = \int_{\Gamma_k} \overline{\frac{g}{\varsigma}\left(\frac{1}{\rho_k}\vec{n}_k \cdot \left(\overline{A}_{d,k}\nabla\right) - i\varsigma\right)\varphi_{k,\ell}} + \int_{\Omega_k} \frac{2i}{\rho_k} f_k \eta_k^2 \overline{\varphi}_{k,\ell} \cdot \tag{4.59}$$

Similarly, it is found that the first term in eqn. (4.59) only exists when the element *k* is located on the exterior boundary. For the second term in eqn. (4.59), it need only be considered for the element Ω_k where the acoustic source exists. By using eqns. (4.24), (4.45) and (4.46), we can rewrite vector *b* as

$$b[row+\ell] =$$

$$\int_{\Gamma_k} \overline{\frac{g}{\varsigma}\left(\frac{1}{\rho_k}\left[n_{kx}, n_{ky}\right] \cdot \left(\begin{bmatrix} \frac{\overline{d_y}}{\overline{d_x}}, & 0 \\ 0, & \frac{\overline{d_x}}{\overline{d_y}} \end{bmatrix} \begin{bmatrix} \cos\left(2\pi \frac{\ell-1}{N(k)}\right)\overline{d_x} \\ \sin\left(2\pi \frac{\ell-1}{N(k)}\right)\overline{d_y} \end{bmatrix}\right) i\overline{\kappa_k} - i\varsigma\right) \exp\left(i\overline{\kappa_k}\vec{a}_{k,\ell} \cdot \vec{\overline{r}}'\right)}$$

$$-\int_{\Omega_k} \frac{2i}{\rho_k} f_k \eta_k^2 \overline{\varphi}_{k,\ell}, \tag{4.60}$$

where *row* equals $N_1+N_2+...+N_{k-1}$; and *row* equals 0 if *k* is 1.

During the process of constructing the matrices *B*, *C* and vector *b*, it is found that the integration on the boundary is necessary. In order to calculate the integration, the normal outgoing unit, and both the upper and lower limits of the integration must be specified. Therefore, a two-dimensional sub-domain (See Figure 4.2) will be taken as an example to introduce how to get the outgoing unit normal and the integration's upper and lower limits.

In Figure 4.2, a triangular element Ω_k is given and three vertices are given by $P_1(x_1, y_1)$, $P_2(x_2, y_2)$ and $P_3(x_3, y_3)$ in counter-clockwise order. The outgoing unit normal $\vec{n}_k$ on the three edges is

$$\vec{n}_k = \left\{\frac{y_2-y_1}{\sqrt{(y_2-y_1)^2+(x_2-x_1)^2}}, \frac{-(x_2-x_1)}{\sqrt{(y_2-y_1)^2+(x_2-x_1)^2}}\right\}, \text{ from } P_1 \text{ to } P_2, \tag{4.61}$$

$$\vec{n}_k = \left\{\frac{y_3-y_2}{\sqrt{(y_3-y_2)^2+(x_3-x_2)^2}}, \frac{-(x_3-x_2)}{\sqrt{(y_3-y_2)^2+(x_3-x_2)^2}}\right\}, \text{ from } P_2 \text{ to } P_3, \tag{4.62}$$

$$\vec{n}_k = \left\{\frac{y_1-y_3}{\sqrt{(y_1-y_3)^2+(x_1-x_3)^2}}, \frac{-(x_1-x_3)}{\sqrt{(y_1-y_3)^2+(x_1-x_3)^2}}\right\}, \text{ from } P_3 \text{ to } P_1. \tag{4.63}$$

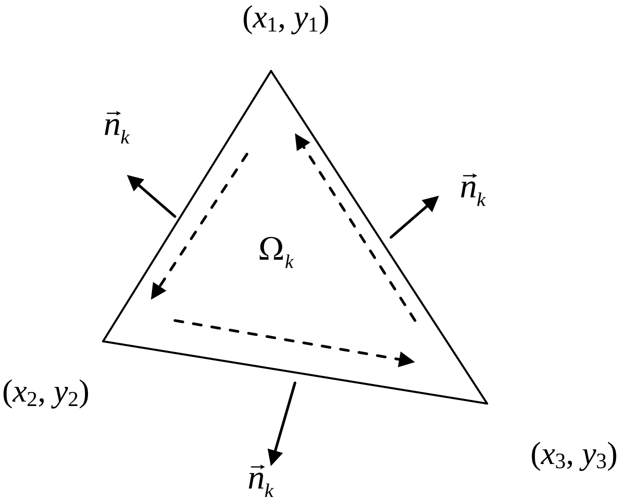

Figure 4.2 Configuration of one element Ω_k.

The three straight edges can be represented by the following equations:
Line 1:

$$y = y_1 + \frac{y_2 - y_1}{x_2 - x_1}(x - x_1), \text{ passing } P_1(x_1, y_1) \text{ and } P_2(x_2, y_2); \tag{4.64}$$

Line 2:

$$y = y_2 + \frac{y_3 - y_2}{x_3 - x_2}(x - x_2), \text{ passing } P_2(x_2, y_2) \text{ and } P_3(x_3, y_3); \tag{4.65}$$

Line 3:

$$y = y_3 + \frac{y_1 - y_3}{x_1 - x_3}(x - x_3), \text{ passing } P_3(x_3, y_3) \text{ and } P_1(x_1, y_1). \tag{4.66}$$

If the direction of integration is chosen as counter-clockwise, the integration is proceeded from (x_1, y_1) to (x_2, y_2) along 'line 1', from (x_2, y_2) to (x_3, y_3) along 'line 2', and from (x_3, y_3) to (x_1, y_1) along 'line 3'. If the direction of integration is chosen as clockwise, all the integration will give a contrary value compared to the integration in the counter-clockwise order. This can be considered as the fact that a '-1' is multiplied on both sides of the linear system. As a result, for the two-dimensional problem, the direction of integration, clockwise or counter-clockwise, has no influence on the solution. However, the Green's theorem prefers the counter-clockwise order and MATLAB provides the mesh information in counter-clockwise order, therefore, in this thesis, the integration is computed in counter-clockwise order.

4.4 Solution of the linear system

Now, how to get the linear system for 2D problem and how to assemble the matrices *B*, *C* and vector *b* have been described in the previous section. In this section, the way to solve the linear system and several advantages of UWVF will be discussed.

4.4.1 Ill conditioning problem

Wave based numerical methods are known to suffer from ill conditioning of the resulting matrix system. Ill conditioning system can lead to poor approximations [51, 52]. It is suggested that equation (4.49) can be solved in the form [52]

$$\left(I - B^{-1}C\right)X = B^{-1}b\,. \tag{4.67}$$

This preconditioned approach requires the inversion of matrix *B*. In order to guarantee the numerical accuracy of the solution, matrix *B* must be well-conditioned. With the fact that the inversion of matrix *B* can be obtained by finding the inversion of block matrix B_k, the well-conditioned matrix *B* can be obtained if the well-conditioned block matrix B_k can be found.

The conditioning of the block matrix B_k is dependent on many factors, such as the properties of the medium, the size of the finite element cell h_k, the number of the basis functions N_k, wave number κ_k and so on [52]. Because the properties of the medium are defined by the problem, the conditioning can only be improved by adjusting the other factors properly. In general, varying the wave number within the computational domain, an uneven element size of the cell or a homogeneous collection of plane wave basis functions in all elements can lead to ill conditioning problems and severe instability. Huttunen et al. [53] have solved this problem by streamlining the condition number of each of the sub matrices B_k by changing the number of basis functions in each cell and this method is adopted in this thesis.

The general procedure to obtain a well-conditioned matrix *B* is summarised here. Firstly, according to the wave frequency, the element is initialised through mesh generation; and in the mesh generation the maximum element size is specified. In the UWVF method, this size can be two times the wavelength without losing accuracy [52]. Secondly, the initial guesses of the number of basis functions in each element are given. Based on these initial guesses, the corresponding block matrices B_k can be assembled and the condition number for each block matrix can be calculated by

$$Cond(B_k) = \left\|B_k\right\| \cdot \left\|B_k^{-1}\right\|, \tag{4.68}$$

where $Cond(\cdot)$ denotes the condition number, and $\|\cdot\|$ denotes the norm of the matrix. If this condition number is greater than the tolerance condition number (10^6 in this thesis according to the value in the Ref. [52]), the number of basis functions for this block matrix must be decreased; or else, the number of basis functions should be increased. For the new basis functions, the block matrix B_k is re-assembled and the condition number is re-calculated. This process will be stopped when the number of basis functions has made the corresponding condition number smaller than the tolerance value and the number of basis function cannot be increased any more. Finally, all the elements have the corresponding block matrices, which are well-conditioned. Then, these block matrices compose the Cholesky factorized matrix *B*.

After the well-conditioned matrix *B* is obtained, the matrix *C* and vector *b* are assembled according to the determined basis functions. Then, equation (4.67) can be solved numerically by iterative method. In this thesis, the bi-conjugate gradient method is used to solve equation (4.67).

4.4.2 Octave band problem

In road traffic noise applications, a wide range of frequencies has to be considered. The optimal number of basis functions for conditioning the matrices depends on the wavelength-to-cell-size ratio and thus the computationally expensive iterative pre-conditioning operation needs to be repeated for every frequency of interest.

For the purpose of reducing the calculation time, a linear interpolation is used to determine the number of basis functions for different frequencies. Firstly, the optimal number of basis functions for the upper, central and lower frequencies in an octave band is calculated. With the determined number of basis function, the condition number of each block matrix B_k is below the tolerance condition number. In this thesis, the condition number is calculated based on the 2-norm of the block matrix. Secondly, a linear function is fitted to the relationship between the average number of basis functions per cell and the frequency. Finally, the required number of basis functions for the other frequencies constituting that octave band can be approximated by this linear function. An example is given in Figure 4.3. The comparison of the average number of basis functions in one grid calculated by iteration procedure and linear interpolation shows good compliance.

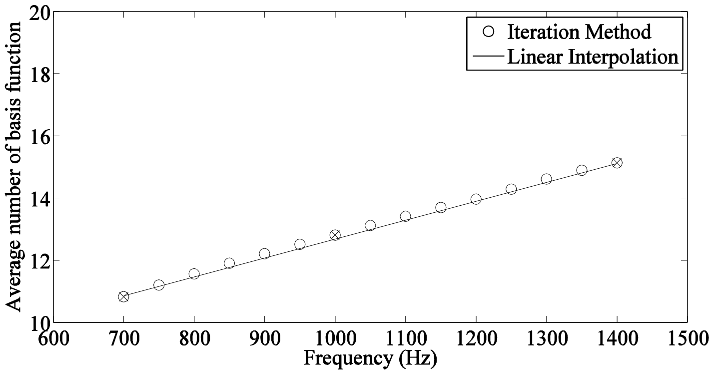

Figure 4.3 Average number of basis function in one grid calculated by an iteration procedure (open circles) and linear interpolation (solid line). The x-signs indicate the three frequencies on which the linear interpolation is based.

The matrices *B*, *C* and vector *b* can now be constructed avoiding the iterative procedure. By the linear interpolation, the computational time can be shortened by 40% to 70%, depending on the frequency. For high frequencies, assembling matrices *B* and *C* occupies an equal amount of CPU time. The interpolation process can only limit the time used to assemble *B*. As a result, only 40% of the CPU time can be saved. For low frequencies, more time is used to assemble *B* when compared to *C*. Therefore, 70% of CPU time can be gained by applying this interpolation. When different octave bands are considered, it is more advantageous to adapt the grid cell size to the wavelength instead of further interpolation. In this thesis, the ratio between grid cell and the minimum wavelength in the octave band is chosen as 2.

4.4.3 Multiple sources problem

The numerical method can be further optimised in typical traffic noise situations with several source positions. Note that the matrices *B* and *C* are only related to the geometrical properties of the triangular meshes, the medium density, and the frequency of the sound wave; the source position has no influence on the entries in *B* and *C*. On the other hand, vector b is derived from the source term and the boundary term, which are closely related to the source position. Therefore, if no parameters are changed except for the source position, the process to assemble matrices *B* and *C* does not have to be repeated, which can reduce the computational cost by 90% for the cases studied in this thesis.

4.5 Numerical validation

In this section, the UWVF method is verified to guarantee that it can provide reliable results. Two examples are considered. The first one deals with sound propagation over porous ground in a refracting atmosphere; and the second case is sound propagation near a porous noise barrier.

4.5.1 Sound propagation over porous ground in a refracting atmosphere

Since UWVF is a volume-discretisation technique, the speed of sound can be location-dependent. Therefore, refraction of sound due to the presence of gradients in air temperature and wind speed can be modelled by the effective sound speed approach. Gradients in air temperature lead to gradients in the sound speed. Furthermore, the effect of wind on sound propagation can be approached by considering the horizontal component of the wind speed, leading to a virtual increase or decrease in the sound speed. In many applications, including sound propagation over noise barriers in wind [142], this is a good approach.

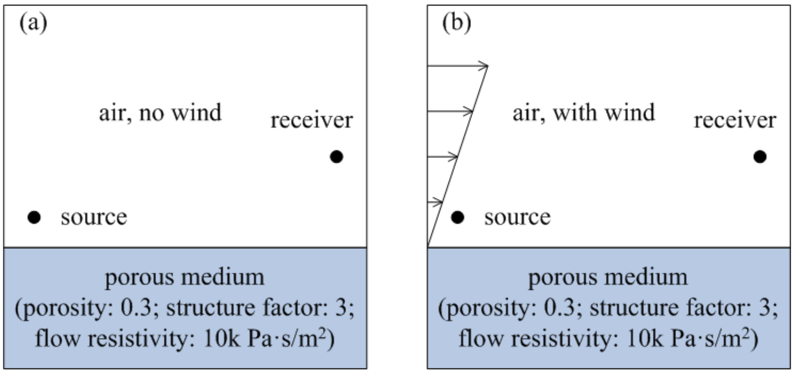

Figure 4.4 Geometry with a point source and a receiver above a porous ground medium: (a) no wind; (b) with wind.

In the first validation test, sound propagation over porous ground in a refracting atmosphere is studied and the results by UWVF are compared to the results by FDTD, which have been published [69, 72]. The two dimensional example chosen here is similar to the one presented in [69, 72]. A source is located at a height of 0.5 m above the ground; the receiver is at a height of 1.5 m (see Figure 4.4). The distance between the source and receiver is 5 m. Sound frequencies between 100 Hz and 1000 Hz are considered. Results are expressed relative to free field sound propagation. In Figure 4.5 and Figure 4.6, a homogeneous and downwardly refracting atmosphere is considered, respectively. In case of the non-homogeneous atmosphere, a linear increase in the speed of sound, with a gradient of 3 /s, is used. The numerical results show that in case of downward refraction, the ground dip is somewhat more pronounced, and a shift towards lower frequencies is observed. At 100 Hz, the difference between both models amounts up to 0.5 dB. The UWVF method is in good agreement with FDTD calculations in both situations, showing its validity in a non-homogeneous sound propagation medium as well.

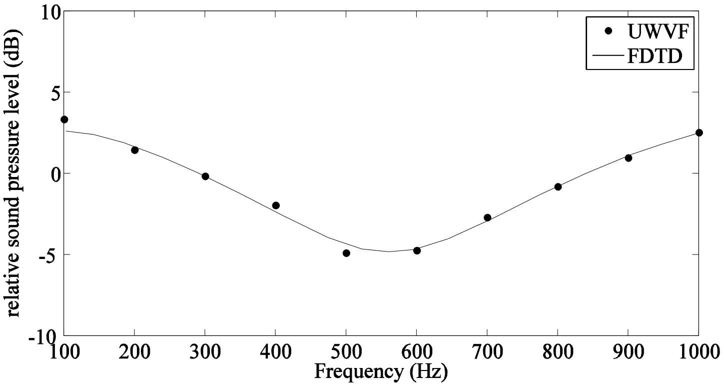

Figure 4.5 Spectra of the relative sound pressure levels in a non-refracting atmosphere. The porosity of the ground equals 0.3, the structure factor equals 3.0 and flow resistivity equals 10k *Pa·s/m*^{2}.

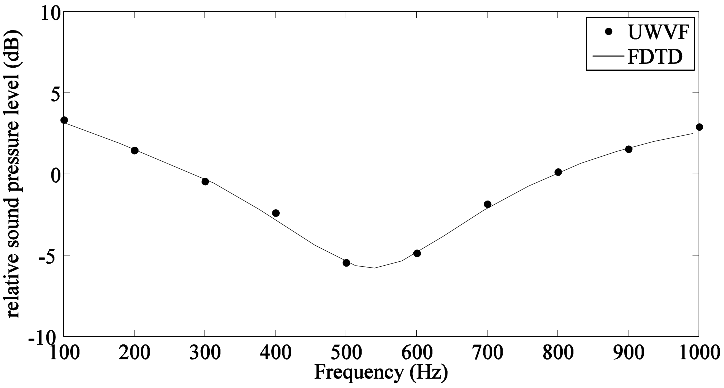

Figure 4.6 Spectra of the relative sound pressure levels in a downwardly refracting atmosphere. A linearly increasing sound speed profile is modelled, with a gradient of 3 /s. The porosity of the ground equals 0.3, the structure factor equals 3.0 and flow resistivity equals 10k *Pa·s/m*^{2}.

4.5.2 Sound propagation near a porous barrier

In the second validation test, the UWVF method is compared to FDTD calculations for the case of sound propagation near a complex-shaped, low-height and porous noise barrier in a still and homogeneous atmosphere. An inverse Γ-shaped porous barrier of 1m high and 1m wide is considered, as shown in Figure 4.7. Two dimensional calculations are performed.

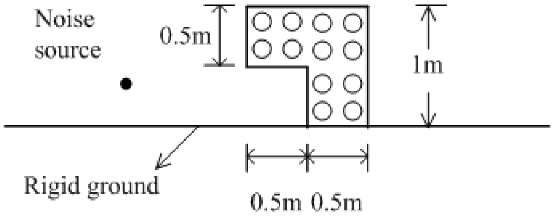

Figure 4.7 Geometry of the porous noise barrier for the validation example.

The computational domain is 4 m wide and 3 m high. Perfectly matched layers are used to border the simulation domain. The frequency of the sound wave under study is 1000 Hz. The noise source is present at 1m in front of the noise barrier and at 0.3 m above the rigid ground. The porosity, structure factor and flow resistivity of the barrier are chosen as 0.4, 1.35 and 50k $Pa\cdot s/m^2$, respectively. Although no particular material is aimed at, such a set of parameters could be representative for uncompacted earth [140, 143]. In the UWVF method, the largest allowed mesh size of 0.68 m is used, which is twice the wavelength which equals 0.34 m when using a speed of sound of 340 m/s. In total, 8666 unknowns are considered in the UWVF computation. For the FDTD calculation, a much larger number of unknowns are used. Since the FDTD method serves as a reference calculation here, a very fine spatial discretisation step of 0.01 m is used. This means that for the sound frequency under study, more than 30 computational cells per wavelength are present. This is far beyond the common practice of 10 computational cells per wavelength, and will lead to a strong reduction of possible phase errors. The Courant number is set to 1. For the porous barrier, an implementation of the Zwikker and Kosten’s model [91] is used as well in FDTD. As in the UWVF method, perfectly matched layers are used to model an unbounded propagation domain. A detailed description of the FDTD implementation can be found in [43].

In Figure 4.8, the insertion loss fields are shown as calculated with UWVF and FDTD. All complex aspects of the sound field near this barrier are very well predicted by the UWVF method, showing its validity in this non-trivial sound propagation problem. The difference between the insertion loss fields calculated with UWVF and FDTD is depicted in Figure 4.9. At most locations, the differences range from -2 dB to +2 dB. The largest differences are found in zones where pronounced interference of sound waves occurs.

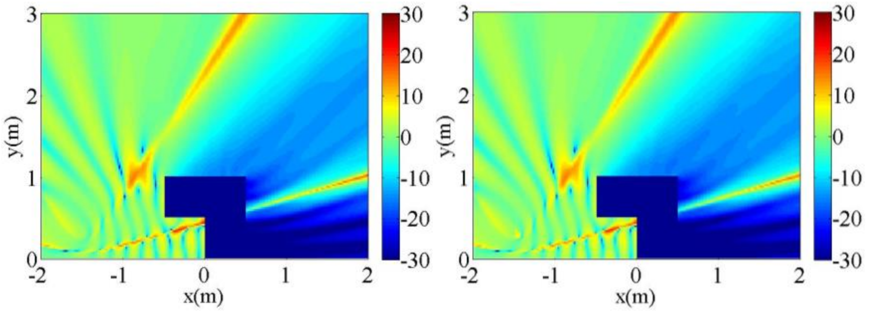

Figure 4.8 Comparison of the noise barrier insertion loss (dB) at a single sound frequency of 1000 Hz. On the left, calculations with FDTD are depicted, on the right UWVF is used.

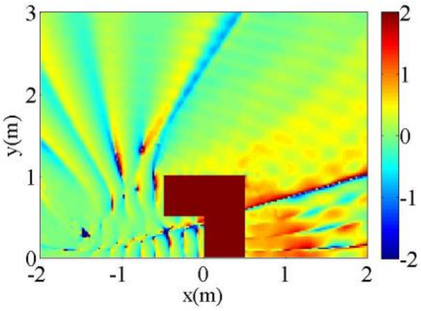

Figure 4.9 Difference between insertion loss (dB) fields of FDTD and UWVF as shown in Figure 4.8.

4.6 Conclusion

In this chapter, the 2D ultra weak variational formulation (UWVF) approach is introduced. This numerical method is extended to simulate sound propagation through a porous medium, based on the Zwikker and Kosten's porous rigid-frame model. Since the UWVF method is a volume-discretisation technique, the effective sound speed approach could be used to model sound propagation in a refracting atmosphere.

Finding the number of basis functions for each frequency is a time-consuming task. It is approached by three initial evaluations per octave band. For the other frequencies constituting that band, the number of basis functions could be linearly interpolated without loss of accuracy. Furthermore, it was shown that the exact source location only influences some of the matrices forming the system to be solved. The presence of different source locations which is typical in many problems, such as mixed multi-lane road traffic, can therefore be solved in an efficient way.

The UWVF method was validated successfully by comparison with 2D finite-difference time-domain (FDTD) calculations. Two important outdoor sound propagation cases were considered, namely sound propagation near a (porous) noise barrier, and sound propagation above porous ground in a refracting atmosphere.

CHAPTER 5
Sound interaction with vegetation

In this chapter, the finite-difference time-domain method is used to simulate sound wave propagation over leaves. In section 5.1, the case of a single leaf is studied. Measurements were conducted in an anechoic room and an impedance tube, and FDTD simulations have been performed. In section 5.2, the FDTD method is used to study sound wave propagation through a group of leaves by considering cyclic boundary conditions.

5.1 Interaction of sound with leaves

5.1.1 Leaf vibration

I. Introduction

Although the acoustics of the leaves of trees and bushes has been studied for several decades [18, 57, 59], an approach to incorporate leaves in detail in propagation models is lacking. In this section, an approach to do so is introduced. It is expected that such a propagation model might help to choose the type of vegetation to enhance noise reduction and combine the influences of vegetation with other propagation-related effects. In order to achieve this goal, a measurement campaign was set up. The easiest way to include the presence of a leaf in FDTD is to assume that the leaf is infinitely thin, and to replace the density of air in the governing equations by an equivalent density. Hence, the measurement campaign aimed at determining this equivalent density.

The work in this section will also be thought of as preparation for that presented in the next section. This section opens with a description of the measurements of leaf vibration. Then, the measurement results are compared with the simulation results in order to find a suitable model.

II. Measurement setup

The measurement was carried out in the anechoic room and its setup is shown schematically in Figure 5.1. A photograph of the setup is given in Figure 5.2. A single loudspeaker with a broad frequency response was used in this experiment to generate quasi-plane incident waves. Two microphones were placed in front of the loudspeaker at a distance of 0.01 m apart. The distance L1 between the loudspeaker and the centre of the two microphones was around 0.8 m. A laser Doppler Vibrometer (LDV) was used to measure the vibrations of a leaf that was placed between the two microphones. A Bruel & Kjaer pulse system 3560C was used to control the measurement. It is connected to the loudspeaker through a Pioneer STEREO AMPLIFIER A-607R. The LDV system is composed of a fiber-coupled vibrometer sensor head OFV-534 and a vibrometer controller OFV-5000 from Polytec. The measurements at the two microphones and the LDV can be done simultaneously by the pulse system.

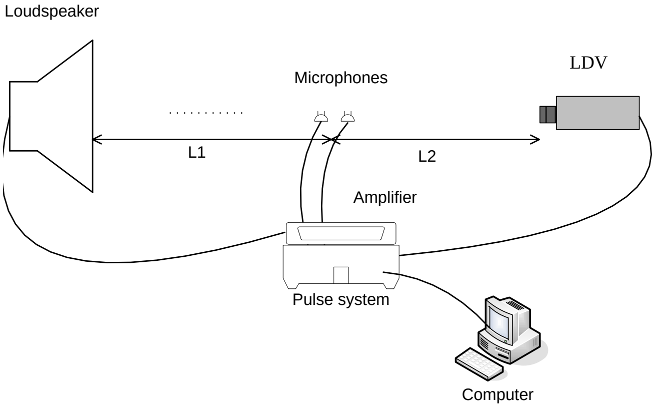

Figure 5.1 Configuration of the measurement setup

Figure 5.2 Picture of the measurement setup in the anechoic chamber. Loudspeaker: left; two microphones and leaf: middle; vibrometer: right.

The measurement procedure consists of several steps:

Step 1: In the first step, the sound intensity calibrator 3541 (Bruel & Kjaer) is used to calibrate the two microphones.
Step 2: The calibrator SV30A (1000Hz 94dB/114dB) is used as a reference in the recorded pressure signals.
Step 3: A measurement without leaf is performed to identify the frequency range where the measurement is valid and not disturbed by the spatial separation between the two microphones or by microphone phase mismatch. This step is comparable to the error checking in vector sound intensity measurements using a two microphone system. The excitation is a logarithmic frequency sweep.
Step 4: The leaf with branch is introduced in the measurement setup and the branch is fixed on a support. This support can be adjusted in order to guarantee the presence of the leaf between the two microphones when the measurement is

ongoing. The measurement points can be chosen at the centre or at the boundary of the leaf. However, the measurement points for LDV are not exactly the same as those for the microphones since the laser beam reflection would otherwise be disturbed by the presence of the microphones. As a result, the measurement points for LDV are usually around 0.01m away from the centres of the microphones. The excitation is also a logarithmic frequency sweep. (Note: the leaves with their branches were taken from a tree about half an hour before the actual measurement. During this time, their branches were put in water to prevent withering.)

Several tests were performed with this measurement setup; the microphones were interchanged each time to reduce the effect of phase error at low frequencies. The following leaf species have been considered: lime tree (*Tilia*), holly (*Ilex*), cherry laurel (*Prunus laurocerasus*), beech (*Fagus*), Japanese cherry (*Prunus serrulata*), elm (*Ulmus*), and butternut (*Juglans cinerea*). Some physical parameters of these leaves are given in Table 5.1 and pictures for each leaf are shown in Figure 5.3.

Table 5.1 Parameters for the leaves used in the measurements.

Name of the Leaf	Weight (g)	Area ($10^{-3}m^2$)	Mass per unit area (g/m^2)	Measurement date
Lime tree (*Tilia*)	1.247	14.3	87.2	Aug. 27, 2010
Holly (*Ilex*)	1.614	5.4	298	Aug. 30, 2010
Cherry laurel (*Prunus laurocerasus*)	2.743	9.6	286	Aug. 30, 2010
Beech (*Fagus*)	0.745	8.4	88	Aug. 31, 2010
Japanese cherry (*Prumus serrulata*)	1.131	6.8	166	Sep. 2, 2010
Elm (*Ulmus*)	1.375	7.2	192	Sep. 2, 2010
Butternut (*Jaglans cinerea*)	0.748	8.1	92	Sep. 2, 2010

The complex equivalent density is calculated from the measured velocity v and the two measured pressures p_1 and p_2 as

$$\rho = \frac{1}{i\omega\Delta r}\frac{p_1 - p_2}{v}, \qquad (5.1)$$

where ω is the angular frequency and Δr is the distance between the two microphones. In order to reduce background noise, especially from the LDV equipment, both nominator and denominator are multiplied by p_1 (or convolved in time domain) and the resulting transfer functions are truncated in the time domain.

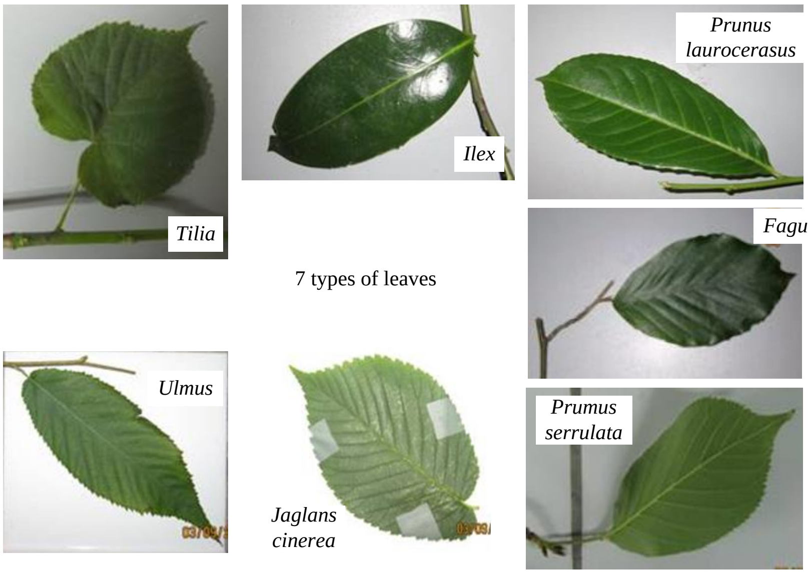

Figure 5.3 Pictures of the seven leaves used in the measurements.

III. Measurement results for different leaves

The measurements for each leaf were repeated at least five times and an average was made for the experimentally defined density. The measurement point was located close to the centre of the leaf.

The velocity spectrum of the lime tree is given in Figure 5.4; and the corresponding pressure spectrum at microphones 1 and 2 is given in Figure 5.5. The measurements at the same point were shown to be repeatable. According to the velocity spectrum of all the seven leaves (see Figure 5.4 and figures in Appendix A), the leaves appear to behave like plates with many different modes of vibration within the frequency range studied, which shows agreement with the findings by Martens and Michelsen [18]. It is noticed in Figure 5.5 that the pressure difference increases with the increase in frequency. At low frequency, the wavelength is much greater than the dimension of the leaf and as a result, the influence of the leaf is negligible. With the increase in frequency, the dimension of the leaf becomes comparable to and then larger than the wavelength, so the leaf has a significant influence on the sound wave and a different pressure spectrum between microphones 1 and 2 is observed.

Figure 5.6 shows the real and imaginary part of the leaf density for the lime tree. For the other six leaves, the results of their density can be found in Appendix A. In this approach, density is frequency dependent. The frequency range where the equivalent density somewhat resembles a real density is extremely narrow to non-existing. It is noticed that below 200 Hz, all the results show an unexpected upward trend. This trend is caused by the integrated high-pass filter in the LDV equipment, resulting in changes in phase and amplitude. These changes can be compensated for according to the characteristic curves of the filter during post-processing. Since the influences of the high-pass filter cannot be fully removed, this trend is still present. Near 500 Hz all density spectra show a little wiggle which originates in the pressure and velocity measurements. This is probably due to a standing wave between loudspeaker and leaf in this particular setup – heavier leaves indeed show a stronger peak near 500 Hz. Between 500 Hz and 8000 Hz, the expected fluctuations can be found; they can be attributed to the different modes of vibration and the fluctuations in pressure spectrum, which are visible in Figure 5.4 and Figure 5.5. At about 8000 Hz, the measured value drops to zero which is due to limitations in the measurement procedure.

Due to the complexity of the structure of the leaves, no trend in the oscillating behaviour seems obvious by comparing the measurements of density. However, it can be found that with the increase of frequency, from 100Hz to 4000Hz, there are more peaks. This is caused by the fact that the wavelength becomes smaller and its value becomes closer to the leaf size. As a result, resonances appear.

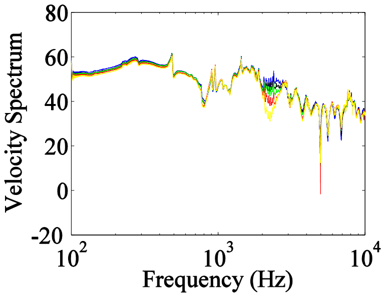

Figure 5.4 Frequency spectrum (dB) of the measured velocity for the leaf of a lime tree. The curves with different colour indicate different repetitions of the measurement. The reference velocity is 10^{-9} m/s, which was used in Ref. [18].

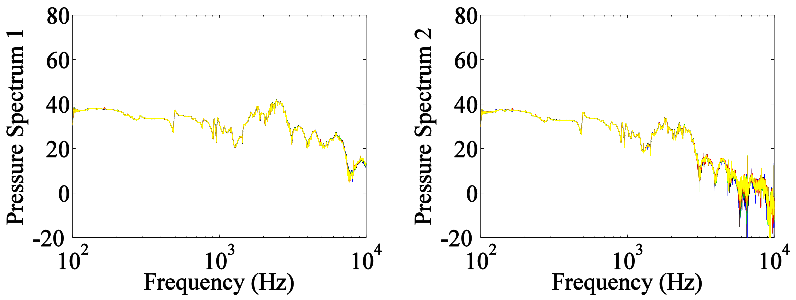

Figure 5.5 Pressure spectrum (dB) for the leaf of a lime tree at 2 microphones. The curves with different colour indicate different repetitions of the measurement. The labels of 'Pressure Spectrum 1' and 'Pressure Spectrum 2' indicate the results for microphones 1 and 2, respectively. The reference pressure is 2×10^{-5} Pa.

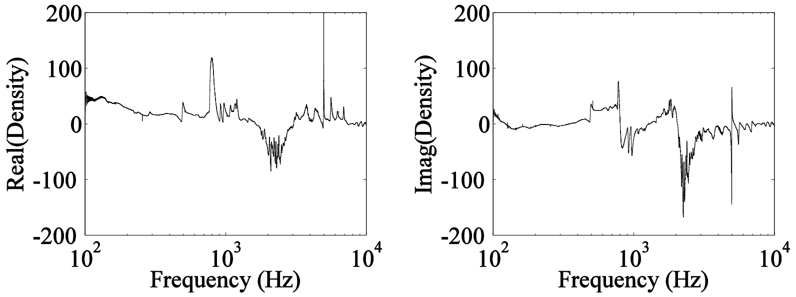

Figure 5.6 Average real part (left) and imaginary part (right) of the density spectrum for the leaf of a lime tree.

IV Comparison between the measurement and FDTD simulation

Representing the complex equivalent density as a simple function of frequency, which could be transformed to a time-domain model, appears almost impossible. Therefore, Chapter 3 presents another approach. In this approach, the bending of the leaf and the damping of the vibration are included (see eqn. (3.9)). This approach couples the leaf vibration to the air-acoustic part by assuming that the air moves at the same velocity as the leaf on its surface. The boundary conditions for the leaf vibration are not easily determined. For simplicity, it is assumed that the leaf is fixed (v_x=0, the leaf is assumed to be on the y-z plane) at one point, thus ignoring the dynamics of the stem. Also, free vibration on all other edges is assumed.

The leaf vibration also requires a stability criterion to be fulfilled. In general, the restrictions imposed by this criterion on *dt* are less stringent than the conditions imposed by the propagation in air, especially for the low bending stiffness encountered in leaves.

The mass per unit area of a leaf is easily determined and the values for the leaves used in the current studies are given in Table 5.1. The way to estimate the bending stiffness and the damping terms for each leaf is presented in section 3.4 and it is assumed that the leaf is isotropic. As there is no accurate method to measure values like Poison's ratio and Young's modulus of a leaf, values appearing in literature will be used.

As an example of this procedure, the leaf of cherry laurel is considered. The spatial discretisation step in the direction normal to the leaf was 0.01m corresponding exactly to the distance between the microphones, which leads to the same error due to approximating spatial derivatives by a finite difference. The spatial discretisation step in the direction parallel to the leaf plane is chosen to be 0.0005m according the discussion in section 3.4. Figure 5.7 shows the results of equivalent density for a cherry laurel leaf with different bending stiffness (between 0.00021N·m and 0.00518N·m). It is worth noting that to some extent, the inclusion of the bending stiffness for the cherry laurel leaf induces fluctuations in the density spectrum. However, the simulated fluctuations cannot match the measured ones. The reason can be attributed to the complex structure of the leaf, such as the uneven density distribution and the irregular surface profile, which is not considered in the required detail in the FDTD model. The pressure difference is plotted in Figure 5.8; and the comparison shows that FDTD can provide reliable simulation results for the pressure field. In this figure, the pressure difference below 1000Hz is very small. This can be attributed to the fact that in this frequency range the wavelength is much larger than the size of leaf. As a result, the influence of the leaf is negligible. From 1000Hz to about 5000Hz, the pressure difference increases with the increase of frequency as the wavelength becomes comparable to the size of leaf and some energy is blocked by the leaf. Above 5000Hz, this difference becomes small perhaps because the leaf vibrates with the incident waves and as a result the energy can propagate through it. In addition, the pressure difference by numerical simulation is always greater than that by measurements. This can be attributed to the fact that in the measurements the leaf was connected with its twig which could vibrate with sound; while in the simulation the leaf was fixed at one point which had no velocity.

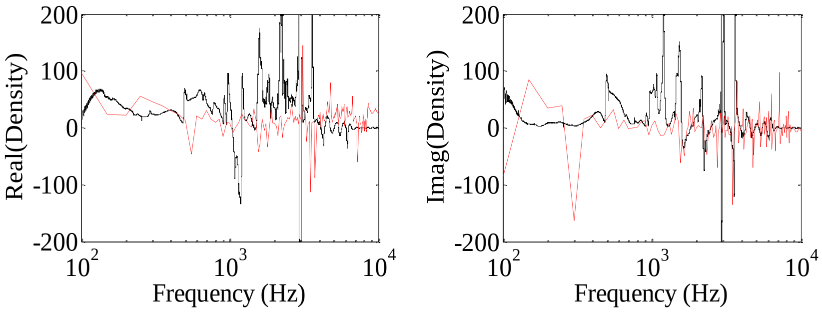

(a) D=0.00021

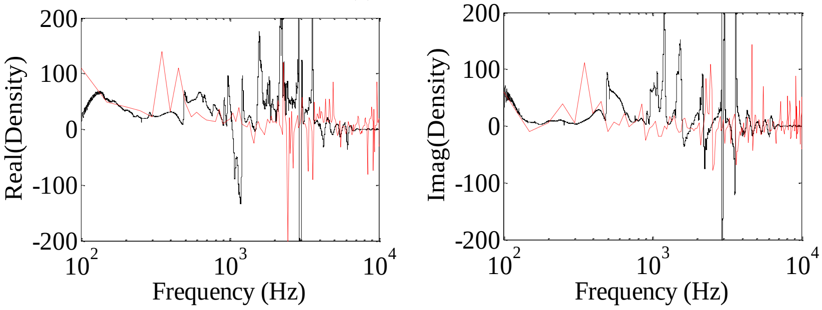

(b) D=0.00052

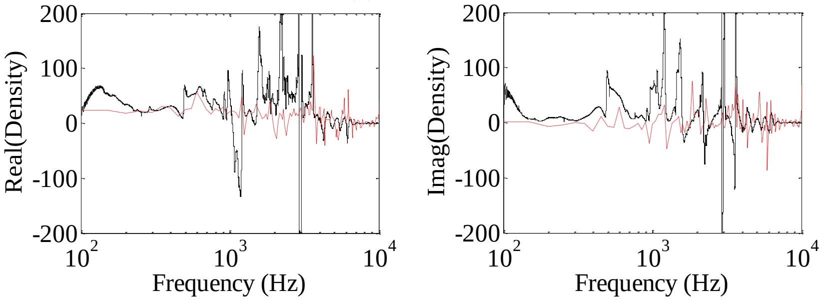

(c) D=0.00104

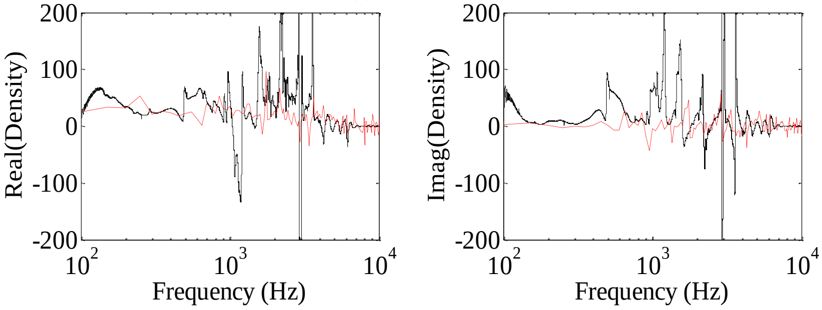

(d) D=0.00207

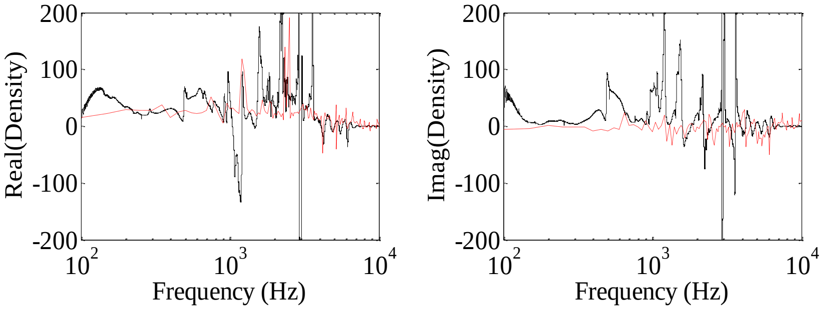

(e) D=0.00415

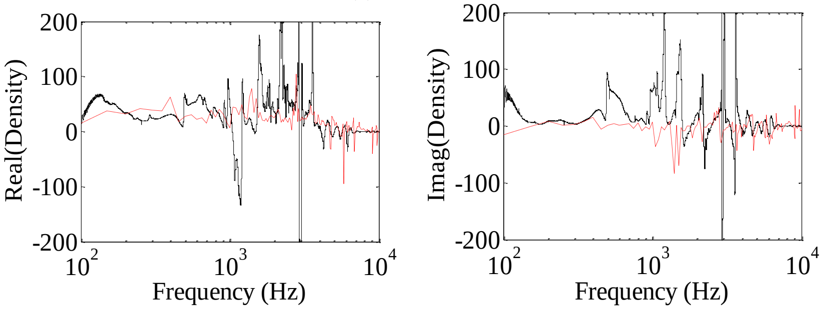

(f) D=0.00518

Figure 5.7 Comparison of equivalent density from the measurement results and the numerical results by FDTD for cherry laurel. The bending coefficient *D* is from 0.00021N·m to 0.00518 N·m. The damping terms R_1=0.013, R_2=0.038 and R_L=2.4 $s^{-1}$with reference to the values used by Chaigne and Lambourg [103].

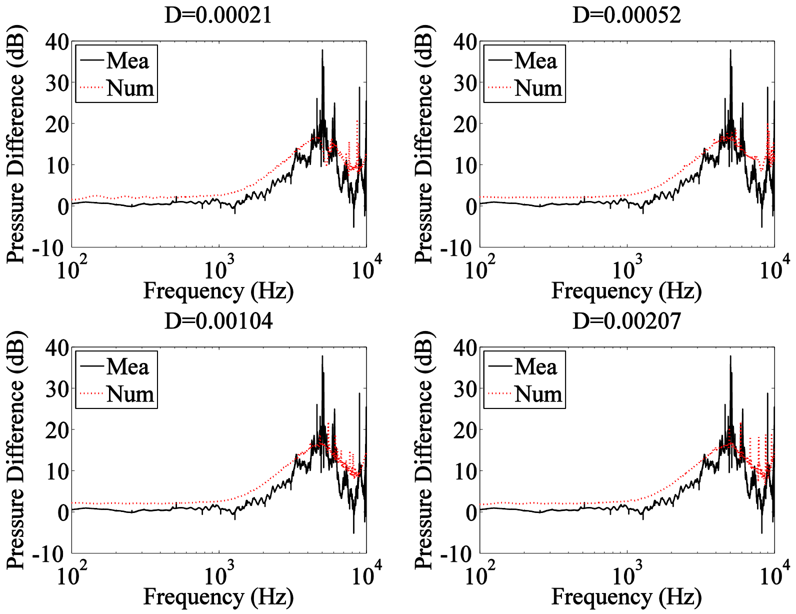

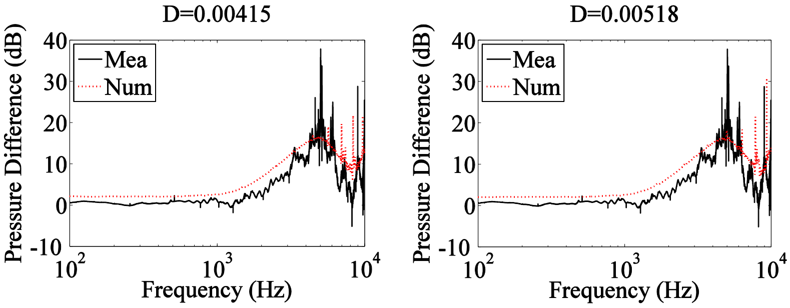

Figure 5.8 Comparison of the pressure difference (dB) from the measurement results and the numerical results by FDTD for cherry laurel. The bending coefficient D is from 0.00021N·m to 0.00518 N·m. The damping terms R_{11}=0.013, R_{12}=0.038 and R_L=2.4 s^{-1} with reference to the values used by Chaigne and Lambourg [103].

Although one cannot expect the FDTD model to predict the oscillation frequencies precisely, there are still possibilities for improvement: (1) vibration damping could be studied further, and the best fitted damping terms can be determined according to the comparison of measured and simulated reverberation time; (2) the bending stiffness could be made location-dependent with a higher stiffness towards the middle of the leaf; (3) the stem of the leaf could be included explicitly; (4) boundary conditions could be improved. The correspondence between measurement and simulation could also be improved further by accounting for the fact that the vibration and pressure measurements are not performed at the exact same location.

5.1.2 Leaf above porous substrate[3]

I. Introduction

This section considers a specific case of a porous medium covered by a plant leaf. This situation is of interest to outdoors sound propagation studies whereby the presence of plant leaves can have an influence on the ground effect, green roof absorption, and the absorption coefficient of green walls.

An important question is whether the presence of plant leaves can result in a noticeable change in the absorption coefficient of a porous material, such as the soil substrate in a green wall or a porous forest floor.

---

[3] The content in section 5.1.2 has been published in JASA:
Lei Ding, Timothy Van Renterghem, Dick Botteldooren, Kirill Horoshenkov and Amir Khan: Sound absorption of porous substrates covered by foliage: experimental results and numerical predictions. J. Acoust. Soc. Am. 134 (6), 4599-4609 (2013).

A porous substrate can often be simulated by a rigid frame model [91], which assumes that only the air inside the porous medium vibrates. Some examples of the application in the time-domain can be found in the work by Van Renterghem and Botteldooren [29, 30, 43], and Salomons et al. [72]. It has been shown that the rigid frame model can provide a reasonable parameter fit to model the reflection from typical outdoor soils [106]. However, there are situations where the frame density is relatively small so that the frame vibration cannot be neglected. In these situations, the acoustic characteristics of the material frame must be taken into account as well. This is the case for one of the low-density porous substrate used in the experiments by Horoshenkov that have been used for validation purposes here. Since the current study looks at much higher frequencies than in typical (outdoor) noise control applications, the use of more advanced models might be needed [140]. Accurately modelling the substrate behaviour is of importance in this study, since the interaction between leaves and substrate is expected to be a secondary effect. Also for consistency, the same model has been applied to both types of substrates considered in this section.

For the case study in this section, the model, which has been derived from Biot's model [88, 89] and introduced in section 3.1, is used to predict the coupled movement of the elastic frame and fluid inside the porous medium. The model is implemented as an extension of the finite-difference time-domain approach.

The bending wave equation for a thin uniform and homogeneous plate [60] is used to model the vibration of a loose leaf rested just above the porous substrate. Plate vibration damping and viscous and thermal conductivity boundary layer absorption on the leaf surface are the main mechanisms for acoustic energy loss.

II. Numerical setup

Figure 5.9 shows the cross-section of the impedance tube used. The diameter of the impedance tube is 0.029 m. The porous substrate is placed at the right end of the impedance tube. The distance between the plane wave sound source and the porous substrate is 0.07 m. The pressure is recorded at two points, M_1 and M_2, representing the positions of the two microphones in the experimental setup. The first microphone (at point M_1) and the second microphone (at point M_2) are at a distance of 0.03 m and 0.035 m from the source, respectively. In the simulations, a perfectly matched layer (PML) [90] is used at the left end of the impedance tube as a non-reflection boundary condition.

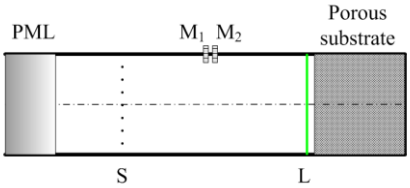

Figure 5.9 Cross-section of the impedance tube used in the numerical simulation. A plane wave sound source is located at S. Points M_1 and M_2 indicate the locations of two microphones. The leaf is placed at L, and the gap between leaf and porous substrate is 0.001 m.

For all the simulations in this section, the spatial discretisation step is 0.001 m in all three directions, and the time step *dt* equals 1.6981×10^{-6} s, yielding a Courant number of 1. To generate the normal incidence plane wave, a Gaussian modulated pulse is added to all grid points lying in the source plane:

$$S_{pulse} = A_S \sin(2\pi f_c t)\exp\left[-a_s(t-t_c)^2\right], \tag{5.2}$$

where A_S is amplitude of the source; f_c is central frequency; t_c is central time; and a_s is the parameter determining the signal bandwidth. The following values are chosen: f_c=3000Hz, $t_c=5dt$, and $a=1.6\times10^7$. The value of A_S has no meaning, since spectral division has been applied during post-processing of the time-domain responses. By these choices, it is guaranteed that all sound frequencies of interest are sufficiently excited, and that a smooth course of the pulse over time is obtained.

For the numerical simulation in the poro-elastic substrate, it is assumed that the adiabatic index equals 1.4 and the ambient pressure (P_0) is 0.1 MPa. The mass of air per unit volume (ρ_0) is 1.2 kg/m^3. Other material parameters are slightly tuned as explained later.

After performing the time-domain simulation, the absorption coefficient can be calculated according to the ISO10534-2 standard [144]. Firstly, the fast Fourier transform is used to get the frequency spectra of the two pressure signals at points M_1 and M_2 (Figure 5.9). Then, these two pressure spectra and the distance between two microphones are used to calculate three parameters: H_I, H_R and H_{12}, which are transfer functions for the incident wave, reflected wave and total sound field, respectively. After that, the reflection coefficient can be calculated by

$$r_c = \frac{H_{12}-H_I}{H_R-H_{12}} e^{2j\kappa x_1}, \tag{5.3}$$

where κ is wave number and x_1 is the coordinate of the first microphone with reference to the origin, the right-end of the impedance tube. Finally, the absorption coefficient can be obtained from

$$\alpha_{pm} = 1-|r_c|^2. \tag{5.4}$$

III. Comparison with experimental results

In this sub-section, the absorption coefficient for the porous substrate with and without leaf is calculated. Firstly, the leaf effect is not considered and the physical parameters of the porous substrate are determined. These parameters are the porosity, flow resistivity, structure factor, bulk modulus and damping coefficient of the material frame. Secondly, the effect of a leaf on the absorption of the porous substrate is studied. In this step, the influences of the bending stiffness of the leaf and the leaf surface density have to be determined as well.

Porous substrate without foliage:

The acoustical properties of a porous substrate were investigated with a 29-mm diameter impedance tube in the Acoustics Laboratory at the University of Bradford. The standard material characterisation procedure as described in Ref. [145] was used to determine the acoustical and related non-acoustical properties of the porous material specimens. Two kinds of porous substrates were used in the measurements. Figure 5.10 illustrates a 25-mm thick sample of Armafoam Sound 240 reconstituted foam supplied by Armacell UK Ltd and a 30-mm thick melamine foam supplied by Foam Techniques Ltd. These materials are well-characterised so that it is possible to use them to represent soil substrates with two contrasting physical properties. Armafoam Sound 240 material has a relatively high density (240 kg/m^3) which does not allow for frame vibration effects in the considered frequency range. This material has a relatively high porosity, $\varphi \approx 0.8$, which is akin to that typical for soil substrates used in green wall systems (Khan *et al*. [146]). The flow resistivity of melamine foam is similar to that of a porous soil substrate used for the design of green walls. The density of Melamine foam is relatively low (40 kg/m^3) so that the frame vibration cannot be neglected and it is likely to have an effect on the acoustic absorption coefficient of the porous substrate.

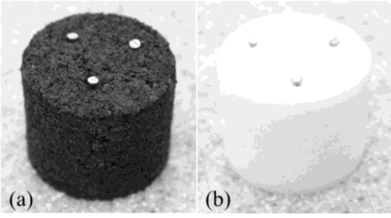

Figure 5.10 Photographs of the porous material samples used in the acoustic experiments, (a) Armafoam Sound 240, (b) Melamine foam.

A trial-and-error approach has been applied in order to obtain a good fit between measurements and simulations. Initial values are the measured quantities and parameters for similar materials as found in literature.

Figure 5.11 shows the absorption coefficient spectrum of a 25-mm thick Armafoam Sound 240 specimen in the presence of a hard termination. A good fit between measurements and predictions is obtained when choosing the following material parameters: the porosity (φ) equal to 0.81; structure factor (k_s) equal to 8.4; flow resistivity (R) equal to 260 kPa·s·m^{-2}; the Young's modulus of the substrate material (K_f) equal to 1 MPa and a damping coefficient (R_f) for the frame of 1600 kPa·s·m^{-2}. The fitted porosity, structure factor and flow resistivity are compared with the non-acoustic measured results using the standard material characterisation procedure; and the comparison is given in Table 5.2. From this comparison and the results in Figure 5.11, it can be concluded that the implemented FDTD equations can provide a good and realistic prediction of the absorption coefficient of this type of porous substrate.

Table 5.2. Comparison between the fitted porosity (φ), structure factor (k_s) and flow resistivity (R: KPa·s·m^{-2}) of the Armafoam Sound 240 foam and the non-acoustic measured results using the standard material characterisation procedure (Ref. [145]).

	Fitted values	Measured value
φ	0.81	0.812
k_s	8.4	7.37
R	260	254

Figure 5.12 shows the absorption coefficient of 30mm thick melamine foam, having a much smaller density of 40kg/m^3. For this substrate, the one-fourth wavelength frame resonance [107] occurs around 2700 Hz. At this frequency, the wavelength is around four times the thickness of the melamine foam. The numerical model is able to simulate this frame resonance and accurately predicts the absorption coefficient of Melamine foam across the considered frequency range. The following values for the five non-acoustical parameters provide the best fit between the acoustic model and measured data: the porosity (φ) equal to 0.98; structure factor (k_s) equal to 1.22; flow resistivity (R) equal to 22 kPa·s·m^{-2}; the bulk modulus of the substrate material (K_f) equal to 1.24 MPa and the damping coefficient (R_f) equal to 20 kPa·s·m^{-2}. The comparison of the fitted porosity, structure factor and flow resistivity for this melamine foam with the measured values published by Dragonetti et al. [147] and Kino and Ueno [148] is given in Table 5.3. It is shown that these fitted parameters for the melamine foam are realistic.

Table 5.3. Comparison between the fitted porosity (φ), structure factor (k_s) and flow resistivity (R: KPa·s·m^{-2}) of the melamine foam with the published measured results by Dragonetti et al.(Ref. [147]) and Kina and Ueno (Ref. [148]).

	Fitted values	Dragonetti et al.	Kino and Ueno
φ	0.98	0.93	0.992-0.995
k_s	1.22	1.05	1.0053-1.0059
R	22	10.7	10.5-17.5

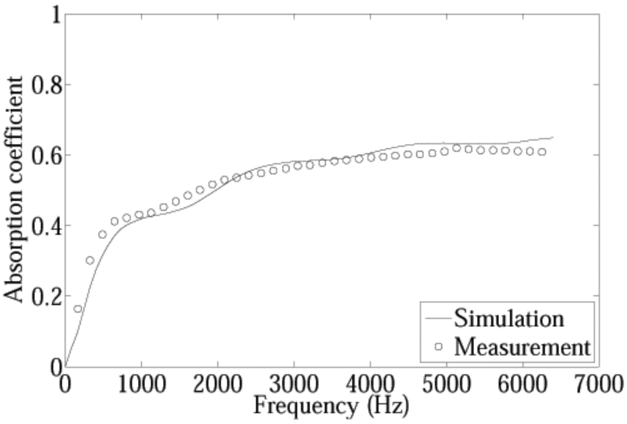

Figure 5.11 The absorption coefficient for a 25 mm hard-backed layer of Armafoam Sound 240 foam.

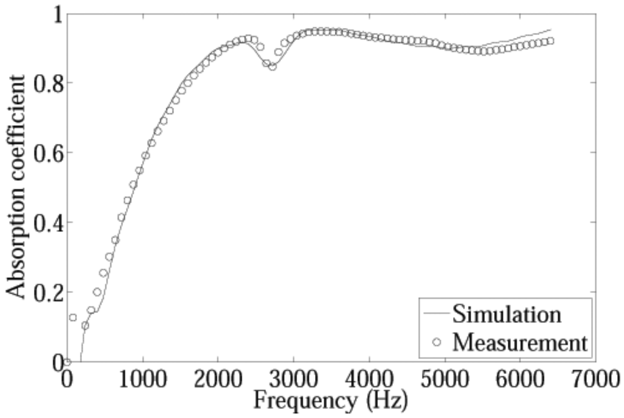

Figure 5.12 The absorption coefficient for a 30 mm hard-backed layer of Melamine foam.

Porous substrate with foliage

In the experiment by K. Horoshenkov, leaves from four plants were used and their properties like surface densities and thickness are given in Table 5.4. A 29-mm round cutter was used to produce a specimen from a leaf tissue that could fit accurately the diameter of the impedance tube. Photographs of these leaf specimens are shown in Figure 5.13.

Table 5.4. Surface density and thickness of the leaves from four plants.

Name	Density (kg/m^2)	Thickness (mm)
Japanese Andromeda (*Pieris japonica*)	0.367	0.41
Scarlett Wonder (*Rhododendron forrestii*)	0.408	0.34
Primrose (*Primula vulgaris*)	0.469	0.74
Corsican Hellebore (*Helleborus argutifolius*)	0.22	0.43

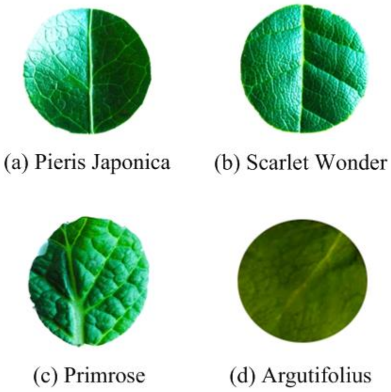

Figure 5.13 Photographs of the leaves used in the acoustic experiment.

Three 1-mm diameter nails were inserted in the porous samples to form a support base for the 29-mm leaf specimen (see Figure 5.14). Measurements of the acoustic absorption of Armafoam Sound 240 material and Melamine foam with and without nails indicated that the effect of the three nails on the acoustic absorption spectra was negligible and comparable to the reproducibility of the adopted measurement procedure. These nails served as small columns to support the leaf specimen during the measurement and to restrain to some extent the frame vibration when melamine foam was used as a porous substrate. The leaf specimen was placed on the top of the nails in the porous sample in the impedance tube so that there was approximately a 1-mm air gap between the leaf and the top surface of the porous sample as illustrated in Figure 5.14. In this way, there was no mechanical contact between the top surface of the porous sample and the bottom surface of the leaf specimen. Therefore, the leaf was simply supported at three points so that we were able to measure the influence of the leaf vibration and its acoustical shielding effect on the acoustic absorption coefficient of the porous sample that was representing the soil.

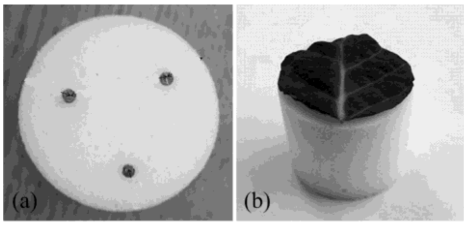

Figure 5.14 The arrangement for the leaf support over the porous substrate: (a) dimensions of leaf support, the distance between two supports is 15 mm and the distance from support to the foam edge is 5.5 mm; (b) leaf on top of melamine foam.

In the numerical simulation, a single leaf, which fully covers the cross section of the impedance tube, is placed in front of the porous substrate and the distance between the leaf and the substrate is set at 1 mm. The four leaves described above were considered and in the cells that form the 'numerical' leaf, the volume density is calculated according to the leaves' surface density. The bending stiffness of each leaf is estimated according to eqn. (3.44) introduced in section 3.4.

For the leaves used in the following simulations, the average thickness has been given in Table 5.4. Earlier work suggests that the Poisson’s ratio of an isotropic leaf specimen is close to 0.25 [138]. For the leaf’s Young’s modulus, eqns. (3.45) and (3.46), based on the work done by Saito et al. [128] and Niinemets [131], can be used as a first estimate. The leaf volume density for Japanese Andromeda, Scarlet Wonder, Primrose and Corsican Hellebore can be calculated according to the surface density and thickness (Table 5.4), yielding 895kg/m^3, 1200kg/m^3, 634kg/m^3 and 512kg/m^3, respectively. According to eqn. (3.46), the bulk elastic modulus for Japanese Andromeda, Scarlet Wonder, Primrose and Corsican Hellebore can be estimated to be 24.8 MPa, 32.5 MPa, 18.1 MPa and 15 MPa, respectively. Then, these values can be used in eqn. (3.45) to get the estimations for the leaves’ Young’s modulus. Finally, the bending stiffness can be calculated using eqn. (3.44). This finally gives as a rough estimate for the bending stiffness equal to 0.0025 N·m, 0.0018 N·m, 0.01 N·m and 0.0017 N·m for each of the four leaves.

The absorption coefficients for the 25 mm Armafoam Sound 240 foam with three different leaves (Japanese Andromeda, Scarlet Wonder and Primrose) are shown in Figure 5.15-Figure 5.17. The simulation results in Figure 5.15(a), Figure 5.16(a) and Figure 5.17(a) do not consider the influence of the leaf bending stiffness. They are smoother, when compared to the measurements. In Figure 5.15(b), Figure 5.16(b) and Figure 5.17(b), the effect of the bending stiffness on the predicted absorption coefficient of the porous substrate covered by a leaf is included in the simulation results. It can be found that when bending stiffness is included, the absorption coefficient follows the same trend as that without considering leaf bending, but obvious fluctuations can be noticed that show qualitative agreement with the measurements. The bending stiffness given in Figure 5.16 and Figure 5.17 is modified from the theoretical estimates discussed above to improve correspondence with measurements. A possible reason for this difference is that (3.45) is based on the leave from *Quercus glauca* and *Quercus serrata*, which both have a relative flat surface. In contrast, the leaves from Scarlet wonder and Primrose have a rather uneven surface (see Figure 5.13). As a result, eqn. (3.45) becomes less accurate and also makes it more difficult to obtain the correct leaf thickness, which has a strong effect on density and an even stronger effect on bending stiffness (third power dependency according to eqn. (3.44)). For the leaf from Japanese Andromeda, using the calculated bending stiffness gives an absorption coefficient that fits the measurements better because this kind of leaf has a flat surface.

Figure 5.18 shows the absorption coefficient for the 30-mm melamine foam with Corsican Hellebore leaf. Unlike Figure 5.15-Figure 5.17, Figure 5.18 does not show results including leaf bending, as no effect of the latter was observed. A possible reason for this phenomenon is that the rather large absorption coefficient of the 30mm melamine foam generates much weaker standing waves between leaf and porous foam. As a result, the leaf bending does not influence the overall absorption characteristics significantly.

The results presented in Figure 5.15-Figure 5.18 show that in the presence of a leaf the absorption coefficient of a porous substrate decreases in the high frequency range above 2000-3000 Hz, increases in the middle frequency range between 500 Hz and 2000 Hz and keeps unaffected in the low frequency range below 250 Hz. Although the agreement between measurements and simulations is generally close, there are some discrepancies. These can be attributed to the complex structure of the leaf, which is simplified in the numerical predictions. For example, the extension of the veins of leaf and the uneven distribution of the leaf surface density could give rise to deviations from the assumed uniform properties of the leaf. It is also difficult to ensure that there is no circumferential gap between the edge of the leaf and the wall of the impedance tube and that the mechanical boundary conditions on the edge of the leaf are accurately modelled.

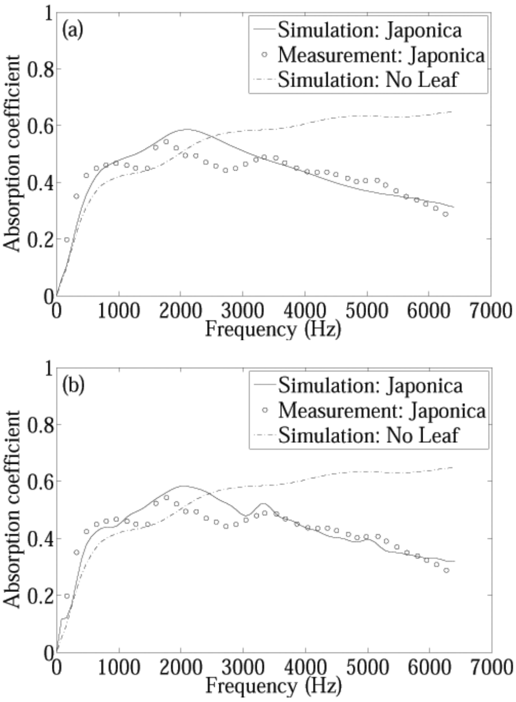

Figure 5.15 The absorption coefficient of a 25 mm hard-backed layer of Armafoam Sound 240 foam covered with a Pieris Japonica leaf: (a) D=0; (b) D=0.0025 N·m.

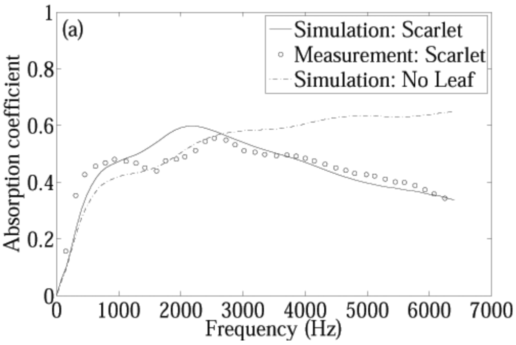

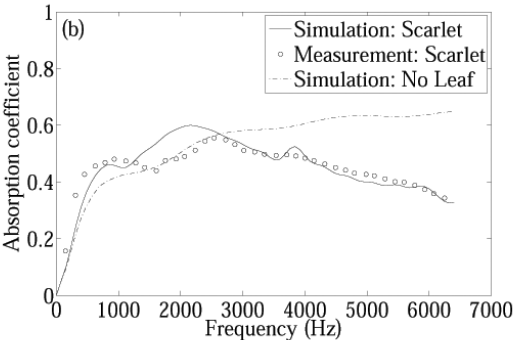

Figure 5.16 The absorption coefficient of a 25 mm hard-backed layer of Armafoam Sound 240 foam covered with a Scarlet wonder leaf: (a) *D*=0; (b) *D*=0.004 N·m.

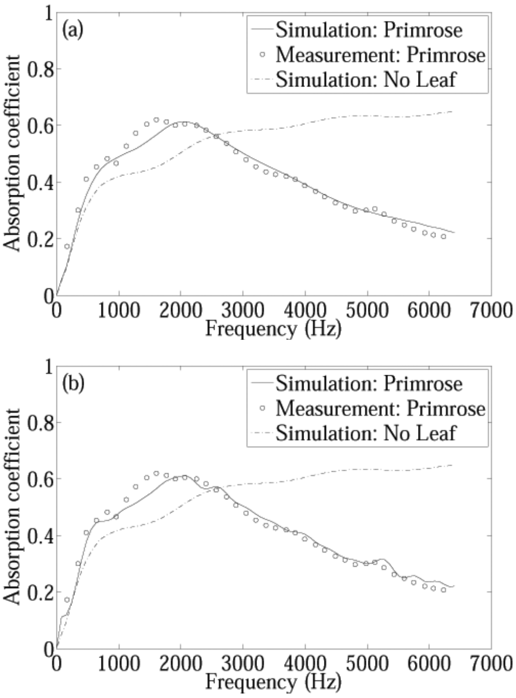

Figure 5.17 The absorption coefficient of a 25 mm hard-backed layer of Armafoam Sound 240 foam covered with a primrose leaf: (a) *D*=0; (b) *D*=0.002 N·m.

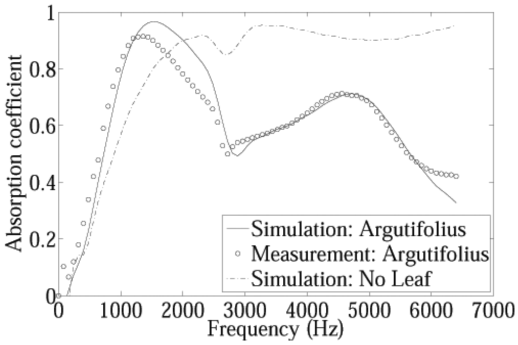

Figure 5.18 The absorption coefficient of a 30 mm hard-backed layer of Melamine foam covered with Argutifolius leaf.

IV. The influence of leaf surface density

In this section, the effect of leaf surface density is numerically studied and the bending stiffness is set to 0. The leaf surface density is a parameter that is likely to vary largely from plant to plant [137]. On the other hand, this is a parameter that is rather easy to quantify and use in the model so that the predicted results can be directly translated into practical applications. The effect of the leaf surface density on the absorption coefficient of the AFS240 foam and Melamine foam samples was modelled here and the results are shown in Figure 5.19 ~ Figure 5.20, respectively.

The results presented in these figures suggest that below 1-2 kHz the effect of leaf surface density on the combined leaf-foam absorption system is relatively small and that above 1-2 kHz this effect becomes more pronounced. The absorption coefficient of the porous substrate covered by a leaf increases with the decreased leaf surface density. Furthermore, the presence of a leaf with a lower surface density results in absorption coefficient enhancement across a wider frequency range than in the case of a leaf with a higher surface density. This effect is particularly obvious for the low-permeability AFS240 foam. Specifically, Figure 5.19 shows that adding a leaf with the surface density of 100 g/m^2 can increase the absorption coefficient by up to 20% below 4000 Hz, while adding a leaf with a larger surface density results in absorption enhancement limited to frequencies below 2500 Hz. For the high-permeability foam, changes in absorption coefficient by adding a leaf are even stronger. The decrease in absorption at higher frequencies is more pronounced for leaves with a higher surface density.

Three conclusions can be drawn from these results: (i) introducing a low-density leaf near a porous surface results in an enhancement of absorbing coefficient in the mid-frequency range (500-2500 Hz); (ii) this effect is particularly pronounced in the case of a low-permeability porous substrate; (iii) at high frequencies, there is a decrease in absorption.

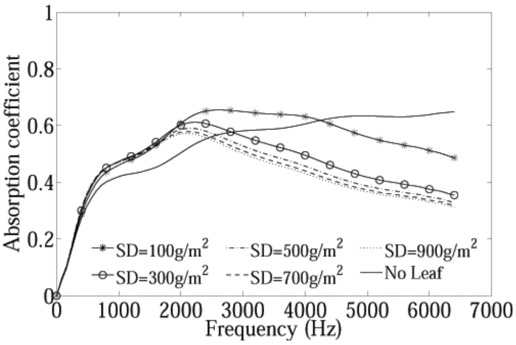

Figure 5.19 The effect of leaf surface density on the absorption coefficient of a 25mm hard-backed layer of Armafoam Sound 240.

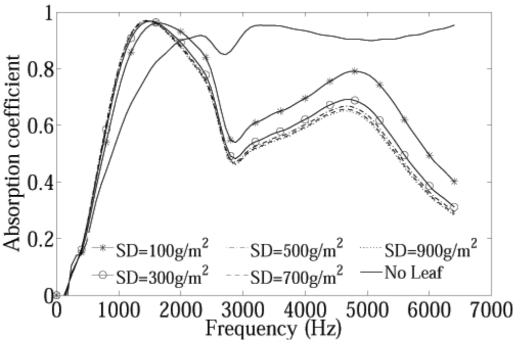

Figure 5.20 The effect of leaf surface density on the absorption coefficient of a 30mm hard-backed Melamine foam.

5.2 Behaviour of a group of leaves[4]

I. Introduction

The 3D finite-difference time-domain model was used to simulate the interaction between a single leave and sound waves in section 5.1 and showed good agreement with measurements.

---

[4] The content in section 5.2 was published in the following conference paper: Lei Ding, Timothy Van Renterghem and Dick Botteldooren: An efficient approach to evaluate multiple scattering by foliage in a 3D-FDTD model. Proceedings of the 41st International Congress and Exposition on Noise Control Engineering (Inter-Noise), New York (2012).

The relative importance of the various interactions between leaves and sound waves remain a question. Scattering is expected to be the main effect, but also leaf vibrations [18, 59] and (viscous) damping near the surface of leaves could add to noise reduction.

In order to simulate the interaction between sound and plant leaves numerically, 3D models are needed. Furthermore, since effects are expected to become important at wavelengths shorter than the dimensions of the leaves, fine numerical discretisations are mandatory. As a result, this leads to a high computational cost. Especially the memory requirement is typically a major bottleneck when using the FDTD technique.

The use of periodic/cyclic boundaries is a possibility to limit the computational cost. Only a small volume is considered, where sound passes through a number of times. In this explicitly modelled volume, only a few leaves are placed, representing a realistic leaf area density. The total propagation time will then define the width of the vegetation zone. A drawback of this approach is that randomness in orientation and spacing of leaves cannot be considered.

Wave reflection and scattering, and also energy dissipation caused by viscosity, thermal conductivity and structural damping, are captured by the implemented FDTD model (see Chapter 3). In order to quantify transmission, the incident wave and reflected wave must be separated, which will be done in frequency domain. Finally, the transmitted amount of energy can be calculated.

II. NUMERICAL MODEL

The numerical model has been introduced in detail in Chapter 3. In between the scattering objects (leaves), lossless isentropic sound propagation is assumed leading to the linearised continuity equation and momentum equation, see eqns. (3.1)-(3.2). Close to the objects, the viscous and thermal conductivity damping in the boundary layer can be modelled by adding additional terms (in frequency domain) to the linearised velocity equations (in the directions which are parallel to the leaf surface plane) and pressure equations, see section 3.1 and ref. [61].

The vibration of a leaf is modelled as a vibrating thin plate [60]. The viscoelastic damping accompanying the leaf vibration can be included by employing the generalised Maxwell model, which has been used by Chaigne et al. [103, 104]. The leaf is approximated by a homogeneous plate having the shape of the leaf since taking into account the fine structure of the leaf is beyond reach of the numerical discretisation. The bending wave can propagate in the two in-plane directions. The details can be found in section 3.1, and the velocity equation for the bending leaf is eqn. (3.9).

The discretisation process by the finite-difference time-domain method has been described in section 3.2 and it has been used in the application for the single leaf problem. The choices of the corresponding parameters for the viscous damping in the boundary layer and viscoelastic damping during leaf bending have been introduced in section 3.4.

Instead of simulating the whole vegetation volume, only a small cubic box is considered and multiple passages through this volume are modelled. For this, the concept of cyclic boundary condition is used: outgoing values on one boundary will be used as the ingoing values in the next time step at the other side of the simulation domain. For example, on the boundaries $x=x_1$ and $x=x_N$, the pressure equation and the velocity equation in x-direction can be written as

$$p_{1,j,k}^{l+1} = p_{1,j,k}^{l} - dt\rho_0 c^2 \left(\frac{v_{x1+0.5}^{\ l+0.5} - v_{xN+0.5}^{\ l+0.5}}{dx} + \sum_{\beta=j,k} \frac{v_{\beta\,\beta+0.5}^{\ l+0.5} - v_{\beta\,\beta-0.5}^{\ l+0.5}}{d\beta} \right), \tag{5.5}$$

$$v_{x(N+0.5),j,k}^{\ l+0.5} = v_{x(N+0.5),j,k}^{\ l-0.5} - \frac{dt}{\rho_0 dx}\left(p_{1,j,k}^{l} - p_{N,j,k}^{l}\right). \tag{5.6}$$

This periodic extension introduces periodicity in the leaf placement which will lead to special effects of periodic structure but these will occur mainly below the frequencies of interest if the basic simulation cell is kept large enough.

Most applications of FDTD assume a spatially localised sound source. Because of the cyclic boundary, such a source would also be periodically extended which is not desired. Hence, we opt for a plane wave as a starting field. To minimise numerical dispersion, the initial plane wave is chosen to propagate along the diagonal of the cubic box [63]. The initial values for pressures and velocities are Gaussian modulated sine waves both in space and time. The centre plane of the Gaussian pulse must be chosen carefully in order to make the pressure and velocities on the edge of this cubic box match the pressure and velocities on the edge of its adjacent cubic boxes. The initial wave fields are therefore centred at three planes as shown in Figure 5.21.

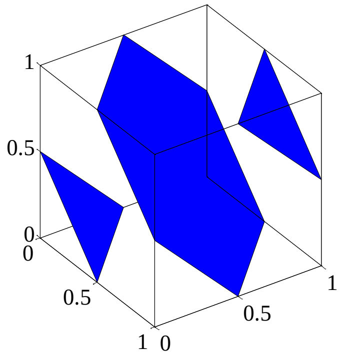

Figure 5.21 Diagram showing the three planes on which the wave fields are centred.

III. Post-processing: directional wave separation

During the time-stepping, the amplitude of the plane wave propagating in the incident direction will be reduced because of scattering and dissipation. In order to quantify these effects, this plane wave has to be separated out of the total field. For this, the velocities and the pressures on the three planes orthogonal to the diagonal propagation shown in Figure 5.21 are recorded and the least-square-method [149] is used to separate the wave fields. The waves in a 3D-problem can be written as

$$s(x_n, y_n, z_n, t) = \int_{-\infty}^{+\infty} \hat{s}_n(\omega) e^{i\omega t} d\omega \, , \tag{5.7}$$

where ω is the angular frequency; $s(x_n, y_n, z_n, t)$ is the signal in time domain and $\hat{s}(\omega)$ is its corresponding frequency spectrum, which can be locally approximated by

$$A_{inc}(\omega)e^{-i\kappa x'} + A_{ref}(\omega)e^{i\kappa x'} + B_1(\omega)e^{-i\kappa y'} + B_2(\omega)e^{i\kappa y'} + C_1(\omega)e^{-i\kappa z'} + C_2(\omega)e^{i\kappa z'} \, , \tag{5.8}$$

where A_{inc} denotes the amplitude of the wave propagating in the original diagonal direction; and A_{ref}, B_1, B_2, C_1 and C_2 denote the amplitudes of scattered waves in three directions. One of the three directions, $x'(x_n, y_n, z_n)$ is parallel to the diagonal direction and the other two directions, $y'(x_n, y_n, z_n)$ and $z'(x_n, y_n, z_n)$, are orthogonal to the diagonal direction. These coefficients can be found for each point on the planes orthogonal to the propagation direction shown in Figure 5.21 based on the recorded data at *m* neighboring measurement points (one of them lying outside the plane) by minimising the quadratic error

$$\begin{aligned} \sum_{n=1}^{m} \Big[& A_{inc}(\omega)e^{-iku} + A_{ref}(\omega)e^{iku} + B_1(\omega)e^{-ikv} + B_2(\omega)e^{ikv} \\ & + C_1(\omega)e^{-ikw} + C_2(\omega)e^{ikw} - \hat{s}_n(\omega) \Big]^2 \end{aligned} \, . \tag{5.9}$$

In order to find the minimum value, the derivatives to these coefficients are set equal to 0. As a result, a linear system of equations can be constructed which must be solved.

The procedure described above is applied to the pressure field and to the x'-component of the velocity field $V_{x'}$ – where in the latter case the *B* and *C* terms can be assumed zero. The cross power spectrum density is used to denote the energy or intensity propagating in the original plane direction *u*, and it is given by

$$S_I(\omega) = P_{inc}(\omega)^* \cdot V_{x',inc}(\omega), \tag{5.10}$$

where $P_{inc}(\omega)$ and $V_{x',inc}(\omega)$ are the frequency spectrum of the pressure and velocity propagating forwards in the diagonal direction; and the * in the superscript denotes the complex conjugate. Finally, intensity is calculated on all points and averaged over the plane.

IV. Numerical calculation

The size of the unit cubic box in the simulation has dimension 0.3m×0.3×m0.3m. The cell size is 0.01m×0.01m×0.01m and the time step is chosen to make the Courant number equal to 1. Three types of leaves, namely Prunus Laurocerasus, Tilia and Prunus Serrulata, are considered. The size (width×length) of the Prunus Laurocerasus leaf, Tilia and Prunus Serrulata is 8cm×16cm, 12.1cm×13.1cm and 7.5cm×12cm, respectively. Their corresponding leaf areas are approximately $1.01\times10^{-2}m^2$, $1.36\times10^{-2}m^2$ and $0.69\times10^{-2}m^2$; and the leaf surface density is 271 g/m^2, 104 g/m^2 and 185 g/m^2. For each type of vegetation, a calculation was made with one, two or three leaves placed in this cubic box (one example of two leaves is given in Figure 5.22). The simulation with one leaf corresponds to a leaf area density (LAD) of $0.374m^{-1}$ for Prunus Laurocerasus, $0.504m^{-1}$ for Tilia and 0.255 m^{-1} for Prunus Serrulata.

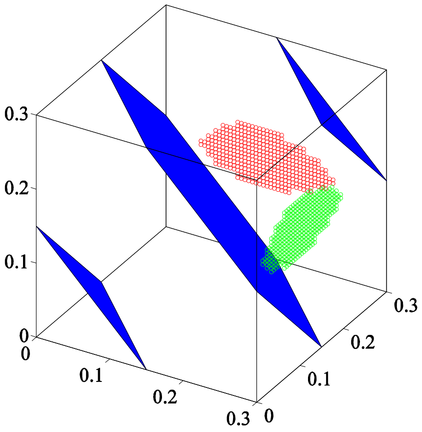

Figure 5.22 Diagram showing the three planes on which the wave fields are centred with 2 leaves.

The bending stiffness of the leaf can be calculated by eqn. (3.44). Published work by Takami Saito et al. [128] suggests that the Young's modulus of the leaves from Quercus glauca and Quercus serrata plants are in the range of 200-800 MPa. Other work suggests that the Poisson's ratio of an isotropic leaf specimen can be taken close to 0.25 [138]. The thickness of the leaf has the order of magnitude of 0.0005m. Based on these values, the bending stiffness can be estimated and in this section it is assumed to be 0.0025N·m for all leaves.

In order to present the sound transmission loss through the foliage, the (dimensionless) approach presented by Aylor [57] is used. The excess attenuation *EA* divided by the square root of the product of LAD and the breadth/width of the vegetation *L*, is shown as a function of *ka*, where *k* is the wave number and *a* is the typical leaf width. This way of representing was shown to be independent of species when looking at sound transmission through reeds and corn [57].

V. Results and discussion

Because of the presence of the leaves, scattering and dissipation will lead to transmission loss. Figure 5.23-Figure 5.25 show the decrease in intensity of the plane wave when it propagates through an area filled with Prunus Laurocerasus, Tilia, or Prunus Serrulata leaves. For the results at 4000Hz, the decrease in intensity is enhanced with propagated distance, when compared to the results at 2000Hz. Two or three leaves attenuate more energy than one leaf because of stronger backscattering and higher energy dissipation. Initially, the attenuation is stronger than linear while after some propagation distance the attenuation is less than linear. The latter is due to multiple scattering resulting in part of the waves returning to the initial direction.

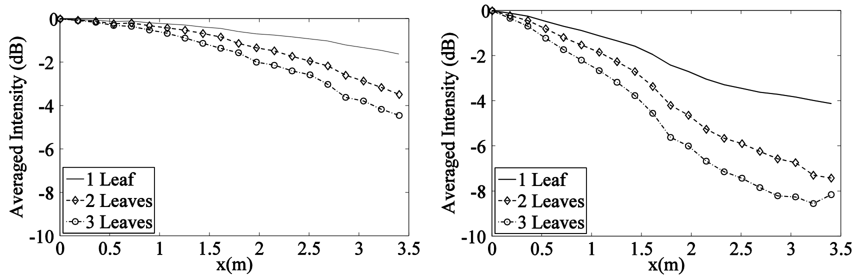

Figure 5.23 Plane sound wave attenuation in Prunus Laurocerasus. The left figure shows the results at 2000Hz and the right one at 4000Hz.

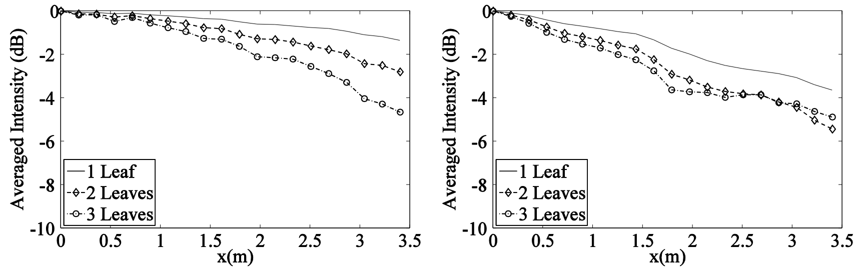

Figure 5.24 Plane sound wave attenuation in Tilia. The left figure shows the results at 2000Hz and the right one at 4000Hz.

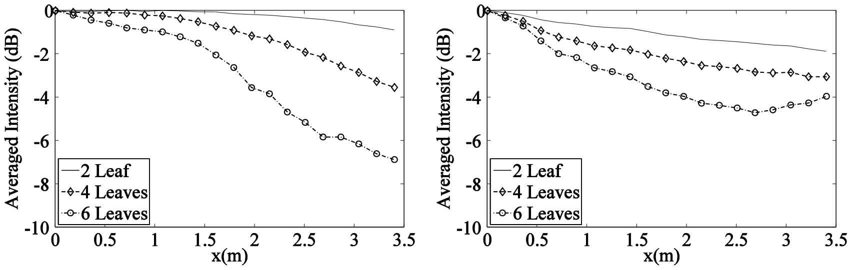

Figure 5.25 Plane sound wave attenuation in Prunus Serrulata. The left figure shows the results at 2000Hz and the right one at 4000Hz.

Figure 5.26-Figure 5.28 show the attenuation normalised by leaf area density and the length of the propagation path. These curves show a similar behaviour as in the measurements performed by Aylor [57]. Furthermore, the values obtained have the same order of magnitude. The dimensionless transmission loss values still depend on the number of leaves (or LAD), in contrast to Ref. [57]. Note however that the LAD is much smaller in the current simulations. The current approach is expected to become invalid above *ka*=10-15. Furthermore, Figure 5.28 shows that at low frequency the excess attenuation is negative, which can be attributed to the fact that the current wave separation approach is not valid at low frequencies.

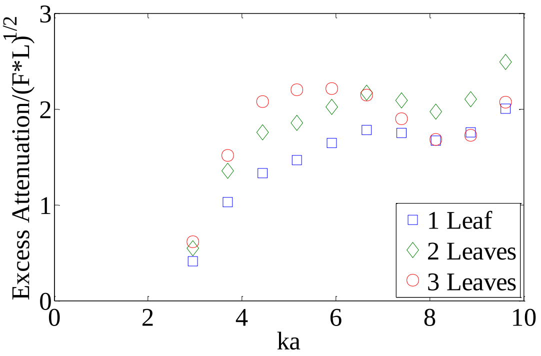

Figure 5.26 Normalized Excess attenuation for the leaf of Prunus Laurocerasus.

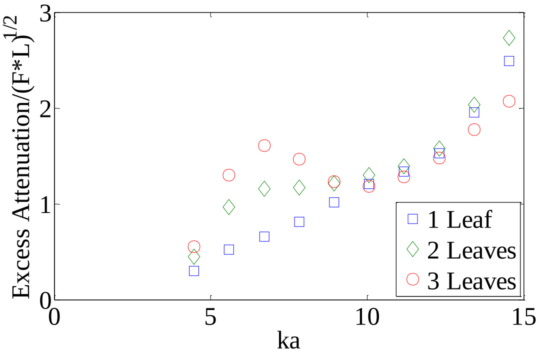

Figure 5.27 Normalized Excess attenuation for the leaf of Tilia.

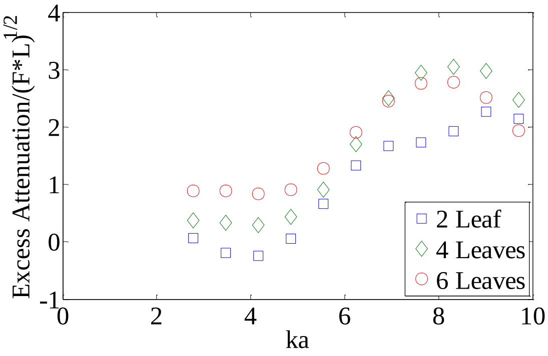

Figure 5.28 Normalized Excess attenuation for the leaf of Prunus Serrulata.

5.3 Conclusions

The FDTD model described in Chapter 3 has been used to simulate single leaf vibrations. Although the complexity of the leaf structure makes the experimental and numerical results difficult to compare, the obvious significant vibration when acoustic wavelengths approach leaf size has been observed both experimentally and numerically.

This FDTD model has been used to numerically study the influence of loose leaves on the acoustic absorption of a porous substrate. Biot's theory is included in this model to simulate elastic frame porous substrates. The leaf vibration is simulated by the isotropic plate vibration theory; the viscoelastic damping during leaf vibration and the energy dissipation in the leaf's vorticity and entropy boundary layer are also considered in this model.

The equations based on the Biot's elastic frame porous medium model and isotropic plate vibration theory are solved using a finite-difference time-domain approach. According to the comparison with experimental results, this approach enables an accurate prediction of the absorption coefficient spectrum of a leaf in front of a porous substrate. The predictions were made using non-acoustical parameters which were deduced from the absorption coefficient spectra of porous specimens measured at normal incidence in the absence of leaf. The changes in the absorption coefficient spectra caused by the leaf vibration were closely predicted. Both the experimental data and numerical model predictions indicate that the absorption characteristics change noticeably when a leaf is added to the porous substrate. Typically, an unaffected change in the absorption coefficient spectrum in low frequency range (below 250 Hz), an increase in the middle frequency range (500 Hz-2000 Hz) and a decrease in the higher frequency range (beyond 2000-3000 Hz) are observed.

The influence of the leaf becomes more pronounced when the leaf is added to a low-permeability substrate and when the leaf surface density is relatively small. The increase in absorption coefficient by leaves is in the typical frequency range of road traffic noise, while the negative effect by the presence of leaves is observed at sound frequencies that are typically too high to be of importance in environmental acoustics.

With the inclusion of the cyclical boundary condition, the model can also be used to model the sound propagation through a cluster of tree leaves. Its prediction about the energy attenuation shows the same trend as the measurements through foliage by Aylor [57].

CHAPTER 6
Acoustic wave propagation over noise barriers

6.1 Numerical assessment of porous barrier by 2D-UWVF[5]

In this section, the effects of the porous and rigid low-height barriers along a two-lane road are studied as shown in Figure 6.1. The width of each traffic lane is 4 m. When mixed traffic (including both light and heavy vehicles) is modelled, sound emitted by six point sources must be considered following the Harmonoise/Imagine road traffic source model [6]. The point sources are located in the middle of the traffic lanes. Points P3 and P6 (at a height of 0.01 m) are for the tire/road noise interaction of both light and heavy cars. P2 and P5 (at a height of 0.30 m) represent the engine noise sources of light vehicles, while P1 and P4 (at a height of 0.75 m) represent the engine noise sources of heavy vehicles.

Two dimensional calculations are performed. This means that the barrier has a constant cross-section, and that a coherent line source is modelled. However, the Harmonoise/Imagine road traffic source model was developed for a point source. To overcome this discrepancy, the equivalence between sound pressure levels, expressed relative to free field sound propagation, of a coherent line source and a point source is assumed [150].

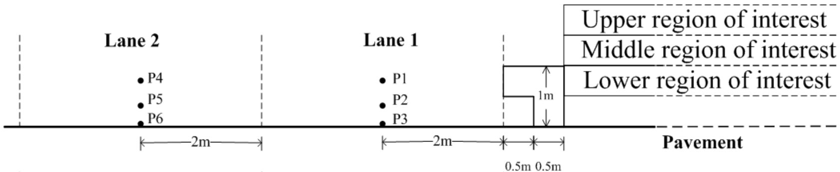

Figure 6.1 Multi-lane traffic noise situation under study for the assessment of low-height noise barriers.

[5] The content in section 6.1 has been published in ACTA ACUSTICA UNITED WITH ACUSTICA:
Lei Ding, Timothy Van Renterghem and Dick Botteldooren: Estimating the effect of semi-transparent low-height road traffic noise barriers with ultra weak variational formulation. ACTA ACUSTICA UNITED WITH ACUSTICA, 97(3), 391-402 (2011).

Both the street surface and pavement are modelled as rigid. A homogeneous and windless atmosphere is assumed. Given the low barrier height and the short propagation distances between the road traffic noise sources and the passengers, screen-induced refraction of sound is most likely very limited.

Various noise barriers were considered in this traffic noise assessment. These are shown in Figure 6.2. Both the height and the width of all barriers is 1 m. It has been found that the T-shaped noise barrier could provide good noise reduction [151]. When the noise barrier is constructed on the pavement, half of the T-shaped noise barrier has been used [5]. This shape is identified as Γ-shaped in this thesis. The exploration of the UWVF method to estimate the effect of low-height noise barriers is limited to Γ-shaped barriers. Five inverse Γ-shaped barriers were tested, with different properties. The first one, barrier (a), is completely rigid. Barriers (b) to (f) are porous and have the same porosity and structure factor, of 0.4 and 1.35, respectively. Barriers (b) and (c) have a flow resistivity of 50k Pa·s/m^2 (sand, Ref. [152]), while (d) and (e) have a lower flow resistivity of 10k Pa·s/m^2 (gravel, Ref. [153]). Furthermore, a rigid thin inner barrier is inserted in barriers (c) and (e) to prevent possible transmission through the porous barrier. Barrier (f) has a rectangular shape and a flow resistivity of 50k Pa·s/m^2.

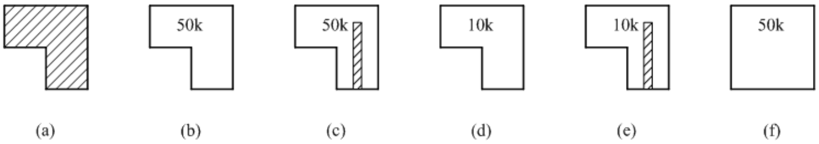

Figure 6.2 Configurations studied: (a) rigid noise barrier (RNB); (b) porous noise barrier, flow resistivity 50k Pa·s/m^2 (PNB50); (c) porous noise barrier with inner rigid barrier, flow resistivity 50k Pa·s/m^2 (PNB50_RI); (d) porous noise barrier, flow resistivity 10k Pa·s/m^2 (PNB10); (e) porous noise barrier with inner rigid barrier, flow resistivity 10k Pa·s/m^2 (PNB10_RI); (e) rectangular porous noise barrier (1 m×1 m), flow resistivity 50k Pa·s/m^2 (PNB50_REC). For all porous noise barriers, the porosity is 0.4 and the structure factor is 1.35.

Three regions of interest were defined behind the barrier where passengers could appear. The upper region extends 5 m behind the noise barrier, at a height between 1.5 m and 2 m. The middle one, at heights between 1.0 m and 1.5 m, and the lower region of interest is located between a height of 0.5 m and 1 m. Results are expressed as the average insertion loss for total A-weighted traffic noise in a given region of interest. The full traffic noise spectrum [6] is modelled by including the octave bands with central frequencies ranging from 63 Hz to 2000 Hz. For each octave band, 21 equally-spaced frequencies were sufficient to reach convergence in octave band level. Three vehicles speeds were considered, namely 30, 50 and 70 km/h.

In Figure 6.3, the total traffic noise insertion loss is shown at different vehicle speeds (30, 50, and 70 km/h), for the different barrier configurations considered. Four traffic noise situations are considered, namely a light vehicle in lane 1, a light vehicle in lane 2, a heavy vehicle in lane 1, and a heavy vehicle in lane 2. The upper region of interest is considered here, since this is the typical ear height of an adult person. Values for the insertion loss range from 2.5 dBA to 9 dBA.

Lane use is an important parameter. The presence of either a light or heavy vehicle in lane 1 gives a higher insertion loss than when the vehicle is present in lane 2. Lane choice has a stronger influence for light vehicles than for heavy vehicles. The presence of vehicles in lane 2 leads to more noise generation sources that can contribute directly, without diffraction, to the upper region.

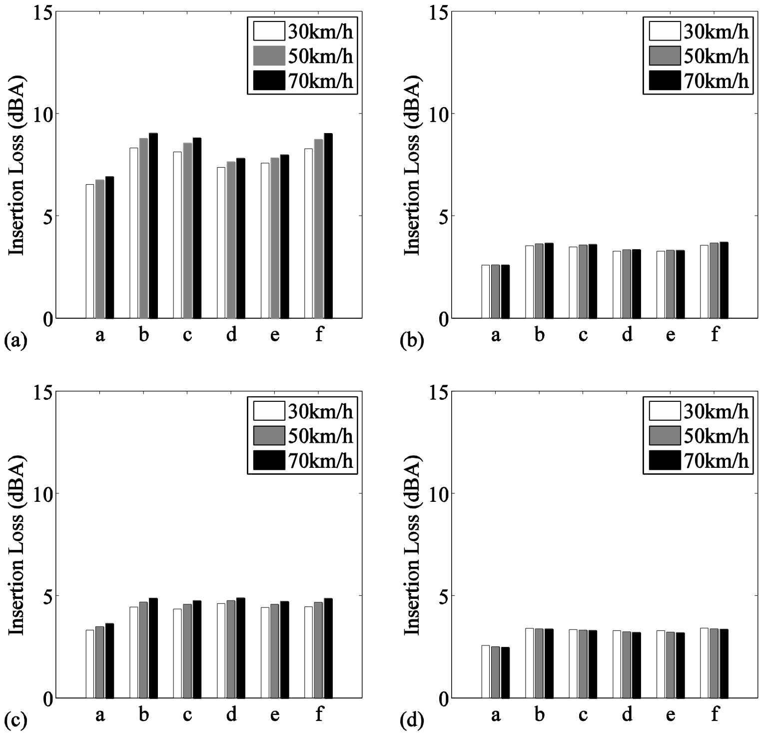

Figure 6.3 Average insertion loss in the upper region of interest: a) Light vehicle in lane 1; b) Light vehicle in lane 2; c) Heavy vehicle in lane 1; d) Heavy vehicle in lane 2.

It is further observed that the insertion loss is higher for light vehicles. For these, high frequencies contribute more to the total traffic noise levels. Diffraction around an obstacle is less pronounced for higher frequencies, and furthermore, the absorption at the barrier top is larger. With increasing vehicle speed, higher frequencies and rolling noise become more dominant, and larger insertion losses are observed. This effect is more pronounced for either light or heavy vehicles present in lane 1. For heavy traffic in lane 2, this trend is not observed, and even a very small decrease in insertion loss with increasing vehicle speed can be found for some barriers.

When comparing the different screens, it is observed that in all cases the porous barriers offer an improvement in shielding relative to the rigid one. At a maximum, an increase in insertion of 2 dBA is observed for light vehicles. For heavy vehicles, an increased shielding up to 1 dBA is found.

The use of a lower flow resistivity of 10k Pa·s/m^2 gives a somewhat worse performance than in the case of 50k Pa·s/m^2, especially for light vehicles in lane 1. In this specific traffic noise situation, the difference may amount up to 1.2 dBA. For heavy traffic, the influence of the flow resistivities considered in this numerical evaluation is very limited.

The presence of a rigid thin inner barrier has only a limited effect for the flow resistivity considered. At 50k Pa·s/m^2, there is sufficient damping when sound propagates through the barrier. As a consequence, transmission through the barrier is subordinate to diffracting waves over it. At a flow resistivity of 10k Pa·s/m^2, the leaking of acoustical energy through the barrier has some influence on the total traffic noise levels. Preventing this transmission path by placing such an inner barrier improves shielding only to a small extent. It is further observed that a inversely Γ-shaped screen shows a similar performance as the rectangular screen with the same porous medium parameters.

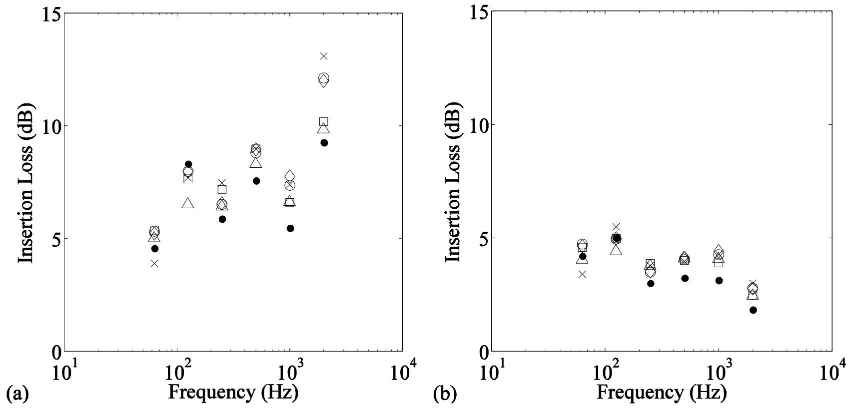

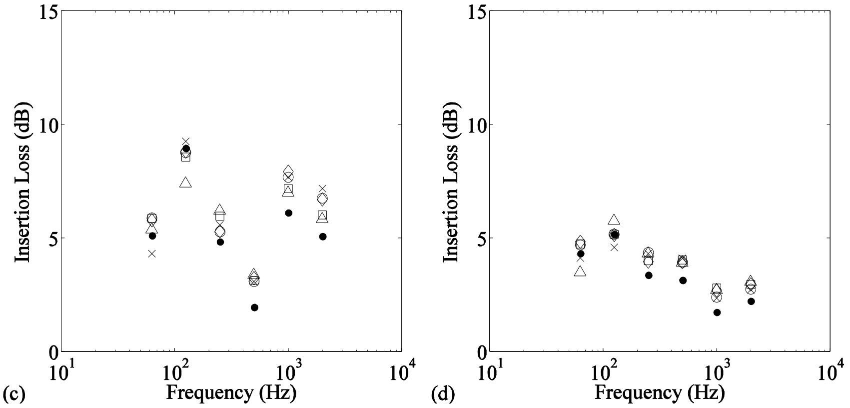

Figure 6.4 Average insertion loss (dB) in the upper region of interest for different octave bands. Vehicle speed is 50 km/h. ●: rigid noise barrier; ◊: porous noise barrier, flow resistivity 50k Pa·s/m^2; ○: porous noise barrier with rigid bar inside, flow resistivity 50k Pa·s/m^2; △: porous noise barrier, flow resistivity 10k Pa·s/m^2; □: porous noise barrier with rigid bar inside, flow resistivity 10k Pa·s/m^2; ×: rectangular porous noise barrier, flow resistivity 50k Pa·s/m^2: a) Light vehicle in lane 1; b) Light vehicle in lane 2; c) Heavy vehicle in lane 1; d) Heavy vehicle in lane 2.

When analysing different octave bands in more detail, as is shown in Figure 6.4 for vehicle speeds of 50 km/h and sound propagation to the upper region, we clearly see the complex nature of this sound propagation problem. When there is a light vehicle in lane 1, an increase in insertion loss with increasing frequency can be observed. For higher frequencies, the differences between the various noise barrier configurations increase. For the other source locations, a more complex behaviour can be observed. For both a light and heavy vehicle in lane 2, the insertion loss is very similar. The main difference here is the presence of the engine noise source at a height of 0.75 m instead of 0.30 m. The difference in engine noise height is much more significant when situated close to the barrier. Note that the sound paths leading to destructive interference in the reference situation (i.e. rigid ground without obstacles) might be prevented by the presence of a barrier. This could lead to a very low insertion loss, as is observed for heavy traffic in lane 1 for the octave band with central frequency 500 Hz. The insertion loss of the gamma shape compared to the full barrier is larger in the 63-Hz octave band due to an internal resonance in the cavity. Its performance is slightly worse only at a few frequencies where insertion loss is high anyhow. An advantage of the gamma-shaped barrier is that the amount of material needed for construction is lower.

The shielding in the middle and lower regions is significantly higher (see Table 6. 1 and Figure 6.5 and Figure 6.6). The area in the receiver zone with direct sound contributions decreases, and only diffracted and transmitted sound energy is found there. In the middle region, values of the insertion loss range from 5.1 dB to 13.0 dB, when considering all barriers, lane choices, vehicle types, and vehicle speeds. In the lower region of interest, these values range from 9.9 dB to 17.9 dB. Lane choice has a less significant effect than in the upper region of interest.

In the middle and lower regions of interest, the presence of a thin rigid barrier inside the 10k Pa·s/m^2 barrier leads to a more significant increase in insertion loss of up to 1 dB. For the 50k Pa·s/m^2 barrier, the effect of the inner rigid barrier stays limited. In the lower region, the typical increase of noise barrier shielding with frequency as for common highway noise barriers is found as shown in Figure 6.6.

Table 6. 1 Average insertion loss (dB) in the three regions of interest. Vehicle speed is 30, 50, and 70 km/h. LV denotes light vehicle, HV denotes heavy vehicle. L1 denotes traffic lane 1, L2 denotes traffic lane 2.

		RNB			PNB50			PNB50_RI		
		30km/h	50km/h	70km/h	30km/h	50km/h	70km/h	30km/h	50km/h	70km/h
LV in L1	Upper	6.54	6.77	6.93	8.32	8.79	9.05	8.13	8.56	8.82
	Middle	9.65	10.20	10.49	11.56	12.51	13.01	11.38	12.27	12.74
	Lower	13.25	14.66	15.32	14.63	16.64	17.69	14.56	16.48	17.47
LV in L2	Upper	2.59	2.61	2.61	3.54	3.64	3.67	3.48	3.58	3.61
	Middle	6.42	6.78	6.93	7.81	8.39	8.66	7.72	8.27	8.54
	Lower	11.41	12.52	13.04	12.36	13.91	14.69	12.28	13.76	14.50
HV in L1	Upper	3.32	3.49	3.65	4.45	4.69	4.89	4.35	4.58	4.77
	Middle	5.54	5.67	5.81	6.81	7.01	7.21	6.68	6.87	7.06
	Lower	10.04	10.29	10.50	11.36	11.73	12.02	11.20	11.55	11.82
HV in L2	Upper	2.57	2.51	2.48	3.41	3.38	3.38	3.35	3.32	3.31
	Middle	5.14	5.13	5.14	6.37	6.45	6.52	6.26	6.32	6.38
	Lower	9.85	10.23	10.47	10.98	11.52	11.89	10.88	11.40	11.74
		PNB10			PNB10_RI			PNB50_REC		
		30km/h	50km/h	70km/h	30km/h	50km/h	70km/h	30km/h	50km/h	70km/h
LV in L1	Upper	7.37	7.65	7.82	7.58	7.84	8.00	8.28	8.75	9.04
	Middle	10.24	10.97	11.34	10.74	11.38	11.71	11.41	12.43	12.99
	Lower	13.22	14.7	15.35	13.98	15.51	16.24	14.3	16.48	17.64
LV in L2	Upper	3.28	3.35	3.36	3.27	3.32	3.32	3.57	3.68	3.72
	Middle	7.15	7.69	7.94	7.41	7.86	8.07	7.84	8.45	8.76
	Lower	11.17	12.31	12.86	12.11	13.38	13.99	12.18	13.79	14.63
HV in L1	Upper	4.62	4.77	4.90	4.42	4.58	4.73	4.46	4.68	4.87
	Middle	7.14	7.30	7.46	6.77	6.92	7.08	6.76	6.95	7.15
	Lower	11.04	11.43	11.72	11.24	11.55	11.79	11.17	11.57	11.88
HV in L2	Upper	3.3	3.24	3.21	3.30	3.23	3.20	3.42	3.38	3.37
	Middle	5.98	6.04	6.09	6.12	6.14	6.18	6.36	6.42	6.48
	Lower	10.14	10.58	10.87	10.73	11.17	11.47	10.98	11.53	11.91

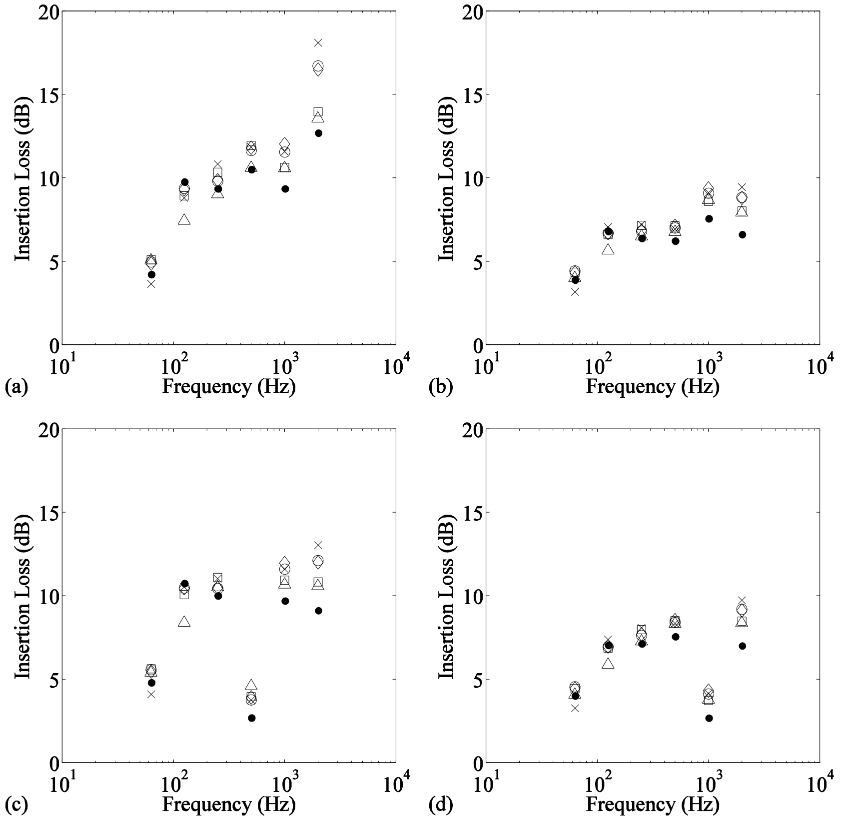

Figure 6.5 Average insertion loss (dB) in the middle region of interest for different octave bands. Vehicle speed is 50 km/h. For a definition of symbols see Figure 6.4: a) Light vehicle in lane 1; b) Light vehicle in lane 2; c) Heavy vehicle in lane 1; d) Heavy vehicle in lane 2.

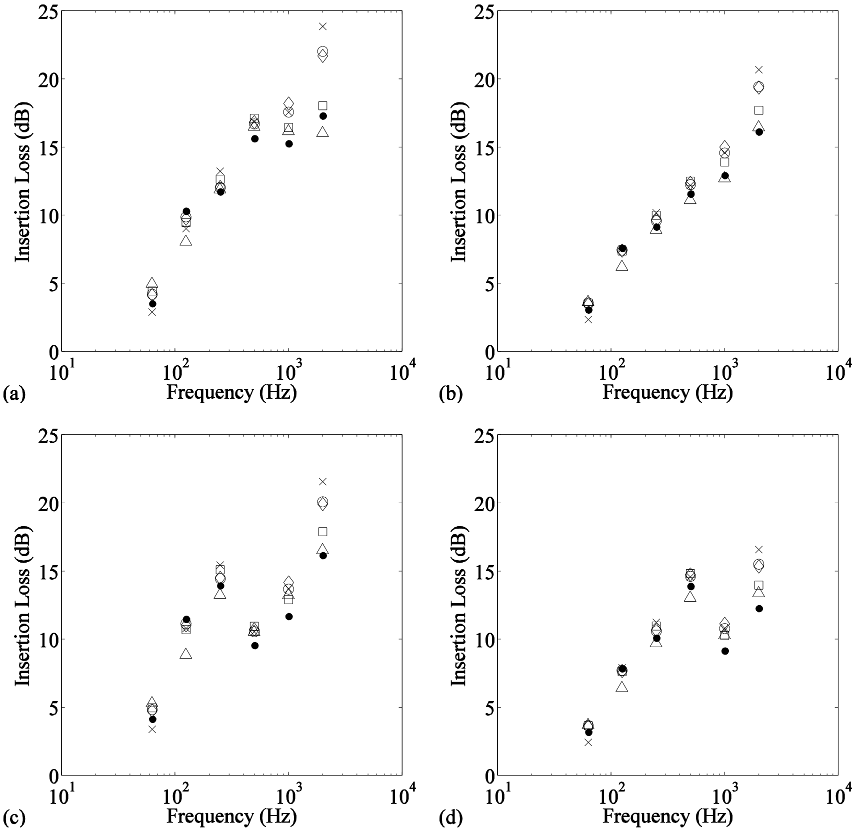

Figure 6.6 Average insertion loss (dB) in the lower region of interest for different octave bands. Vehicle speed is 50 km/h. For a definition of symbols see Figure 6.4: a) Light vehicle in lane 1; b) Light vehicle in lane 2; c) Heavy vehicle in lane 1; d) Heavy vehicle in lane 2.

6.2 Scale model measurement of a noise barrier

In this section, a highly detailed 1:30 scale model is used to study the sound propagation in an existing street canyon. The effect of absorbing low-height noise barriers constructed on the pavements are analysed. The scale model results are compared with full-scale measurements and 2D FDTD simulations.

6.2.1 Scale model set-up and data analysis

Scale model of a street canyon

A highly detailed 1:30 scale model was constructed according to the profile of an existing street canyon, namely the Gustaaf Magnelstraat, which is located in

Ghent, Belgium. The length and the width of the street are around 105m and 10m, respectively. In Figure 6.7, a drawing of the geometry of the street canyon is depicted. The detailed model is created by laser-cutting 3.6-mm thick plywood, based on these drawings [154]. After assembly, the model was vanished to make the material acoustically harder.

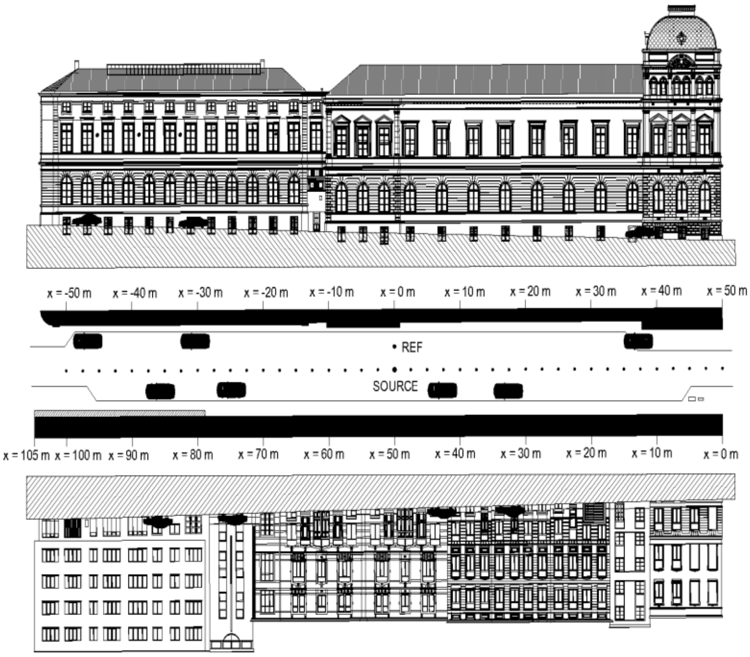

Figure 6.7 Detailed geometry of the 105m long street canyon used for the scale model

Data acquisition system

A synchronization system is used to control the scale model measurements. A wav-file is played by the loudspeaker, and at the same time the receiver records the signal. This system is implemented with NI's Labview, as summarised in Figure 6.8. Two modules have been used. The first module is used to play the signal. A DMX 6Fire USB sound card, produced by TERRATEC, is used and it can provide a sampling frequency up to 192 kHz. Then, a VSX-521 amplifier, produced by Pioneer, was used to control the volume of the output signal and 'pure direct' setting was chosen in order not to affect the signal. Finally, the signal is played by the loudspeakers.

The second module is used to record the signal. The receiver is a G.R.A.S. 40DP 1/8 inch externally polarized pressure microphone, and it was connected to a preamplifier (type: 2669), produced by Bruel & Kjaer. In the measurements, the preamplifier with the microphone is placed horizontally. The microphone power supplier (type: 5935) is connected to the preamplifier and the microphone to guarantee a 200 V polarization required by the microphone. They are then connected to the PC through a NI PXIe-1082, in which a 192 kHz sampling frequency is chosen.

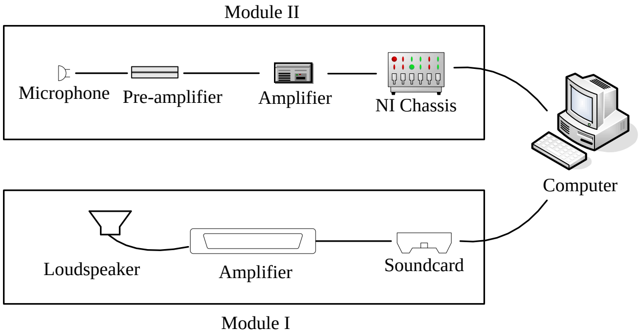

Figure 6.8 The measurement system of the scale model.

To approach a point sound source, two types of loudspeakers were used. The first loudspeaker is the SB29RDC-C000-4, which was produced by SB ACOUSTICS emitting in the frequency range between 400 Hz and 40 kHz; the second loudspeaker is Murata ESTD02, which was produced by Murata Manufacturing Co. Ltd., and could produce sound signals in a frequency range between 30 kHz and 100 kHz. Their frequency ranges correspond to 13.3-1333 Hz and 1000-3333 Hz at full scale, respectively. They sufficiently cover the frequencies of interest in road traffic noise applications. The two loudspeakers are placed in a plastic box and they are separated by a plastic beam. The plastic box is fixed below the rigid ground and one 3mm cushion is placed between them as a buffer. On the rigid ground, there are two holes above the centres of both loudspeakers. A steel tube, whose inner diameter is 6 mm, can be inserted into the larger hole and was designed for the SB29RDC-C000-4 loudspeaker. Similarly, another steel tube, with an inner diameter of 4 mm, can be inserted into the smaller hole and was designed for the Murata ESTD02 loudspeaker. The height of the tubes above the ground can be adjusted to satisfy the measurement requirements. In this study, the height of the tubes is set at 1 cm in the scale model.

The reliability of the approximated point source, constructed in this way, has been verified. The test measurements were carried out in a high-frequency anechoic room at Ghent University. These tests were conducted with a flat rigid ground plate in the anechoic room in absence of obstacles. The heights of the source and receiver are 1.8 cm and 3.8 cm, respectively. The measurement set-up is described in Figure 6.9. In total, six receiver positions were considered. The horizontal distances between the source and the receiver are 0.05 m, 0.1 m, 0.2 m, 0.3 m, 0.4 m and 0.6 m. The results are depicted in Figure 6.10. It can be found that the design of the point source is reliable.

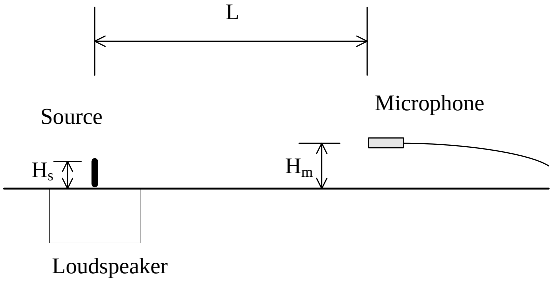

Figure 6.9 Measurement set-up for the verification of point source in anechoic chamber.

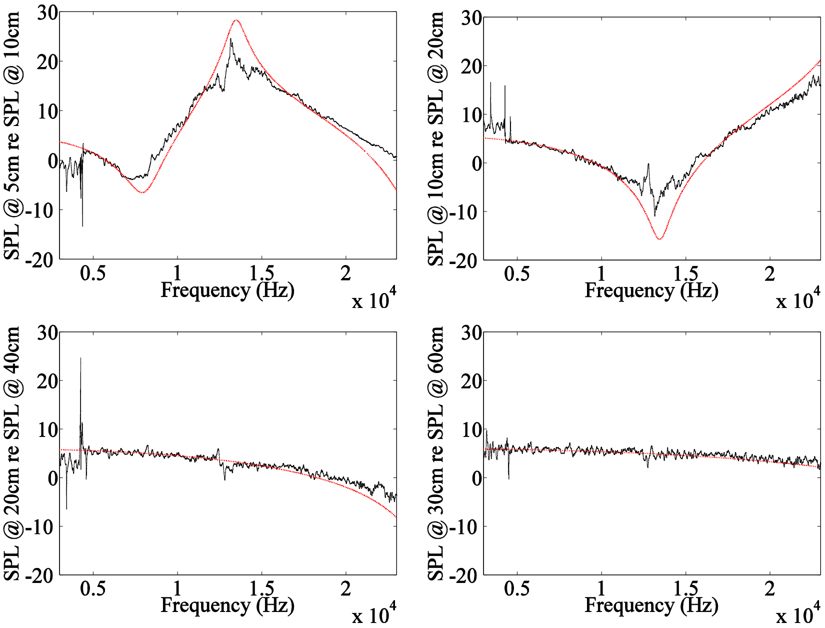

Figure 6.10 Comparison between measurements (black line) and analytical solutions (red line) for sound propagation over rigid ground. The unit of SPL is dB.

In the scale measurements, the influences of an absorbing low-height noise barrier has been studied. The length of the absorbing noise barrier is 1.8 m, and its height and width are 0.0320 m and 0.0213 m, respectively (dimensions as in the scale model). It has a wooden inner bar, which is 0.008 m wide and 0.0253 m tall. One layer of 0.0066 mm rock-wool (density: 70 kg/m^3) is glued on three sides (left, right and top) of the wooden bar and a double-side adhesive tape is glued on the bottom side. In the measurement, the wooden bar can be pasted on the rigid ground and this prevents sound leaking underneath.

Measurement method

The scale model is placed in the high-frequency anechoic room. The movement of the microphone is controlled by VXM Stepping Motor Controller, produced by VELMEX. The atmospheric pressure, temperature and relative humidity are recorded during all the experiments. These values are used to compensate the excess air attenuation, which will be introduced later.

Two types of measurements were performed. In the first group, the scale-model measurements have been compared to the measurements in the (full-scale) street. Only the rigid ground and the building facades are considered then. The source and the receivers are placed along the central length axis of the street canyon (see Figure 6.11). The source position is fixed. On both sides of the sound source, five measurement positions were chosen. The interval between the measurements points is 33 cm (at scale), which corresponds to 10 m in the in-situ measurements. In both scale and in-situ experiment, a reference microphone was placed in the same cross-section as the source (see Figure 6.11).

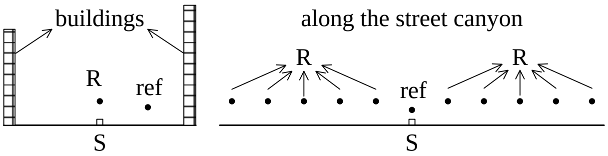

Figure 6.11 Configurations of the scale model for the first group of measurements. The two figures denote different angles of view. In the scale model, the heights of receiver (R) and reference microphone (ref) are 0.06m and 0.05m, respectively.

In the second set of measurements, two 1.8-m long absorbing noise barriers were added to the street canyon, along the interface between the road and the pavements. The receivers were placed above one of these pavements. Three receiver-height levels were used, namely 3.3cm, 5cm and 13.3cm, which correspond to 1m, 1.5m and 4m at full scale. At each receiver-height level, in total nine measurement positions were chosen and the middle position (point 5) is in the same cross-section as the sound source (see Figure 6.12). The interval between adjacent points is 20cm at scale.

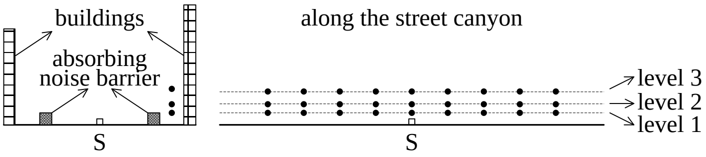

Figure 6.12 Illustration of three receiver-height levels in the scale model. The two figures denote different angles of view. In the scale model, the heights for receiver levels 1, 2 and 3 are 0.033m, 0.05m and 0.133m, respectively.

In the scale model measurements, logarithmical sweep signals were used. The SB29RDC-C000-4 loudspeaker played back a sweep signal from 500 Hz to 35 kHz and afterwards, the Murata ESTD loudspeaker produced a sweep signal from 15 kHz to 96 kHz.

Data analysis

In the measurements, the time-domain pressure was recorded and the fast Fourier transform is used to transfer to the frequency domain. The results were analysed and presented per 1/3-octave band.

Compensation for the excess attenuation of sound by air is needed during the scale-model experiment [86, 87]. This attenuation of sound is caused by classical absorption due to viscous and thermal conduction effects, and relaxation effects of nitrogen and oxygen molecules. Those effects increase non-linearly with frequency. Although the attenuation loss for the frequencies of interest in full scale can be negligible (e.g., up to 0.01 dB/m for 1000Hz according to ISO9613-1:1993), it must be compensated for the frequency range employed at scale (e.g., attenuation loss is around 1 dB/m at 30 KHz for sound propagation through air at 293 K, 53% relative humidity and 1.013 hPa according to ISO 9613-1:1993). In this thesis, a wavelet-based method is applied to correct the excess air attenuation and more details can be found in Hornikx and Forssen's work [87]. Based on the original and measured time signals, a corresponding impulse response can be obtained. In the time-scale plane, the impulse response is corrected for the time and frequency dependent excess air attenuation according to ISO9613-1:1993. A reconstruction gives a new impulse response, corrected for the excess attenuation. The frequency spectrum of the measured signals without air attenuation can be obtained from this new impulse response.

6.2.2 Comparison between in-situ measurement and scale model

The analysis for the in-situ measurements in the Gustaaf Magnelstraat has been presented by Thomas et al. [154, 155]. The comparison is shown in Figure 6.13. For the measurements whose central frequencies of 1/3 octave band at full scale are smaller than or equal to 630 Hz, the temperature and relative humidity in the measurements were 25 °C and 51%, respectively. For the measurements whose central frequencies of 1/3 octave band at full scale are greater than 630 Hz, the temperature and relative humidity in the measurements were 23 °C and 59%, respectively. The relative SPL is the difference of SPL between the measurement point and the reference position (see Figure 6.11 for the configuration of scale model). The value at distance=0m is therefore always 0. The other values are related to the 10 measurement positions. It can be found that although there were obvious differences between scale model and in-situ measurements, they show the similar trend of changes. At some 1/3 octave bands, such as 125, 200, 250, 630, 800, 1600, and 2000Hz, the deviation is much smaller that that at others 1/3-

octave bands, such as 400, 500, 1000 and 2500 Hz. One possible reason can be the presence of destructive or constructive interferences at the reference position. In the scale model, small deviations in the exact positioning between scale model and full scale could lead to large deviations in sound pressure levels under such conditions.

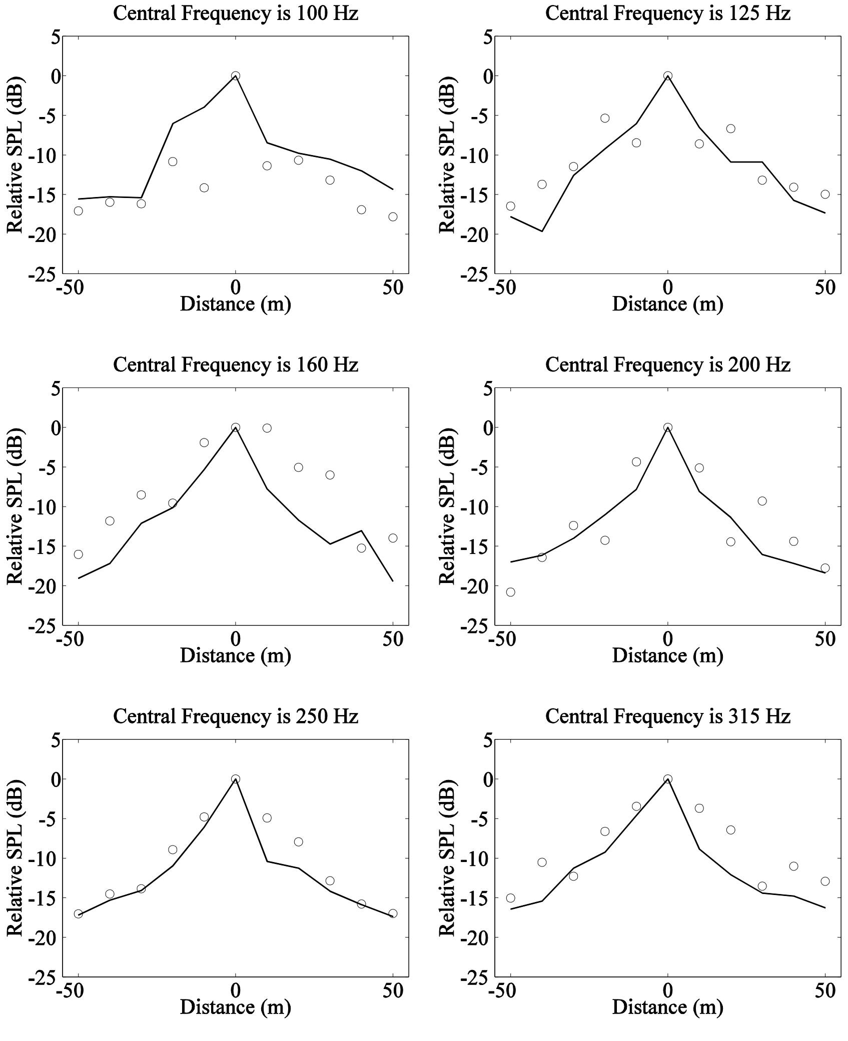

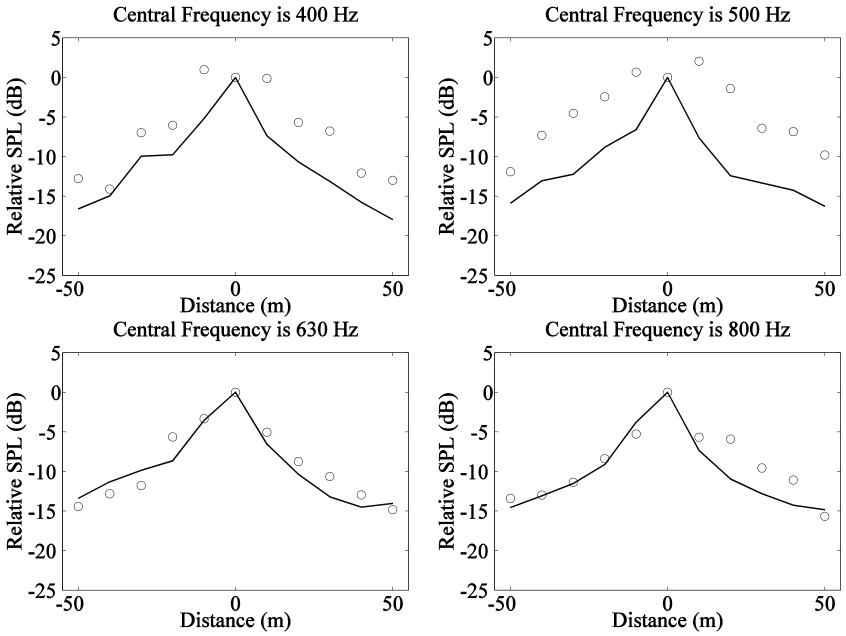
Central Frequency is 400 Hz
Central Frequency is 500 Hz
Central Frequency is 630 Hz
Central Frequency is 800 Hz
Relative SPL (dB)
Distance (m)
5
0
-5
-10
-15
-20
-25
-50
0
50

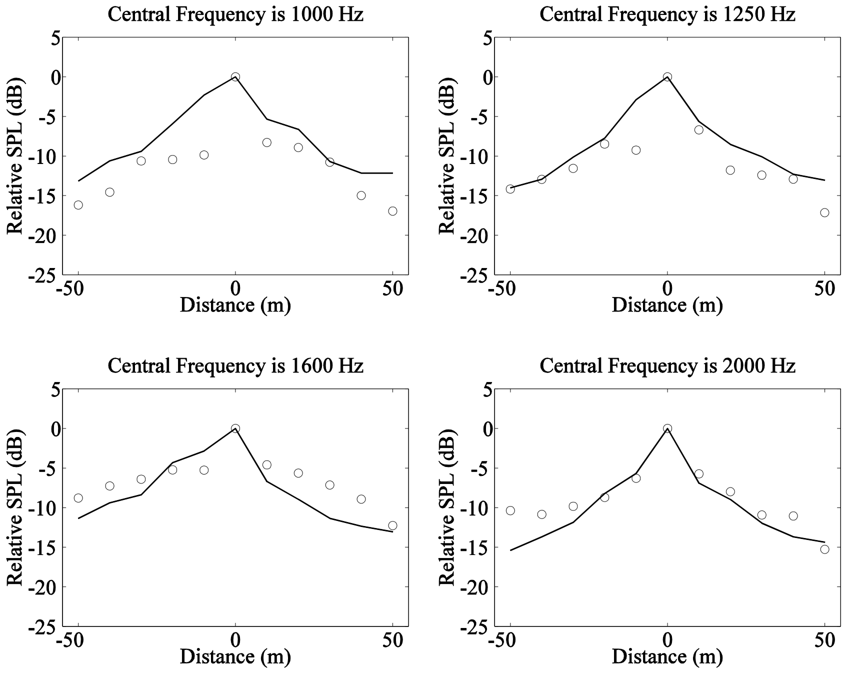
Central Frequency is 1000 Hz
Central Frequency is 1250 Hz
Central Frequency is 1600 Hz
Central Frequency is 2000 Hz
Relative SPL (dB)
Distance (m)
5
0
-5
-10
-15
-20
-25
-50
0
50

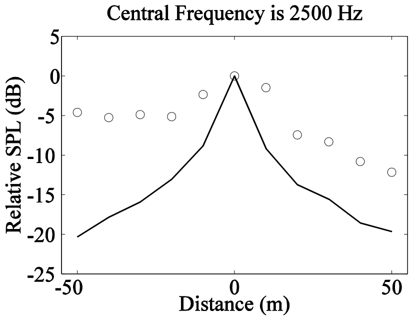

Figure 6.13 Comparison of 1/3-octave band sound pressure levels between the scale model measurements (circles) and the in-situ measurements (solid line). The excess air attenuation has been compensated. Sound pressure levels are referenced to the level at 0 m.

6.2.3 Influence of absorbing noise barrier

The influence of the absorbing noise barrier is studied by the same scale model. Two absorbing noise barriers with a wooden inner bar were placed at both sides of the street canyon. In total, four situations (see Figure 6.14) were considered, which are a rigid ground only (RG), an absorbing noise barrier on a rigid ground (ANB), an empty street canyon (SC) and a street canyon plus an absorbing noise barrier (SC+ANB). In each of these situations, nearly exact positioning was guaranteed by using the VXM Stepping Motor Controller.

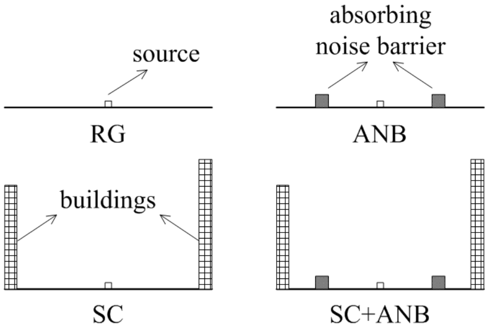

Figure 6.14 Four situations considered in the scale-model measurements.

Three receiver-height levels were considered (see Figure 6.12). The first height is 3.3 cm above the pavement and corresponds to the height of the absorbing noise barrier. This height corresponds to 1m at full scale, which is close to the average height of the ear of a five-year-old child. The second height is 5 cm above the pavement; a direct sound path could reach this receiver. This height corresponds to 1.5m at full scale and is close to the height of the ear of adults. The third height is 13.3 cm above the pavement and the absorbing noise barrier is again too low to block the direct sound. This height corresponds to 4m at full scale and is close to the height of the balcony of the first floor and is the standard height in noise mapping. At each height, there are nine measurement positions. Point 5 is the middle position and is located in the same cross-section as the point source. On both sides of point 5, there are four measurement positions. For the measurements whose central frequencies of 1/3 octave band at full scale are smaller than or equal to 630 Hz, the temperature and relative humidity in the measurements were 18 °C and 48%, respectively. For the measurements whose central frequencies of 1/3 octave band at full scale are greater than 630 Hz, the temperature and relative humidity in the measurements were 23 °C and 54%, respectively.

The relative sound pressure levels for each 1/3 octave band along the measurement points at level 1 is given in Figure 6.15. The SPL at the middle point at receiver-height level 1 in case of a rigid ground only is taken as a reference. The multiple reflections and diffusion in the street canyon have significant influences on the SPL. This conclusion can be drawn by looking at the comparisons between rigid ground (RG: rigid line) and street canyon (SC: solid line with circles) or between absorbing low-height noise barrier (ANB: rigid line with star) and street canyon plus absorbing low-height noise barrier (SC+ANB: dashed line). There are some exceptions, however, such as the difference between SC and RG at 250 Hz and the difference between SC+ANB and ANB at 160 Hz, and these can be attributed to the influences of wave interference. The insertion loss at this receiver-height level can be greater than 10 dB (see Figure 6.16). When the absorbing low-height noise barrier is applied, the direct sounds are blocked. If the street canyon is considered, the reflected and diffused sounds can be absorbed by this noise barrier.

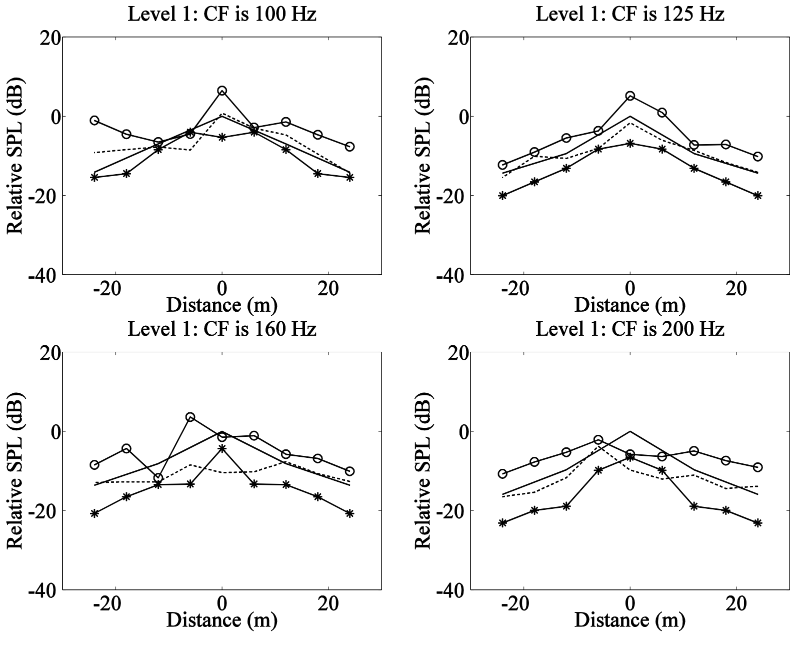

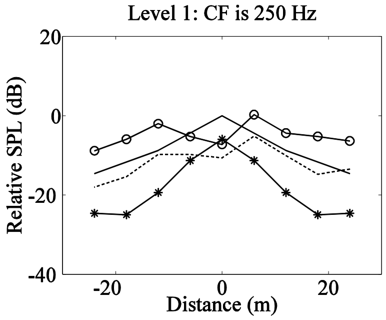
Level 1: CF is 250 Hz

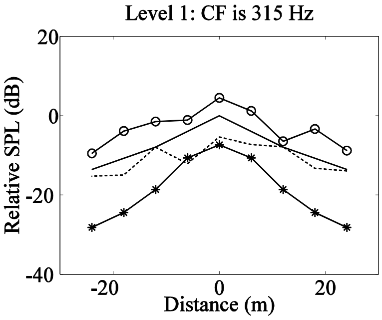
Level 1: CF is 315 Hz

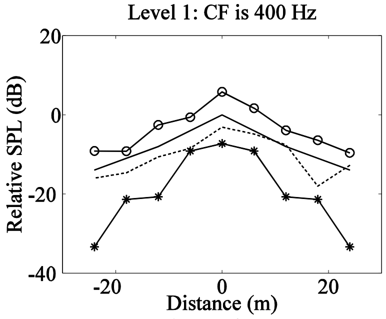
Level 1: CF is 400 Hz

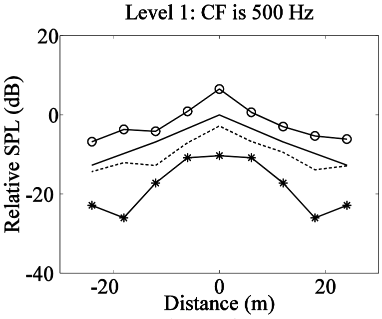
Level 1: CF is 500 Hz

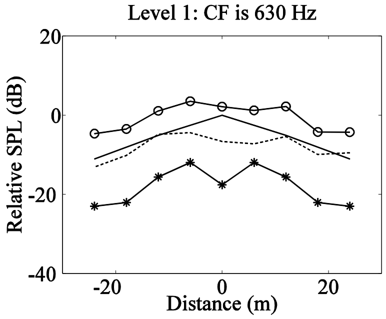
Level 1: CF is 630 Hz

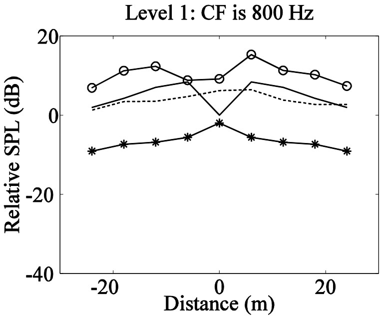
Level 1: CF is 800 Hz

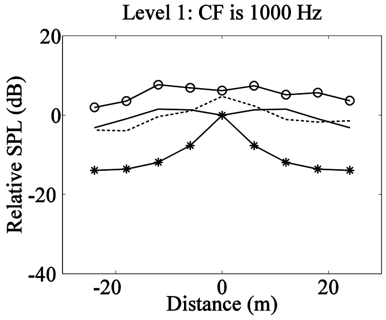
Level 1: CF is 1000 Hz

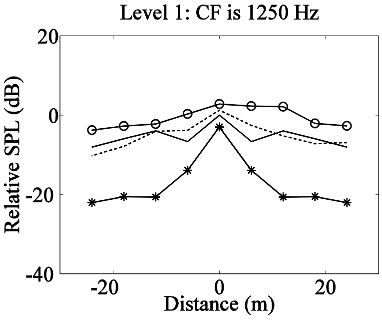
Level 1: CF is 1250 Hz

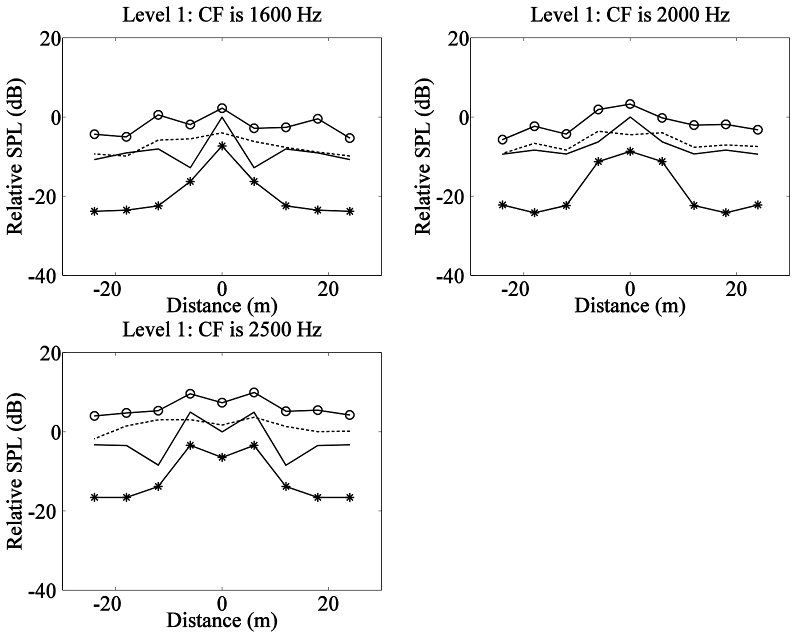

Figure 6.15 Relative sound pressure levels per 1/3 octave band at level 1 for 4 situations: rigid ground (solid line), absorbing noise barrier (solid line with star), street canyon (solid line with circle), street canyon plus absorbing noise barrier (dashed line). CF denotes central frequency and the x-coordinate is the distance from the cross section of the sound source in full scale.

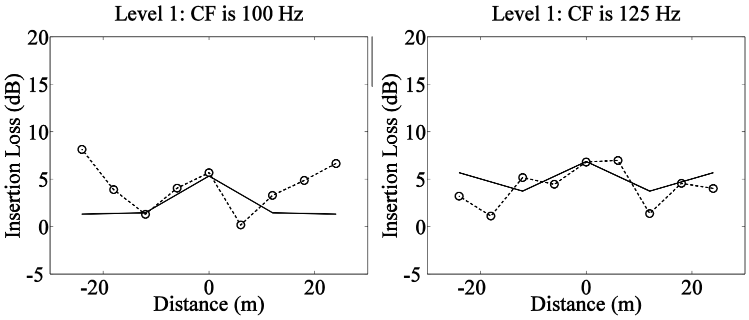

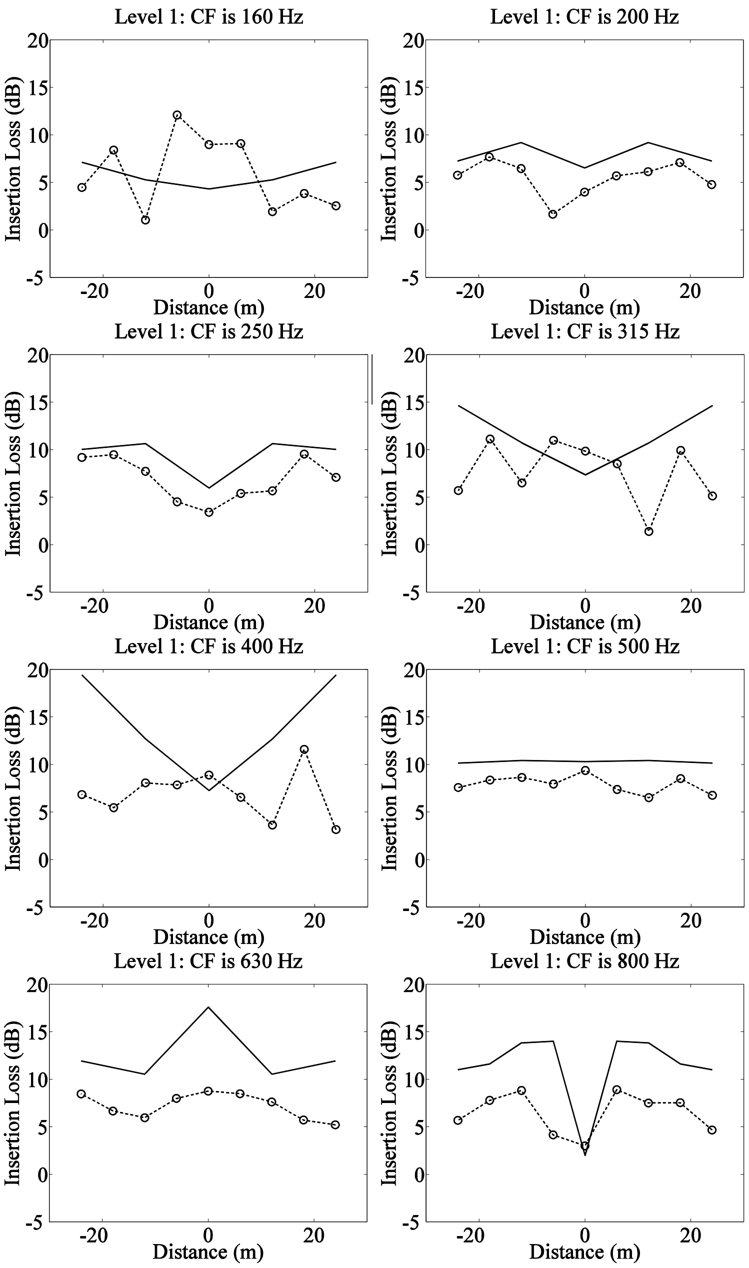
Level 1: CF is 160 Hz
Level 1: CF is 200 Hz
Level 1: CF is 250 Hz
Level 1: CF is 315 Hz
Level 1: CF is 400 Hz
Level 1: CF is 500 Hz
Level 1: CF is 630 Hz
Level 1: CF is 800 Hz
Insertion Loss (dB)
Distance (m)
20
15
10
5
0
-5
-20
0
20

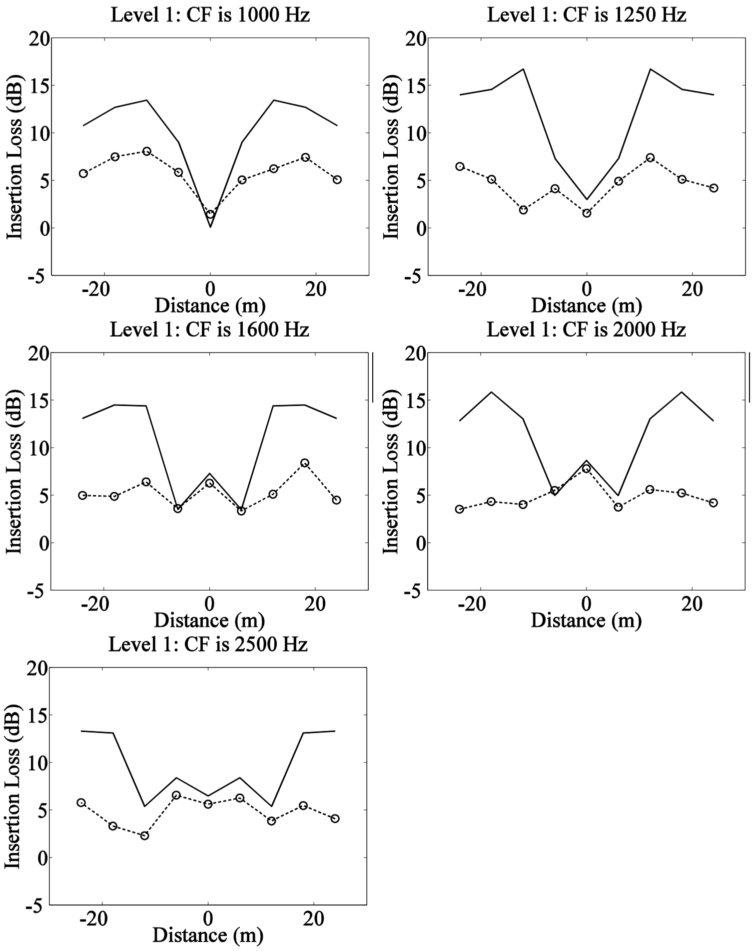

Figure 6.16 Insertion loss of the absorbing noise barriers on rigid ground (solid line) and in street canyon (dashed line with circles) at level 1. CF denotes central frequency and the x-coordinate is the distance from the cross section of the sound source in full scale.

The relative sound pressure levels for each 1/3-octave band along the measurement points at level 2 is given in Figure 6.17. The SPL at the middle point at level 2 in the measurements with rigid ground only is taken as the reference SPL. The influences of the absorbing low-height noise barrier are still important when comparing the results between RG (solid line) and ANB (solid line with stars) and between SC (solid line with circles) and SC+ANB (dashed line). However, the insertion loss of the absorbing noise barrier at level 2 (shown in Figure 6.18) is smaller than that at level 1 (shown in Figure 6.16). Figure 6.17 shows that the effects of multiple reflections and diffusion are also significant, because SC (solid line with circles) and SC+ANB (dashed line) in general have larger sound pressure levels than RG (solid line) and ANB (solid line with stars), respectively. The exceptions can be found because of the effect of wave interferences.

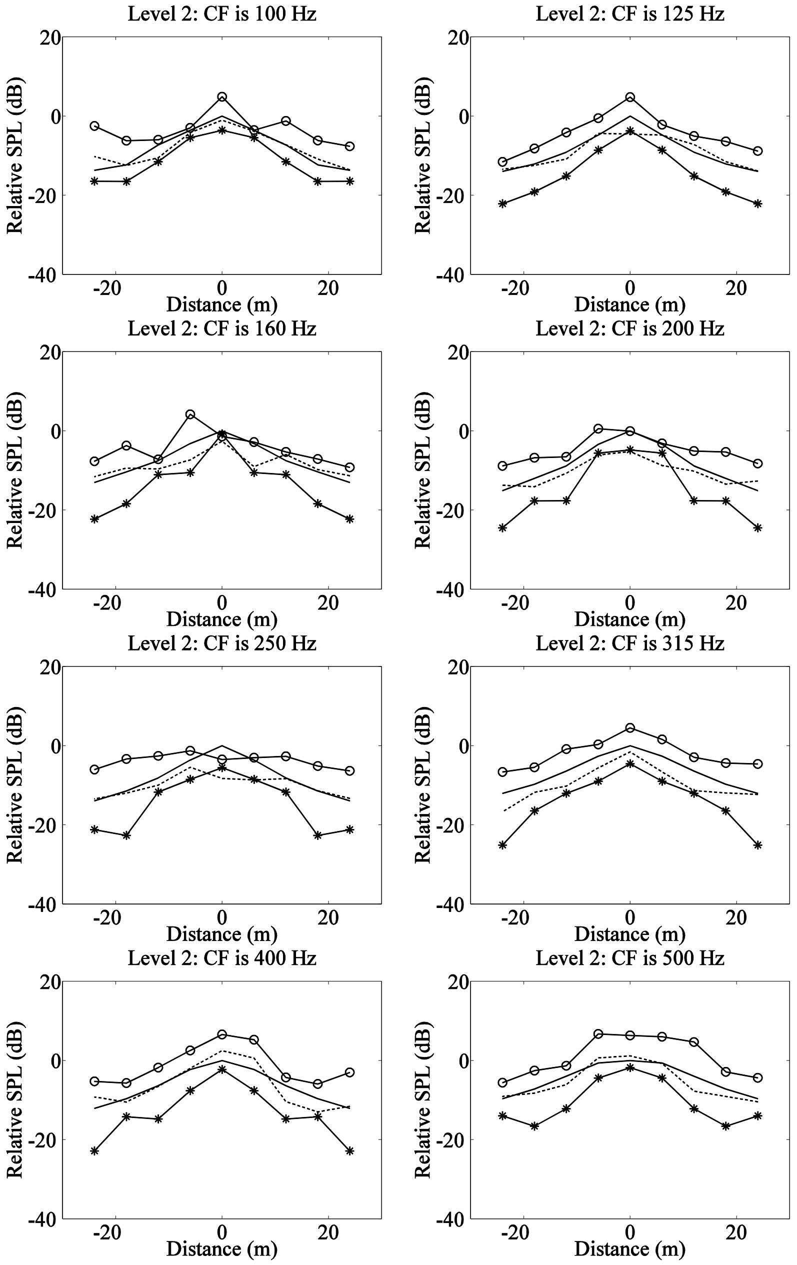

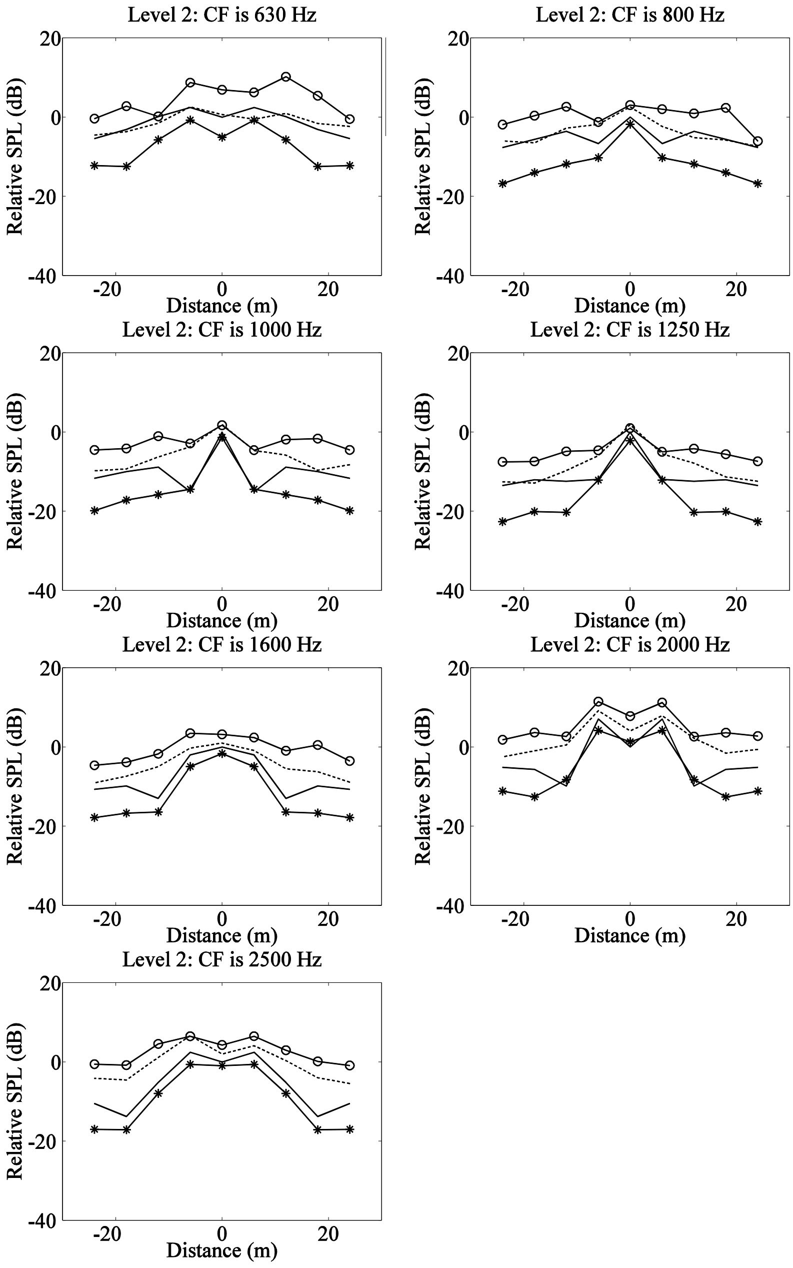

Figure 6.17 Relative sound pressure levels per 1/3 octave band at level 2 for 4 situations: rigid ground (solid line), absorbing noise barrier (solid line with star), street canyon (solid line with circle), street canyon plus absorbing noise barrier (dashed line). CF denotes central frequency and the x-coordinate is the distance from the cross section of the sound source in full scale.

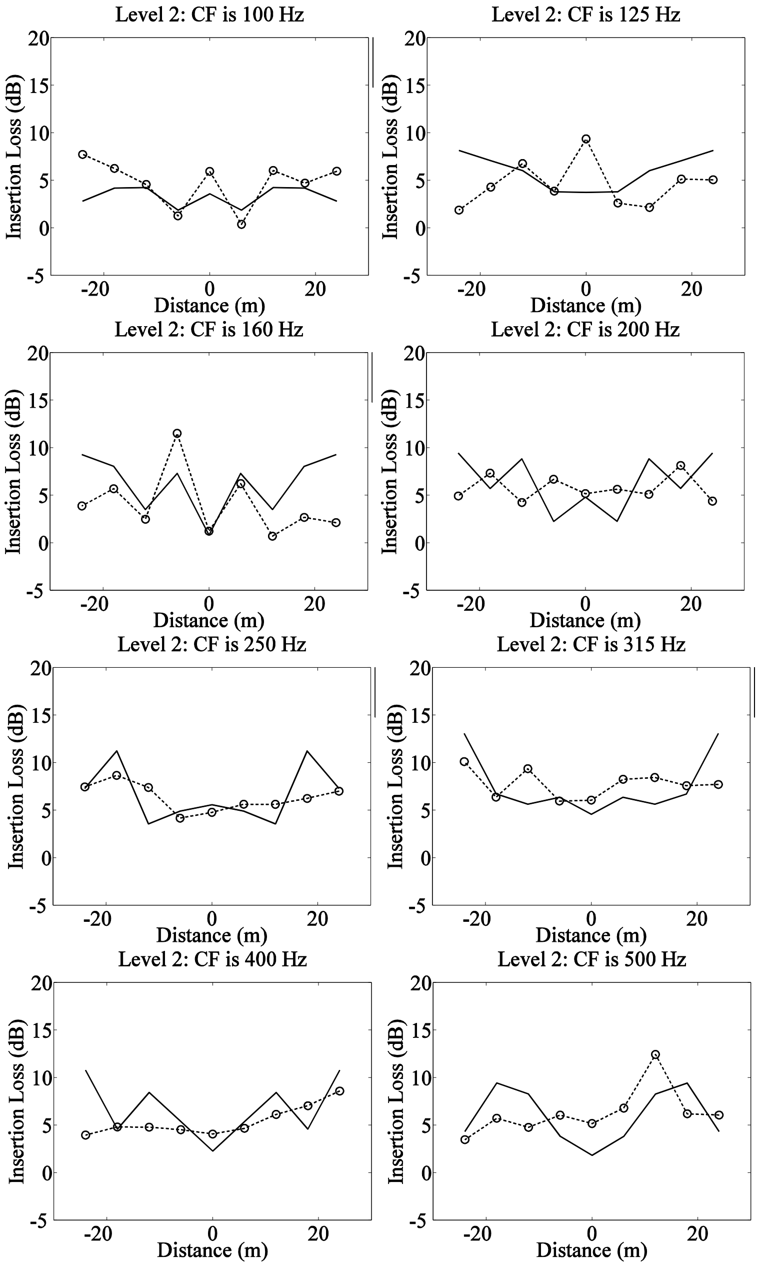

Level 2: CF is 100 Hz

Level 2: CF is 125 Hz

Level 2: CF is 160 Hz

Level 2: CF is 200 Hz

Level 2: CF is 250 Hz

Level 2: CF is 315 Hz

Level 2: CF is 400 Hz

Level 2: CF is 500 Hz

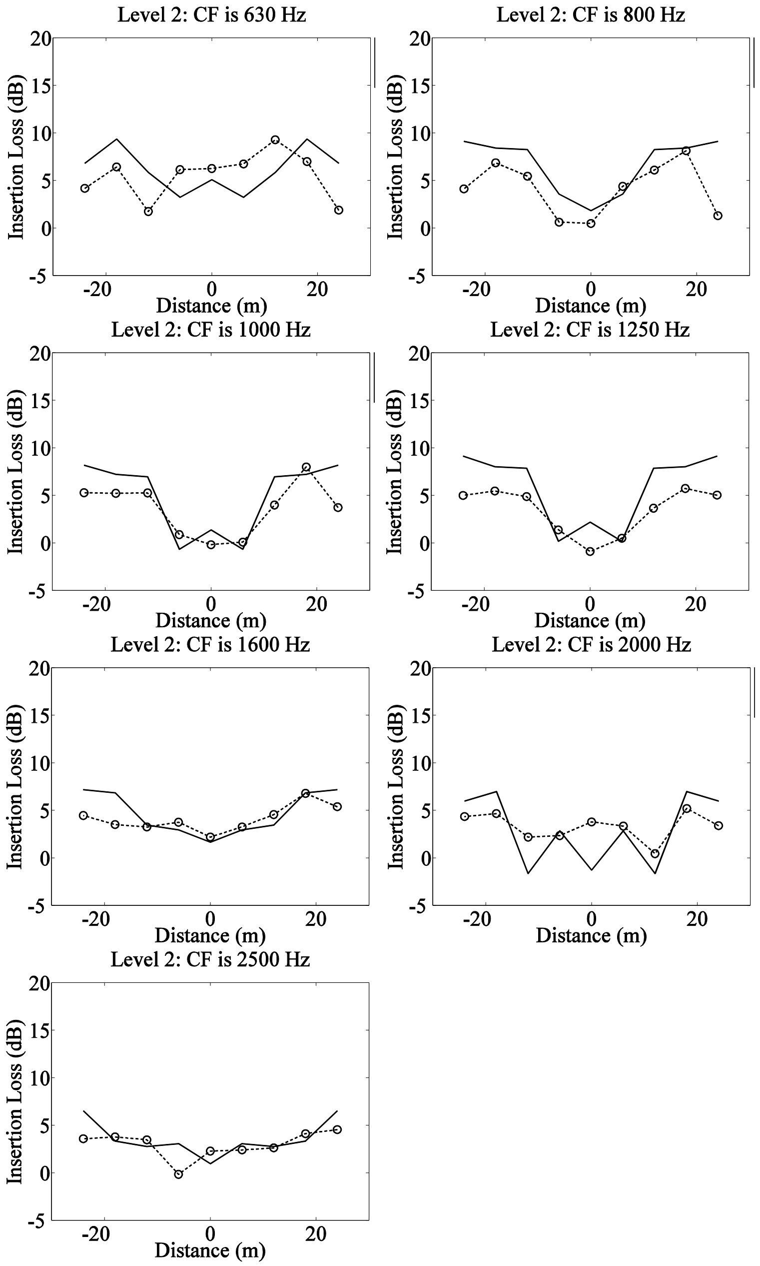

Figure 6.18 Insertion loss of the absorbing noise barriers on rigid ground (solid line) and in street canyon (dashed line with circles) at level 2. CF indicates central frequency and the x-coordinate is the distance from the cross section of the sound source in full scale.

The relative sound pressure levels for each 1/3-octave band along the measurement points at level 3 is given in Figure 6.19. The SPL at the middle point at level 3 in the measurements with rigid ground only is taken as the reference SPL. The insertion loss is shown in Figure 6.20. Similar conclusions as those at levels 1 and 2 can be drawn. According to the insertion loss of these three levels in Figure 6.16, Figure 6.18, and Figure 6.20, it can be concluded that with the increase of the height of the receivers, the influences of absorbing low-height noise barrier become less significant.

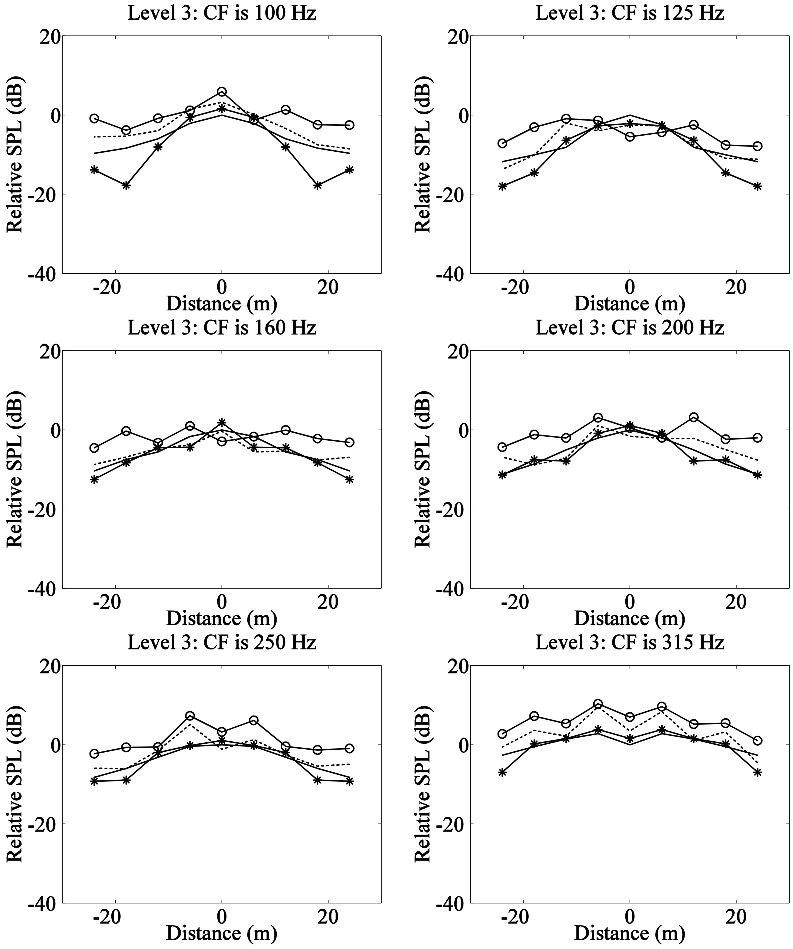

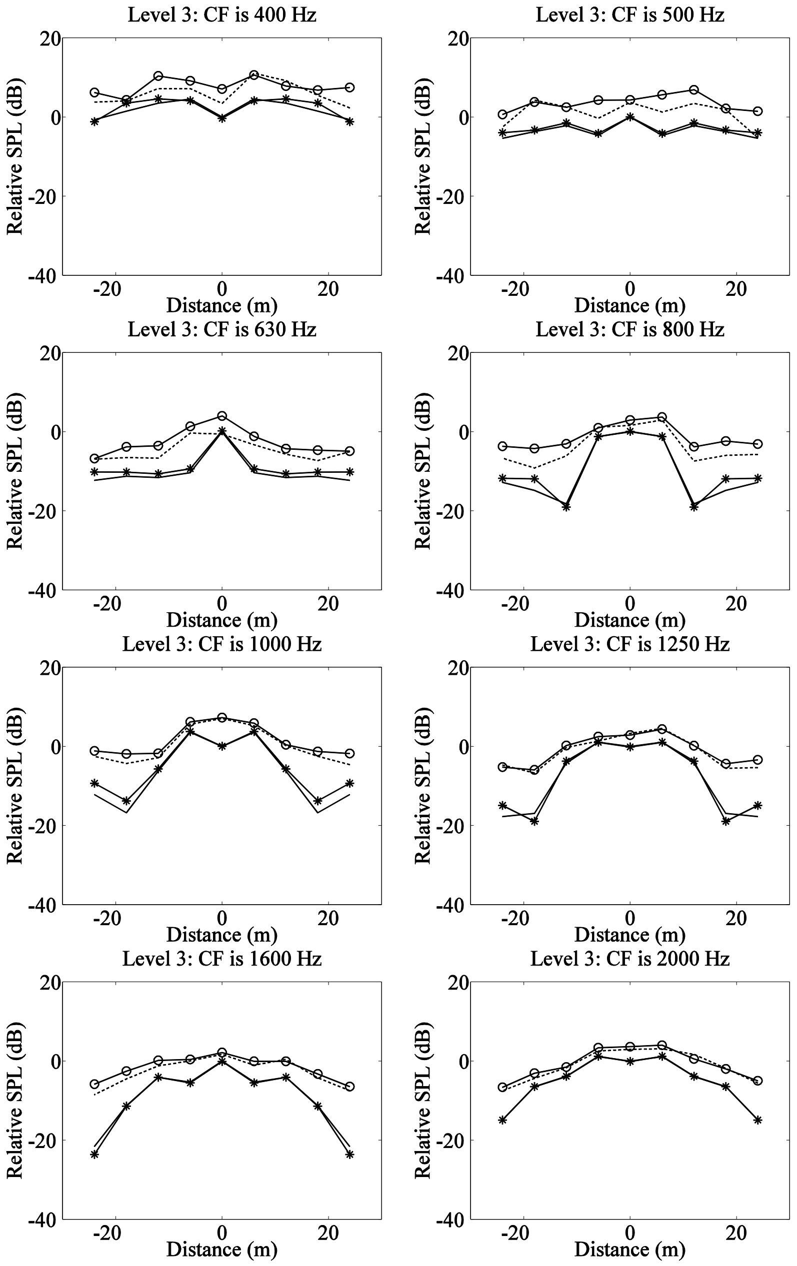
Level 3: CF is 400 Hz
Level 3: CF is 500 Hz
Level 3: CF is 630 Hz
Level 3: CF is 800 Hz
Level 3: CF is 1000 Hz
Level 3: CF is 1250 Hz
Level 3: CF is 1600 Hz
Level 3: CF is 2000 Hz
Relative SPL (dB)
20
0
-20
-40
Distance (m)
-20
0
20

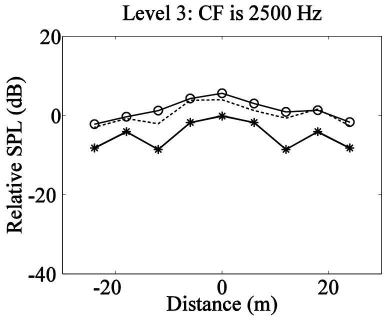

Figure 6.19 Relative sound pressure levels per 1/3 octave band at level 3 for 4 situations: rigid ground (solid line), absorbing noise barrier (solid line with star), street canyon (solid line with circle), street canyon plus absorbing noise barrier (dashed line). CF denotes central frequency and the x-coordinate is the distance from the cross section of the sound source in full scale.

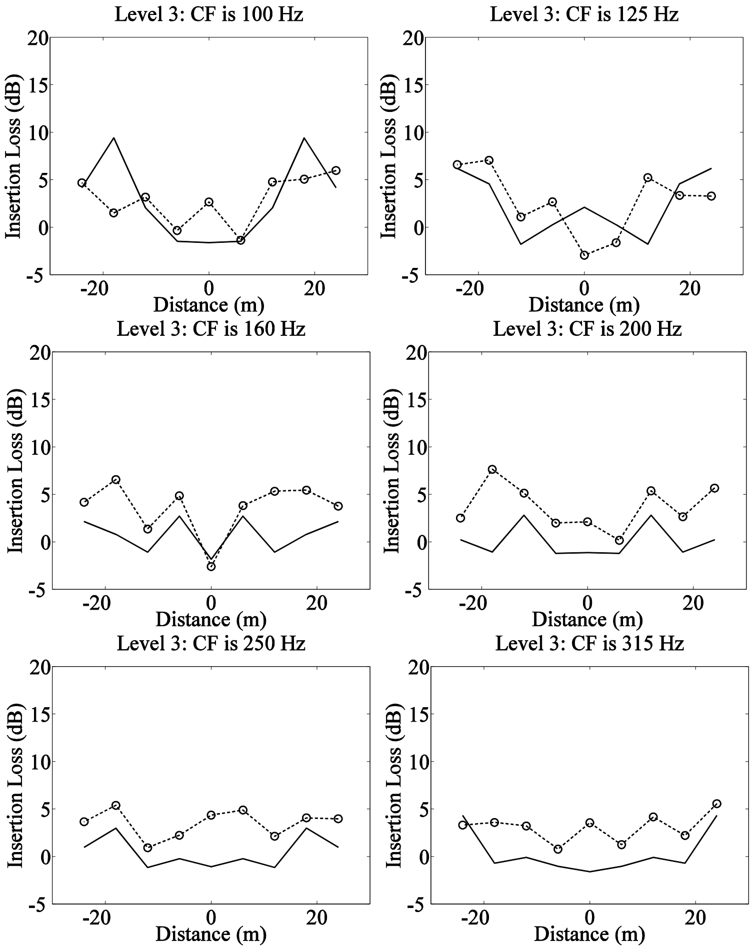

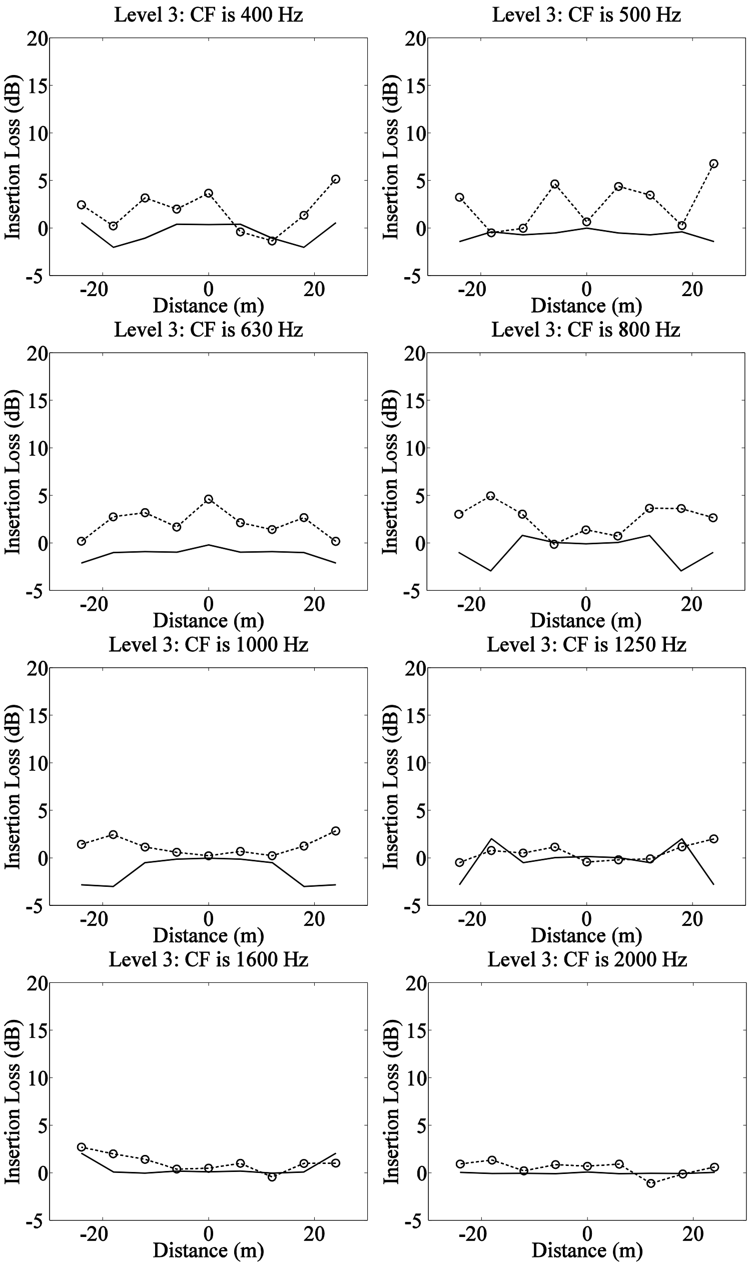
Level 3: CF is 400 Hz
Level 3: CF is 500 Hz
Level 3: CF is 630 Hz
Level 3: CF is 800 Hz
Level 3: CF is 1000 Hz
Level 3: CF is 1250 Hz
Level 3: CF is 1600 Hz
Level 3: CF is 2000 Hz
Insertion Loss (dB)
20
15
10
5
0
-5
Distance (m)
-20
0
20

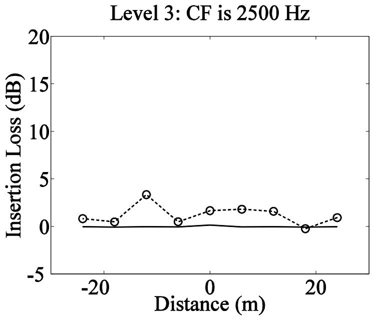

Figure 6.20 Insertion loss of the absorbing noise barriers on rigid ground (solid line) and in street canyon (dashed line with circles) at level 3. CF indicates central frequency and the x-coordinate is the distance from the cross section of the sound source in full scale.

6.2.4 2D-FDTD simulation results

In this section, the measurement results in the cross-section of the sound source are compared with the simulation results by 2D-FDTD model. The measurements were described in section 6.2.3 and in total four situations (rigid ground, absorbing noise barrier, street canyon and street canyon plus an absorbing noise barrier) are considered. The settings in the 2D-FDTD model are the same as those in the scale model measurements. There are two types of building facades considered in the 2D-FDTD model; one is a flat facade and the other is a simplified representation of the facade in the scale model (Figure 6.21). In the 2D-FDTD model, the grid is 0.0005m and the time step is 8.4903×10^{-7}s.

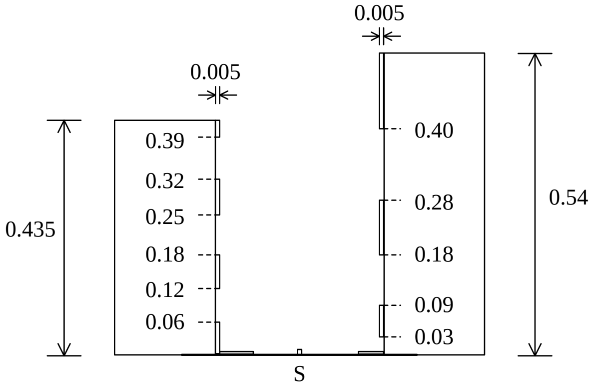

Figure 6.21 Street canyon cross-section, used for the FDTD simulations in case of a uneven facade. The unit is meter.

In the 2D-FDTD model, the building facades and the wooden inner bars are assumed to be rigid. The absorption coefficient of a 7 mm rock-wool sample, which was the same material as used in the scale model, was measured in an impedance tube. Then, a FDTD simulation was conducted and a trail-and-error approach was applied to find a good fit between measurement and simulation. Two FDTD calculations were considered; one calculation uses Zwikker and Kosten's model [91] to simulate the rock-wool and the other uses Biot's model [88, 89]. Although the rigid frame model has been used to simulate rock-wool [156], some other researchers mentioned that a poro-elastic model should be used instead [157]. Biot's model and Zwikker and Kosten's model are both tested here. One of the best fitting results is shown in Figure 6.22; the corresponding porosity, flow resistivity and structure factor for both two models are 0.97, 80 kPa·s·m^{-2}, and 1.02, respectively. The simulations with Biot's model and Zwikker and Kosten's model are in good agreement, except that Biot's model predicts the frame resonance at around 5000 Hz. As the effect of frame resonance on the absorption coefficient is rather small, and focused in a narrow frequency region only, it was chosen to use the rigid-frame model given the significant increase in memory use and computing cost.

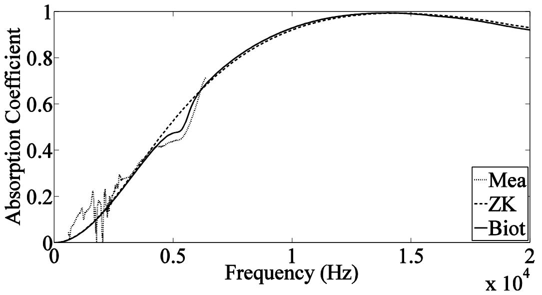

Figure 6.22 Absorption coefficient of a 7mm rock-wool. The dotted line, dashed line and solid line denote the measurement results, the FDTD simulation with Zwikker and Kosten's model and the FDTD simulation with Biot's model, respectively. In both FDTD models, the porosity, flow resistivity and structure factor are 0.97, 80 kPa·s·m^{-2}and 1.02, respectively.

The insertion losses of the absorbing noise barriers on the rigid ground are given in Figure 6.23 - Figure 6.25. It is noticed that there are more obvious differences between FDTD simulation and scale measurements at lower receiver heights, where the influences of low height absorbing noise barrier is significant. For example, in Figure 6.23, the strong fluctuation is not simulated by the FDTD model. One possible reason, which can cause this disagreement between the measurements and the simulations, is the frequency-dependent characteristics of the absorbing materials [88, 89]. In the impedance tube measurement, the maximum frequency should not exceed 6400 Hz (See Figure 6.22), corresponding to 213 Hz at full scale. The characteristics of the absorbing materials at higher frequencies cannot be verified and rely on the suitability of the Zwikker and Kosten’s model with the fitted parameters from the low-frequency range.

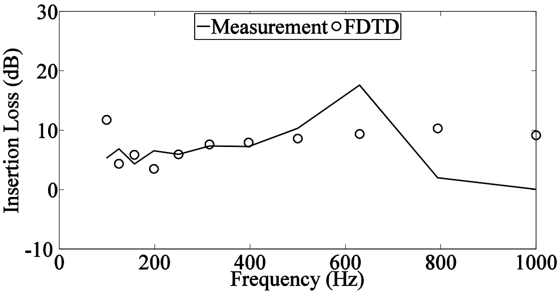

Figure 6.23 Insertion loss of the absorbing noise barrier on the rigid ground at level 1 (1 m above the pavement in full scale).

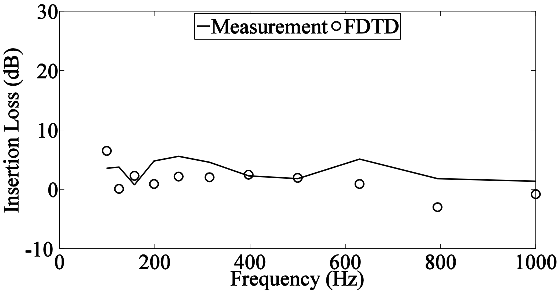

Figure 6.24 Insertion loss of the absorbing noise barrier on the rigid ground at level 2 (1.5 m above the pavement in full scale).

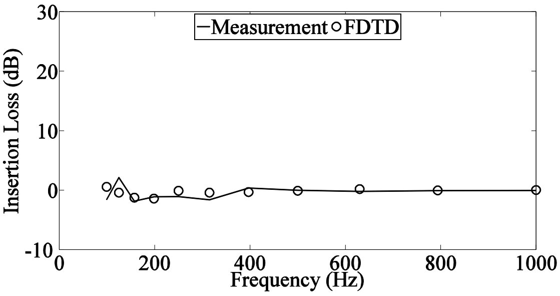

Figure 6.25 Insertion loss of the absorbing noise barrier on the rigid ground at level 3 (4 m above the pavement in full scale).

The insertion losses of the absorbing noise barriers for the street canyon are given in Figure 6.26-Figure 6.28. The simulation results with flat and uneven facades are provided. FDTD simulation results (stars) with uneven building facade are in better agreement with the measurement results (solid line) than the FDTD simulation results (circles) with flat building facades. This shows the importance of incorporating the surface profile of the buildings. However, large differences between FDTD simulations and the scale model can be found, especially at higher frequencies and at lower receiver heights, such as 1000 Hz at levels 1 and 2. The scale model has a complex 3D profile, and the 2D-FDTD simulation assumes that its 2D profile is extended infinitely. Furthermore, the real profile has been simplified. The backscattered waves from further in the street cannot be correctly modelled by a 2D model. Especially at high frequencies, this could be relevant: direct sound cannot reach the measurement point and the diffracted waves are weak compared to the scattered waves.

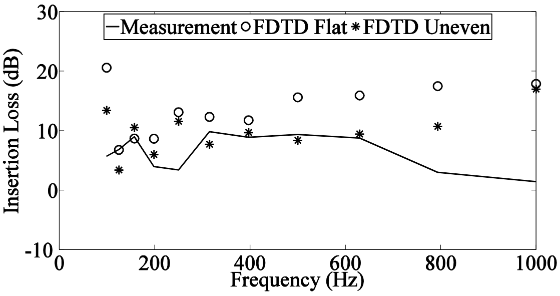

Figure 6.26 Insertion loss of the absorbing noise barrier in the street canyon at level 1 (1 m above the pavement in full scale).

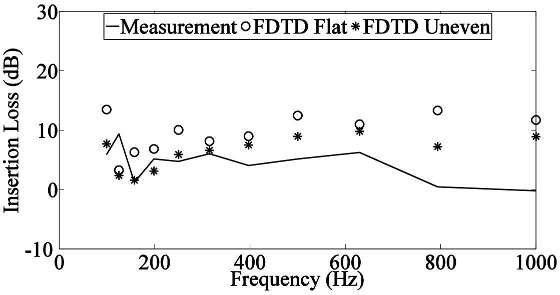

Figure 6.27 Insertion loss of the absorbing noise barrier in the street canyon at level 2 (1.5 m above the pavement in full scale).

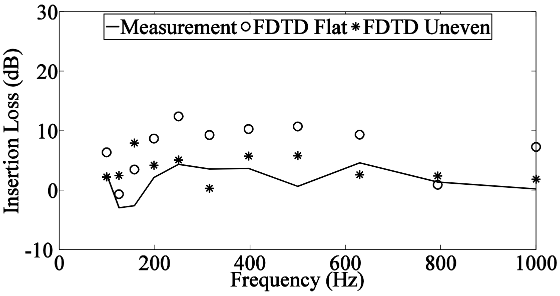

Figure 6.28 Insertion loss of the absorbing noise barrier in the street canyon at level 3 (4 m above the pavement in full scale).

6.3 Conclusions

In section 6.1, the ultra weak variational formulation (UWVF) approach is used to study the effect of semi-transparent road traffic noise barriers of limited height for passengers on the pavement. This numerical method is extended to simulate sound propagation through a porous medium, based on the Zwikker and Kosten’s porous rigid-frame model. Since the UWVF method is a volume-discretisation technique, the effective sound speed approach could be used to model sound propagation in a refracting atmosphere.

Focus is on an efficient approach to calculate noise levels in multi-lane road traffic noise situations. Finding the number of basis functions for each frequency is a time-consuming task. It is approached by three initial evaluations per octave band. For the other frequencies constituting that band, the number of basis functions could be linearly interpolated without any loss in accuracy. Furthermore, it was shown that the exact source location only influences some of the matrices forming the system to be solved. The presence of different source locations, which is typical in mixed multi-lane road traffic, can therefore be solved in an efficient way.

An assessment is made of the use of various porous low-height noise barriers of 1 m high near multi-lane road traffic noise sources. Focus is on the zone were the human ear might be present. The Harmonoise/Imagine road traffic source model is used to predict total traffic noise levels. Depending on the type of traffic and the lane choice, values for the average insertion loss in a zone with heights between 1.5 m to 2 m (and for a distance of up to 5 m behind the noise barrier) range from 2.5 dBA to 9 dBA. The vehicle speeds considered were 30, 50, and 70 km/h. It can therefore be concluded that although such zones are not completely shielded, significant reductions in the sound pressure levels are nevertheless found. The effect of vehicle speed on the insertion loss was shown to be very limited. At lower receiver-height levels, the values for the insertion loss are much higher, and may amount up to 18 dBA. These calculations were performed excluding facade reflections.

Porous barriers can improve noise shielding up to 2 dBA for total road traffic noise, when compared to geometrically identical rigid noise barriers. The flow resistivity of the porous medium was shown to be an important property. However, a detailed optimisation of the porous medium properties is not considered in this study. For more transparent low-height noise barriers, the use of an inner rigid barrier leads to a small improvement in shielding, mainly at lower receiver heights.

In section 6.2, scale model measurements, considering the full geometrical detail of the building facade, have been described. The comparison between the results from the scale model and the in-situ measurements shows good agreement for most 1/3 octave bands.

When porous noise barriers are placed at both sides of the street canyon, the insertion loss significantly decreases compared to a situation without facade reflections (e.g. a non-urban situation). Numerical simulations further show the relevance of including facade irregularities that have a significant impact on the insertion loss of a low-height absorbing noise barrier placed in an urban canyon.

CHAPTER 7 General conclusions and future work

Recently, natural and sustainable materials, such as vegetation, green roofs, green facades, and vegetated low-height noise barriers have been studied to elucidate their potential with respect to noise reduction in urban areas. This thesis aims at enriching already available methods by including the interaction between sound waves and such green materials. Low-height noise barriers and leaves are the focus in this work. Several new schemes have been integrated in the finite-difference time-domain model. The model is then used to study the influence of leaves on the sound field and predict the performance of two-dimensional low-height noise barriers in a street canyon. A highly detailed scale model is constructed to investigate the influence of low-height noise barriers in a street canyon. In view of the important interaction between the street canyon and the barrier that was observed, an improved method, which could tackle some limitations in traditional techniques, and has the potential to be coupled to geometrical acoustic approaches, was sought. A possible candidate, the UWVF method, is used to estimate the effects of two-dimensional low-height noise barriers.

A three-dimensional time-domain (3D-FDTD) model was developed to simulate the effects of leaves on the sound field because the bending and twisting of the leaf caused by the sound could be more easily implemented in the time-domain model. It is assumed that the leaf is isotropic and the air on the leaf surface moves at the same velocity as the leaf in the direction orthogonal to the leaf surface. The theory of thin plates was used to model the bending of leaves and their damping. Besides, the energy damping in the vorticity and entropy boundary layers of leaves was also included in the model.

This model was verified by two types of measurements. The first type measured the pressure difference over the leaf and the velocity of a particular point on the leaf. Seven different leaf species were considered. The measurements agreed reasonably well with the simulations. In the second type of measurements, the sound absorption coefficient of a porous material covered by a leaf was measured in an impedance tube. Two porous materials and four leaves were used. Biot's poro-elastic frame model was implemented in FDTD to simulate frame resonances in the porous materials. The simulations show a good agreement with the measurements and the fluctuations in the measured absorption coefficient can be modelled when the leaf bending is included.

The extended FDTD method was used to study the influences of leaf surface density (LSD) on the materials' absorption coefficient. It showed that the leaves with small LSD resulted in a stronger enhancement in the mid-frequency range (500-2500 Hz). In a next step, the model was applied to study the behaviour of a group of leaves. The efficiency of the calculation was improved by using cyclic boundary conditions. Although the introduced periodicity in the leaf placement can lead to special effects, these occur mainly below the frequencies of interest if the basic simulation cell is kept large enough. An initial field, more particularly a plane wave, was used and the least-square-method was applied to separate the reflected and scattered wave fields. The case studies considered three types of vegetation. The normalized excess attenuation curves show a similar behaviour as in the measurements performed by Aylor [57]. It is also noted that two or three leaves attenuate more energy than one leaf because of stronger backscattering and higher energy dissipation.

A two-dimensional finite-difference time-domain model was used to study the effect of low-height noise barriers in a street canyon. In the FDTD calculations, the absorbing low-height noise barriers were modeled by the Zwikker and Kosten’s model because the effect of frame resonances on the material's absorption coefficient is rather small and the Biot's model involves a higher computational cost. Both flat and uneven facades have been considered in the 2D-FDTD simulation. A highly detailed 1:30 scale model was developed based on a real street canyon. The comparison between the scale model and full-scale measurements confirmed the reliability of the scale model measurements. Furthermore, the measurements in the cross-section of the sound source were compared to simulations showing the importance of accounting for diffuse reflection at the facades.

The scale model measurements investigated the effect of absorbing low-height noise barriers along the street canyon. Three receiver-height levels above the pavement were considered. It was found that absorbing low-height noise barriers have a significant influence on the sound pressure levels at the lowest observation height. This influence decreases when the height of observation increases. The presence of building facades strongly reduces the shielding provided by such low-height barriers.

This work also aimed at developing a full three-dimensional model in order to include effects such as finite length low-height noise barriers or 3D scattering on facades. Because of the high computational cost in full-wave techniques, the method should be sufficiently flexible to allow coupling to other methods. Therefore, the ultra-weak variational formulation (UWVF) method was studied. It was successful in calculating the effects of low-height noise barriers in a two-dimensional problem. Unlike the traditional finite-difference and finite-element methods, needing 10 grid cells per wavelength, two grid cells per wavelength can be used in the UWVF method. Moreover, the sound source doesn't need to be included in the computational domain. Although the application of angularly equal-distributed plane wave basis functions in the UWVF method could cause numerical instability or ill-conditioning, the conditioning of the UWVF could be improved by allowing the number of basis functions to vary within each computational grid cell, because one property of the UWVF method is that its overall conditioning depends on the conditioning of each grid cell. In this thesis, the largest number of basis functions in each grid cell, which allowed the stable solution of the UWVF problem, is used.

As with any frequency domain technique, the UWVF method needs one calculation for each frequency, and a lengthy process is needed to determine the number of basis functions each time the frequency is changed. This work used an efficient way to determine the number of basis functions for the frequencies in the same octave band. The numbers of basis functions in each grid cell are determined at lower, central and upper frequencies of the octave band, and interpolation was used to determine the number of basis function at other frequencies. This approach did not lead to a loss in accuracy, while the computing time was shortened by 40% to 70%, depending on the octave band considered. Besides, when the position of the sound source is changed, the linear system in UWVF method doesn't need to be fully reassembled. This also helps reducing the computational cost in realistic traffic situations (e.g. involving different traffic lanes). Zwikker and Kosten’s model was implemented in the UWVF method to model sound propagation in porous media by introducing a Helmholtz equation with complex wave number and modified fluid density. The Perfectly Matched Layer (PML) theory was applied in the UWVF technique to truncate the unlimited propagation domain.

The UWVF method used in this work was verified by comparison with the finite-difference time-domain (FDTD) method. Two test cases were considered. The first one considers sound propagation over porous ground in a refracting atmosphere and the second one considers sound propagation near a porous barrier. For both cases the results from the UWVF and FDTD were in very good agreement.The potential of the UWVF method in a realistic multi-lane road traffic noise situation was illustrated by studying the effect of a Γ-shaped low-height noise barrier

In the remaining paragraphs, some suggestions for future work are provided. An interesting approach is using an equivalent fluid model to study sound propagation through foliage. Typically, effective medium parameters are deduced by fitting to detailed numerical or analytical techniques. Such an equivalent fluid model is simpler and needs less computational cost. A drawback, however, is that such a model only simulates absorption and neglects the scattering caused by the trunks and leaves. The extended FDTD model could be a good alternative as homogeneity of such an equivalent porous medium does not need to be imposed. The extended FDTD model therefore provides a way to determine the local effective parameters and could improve such an equivalent fluid model.

The methods studied in this thesis, including the FDTD method and the UWVF method, can be coupled with other methods, such as the pseudospectral time-domain method or ray tracing method, in order to solve three-dimensional or large-domain problems. In two-dimensional simulations, the low-height noise barriers and the facades are assumed to be infinitely long with a constant cross-section. This means that the influences of cross roads and complex facades cannot be included. In such a coupled method, the demanding FDTD or UWVF method can be used in the domains surrounding the barriers or the facades, while faster techniques are applied to zones where the sound propagation problem is less complicated.

In this work, focus is primarily on physical noise reduction. An important question remains about how such sounds are perceived, especially for the case that the effect of leaves on sound propagation is in general rather limited. On condition that a sufficiently wide range of sound frequencies can be captured by the numerical approaches, calculated impulse responses could be used to auralise the presence of foliage in different environments (like in an urban street). Based on listening tests the importance of e.g. facade irregularities for the human perception of sound could be assessed as well.

APPENDIX A: Measurement results for leaf vibration

In this appendix, the measurement results for six leaves' vibration are provided below. These 6 leaves include holly (*Ilex*), cherry laurel (*Prunus laurocerasus*), beech (*Fagus*), Japanese cherry (*Prunus serrulata*), elm (*Ulmus*), and butternut (*Juglans cinerea*). Detailed measurement settings and discussion has been given in section 5.1.1, based on the results of the leaf of a lime tree. For the frequency spectrum of the measured velocities, the curves with different colours indicate different repetitions of the measurement and the reference velocity is 10^{-9} m/s.

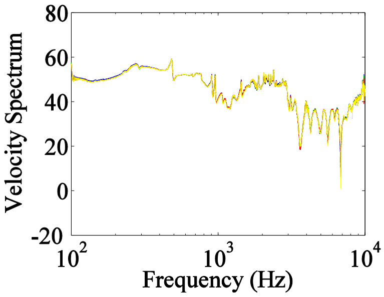

Figure A.1 Frequency spectrum (dB) of the measured velocity for the leaf of a holly tree. The curves with different colour indicate different repetitions of the measurement. The reference velocity is 10^{-9} m/s, which was used in Ref. [18].

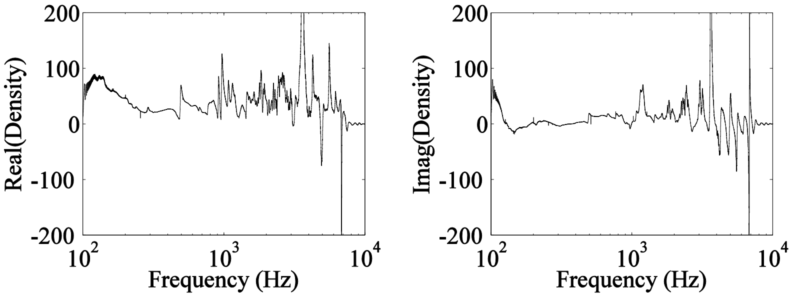

Figure A.2 Average real part (left) and imaginary part (right) of the density spectrum for the leaf of a holly tree.

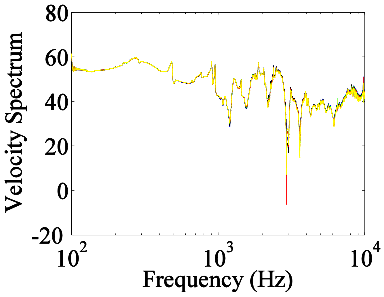

Figure A.3 Frequency spectrum (dB) of the measured velocity for the leaf of a cherry laurel tree. The curves with different colour indicate different repetitions of the measurement. The reference velocity is 10^{-9} m/s, which was used in Ref. [18].

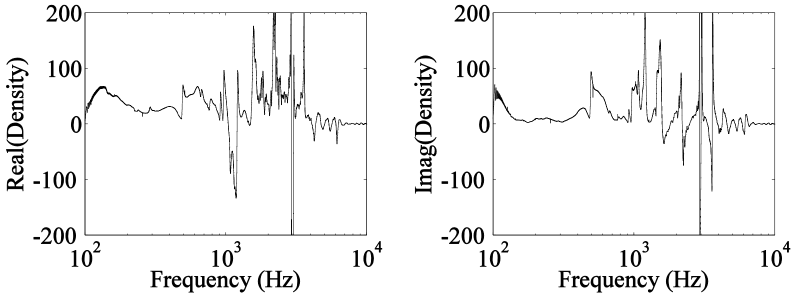

Figure A.4 Average real part (left) and imaginary part (right) of the density spectrum for the leaf of a cherry laurel tree.

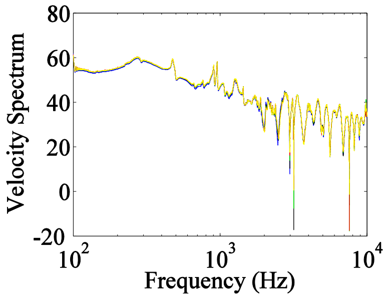

Figure A.5 Frequency spectrum (dB) of the measured velocity for the leaf of a beech tree. The curves with different colour indicate different repetitions of the measurement. The reference velocity is 10^{-9} m/s, which was used in Ref. [18].

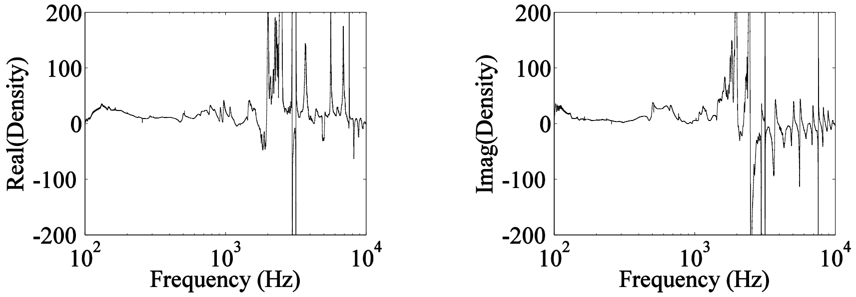

Figure A.6 Average real part (left) and imaginary part (right) of the density spectrum for the leaf of a beech tree.

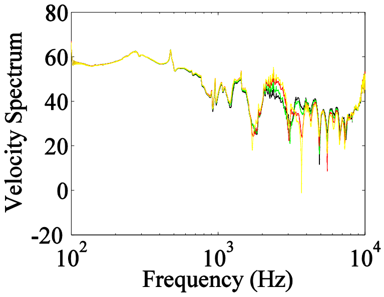

Figure A.7 Frequency spectrum (dB) of the measured velocity for the leaf of a Japanese cherry tree. The curves with different colour indicate different repetitions of the measurement. The reference velocity is 10^{-9} m/s, which was used in Ref. [18].

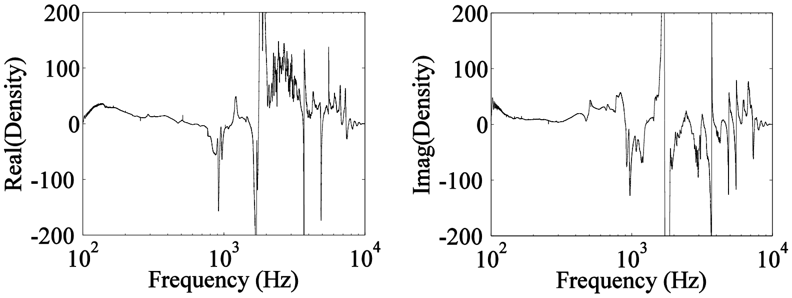

Figure A.8 Average real part (left) and imaginary part (right) of the density spectrum for the leaf of a Japanese cherry tree.

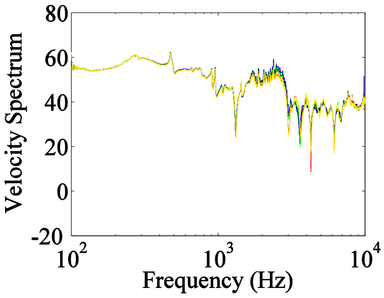

Figure A.9 Frequency spectrum (dB) of the measured velocity for the leaf of a elm tree. The curves with different colour indicate different repetitions of the measurement. The reference velocity is 10^{-9} m/s, which was used in Ref. [18].

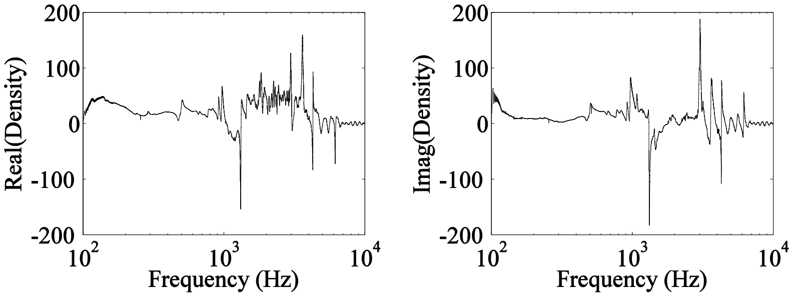

Figure A.10 Average real part (left) and imaginary part (right) of the density spectrum for the leaf of a elm tree.

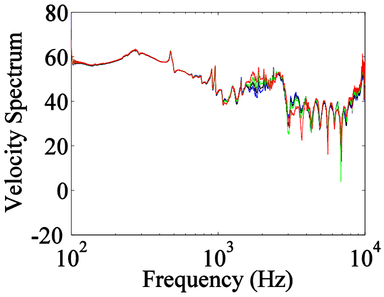

Figure A.11 Frequency spectrum (dB) of the measured velocity for the leaf of a butternut tree. The curves with different colour indicate different repetitions of the measurement. The reference velocity is 10^{-9} m/s, which was used in Ref. [18].

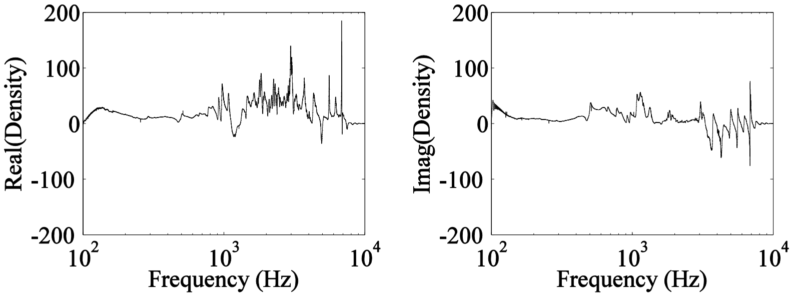

Figure A.12 Average real part (left) and imaginary part (right) of the density spectrum for the leaf of a butternut tree.

References

[1] D. Ouis: Annoyance from road traffic noise: a review. Journal of Environmental Psychology **21**, 101-120 (2001).

[2] R. Klaeboe: Are adverse impacts of neighbourhood noisy areas the flip side of quiet area benefits? Applied Acoustics **68**, 557–575 (2007).

[3] K. V. Horoshenkov, D. C. Hothersall, S. E. Mercy: Scale modeling of sound propagation in a city street canyon. J. Sound Vib. **223,** 795–819 (1999).

[4] P. J. Thorsson: Optimisation of low-height noise barriers using the equivalent sources method. Acta Acustica united with Acustica **86**, 811–820 (2000).

[5] M. Baulac, J. Defrance, P. Jean, F. Minard: Efficiency of noise protections in urban areas: predictions and scale model measurements. Acta Acustica united with Acustica **92**, 530–539 (2006).

[6] H. G. Jonasson: Acoustical source modelling of road vehicles. Acta Acustica united with Acustica **93**, 173–184 (2007).

[7] F. M. Wiener, C. I. Malme and C. M. Gogos: Sound propagation in urban areas. J. Acoust. Soc. Am. **37**, 738-747 (1965).

[8] J. Kang: Sound propagation in street canyons: comparison between diffusely and geometrically reflecting boundaries. J. Acoust. Soc. Am., **107**, 1394-1404 (2000).

[9] J. Kang: Numerical modeling of the sound fields in urban streets with diffusely reflecting boundaries. J. Sound. Vib., **258**, 793-813 (2002).

[10] J. Picaut, L. Simon and J. Hardy: Sound field modeling in a street with a diffusion equation. J. Acoust. Soc. Am., **106**(5), 2638-2645 (1999).

[11] M. Hornix and P. J. Thorsson: On the statistical approach of sound propagation through urban areas. Proceedings of ICSV10, Stockholm, **3**, 1421-1428 (2003).

[12] K. V. Horoshenkov, D. C. Hothersall and S. E. Mercy: Scale modeling of sound propagation in a city street canyon. J. Sound Vib., **223**(5), 795-819 (1999).

[13] C. F. Eyring: Jungle acoustics. J. Acoust. Soc. Am. **18**, 257–270 (1946).

[14] C. F. Fang and D. L. Ling: Investigation of the noise reduction provided by tree belts. Landscape and Urban Planning **63**, 187–195 (2003).

[15] J. Kragh: Road Traffic Noise Attenuation by Belts of Trees. J. Sound Vib. **74**, 235–241 (1981).

[16] D. Heimann: Numerical Simulations of wind and sound propagation through an idealised stand of trees. Acta Acustica united with Acustica **89**, 779–788 (2003).

[17] J. M. Wunderli and E. M. Salomons: A model to predict the sound reflection from forests. Acta Acustica united with Acustica **95**, 76–85 (2009).

[18] M. J. M. Martens and A. Michelsen: Absorption of acoustic energy by

plant leaves. J. Acoust. Soc. Am. **69**, 303–306 (1981).

[19] S. Yamada, T. Watanake, S. Nakamura, H. Yokoyama and S. Takeoke: Noise reduction by vegetation. Inter-Noise **77**, (1977).

[20] M. J. M. Martens: Foliage as a Low-Pass Filter - Experiments with Model Forests in an Anechoic Chamber. J. Acoust. Soc. Am. **67**, 66–72 (1980).

[21] W. Huisman and K. Attenborough: Reverberation and Attenuation in a Pine Forest. J. Acoust. Soc. Am. **90**, 2664-2677 (1991).

[22] K. Attenborough, Kai Ming Li and Kirill Horoshenkov, *Predicting Outdoor Sound*, Taylor & Francis, New York, 2007.

[23] T. Van Renterghem and D. Botteldooren: Effect of a row of trees behind noise barriers in wind. Acta Acustica United with Acustica **88**, 869-878 (2002).

[24] K.V. Horoshenkov, A. Khan, H. Benkreira and A. Mandon: The effect of moisture and soil type on the acoustical properties of green noise control elements. Proc. Forum Acusticum 2011 Aalborg: 845-849 (2011).

[25] N. H. Wong, A. Y. K. Tan, P. Y. Tan, K. Chiang, and N. C. Wong: Acoustics evaluation of vertical greenery systems for building walls. Building and Environment **45**, 411-420 (2010).

[26] T. Van Renterghem, E. Salomons and D. Botteldooren: Parameter study of sound propagation between city canyons with a coupled FDTD-PE model. Appl. Acoust. **67**, 487–510 (2006).

[27] M. Hornikx and J. Forssén: Noise abatement schemes for shielded canyons. Applied Acoustics **70**, 267-283 (2009).

[28] T. Van Renterghem and D. Botteldooren: In-situ measurements of sound propagating over extensive green roofs. Building and Environment, **46** (3), 729-738 (2011).

[29] T. Van Renterghem, D. Botteldooren: Reducing the acoustical façade load from road traffic with green roofs. Building and Environment **44**, 1081–1087 (2009).

[30] T. Van Renterghem, D. Botteldooren: Numerical evaluation of sound propagating over green roofs. J. Sound Vib. **317**, 781–799 (2008).

[31] J. Kang: Sound propagation in street canyons: Comparison between diffusely and geometrically reflecting boundaries. J. Acoust. Soc. Am. **107**, 1394–1404 (2000).

[32] M. Hornikx and J. Forrsén: A scale model study of parallel urban canyons. Acustica united with Acta acustica **94**, 265–281 (2008).

[33] N. Tyurina, A. Nikolski and I. Shubin: Computational and experimental study of acoustical barriers used for traffic noise reduction. Twelfth International Congress on Sound and Vibration, July 11-14, Lisbon (2005).

[34] S. M. B. Fard, N. Kessissoglou, S. Smuels and M. Burgess: Numerical study of noise barrier designs. Proceeding of Acoustics, November 17-20,

Victor Harbor, Australia (2013).

[35] R. Seznec: Diffraction of sound around barriers: use of the boundary element technique. J. Sound Vib. **73**, 195-209 (1980).

[36] D. C. Hothersall, S. N. Chandler-Wilde and M. N. Hajmirzae: Efficiency of single noise barriers. J. Sound Vib. **146**(2), 303-322 (1991).

[37] S. J. Martin and D. C. Hothersall: Numerical modeling of median road traffic noise barriers. J. Sound Vib. **251** (4), 671–681 (2000).

[38] D. Duhamel and P. Sergent: Sound propagation over noise barriers with absorbing ground. J. Sound Vib. **218**(5), 799-823 (1998).

[39] K. M. Li and Q. Wang: A BEM approach to assess the acoustic performance of noise barriers in a refracting atmosphere. J. Sound Vib. **211**(4), 663-681 (1998).

[40] E. Premat and Y. Gabillet: A new boundary-element method for predicting outdoor sound propagation and application to the case of a sound barrier in the presence of downward refreaction. J. Acoust. Soc. Am. **108**, 2775-2783 (2000).

[41] M. Baulac, J. Defrance and P. Jean: Optimisation with genetic algorithm of the acoustic performance of T-shaped noise barriers with a reactive top surface. Applied Acoustics **69**, 332-342 (2008).

[42] T. Ishizuka and K. Fujiwara: Performance of noise barriers with various edge shapes and acoustical conditions. Applied Acoustics **65**, 125-141 (2004).

[43] T. Van Renterghem and D. Botteldooren: Numerical simulation of the effect of trees on downwind noise barrier performance. Acta Acustica united with Acustica **89**, 764–778 (2003).

[44] J. D. Benamou and B. Despres: A domain decomposition method for the helmholtz equation and related optimal control problems, Journal of computational physics **136**, 68-82 (1997).

[45] I. Harari and T. J. R. Hughes: Galerkin/least-square finite element methods for the reduced wave equation with non-reflecting boundary conditions in unbounded domains, Computer Methods in Applied Mechanics and Engineering, **98**, 411-454 (1992).

[46] I. M. Babuska and J. M. Melenk: The partition of unity method, International journal for numerical methods in engineering **40**, 727-758 (1997).

[47] T. Strouboulis, I. Babuska and K. Copps: The design and analysis of the generalized finite element method, Comput. Methods Appl. Mech. Engrg. **181**, 43-69 (2000).

[48] M. Stojek: Least-squares Trefftz-type elements for the Helmholtz equation, International Journal for Numerical methods in Engineering **41**, 831-849 (1998).

[49] P. Monk and D. Q. Wang: A least-squares method for the Helmholtz equation, Comput. Methods Appl. Mech. Engrg. **175**, 121-139 (1999).

[50] B. Pluymers, W. Desmet, D. Vandepitte and P. Sas: Wave based modeling methods for steady-state interior acoustics: an overview, Proceeding of ISMA 2006, 2303-2358 (2006).

[51] O. Cessenat and B. Despres, Application of an ultra weak variational formulation of elliptic PDEs to the two-dimensional Helmholtz problem, SIAM J. Numer. Anal. **35**, 255-299 (1998).

[52] T. Huttunen: The ultra weak variational formulation for ultrasound transmission problems. PhD Thesis, Kuopio University, 2004.

[53] T. Huttunen, P. Monk and J. P. Kaipio: Computational aspects of the ultra-weak variational formulation. Journal of Computational Physics **182**, 27-46 (2002).

[54] O. Cessenat and B. Despres: Using plane waves as base functions for solving time harmonic equations with the ultra weak variational formulation, Journal of Computational Acoustics **11**, 227-238 (2003).

[55] T. F. W. Embleton: Sound propagation in homogeneous deciduous and evergreen woods. J. Acoust. Soc. Am. **35**, 1119-1125 (1963).

[56] D. Aylor: Noise reduction by vegetation and ground. J. Acoust. Soc. Am. **51**, 197-205 (1972)

[57] D. Aylor: Sound transmission through vegetation in relation to leaf area density, leaf width, and breadth of canopy. J. Acoust. Soc. Am. **51**, 411-414 (1972).

[58] C. Magal, M. Scholler, J. Tautz and J. Casas: The role of leaf structure in vibration propagation. J. Acoust. Soc. Am. **108**, 2412-2418 (2000).

[59] S. H. Tang, P. P. Ong and H. S. Wong: Monte Carlo simulation of sound propagation through leafy foliage using experimentally obtained leaf resonance parameters, J. Acoust. Soc. Am. **80**(6), 1740-1744 (1986).

[60] F. Fahy: *Foundation of Engineering Acoustics*, Academic Press, 2001.

[61] D. Botteldooren: Vorticity and entropy boundary conditions for acoustical finite-difference time-domain simulations, J. Acoust. Soc. Am. **102**, 170-178 (1997).

[62] D. Botteldooren: Acoustical finite-difference time-domain simulations in a quasi-Cartesian grid. J. Acoust. Soc. Am. **95**, 2313-2319 (1994).

[63] D. Botteldooren: Numerical model for moderately nonlinear sound propagation in three-dimensional structures. J. Acoust. Soc. Am. **100**(3), 1357-1367 (1996).

[64] K. Yee, Numerical solution of initial boundary values problems involving Maxwell's equations in isotropic media, IEEE Transactions on Antennas and Propagation **14** (3): 302-307 (1966).

[65] D. Botteldooren, Finite-difference time-domain simulation of low-

frequency room acoustic problems, J. Acous. Soc. Am. **98** (6): 3302-3308 (1995).

[66] K. Kowalczyk and M. van Walstijn, Modelling frequency-dependent boundaries as digital impedance fitlers in FDTD and K-DWM room acoustics simulations, Journal of the Audio engineering Society **56**, 569-583 (2008).

[67] L. Savioja, Real-time 3D finite-difference time-domain simulation of low- and mid-frequency room acoustics, Proc. Of the 13th Int. Conference on Digital Audio Effects, Graz, Austria, September 6-10 (2010).

[68] K. Kowalczyk and M. van Walstijn, Room acoustics simulation using 3-D compact explicit FDTD schemes, IEEE Transactions on Audio, Speech, and Language Processing **19** (1), 34-46 (2011).

[69] Timothy Van Renterghem: The finite-difference time-domain method for simulation of sound propagation in a moving medium. PhD thesis 2003.

[70] D. Botteldooren, Time-domain simulation of the influence of close barriers on sound propagation to the environment, J. Acoust. Soc. Am. **101**, 1278-1285 (1997).

[71] R. Blumrich and D. Heimann: A linearized Eulerian sound propagation model for studies of complex meteorological effects. J. Acoust. Soc. Am. **112**, 446–455 (2002).

[72] E. M. Salomons, R. Blumrich and D. Heimann: Eulerian time-domain model for sound propagation over a finite-impedance ground surface. Comparison with frequency-domain models, Acta Acustica United with Acustica **88**, 483-492 (2002).

[73] S. Wang: Finite-difference time-domain approach to underwater acoustic scattering problems. J. Acoust. Soc. Am. **99**, 1924-1931 (1996).

[74] J. Virieux: P-SV wave propagation in heterogeneous media: Velocity-stress finite difference method, Geophysics **51**, 889-901 (1986).

[75] T. Van Renterghem, D. Botteldooren, M. Hornikx, P. Jean, J. Defrance, Y. Smyrnova and J. Kang: Road traffic noise reduction by vegetated low noise barriers in urban streets, EURONOISE 2012, 10-13 June 2012, Prague.

[76] R. H. Lyon: Role of multiple reflections and reverberation in urban noise propagation, J. Acoust. Soc. Am. **55**, 493-503 (1974).

[77] R. Bullen and F. Fricke: Sound propagation in a street, J. Sound Vib. **46**, 33-42 (1976).

[78] D. C. Hothersall, K. V. Horoshenkov and S. E. Mercy: Numerical modelling of the sound field near a tall building with balconies near a road, J. Sound Vib. **198**(4), 507-515 (1996).

[79] J. Picaut: Numerical modeling of urban sound fields by a diffusion process. Applied Acoustics **63**, 965-991 (2002).

[80] J. Kang: Numerical modelling of the sound fields in urban streets with diffusely reflecting boundaries. J. Sound Vib. **258** (5), 793-813 (2002).

[81] M. Ogren and J. Forssen: Modelling of a city canyon problem in a turbulent atmosphere using an equivalent sources approach. Applied Acoustics **65**, 629-642 (2004).

[82] M. Hornikx and J. Forssen: Noise abatement schemes for shielded canyons. Applied Acoustics **70**, 267-283 (2009).

[83] M. Schiff, M. Hornikx and J. Forssen: Excess attenuation for sound propagation over an urban canyon. Applied Acoustics **71**(6), 510-517 (2010).

[84] M. Hornikx an J. Forssen: Modelling of sound propagation to three-dimensional urban courtyards using the extended fourier PSTD method. Applied Acoustics **72**, 665-676 (2011).

[85] K. V. Horoshenkov, D. C. Hothersall and S. E. Mercy: Scale modeling of sound propagation in a city street canyon, J. Sound Vib. **223**(5), 795-819 (1999).

[86] J. Picaut and L. Simon: A scale model experiment for the study of sound propagation in urban areas, Applied Acoustics **62**, 327-340 (2001).

[87] M. Hornikx and J. Forssen: A scale model study of parallel urban canyons, ACTA ACUSTICA UNITED WITH ACUSTICA **94**, 265-281 (2008).

[88] M. A. Biot, Theory of propagation of elastic waves in a fluid-saturated porous solid. I. Low-frequency range, J. Acoust. Soc. Am. **28**, 168-178 (1956).

[89] M. A. Biot, Theory of propagation of elastic waves in a fluid-saturated porous solid. II. Higher frequency range, J. Acoust. Soc. Am. **28**, 179-191 (1956).

[90] J. P. Berenger: A Perfectly Matched Layer for the Absorption of Electromagnetic Waves. Journal of Computational Physics **114**, 185-200 (1994).

[91] C. Zwikker and C. W. Kosten: Sound absorbing materials, Elsevier, New York, 1949.

[92] P. K. Kundu and I. M. Cohen: Fluid Mechanics (Second Edition), Academic Press, San Diego, 2002.

[93] P. M. Morse and K. U. Ingard: Theoretical Acoustics, McGraw-Hill Book Company, 1968.

[94] M. W. Sprague and J. M. Sabatier: Acoustic scattering from vegetation. J. Acoust. Soc. Am. **99** (4), 2488-2500 (1996).

[95] M. A. Price, K. Attenborough and N. W. Heap: Sound attenuation through trees: measurements and models. J. Acoust. Soc. Am. **84**(5), 1836-1844 (1988).

[96] W. H. T. Huisman and K. Attenborough: Reverberation and attenuation in a

pine forest. J. Acoust. Soc. Am. **90**(5), 2664-2677 (1991).

[97] O. Umnova, K. Attenborough and C. M. Linton: Effects of porous covering on sound attenuation by periodic arrays of cylinders. J. Acoust. Soc. Am. **119**(1), 278-284 (2006).

[98] C. Gromke and B. Ruck: Aerodynamic modelling of trees for small-scale wind tunnel studies. Forestry **81**(3), 243-258 (2008).

[99] Standard handbook for mechanical engineers, McGraw-Hill, New York, 3-66, 2007.

[100] H. Hosaka, K. Itao and S. Kuroda: Evaluation of energy dissipation mechanisms in vibrational microactuators. MEMs ’94, 193-198 (1994).

[101] L. Rhaouti, A. Chaigne and P. Joly: Time-domain modeling and numerical simulation of a kettledrum. J. Acoust. Soc. Am. **105**, 3545-3562 (1999).

[102] M. S. Howe: *Acoustics of Fluid-Structure Interactions*. Cambridge University Press 1998

[103] A. Chaigne and C. Lambourg: Time-domain simulation of damped impacted plate. I. Theory and experiments, J. Acoust. Soc. Am. **109** (4), 1422-1432 (2001).

[104] C. Lambourg, A. Chaigne and D. Matignon: Time-domain simulation of damped impacted plate. II. Numerical model and results, J. Acoust. Soc. Am. **109** (4), 1433-1447 (2001).

[105] A. D. Pierce, Acoustics, McGraw-Hill, New York, 1981.

[106] K. Attenborough, I. Bashir and S. Taherzadeh: Outdoor ground impedance models, J. Acoust. Soc. Am. **129**, 2806–2819 (2011).

[107] J. F. Allard and N. Atalla: Propagation of sound in porous media: modelling sound absorbing materials (2rd version). John Wiley & Sons, Ltd. pp130 2009.

[108] Yan Qing Zeng and Qing Huo Liu: Acoustic detection of buried objects in 3-D fluid saturated porous media: Numerical Modeling. IEEE TRANSACTIONS ON GEOSCIENCE AND REMOTE SENSING. **39**(6) 1165-1173 (2001).

[109] Hefeng Dong, Amir M. Kaynia, Christian Madshus and Jens M. Hovem: Sound propagation over layered poro-elastic ground using a finite-difference model. J. Acoust. Soc. Am. **108**(2) 494-502 (2000).

[110] C. N. Wang, Y. M. Kuo and S. K. Chen: Effects of compression on the sound absorption of porous materials with an elastic frame. Applied Acoustics **69**, 31-39 (2008).

[111] M. A. Biot: Mechanics of deformation and acoustic propagation in porous media. Journal of Applied Physics **33**, 1482-1498 (1962).

[112] A. Sommerfeld: Lectures on Theoretical Physics, Academic Press, New York, 1964.

[113] J. B. Keller and D. Givoli: Exact non-reflecting boundary conditions,

Journal of computational physics **82**(1), 172-192 (1989).

[114] J. G. Marcus and B. K. Joseph: On Nonreflecting Boundary Conditions. Journal of Computational Physics **122**, 231-243 (1995).

[115] B. Engquist and A. Majda: Absorbing boundary conditions for the numerical simulation of waves, Mathematics of Computation **31**(139), 629-651 (1977).

[116] F. Treves: Introduction to pseudodifferential and Fourier integral operators, Vol. 1. Pseudodifferential operators, Plenum Press, New York, 1980.

[117] A. Bayliss and E. Turkel: Radiation boundary conditions for wave-like equations, Communications in Pure and Applied Mathematics **33**, 707-725 (1980).

[118] K. Feng: Finite element method and natural boundary reduction, Proceedings of the International Congress of Mathematicians, Warsaw, Poland, 1983.

[119] G. Kriegsmann and C. Morawetz: Solving the Helmholtz equation for exterior problems with variable index of refraction: I, SIAM Journal on Scientific and Statistical Computing **1**(3), 371-385 (1980).

[120] R. L. Higdon: Absorbing boundary conditions for difference approximations to the multi-dimensional wave equation, Mathematics of Computation **47**(176), 437-459 (1986).

[121] L. N. Trefethen and L. Halpern: Well-posedness of one-way wave equations and absorbing boundary condition, Mathematics of Computation, **47** 421-435 (1986).

[122] E. L. Lindman: Free space boundary conditions for the time dependent wave equation, J. Comput. Phys. **18**, 66-78 (1975).

[123] J. P. Berenger: Perfectly matched layer for the FDTD solution of wavestructure interaction problems. IEEE Antennas Propagation Symposium **44**, 110-117 (1996).

[124] F. D. Hastings, J. B. Schneider, S. L. Broschat: Application of the perfectly matched layer (PML) absorbing boundary condition to elastic wave propagation. J. Acoust. Soc. Am. **100**, 3061-3069 (1995).

[125] Annelies Bockstael: Modelling, measurement and optimization of passive and active custom-made hearing protectors. PhD thesis, Ghent University, 2010.

[126] A. Bockstael, B. de Greve, T. Van Renterghem, D. Botteldooren, W. D’Haenens, H. Keppler, L. Maes, B. Philips, F. Swinnen and B. Vinck: Verifying the attenuation of earplugs in situ: Method validation using artificial head and numerical simulations, J. Acoust. Soc. Am. **124**, 973-981 (2008).

[127] Joho C. Strikwcrda: *Finite Difference Schemes and Partial Differential Equations*, Society for Industrial and Applied Mathematics, 2004.

[128] T. Saito, K. Soga, T. Hoson and I. Terashima: The bulk elastic modulus and the reversible properties of cell walls in developing Quercus leaves, Plant Cell Physiol. **47**(6), 715-725 (2006).

[129] K. G. Satyanarayana, C. K. S. Pillai, K. Sukumaran, S. G. K. Pillai, P. K. Rohatgi and K. Vijayan: Structure property studies of fibres from various parts of the coconut tree, Journal of materials science **17,** 2453-2462 (1982).

[130] R. M. N. Arib, S. M. Sapuan, M. M. H. M. Ahmad, M. T. Paridah and H. M. D. Khairul Zaman: Mechanical properties of pineapple leaf fibre reinforced polypropylene composites, Materials and Design **27**, 391-396 (2006).

[131] U. Niinemets, “Global-scale climatic controls of leaf dry mass per area, density, and thickness in trees and shrubs,” Ecology **82**, 453–469 (2001).

[132] T. Saito, T. Tanaka, H. Tanabe, Y. Matsumoto and Y. Morikawa: Variations in transpiration rate and leaf cell turgor maintenance in saplings of deciduous broad-leaved tree species common in cool temperate forests in Japan, Tree Physiology **23**, 59-66 (2003).

[133] F. G. Scholz, S. J. Bucci, G. Goldstein, F. C. Meinzer, A. C. Franco and F. Miralles-Wilhelm: Boiphysical properties and functional significance of stem water storage tissues in Neotropical savanna trees, Plant, Cell and Environment **30**, 236-248 (2007).

[134] A. Nardini, E. Gortan, M. Ramani and S. Salleo: Heterogeneity of gas exchange rates over the leaf surface in tobacco: an effect of hydraulic architecture?, Plant, Cell and Environment **31**, 804-812 (2008).

[135] J. W. White and C. Montes-R.: Variation in parameters related to leaf thickness in common bean (Phaseolus vulgaris L.), Field Crops Research **91**, 7-21 (2005).

[136] R. A. Marenco, S. A. Antezana-Vera and H.C.S. Nascimento: Relationship between specific leaf area, leaf thickness, leaf water content and SPAD-502 reading in six Amazonian tree species, Photosynthetica **47**(2): 184-190 (2009).

[137] D. Vile, E. Garnier, B. Shipley, G. Laurent, M. L. Navas, C. Roumet, S. Lavorel, S. Diaz, J. G. Hodgson, F. Lloret, G. F. Midgley, H. Poorter, M. C. Rutherford, P. J. Wilson and I. J. Wright: Specific leaf area and dry matter content estimate thickness in laminar leaves, Annals of Botany **96**, 1129-1136 (2005).

[138] K. J. Niklas: Plant Biomechanics: An Engineering Approach to Plant form and Function, pp. 68-75, The University of Chicago Press, Chicago, 1992.

[139] http://cronodon.com/BioTech/Plant_Bodies_Cell_Types.html

[140] K. Wilson, V. Ostashev, S. Collier, N. Symons, D. Aldridge and D. Marlin: Time-domain calculations of sound interactions with outdoor ground

surfaces. Applied Acoustics **68**, 173–200 (2007).

[141] T. Huttunen, J. P. Kaipio, P. Monk: The perfectly matched layer for the ultra weak variational formulation of the 3D Helmholtz equation. International Journal for Numerical Methods in Engineering **61,** 1072–1092 (2004).

[142] R. Blumrich and D. Heimann: Numerical estimation of atmospheric approximation effects in outdoor sound propagation modeling. Acta Acustica united with Acustica **90**, 24–37 (2004).

[143] K. Attenborough: Ground parameter information for propagation modeling. J. Acoust. Soc. Am. **92**, 418–427 (1992).

[144] ISO 10534-2, Acoustics-Determination of sound absorption coefficient and impedance in impedance tubes-Part 2: Transfer-function method, International Organization for Standardization (Geneva, Switzerland, 1998).

[145] S. Mahasaranon, K. V. Horoshenkov, A. Khan and H. Benkreira: The effect of continuous pore stratification on the acoustic absorption in open cell foams, J. Appl. Phys. **111**, 084901 (2012).

[146] K. V. Horoshenkov, A. Khan, H. Benkreira, A. Mandon and R. Rohr, “The effect of moisture and soil type on the acoustical properties of green noise control elements,” Proceedings of Forum Acusticum 2011, Aalborg, Denmark, (2011).

[147] R. Dragonetti, C. Ianniello and R. A. Romano: Measurement of the resistivity of porous materials with an alternating air-flow method, J. Acoust. Soc. Am. **129**, 753-764 (2008).

[148] N. Kino and T. Ueno: Comparisons between characteristic lengths and fibre equivalent diameters in glass fibre and melamine foam materials of similar flow resistivity, Appl. Acoust. **69**, 325–331 (2008).

[149] E. P. D. Mansard and E. R. Funke: The measurement of incident and reflected spectra using a least square method, Proc. 17th Coastal Engrg. Conf. **1**, 154-172 (1980).

[150] T. Van Renterghem, E. M. Salomons and D. Botteldooren: Efficient FDTD-PE model for sound propagation in situations with complex obstacles and wind profiles. Acta Acustica united with Acustica **91**, 671–679 (2005).

[151] D. N. May and M. M. Osman: Highway noise barriers: new shapes. J. Sound Vib. **71**(1), 73-101 (1980).

[152] M. J. Crocker: Handbook of Acoustics, John Wiley & Sons, Inc. pp310 1998.

[153] Collaborative Project: HOSANNA-Holistic and sustainable abatement of noise by optimized combinations of natural and artificial means, Technical Report, N°234306 (2010).

[154] P. Thomas, L. Dragonetti, T. Van Renterghem and D. Botteldooren: Detailed analysis of the sound field in a scale model of a street canyon, EAA EuroRegio 2010, 15-18 September 2010, Ljubljana, Slovenia (2010).

[155] P. Thomas, T. Van Renterghem, E. De Boeck, L. Dragonetti and D. Botteldooren: Reverberation-based urban street sound level prediction. J. Acoust. Soc. Am. **133**(6), 3929-3939 (2013).

[156] P. H. Mareze, A. Lenzi and C. Pellegrini: Rigid-frame porous material acoustic attenuation on compressor discharge. 21st International Compressor Engineering Conference, July, Purdue University, (2012).

[157] N. Geebelen: Structure-borne sound sensitivity of building structures. PhD Thesis, Katholieke Universiteit Leuven (2008).